An experimental approach to the realization and characterization of the two-dimensional Dirac nodal line materials Cu2Si and Cu2Ge. Influence of the substrate and of Pb deposition on the electronic band structure

Mathis Cameau

▶ To cite this version:

Mathis Cameau. An experimental approach to the realization and characterization of the two-dimensional Dirac nodal line materials Cu2Si and Cu2Ge. Influence of the substrate and of Pb deposition on the electronic band structure. Materials Science [cond-mat.mtrl-sci]. Sorbonne Université, 2022. English. NNT : 2022SORUS075 . tel-03828417

HAL Id: tel-03828417

https://theses.hal.science/tel-03828417

Submitted on 25 Oct 2022

Sorbonne Université
École Doctorale 397 Physique et Chimie des Matériaux
Institut des Nanosciences de Paris

An experimental approach to the realization and characterization of the two-dimensional Dirac nodal line materials Cu_2Si and Cu_2Ge

Influence of the substrate and of Pb deposition on the electronic band structure

By Mathis CAMEAU

PhD Thesis in Physics and Chemistry of Materials

Presented and defended on the 19/05/2022

In front of a jury constituted of:

Antonio TEJEDA	Directeur de recherche	Reviewer
Christine RICHTER	Professeur	Reviewer
Thomas JAOUEN	Chargé de recherche	Jury member
Sergio VLAIC	Maître de conférences	Jury member
Laurent SIMON	Directeur de recherche	Jury member
Andrea GAUZZI	Professeur	Invited member
Marie D'ANGELO	Maître de conférences	Supervisor

À ma famille, à mes amis,
à Juliette et Coriolis,
pour leur soutien.

Contents

List of Figures

List of Tables

Acknowledgements

During this thesis, made in the SNEQ team of the INSP laboratory, I was fortunate to have the support of many people, both on a scientific and personal level.

To start, I would like to thank Marie D'angelo, my supervisor, without whom this whole work would have obviously not happened. I really appreciated your availability and level-headedness regarding this work, from the master internship to the end of the PhD, keeping me on track. I appreciated your friendliness even more, crucial when spending stressful weeks on beamlines together.

Many thanks to the permanent members of the SNEQ team, for being friendly people who in addition to being good scientists can discuss interesting matters outside of science, and for finding many reasons to organize a drink, a picnic or bring some cake. More specifically, thank you Marie H., for your experimental knowledge friendly shared, and for doing the nights without complaint at Soleil. Tristan for the scientific discussions and your decisive help at Solaris. François, I don't know how the experiments would have gone without your capacity at finding and fixing stuff. You also helped me get my bearings on most of the new equipment I encountered. Pascal, I enjoyed our time at Solaris and your constant technical support. Christophe, thanks for your help on the STM and the discussions. Yves for your overall friendliness. Thanks to all the administrative teams from INSP, and particularly Cécile: when I was lost in administrative procedures I knew you would be of help. Thanks to everyone contributing to keep the labs and offices cleans, up and running. Thank you Imad for sharing your STM and helping me with it. Andrea, for following this work and providing insight.

I would like to thank our Japanese collaborators, especially I. Matsuda: I learned a lot during my internship you co-supervised, and your enthusiasm for science is pleasantly contagious. I am grateful for all the support provided by the synchrotron people : Mathieu, Paolo, Polina, Matteo, Natalia, Marcin, Jaime, and Oliver, for their patience in showing me the ropes of their endstations and for answering their

phones at all times. Thank you to the LPMS team of Cergy University for letting me use their ARPES setup. The Igor macro used in this work were developed and freely shared by Remi Lazzari for XPS and Ryu Yukawa, Polina Sheverdyaeva, Marcin Rosmus and Zhang Peng for ARPES. Much more time would have been needed for data analysis without you.

Teaching would not have been as interesting without all the colleagues doing a great work. Special thanks to Nadia, it was fun to create a course with you.

Finally, I am grateful to the jury members who agreed to evaluate my work, and especially to the reviewers, for reading the whole thing.

A happy PhD student is never alone, so I'd like to thanks all the other PhD students, postdocs and interns of the lab I've met through the years: Violette (you're cool), Angus (best Brit around), Oliviero (best co-bureau), Ronan, Camille, Thibaut and Thibault, Sarah, Angela, Axel, Thomas, Medhi, Raphaël, Pedro, Angeline, Dan, Ronei, Maryam, Dylan, Sophie, Marine and all the others. Thanks for being around to share many coffees, delicious CROUS food, venting, and occasionally and with moderation a well-deserved pint. I wish you all luck with whatever you'll be doing next. Thanks to the other scientific friends: Basile, Stelios, Leon, Nanna, Kevin, Alexis (winner of the proofreader award), Mathieu, all the friends from the M1, M2 and CurieOsity. Without you, it would have been less fun. Good luck to you too guys.

On a more personal note, I want to extend my thanks to my friends, who were supportive during these years. To my family, my mother, my father and my sister, for believing in me, even if you're still not exactly sure of what I've been doing this whole time. Finally, I'd like to thank Coriolis, my cat, for being a great companion, and Juliette, for being an even better one. Your support throughout this journey was invaluable. Thank you.

Résumé

Le domaine de la matière condensée est l'une des branches les plus vastes et les plus polyvalentes de la physique. Il traite des propriétés quantiques de la matière cristalline et des effets résultant de l'interaction des grandes quantités d'atomes et d'électrons mis en jeu : de l'ordre de 10^{10} à 10^{23}. C'est aussi le domaine de la physique qui a fourni le plus d'avancées technologiques au cours des dernières décennies. Citons par exemple le développement de l'électronique moderne avec les transistors à base de silicium, la technologie laser, les disques durs mécaniques et à mémoire flash, l'imagerie à résonance magnétique, et plus récemment le développement des nano-technologies.

Une nouvelle branche de recherche a été ouverte en 2004, suivant la découverte expérimentale du graphène [1], le tout premier matériau bidimensionnel (2D), constitué d'atomes de carbone disposés en nid d'abeille. Pour cette découverte, A. Geim et K. Novoselov ont reçu le prix Nobel de physique 2010. Avant cela, les matériaux 2D n'étaient étudiés que théoriquement, car il était communément admis qu'ils ne pouvaient pas être thermodynamiquement stables [2–4]. Depuis lors, la communauté scientifique a déployé des efforts considérables pour prédire, synthétiser et caractériser de nouvelles structures 2D, tout en développant les modèles théoriques qui leur sont applicables. Dans le cadre de la mécanique quantique, le confinement à deux dimensions d'espace est à l'origine de nombreuses propriétés exotiques, la plupart d'entre elles provenant de la structure électronique du système.

Les applications envisagées couvrent de nombreux domaines, avec un fort penchant vers l'électronique [5]. L'une des plus attrayantes est la réalisation de transistors à partir d'hétérostructures 2D [6, 7], plus efficaces et brisant la limite de taille de la technologie actuelle basée sur le silicium. Les autres applications vont du photovoltaïque [8–10] aux batteries solides [11], aux capteurs de gaz [12, 13], ou aux catalyseurs [14]. Cependant, avant de parvenir à des dispositifs fonctionnels, certains défis doivent être relevés. L'un d'eux est la stabilité à l'air des systèmes 2D,

qui peut être résolue par des procédés d'encapsulation en cours de développement. Un autre est de trouver des substrats non conducteurs : en effet, la plupart des matériaux 2D sont synthétisés sur un substrat métallique, ce qui rend impossible les mesures de conduction et les applications électroniques.

Parallèlement, le domaine des matériaux topologiques est également en plein essor, comme en témoigne le prix Nobel 2016 attribué à D.J. Thouless, F.D.M. Haldane et JM. Kosterlitz "pour les découvertes théoriques des transitions de phase topologiques et des phases topologiques de la matière". Dans ce nouveau paradigme, certaines propriétés de la structure de bande des cristaux peuvent être expliquées et prédites à partir de leur ordre topologique, plutôt que par leur géometrie. Les isolants topologiques, qui hébergent des états métalliques robustes à leur surface, ont été les premiers à être mis en évidence [15, 16], et il n'a pas fallu longtemps pour que le concept soit étendu aux matériaux bidimensionnels [17] et aux semi-métaux [18]. Leurs caractéristiques sont encore à l'étude, avec un double intérêt. Le premier, d'un point de vue fondamental, pose des questions sur l'origine de ces propriétés topologiques, et sur la façon dont les transitions de phase topologiques pourraient être réalisées. Le second, plus appliqué, vise à réaliser des systèmes expérimentaux, avec les promesses futures de courants sans dissipation et à haute fréquence [6]. Ces concepts sont développés dans le chapitre 1

Située à l'intersection de ces deux domaines, cette thèse de doctorat se concentre sur les matériaux bidimensionnels à lignes nodales de Dirac (LND), un type de semi-métal topologique où un croisement de bande protégé par symétrie se produit le long d'une boucle fermée ou d'une ligne ouverte dans l'espace réciproque, au lieu de points discrets comme c'est le cas pour les semi-métaux de Dirac tels que le graphène.
La première preuve expérimentale d'un système bidimensionnel à lignes nodales de Dirac, Cu_2Si sur Cu(111), a été publiée en 2017 par Feng *et al.* [19], et a été un point de départ pour notre travail. Malgré un nombre croissant de travaux prédisant par le calcul des matériaux 2D stables à LND, il n'existe pratiquement aucune réalisation expérimentale à ce jour, ce qui entrave la compréhension pratique de ces systèmes. L'une des difficultés de la synthèse des matériaux 2D réside dans l'indépendance requise vis-à-vis du substrat. Une première approche consiste à ex-

folier une couche 2D et à la transférer, au risque de l'endommager, tandis qu'une seconde approche consiste à faire croître une monocouche directement sur un substrat par évaporation sous ultra-vide, en supposant des interactions négligeables entre la surface 2D et son substrat. C'est cette seconde approche que nous avons adoptée ici.

Ce travail se veut une étape vers la réalisation expérimentale de matériaux bidimensionnels à lignes nodales de Dirac. Il se concentre sur la réalisation et la caractérisation de surfaces 2D et compare leur structure électronique avec celles simulées publiées dans la littérature. Les principales techniques employées pour la caractérisation des échantillons sont la photoémission de rayons X (XPS) et la spectroscopie de photoémission résolue en angle (ARPES), principalement utilisant des rayonnements synchrotron, avec l'aide de la diffraction d'électrons à basse énergie (LEED) et de la microscopie à effet tunnel (STM). Ces techniques sont décrites dans le chapitre 2.

En ce qui concerne les systèmes étudiés, deux d'entre eux sont au cœur de notre travail : Cu_2Si et Cu_2Ge. Tous deux sont des monocouches atomiquement planes ayant un réseau hexagonal, et sont prédits héberger des LNDs [19, 20].

Dans le chapitre 3, nous présentons notre travail sur Cu_2Si. Dans un premier temps, nous reproduisons les résultats de la littérature existante, confirmant les résultats principaux : la présence de deux lignes nodales de Dirac concentriques centrées autour de Γ, situées dans le premier eV sous le niveau de Fermi. Ceci indique des interactions négligeables entre la monocouche de surface et le substrat de cuivre. Nous étendons ensuite notre étude à l'effet d'un dépôt de Pb sur la structure électronique de Cu_2Si/Cu(111). Il a en effet été démontré que l'adsorption d'un élément peut augmenter couplage spin-orbite dans les monocouches 2D [21], pouvant donner lieu à des ouvertures de gaps ou à des levées de dégénérescence de bandes. Nous montrons que dans le cas de Pb/Cu_2Si/Cu(111), une séparation de bande se fait, et qu'aucune ouverture de gap n'est observée près des ligne nodales, indiquant une robustesse des LND plus importante qu'attendue. Des mesures résolues en spin ont été réalisée sur les bandes séparées pour déterminer si elles étaient ou non polarisées en spin, mais n'ont pas été concluantes.

Nous poursuivons par l'étude de la croissance de Cu_2Si sur le substrat semi-conducteur Si(111). Ce système, présentant à première vue une surface similaire à celle de Cu_2Si/Cu(111), a l'avantage d'avoir sa structure atomique déjà décrite dans la littérature [22], mais une comparaison de la structure de bande avec la monocouche de Cu_2Si faisait défaut. De plus, l'utilisation de rayonnement synchrotron nous permet de réaliser une caractérisation plus détaillée que celles existantes. Nous montrons d'importantes modifications de la structure de bande, et les attribuons à une forte hybridation hors-plan existant entre la couche de Cu_2Si et son substrat Si(111), justifiés par des calculs de théorie de la fonctionnelle de la densité (DFT). En particulier, Une des bandes prédites pour le système libre s'hybride fortement avec le substrat, empêchant l'existence de lignes nodales dans ce système. Les deux autres bandes électroniques ne sont pratiquement pas perturbées et présentent une dispersion linéaire. Le défi de trouver un substrat non métallique pour Cu_2Si reste donc ouvert.

Dans le chapitre 4, nous nous intéressons à la monocouche plane de Cu_2Ge, dans laquelle l'existence de LND a été prédite en 2020 [20], mais qui n'a encore fait l'objet d'aucune réalisation expérimentale. Nous avons montré, en nous appuyant sur un ensemble de mesures, que la surface synthétisée présente des propriétés compatibles avec la réalisation réussie de Cu_2Ge sur Cu(111). En ce qui concerne la structure atomique, une reconstruction de surface $(\sqrt{3} \times \sqrt{3})$ R30° a été observée après évaporation de Ge sur Cu(111), et les mesures XPS ont montré un unique site d'adsorption pour les atomes de Ge, en accord avec les attentes pour la monocouche de Cu_2Ge. Plus important encore, nous avons observé par ARPES la présence de trois bandes se croisant sans aucun gap détectable, en excellent accord avec les prédictions de la DFT, à l'exception d'un décalage vertical de 0,15 eV attribué au transfert de charge depuis le substrat. Nous concluons donc avoir synthétisé avec succès pour la première fois Cu_2Ge, avec des interactions suffisamment faibles avec son substrat Cu(111) pour ne pas perturber ou induire une ouverture dans les LND. Ce serait également l'un des rares rapports expérimentaux d'un matériau bidimensionnel à LND.

En parallèle, nous avons étudié la croissance de Ge sur Cu(111), résultant en une reconstruction de surface ("8.88×8.88")R30°, dans une tentative d'obtenir Cu_2Ge sur un substrat semi-conducteur. La structure électronique de la surface obtenue

diffère grandement de la monocouche de Cu_2Ge, avec une absence notable de croisement de bandes, de la présence de bandes intenses près du point Γ provenant de Ge(111), et de fortes caractéristiques Umklapp observées sur la surface de Fermi. Deux éléments sont proposés pour expliquer ces différences. Le plus évident provient de l'étude de la structure atomique : en effet, d'après la littérature existante et nos résultats, il semble clair que Cu/Ge(111) ne forme pas une surface plane et pourrait avoir une stœchiométrie de surface différente de celle de Cu_2Ge, résultant en un système entièrement différent du Cu_2Ge théorique ou du Cu_2Ge/Cu(111) expérimental. Cependant, nous notons qu'une surface de Cu_2Ge déformée aurait pu conduire à des états de LND gapés, intéressants en soi. Ceci nous amène au deuxième élément expliquant la différence de structure de bande électronique : le choix du substrat.
En effet, le substrat Ge(111) présente des liaisons pendantes et forme des liaisons fortes avec le Cu évaporé sur le dessus, rendant impossible dans ce cas l'obtention d'une surface découplée du substrat comme dans le cas du Cu_2Ge/Cu(111), ce qui conduit également à la discommensuration et donc aux états Umklapp. Par analogie avec le Cu_2Si/Si(111), nous émettons également l'hypothèse que l'absence d'une bande de type électronique pourrait provenir de l'hybridation des orbitales hors plan du substrat avec la surface. Malgré l'absence de LND dans ce système, ce travail constitue, à notre connaissance, la première caractérisation complète de la structure électronique de la reconstruction de la surface ("8,88×8,88")R30° de Cu/Ge(111).

Dans le dernier chapitre, chapitre 5, nous présentons un travail préliminaire sur le système Pb/SiC, motivé par la prédiction d'un effet Hall de spin quantique à large gap prédit dans une monocouche hexagonale de Pb [23], et le fait que le SiC soit un substrat approprié pour les applications électroniques. Pb a été évaporé sur les trois principales reconstructions de surface de SiC(0001), et les spectres XPS sont présentés. Une reconstruction de surface (2×2) a été observée pour la première fois après dépôt de Pb sur la surface de SiC $(\sqrt{3} \times \sqrt{3})$, montrant une organisation cristalline, et nos mesures indiquent également l'existence d'une phase cristalline (3×3) induite par Pb sur le substrat SiC-(3×3). Ce travail sera poursuivi dans le cadre d'une thèse de doctorat à part entière.

Le travail présenté ici est une étape vers la compréhension et l'utilisation des matériaux à ligne nodale de Dirac bidimensionnelle. Nous illustrons les difficultés liées aux substrats semi-conducteurs, tout en préparant avec succès des monocouches sur le substrat Cu(111). Nous avons confirmé les propriétés du Cu_2Si et montré leur stabilité même après adsorption de Pb, tout en réalisant pour la première fois le matériau bidimensionnel à lignes nodales de Dirac Cu_2Ge. Ces systèmes sont des candidats possibles pour des applications électroniques à haute fréquence en raison des porteurs de charges à grande vitesse provenant de la dispersion linéaire et de la forte densité d'états à la LND. Les applications potentielles comprennent également les capteurs à l'échelle nanométrique et les capteurs de gaz.

Références

[1] K. S. Novoselov, A. K. Geim, and S. V. Morosov, "Electric Field Effect in Atomically Thin Carbon Films", *Science*, vol. 306, no. 5696, pp. 666–669, Oct. 2004. DOI: `10.1126/science.1102896` (cited on p. xiii).

[2] R. Peierls, "Quelques propriétés typiques des corps solides", *Annales de l'institut Henri Poincaré*, vol. 5, no. 3, pp. 177–222, 1935 (cited on p. xiii).

[3] L. D. Landau, "Zur Theorie der phasenumwandlungen II", *Phys. Z. Sowjetunion*, vol. 11, pp. 26–35, 1937 (cited on p. xiii).

[4] N. D. Mermin, "Crystalline order in two dimensions", *Phys. Rev.*, vol. 176, pp. 250–254, 1 Dec. 1968. DOI: `10.1103/PhysRev.176.250` (cited on p. xiii).

[5] N. Briggs, S. Subramanian, Z. Lin, X. Li, X. Zhang, K. Zhang, K. Xiao, D. Geohegan, R. Wallace, L.-Q. Chen, M. Terrones, A. Ebrahimi, S. Das, J. Redwing, C. Hinkle, K. Momeni, A. van Duin, V. Crespi, S. Kar, and J. A. Robinson, "A roadmap for electronic grade 2D materials", *2D Materials*, vol. 6, no. 2, p. 022 001, Jan. 17, 2019, Publisher: IOP Publishing. DOI: `10.1088/2053-1583/aaf836` (cited on p. xiii).

[6] A. D. Franklin, "Nanomaterials in transistors: from high-performance to thin-film applications", *Science*, vol. 349, no. 6249, aab2750–aab2750, Aug. 14, 2015. DOI: `10.1126/science.aab2750` (cited on pp. xiii, xiv).

[7] M. Chhowalla, D. Jena, and H. Zhang, "Two-dimensional semiconductors for transistors", *Nature Reviews Materials*, vol. 1, no. 11, p. 16 052, Aug. 17, 2016, ISSN: 2058-8437. DOI: `10.1038/natrevmats.2016.52` (cited on p. xiii).

[8] S. Das, D. Pandey, J. Thomas, and T. Roy, “The role of graphene and other 2D materials in solar photovoltaics”, *Advanced Materials*, vol. 31, no. 1, p. 1 802 722, Jan. 1, 2019, Publisher: John Wiley & Sons, Ltd. DOI: `10.1002/adma.201802722` (cited on p. xiii).

[9] L. Wang, L. Huang, W. C. Tan, X. Feng, L. Chen, X. Huang, and K.-W. Ang, “2D photovoltaic devices: progress and prospects”, *Small Methods*, vol. 2, no. 3, p. 1 700 294, Mar. 1, 2018. DOI: `10.1002/smtd.201700294` (cited on p. xiii).

[10] L. Chiodo, “Two-dimensional innovative materials for photovoltaics”, *Novel materials for energy production and storage*, vol. 17, Jun. 1, 2019. DOI: `10.1016/j.cogsc.2019.04.004` (cited on p. xiii).

[11] Q. Ma, Y. Zheng, D. Luo, T. Or, Y. Liu, L. Yang, H. Dou, J. Liang, Y. Nie, X. Wang, A. Yu, and Z. Chen, “Two-dimensional materials for all-solid-state lithium batteries”, *Advanced Materials*, vol. 34, no. 16, p. 2 108 079, Dec. 28, 2021, Publisher: John Wiley & Sons, Ltd. DOI: `10.1002/adma.202108079` (cited on p. xiii).

[12] M. Donarelli and L. Ottaviano, “2D materials for gas sensing applications: a review on graphene oxide, mos2, ws2 and phosphorene”, *Sensors*, vol. 18, no. 11, 2018. DOI: `10.3390/s18113638` (cited on p. xiii).

[13] J. Zhang, L. Liu, Y. Yang, Q. Huang, D. Li, and D. Zeng, “A review on two-dimensional materials for chemiresistive- and FET-type gas sensors”, *Physical Chemistry Chemical Physics*, vol. 23, no. 29, pp. 15 420–15 439, 2021, Publisher: The Royal Society of Chemistry. DOI: `10.1039/D1CP01890F` (cited on p. xiii).

[14] F. R. Fan, R. Wang, H. Zhang, and W. Wu, “Emerging beyond-graphene elemental 2D materials for energy and catalysis applications”, *Chemical Society Reviews*, vol. 50, no. 19, pp. 10 983–11 031, 2021, Publisher: The Royal Society of Chemistry. DOI: `10.1039/C9CS00821G` (cited on p. xiii).

[15] C. L. Kane and E. J. Mele, “Quantum spin Hall effect in graphene”, *Phys. Rev. Lett.*, vol. 95, p. 226 801, 22 Nov. 2005. DOI: `10.1103/PhysRevLett.95.226801` (cited on p. xiv).

[16] C. L. Kane and E. J. Mele, “Z_2 topological order and the quantum spin Hall effect”, *Phys. Rev. Lett.*, vol. 95, p. 146 802, 14 Sep. 2005. DOI: `10.1103/PhysRevLett.95.146802` (cited on p. xiv).

[17] S. M. Young and C. L. Kane, “Dirac semimetals in two dimensions”, *Physical Review Letters*, vol. 115, no. 12, Sep. 16, 2015. DOI: `10.1103/PhysRevLett.115.126803` (cited on p. xiv).

[18] A. A. Burkov, “Topological semimetals”, *Nature Materials*, vol. 15, no. 11, pp. 1145–1148, Nov. 2016. DOI: `10.1038/nmat4788` (cited on p. xiv).

[19] B. Feng, B. Fu, S. Kasamatsu, S. Ito, P. Cheng, C.-C. Liu, Y. Feng, S. Wu, S. K. Mahatha, P. Sheverdyaeva, P. Moras, M. Arita, O. Sugino, T.-C. Chiang, K. Shimada, K. Miyamoto, T. Okuda, K. Wu, L. Chen, Y. Yao, and I. Matsuda, “Experimental realization of two-dimensional Dirac nodal line fermions in monolayer Cu_2Si”, *Nature Communications*, vol. 8, no. 1, p. 1007, Dec. 2017. DOI: `10.1038/s41467-017-01108-z` (cited on pp. xiv, xv).

[20] L. Liu, C. Wang, J. Li, X.-Q. Chen, Y. Jia, and J.-H. Cho, “Two-dimensional topological semimetal states in monolayer Cu_2Ge, Fe_2Ge, and Fe_2Sn”, *Physical Review B*, vol. 101, no. 16, p. 165 403, Apr. 2020. DOI: `10.1103/PhysRevB.101.165403` (cited on pp. xv, xvi).

[21] I. I. Klimovskikh, M. M. Otrokov, V. Y. Voroshnin, D. Sostina, L. Petaccia, G. Di Santo, S. Thakur, E. V. Chulkov, and A. M. Shikin, “Spin–orbit coupling induced gap in graphene on Pt(111) with intercalated Pb monolayer”, *ACS Nano*, vol. 11, no. 1, pp. 368–374, Jan. 24, 2017. DOI: `10.1021/acsnano.6b05982` (cited on p. xv).

[22] J. Zegenhagen, E. Fontes, F. Grey, and J. R. Patel, “Microscopic structure, discommensurations, and tiling of Si (111)/Cu-“5x5””, *Physical Review B*, vol. 46, no. 3, p. 1860, Jul. 1992. DOI: `10.1103/PhysRevB.46.1860` (cited on p. xvi).

[23] H. Zhao, C.-W. Zhang, W.-X. Ji, R.-W. Zhang, S.-S. Li, S.-S. Yan, B.-M. Zhang, P. Li, and P.-J. Wang, “Unexpected giant-gap quantum spin hall insulator in chemically decorated plumbene monolayer”, *Scientific Reports*, vol. 6, no. 1, Apr. 2016. DOI: `10.1038/srep20152` (cited on p. xvii).

Introduction

Introduction

«*The beginning of knowledge is the discovery of something we do not understand.*» - Frank Herbert

The field of condensed matter is one of the largest and most versatile branches of physics. It deals with the quantum properties of crystalline matter, and with the effects resulting from the large amounts of atoms (10^{10} - 10^{23}) and electrons interacting. It is arguably the domain of physics that provided the most technological advances in the past decades, from the development of modern electronics with silicon-based transistors to laser technology, hard drives, magnetic resonance imaging, and more recently taking the lead role in the understanding of nanotechnology.

A new line of research was opened in 2004 by the experimental realization of graphene [1], the first-ever two-dimensional (2D) material, constituted of carbon atoms arranged in a honeycomb structure, for which A. Geim and K. Novoselov were awarded the 2010 Nobel Prize in Physics. Before that, 2D materials were theoretically studied for their exotic properties and as toy models only, as it was commonly accepted that they could not be thermodynamically stable [2–4]. Since then, a tremendous effort has been made by the scientific community to predict, synthesize and characterize new 2D structures, while expanding on the theoretical models applicable to them. In the framework of quantum mechanics, the confinement to two dimensions in space results in many exotic properties, most of them originating from the electronic structure of the system.

The applications envisioned span numerous domains, with a strong trend towards electronics [5]. One of the most appealing is the realization of transistors from 2D hetero-structures [6, 7], more efficient and breaking the size limit of the current silicon-based technology. Others range from photovoltaics [8–10] to solid-state batteries[11], gas sensors [12, 13], or catalysts [14]. However, before reaching functional devices, some challenges are to be overcome. One issue is the air-stability of 2D systems, which can be addressed by encapsulation processes under development. Another is finding non-conductive substrates: indeed most 2D materials are synthesized on a metallic substrate, making conduction measures and electronic applications impossible.

Concurrently, the field of topological materials is in full swing, exemplified by the 2016 Nobel Prize awarded to D.J. Thouless, F.D.M. Haldane and JM. Kosterlitz “for theoretical discoveries of topological phase transitions and topological phases of matter”. In this new paradigm, properties of the band structure of crystals can be explained and predicted from their topological order. Topological insulators, i.e. bulk insulators hosting robust metallic states on their surface, were the first to be evidenced [15, 16], and it was not long before the concept was extended to two-dimensional materials and to semimetals [17, 18].
Their characteristics are still under study, with a two-fold interest. The first, from a fundamental approach, asks questions about the origins of those topological properties, and how topological phase transitions could be realized. The second, more applied, aims at realizing experimental systems, with the future promises of dissipationless and high-frequency currents [6].

At the intersection of these two fields, the focus of this PhD thesis is on two-dimensional Dirac nodal line materials, a type of topological semimetal where a symmetry protected band crossing happens either along a closed loop or an open line in the reciprocal space, instead of discrete points as is the case for Dirac semimetals such as graphene. The first experimental evidence of a two-dimensional Dirac nodal line (DNL) system was published in 2017 by Feng *et al.* [19], using a Cu_2Si monolayer grown on a Cu(111) substrate, and was a starting point for our work. Despite a growing number of computational work predicting stable 2D DNL materials, there are hardly any experimental realizations so far, hindering the practical understanding of these systems. One of the difficulties in synthesizing 2D materials resides in the independence required from the substrate. One approach consists in exfoliating a 2D layer and transferring it, at the risk of damaging it, while a second approach consists of growing a monolayer directly on a substrate by evaporation in ultra-high vacuum, assuming negligible interactions between the 2D surface and its substrate. It is this second approach we adopted here.

This work is intended to be a step towards the experimental realization of two-dimensional Dirac nodal lines materials. It focuses on the realization and characterization of 2D surfaces and compares their electronic structure with simulated ones published in the literature. The key techniques employed for sample characterization are x-ray photoemission and angle-resolved photoemission spectroscopy, with the help of low energy electron diffraction and scanning tunnelling microscopy. These techniques are described in chapter 1.

Regarding the systems studied, two of them are at the heart of our work: Cu_2Si and Cu_2Ge. Both are atomically flat monolayers with a hexagonal lattice and are predicted to host DNLs [19, 20].

In chapter 3 we present our work on Cu_2Si. As a first step, we replicate the existing literature results, and extend our study to the effect of Pb-deposition on the electronic structure of Cu_2Si/Cu(111) in an attempt to get insight into the manipulation and robustness of Dirac nodal lines, as adsorption of a heavy element has been shown to act as an effective intrinsic spin-orbit coupling enhancer in 2D monolayers [21]. We show for Pb on Cu_2Si/Cu(111) that a band splitting is seen, and that no gap opening is observed near the DNLs, indicated an unexpected robustness of the DNLs. We follow by the study of the growth of Cu_2Si on a Si(111) substrate. This system, presenting at first glance a surface layer similar to Cu_2Si/Cu(111) has the advantage of having its atomic structure already described in the literature, but a band structure comparison with the Cu_2Si monolayer was lacking. We show important modifications in the band structure, and attribute it to strong out-of-plane hybridization existing between the Cu_2Si layer and its Si(111) substrate.

In chapter 4 we present a study of a surface realized by Ge evaporation on a Cu(111) substrate, and compare it to the expected band structure for a Cu_2Ge monolayer, finding good agreement. We emphasize that monolayer Cu_2Ge has not been the object of any reported experimental realization so far and that the computational work predicting its electronic properties dates from 2020. Our work would then be the first to successfully synthesize a Cu_2Ge monolayer, mostly decoupled from its substrate. In a second part, we study a Cu-Ge surface alloy obtained by Cu evaporation on Ge(111) and compare its properties with the previous system. We find that its atomic and electronic structure are different from freestanding Cu_2Ge, highlighting once again the strong interactions originating from semiconductor substrates.

Finally, in chapter 5, we show the first steps of a study of the growth of Pb on SiC(0001), motivated by the prediction of a large gap topological insulator in monolayer Pb [22] with honeycomb structure. SiC being a robust large bandgap semiconductor makes a convenient substrate for further applications. A (2×2) Pb-induced surface reconstruction was observed for the first time after deposition of the SiC $(\sqrt{3} \times \sqrt{3})$ surface, showing a crystalline organisation, and our measurement point towards the existence of a crystalline (3×3) Pb-induced phase on the SiC-(3×3) substrate.

References

[1] K. S. Novoselov, A. K. Geim, and S. V. Morosov, “Electric Field Effect in Atomically Thin Carbon Films”, *Science*, vol. 306, no. 5696, pp. 666–669, Oct. 2004. DOI: `10.1126/science.1102896` (cited on p. 3).

[2] R. Peierls, “Quelques propriétés typiques des corps solides”, *Annales de l’institut Henri Poincaré*, vol. 5, no. 3, pp. 177–222, 1935 (cited on p. 3).

[3] L. D. Landau, “Zur Theorie der phasenumwandlungen II”, *Phys. Z. Sowjetunion*, vol. 11, pp. 26–35, 1937 (cited on p. 3).

[4] N. D. Mermin, “Crystalline order in two dimensions”, *Phys. Rev.*, vol. 176, pp. 250–254, 1 Dec. 1968. DOI: `10.1103/PhysRev.176.250` (cited on p. 3).

[5] N. Briggs, S. Subramanian, Z. Lin, X. Li, X. Zhang, K. Zhang, K. Xiao, D. Geohegan, R. Wallace, L.-Q. Chen, M. Terrones, A. Ebrahimi, S. Das, J. Redwing, C. Hinkle, K. Momeni, A. van Duin, V. Crespi, S. Kar, and J. A. Robinson, “A roadmap for electronic grade 2D materials”, *2D Materials*, vol. 6, no. 2, p. 022 001, Jan. 17, 2019, Publisher: IOP Publishing. DOI: `10.1088/2053-1583/aaf836` (cited on p. 3).

[6] A. D. Franklin, “Nanomaterials in transistors: from high-performance to thin-film applications”, *Science*, vol. 349, no. 6249, aab2750–aab2750, Aug. 14, 2015. DOI: `10.1126/science.aab2750` (cited on pp. 3, 4).

[7] M. Chhowalla, D. Jena, and H. Zhang, “Two-dimensional semiconductors for transistors”, *Nature Reviews Materials*, vol. 1, no. 11, p. 16 052, Aug. 17, 2016, ISSN: 2058-8437. DOI: `10.1038/natrevmats.2016.52` (cited on p. 3).

[8] S. Das, D. Pandey, J. Thomas, and T. Roy, “The role of graphene and other 2D materials in solar photovoltaics”, *Advanced Materials*, vol. 31, no. 1, p. 1 802 722, Jan. 1, 2019, Publisher: John Wiley & Sons, Ltd. DOI: `10.1002/adma.201802722` (cited on p. 3).

[9] L. Wang, L. Huang, W. C. Tan, X. Feng, L. Chen, X. Huang, and K.-W. Ang, “2D photovoltaic devices: progress and prospects”, *Small Methods*, vol. 2, no. 3, p. 1 700 294, Mar. 1, 2018. DOI: `10.1002/smtd.201700294` (cited on p. 3).

[10] L. Chiodo, “Two-dimensional innovative materials for photovoltaics”, *Novel materials for energy production and storage*, vol. 17, Jun. 1, 2019. DOI: `10.1016/j.cogsc.2019.04.004` (cited on p. 3).

[11] Q. Ma, Y. Zheng, D. Luo, T. Or, Y. Liu, L. Yang, H. Dou, J. Liang, Y. Nie, X. Wang, A. Yu, and Z. Chen, “Two-dimensional materials for all-solid-state lithium batteries”, *Advanced Materials*, vol. 34, no. 16, p. 2 108 079, Dec. 28, 2021, Publisher: John Wiley & Sons, Ltd. DOI: `10.1002/adma.202108079` (cited on p. 3).

[12] M. Donarelli and L. Ottaviano, “2D materials for gas sensing applications: a review on graphene oxide, mos2, ws2 and phosphorene”, *Sensors*, vol. 18, no. 11, 2018. DOI: `10.3390/s18113638` (cited on p. 3).

[13] J. Zhang, L. Liu, Y. Yang, Q. Huang, D. Li, and D. Zeng, “A review on two-dimensional materials for chemiresistive- and FET-type gas sensors”, *Physical Chemistry Chemical Physics*, vol. 23, no. 29, pp. 15 420–15 439, 2021, Publisher: The Royal Society of Chemistry. DOI: `10.1039/D1CP01890F` (cited on p. 3).

[14] F. R. Fan, R. Wang, H. Zhang, and W. Wu, “Emerging beyond-graphene elemental 2D materials for energy and catalysis applications”, *Chemical Society Reviews*, vol. 50, no. 19, pp. 10 983–11 031, 2021, Publisher: The Royal Society of Chemistry. DOI: `10.1039/C9CS00821G` (cited on p. 3).

[15] C. L. Kane and E. J. Mele, “Quantum spin Hall effect in graphene”, *Phys. Rev. Lett.*, vol. 95, p. 226 801, 22 Nov. 2005. DOI: `10.1103/PhysRevLett.95.226801` (cited on p. 4).

[16] C. L. Kane and E. J. Mele, “Z_2 topological order and the quantum spin Hall effect”, *Phys. Rev. Lett.*, vol. 95, p. 146 802, 14 Sep. 2005. DOI: 10.1103/PhysRevLett.95.146802 (cited on p. 4).

[17] S. M. Young and C. L. Kane, “Dirac semimetals in two dimensions”, *Physical Review Letters*, vol. 115, no. 12, Sep. 16, 2015. DOI: 10.1103/PhysRevLett.115.126803 (cited on p. 4).

[18] A. A. Burkov, “Topological semimetals”, *Nature Materials*, vol. 15, no. 11, pp. 1145–1148, Nov. 2016. DOI: 10.1038/nmat4788 (cited on p. 4).

[19] B. Feng, B. Fu, S. Kasamatsu, S. Ito, P. Cheng, C.-C. Liu, Y. Feng, S. Wu, S. K. Mahatha, P. Sheverdyaeva, P. Moras, M. Arita, O. Sugino, T.-C. Chiang, K. Shimada, K. Miyamoto, T. Okuda, K. Wu, L. Chen, Y. Yao, and I. Matsuda, “Experimental realization of two-dimensional Dirac nodal line fermions in monolayer Cu_2Si”, *Nature Communications*, vol. 8, no. 1, p. 1007, Dec. 2017. DOI: 10.1038/s41467-017-01108-z (cited on pp. 4, 5).

[20] L. Liu, C. Wang, J. Li, X.-Q. Chen, Y. Jia, and J.-H. Cho, “Two-dimensional topological semimetal states in monolayer Cu_2Ge, Fe_2Ge, and Fe_2Sn”, *Physical Review B*, vol. 101, no. 16, p. 165 403, Apr. 2020. DOI: 10.1103/PhysRevB.101.165403 (cited on p. 5).

[21] I. I. Klimovskikh, M. M. Otrokov, V. Y. Voroshnin, D. Sostina, L. Petaccia, G. Di Santo, S. Thakur, E. V. Chulkov, and A. M. Shikin, “Spin–orbit coupling induced gap in graphene on Pt(111) with intercalated Pb monolayer”, *ACS Nano*, vol. 11, no. 1, pp. 368–374, Jan. 24, 2017. DOI: 10.1021/acsnano.6b05982 (cited on p. 5).

[22] H. Zhao, C.-W. Zhang, W.-X. Ji, R.-W. Zhang, S.-S. Li, S.-S. Yan, B.-M. Zhang, P. Li, and P.-J. Wang, “Unexpected giant-gap quantum spin hall insulator in chemically decorated plumbene monolayer”, *Scientific Reports*, vol. 6, no. 1, Apr. 2016. DOI: 10.1038/srep20152 (cited on p. 6).

Chapter 1

Basic concepts

Chapter 1: Basic concepts

1.1 A view of the 2D materials landscape

«*Graphene is dead, long live graphene*» A. K. Geim

1.1.1 The countless 2D materials

A material is considered purely two-dimensional (2D) if it is constituted of only one atomic layer, preferably with all its atoms being co-planar. The denomination of 2D is however often extended to buckled materials, and to some systems made of two or three non-identical atomic layers.

Until recently, the existence of isolated or free-standing two-dimensional materials was believed to be physically impossible. Various renowned physicists such as Peierls [1], Landau [2] and later Mermin [3] argued, backed by experimental observations, that such low dimensional crystal lattices would be thermodynamically unstable at any temperature, and should either melt or aggregate, as thermal fluctuations would be of the order of the interatomic distance. The study of 2D materials was thus restrained to purely theoretical work, or by considering them as a surface layer on a 3D material of similar lattice parameters.

A sudden paradigm shift occurred in 2004 when Geim and Novoselov [4] experimentally isolated graphene, a purely 2D layer made of carbon atoms with a honeycomb structure. For this and their subsequent studies, they were awarded in 2010 the Nobel Prize “for groundbreaking experiments regarding the two-dimensional material graphene”. Since then, the research on 2D materials has become an extremely popular subject area, interested in the fundamental properties of these materials as well as their possible applications. Among the most studied systems, let us cite two families: the transition metal dichalcogenides (TMDs), created from combinations of transition metals (e.g., Mo, W, Hf) and chalcogens (e.g., S, Se, Te) [5–8], and the X-enes [9], usually created from group IV or V elements, which exhibit structures that are some variation of the (buckled) honeycomb one. Silicene [10, 11], germanene [12, 13], bismuthene [14] , phosphorene [15, 16], borophene [17–23] or plumbene [24–29] (respectively for Si, Ge, P, B and Pb based structures) are examples of promising X-enes.

More recently, a few 2D binary compounds with copper have been shown to exhibit a hexagonal lattice with a planar configuration. Cu_2Si [30, 31] and Cu_2Ge [32, 33], which have been the focus of most of the work presented here, as well as CuSe [34] and Cu_2Te [35].

1.1.2 For which applications?

Possible applications of 2D materials seem almost unlimited, due to the highly versatile properties achievable with the various 2D materials.The most widespread applications reside in the field of electronics [36], especially as part of transistors [8, 10, 37, 38]. Ideally, transistors could be fully made of 2D materials heterostructures, enabling much smaller sizes. The size limit of silicon-based transistors is partly due to the apparition of undesirable quantum effects. In 2D materials, quantum confinement is often what is at the origin of the specific physical properties: what is now inconvenient in the miniaturization of transistors could be turned into a controlled asset. The possibility of almost perfect conduction without heat dissipation and high carrier speed [39] would also enable much cleaner and more efficient processes, and the potential for flexible and transparent materials would open original perspectives. Furthermore, 2D materials could be used for valleytronics applications [40, 41], and the possibility to obtain spin-polarized conduction channels could lead towards spintronics applications [42].

2D materials are also of great interest to the field of energy production and transformation. The possibility to achieve 2D heterostructures, with some transparent and/or flexible layers would find application in photovoltaics [43–45], and can readily be used to improve the efficiency of existing solar cells. Staying in the energy domain, 2D materials will likely be future components of all-solid-state lithium batteries [46], while the surface-to-volume ratio of 2D materials makes them efficient electrocatalysts in electrolysis processes for hydrogen production [47, 48], and for energy storage [48]. Highly reactive 2D surfaces are appealing as well for efficient catalysis [49], and for the realization of gas sensors [50, 51], which now extends to biosensors [52, 53] for use in medicine, where 2D materials are additionally considered as plausible therapeutic treatment agents [53]. Finally, while not the focus of this work, 2D materials often display impressive mechanical properties, such as outstanding mechanical strength and toughness [54, 55], as well as piezoelectric and ferroelectric capacity [56].

Before reaching those applications, major challenges still need to be addressed [36, 37, 57]. These issues are found in all the aforementioned fields, more or less strongly depending on the considered material. The fragility of 2D sheets makes them difficult to transfer without inducing unwanted holes or dislocations, complicating the fabrication of heterostructures with precise layer placement and interfaces. The growth is often made on a substrate, but the decoupling is often not discussed. Some materials can however be exfoliated, either mechanically or chemically. Additionally, some 2D materials are not air-stable and would necessitate specific encapsulation techniques to be used outside of a vacuum. Finally, most of the 2D materials are made and studied in laboratories, and processes for large-scale fabrication are yet to be implemented.

1.2 Topological materials

Another rapidly growing field of research in condensed matter physics is the one of topological materials, providing a new paradigm in material description and classification. Indeed, while the most common way to classify materials is based on their geometrical properties and symmetries, it is now proposed to classify materials by their topological order. A non-trivial topology leads to unusual properties, that are robust against continuous deformation of the system parameters as the topological order is an invariant.

1.2.1 A short background on topological matter

The “classical” Hall effect was discovered in 1879 by E. H. Hall, when he observed that an electric current flowing through a material subjected to a magnetic field produces a voltage perpendicular to the field. One century later, in 1980, Klaus von Klitzing discovered unexpectedly that in two-dimensional electron systems, when subjected to low temperatures and strong magnetic fields, the Hall resistance would take quantized values [58]. This phenomenon is called the quantum Hall effect, or integer quantum Hall effect. It was then found that the Hall conductance σ_H, is a topological invariant [59, 60].

For more than two decades, the domain of topological materials was limited to QHE materials, until the discovery of topological insulators which suggested that it involved a much broader class of materials. Evidenced in the 2000s, topological insulators (TI) are characterized by the quantum spin Hall (QSH) effect [61–63]. Topological insulators and QSH systems are thus often used interchangeably in the literature. A schematic representation of QH and QSH systems is shown in Figure 1.1 (a). QSH systems are insulators in the bulk but are characterized by the presence of metallic states along their edges with linear dispersion, forming spin-polarized conduction channels counter-propagating on the edge, as represented in Figure 1.1 (b). The spatial separation of these edge states forbids backscattering, opening the possibility of dissipationless spin current at room temperature in QSH systems. This was first described by Murakami *et al.* in 2003 [61], soon followed by Kane and Mele in 2005 who proposed graphene as a possible QSH material [62] and developed further the theoretical description of topological insulators [63] with the introduction of the Z_2 number, a topological invariant that can determine if a material can exhibit QSH states or not. QSH at room temperature in graphene was then later experimentally confirmed [64].

We will now try to give here a (very) simplified way to understand the topological order. The question to answer is: after one turn around the Brillouin zone, do we obtain the same set of wave functions, or a modified one? An analogy can be made with two closed strips: a simple one and a Möbius strip. After one turn, independently of the starting point or the trajectory chosen, one will end up in the same position in the simple strip, while with the Möbius strip one will end up at a different point.

Let's consider one filled electronic band of a crystal, whose electronic states are described by Bloch wave functions $\psi_{\mathbf{k}}$, $\mathbf{k}$ being the crystal momentum vector. It

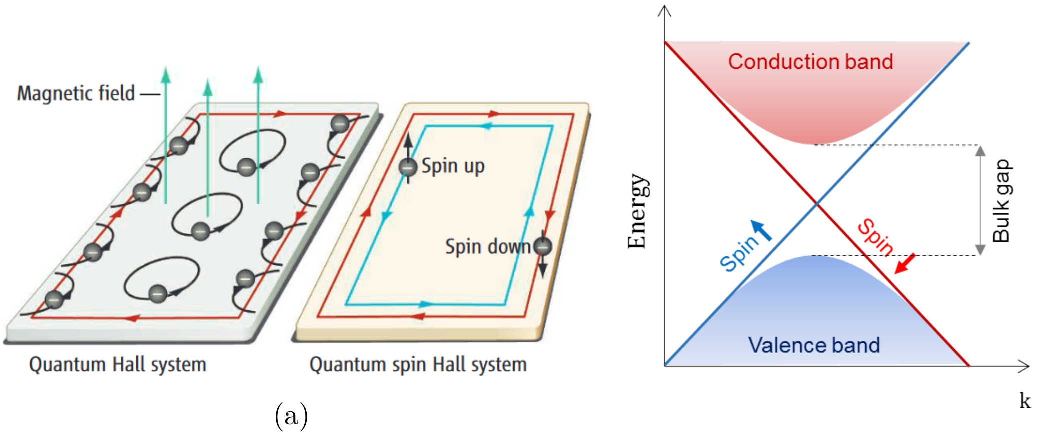

(a)

(b)

Fig. 1.1 – *(a) In the quantum Hall system (left), an applied magnetic field causes electrons to bounce off the edge of the sample in circular orbits, forming a flow of charges around the edges of the material. In the quantum spin Hall system (right) the spin-up and spin-down charge carriers flow in opposite directions in edge channel states, without the need for any external field, as this role is played by the intrinsic spin-orbit coupling of the system. Figure and caption adapted from [65]. (b) In a QSH system, edge states cross the bulk bandgap. The states are spin-polarized, with linear dispersion.*

follows from Bloch's theorem that $\psi_{\mathbf{k}}$ is defined only up to a reciprocal lattice vector $\mathbf{K}$, up to a phase factor α, such as $\psi_{\mathbf{k}}(\mathbf{r}) = e^{i\alpha}\psi_{\mathbf{k}+\mathbf{K}}(\mathbf{r})$. The same applies to the eigen energies: $E_k = E_{k+K}$. The energy is then periodical in the reciprocal space, which is reflected in the periodic boundary conditions of the Brillouin zone. Thus, the Brillouin zone of a 2D system is equivalent to a 2D-torus (i.e. homeomorphic to a donut), as it has periodical boundary conditions in the direction k_x and k_y. The reasoning is the same in 3D, with the addition of the k_z dimension, A 3D-torus is however more difficult to visualize. As physical measurements deal with $|\psi_{\mathbf{k}}|^2$ rather than $\psi_{\mathbf{k}}$, the phase has long been overlooked. The work of M. Berry [66] was a pioneer in uncovering its importance. Indeed, it was found that while for most materials the phase change after a turn around the Brillouin zone was null, it was not the case for a few of them: the topological insulators. This topological order is characterized, for 2D TIs, by the topological invariant Z_2 [63] derived from the Berry curvature, which is zero for 0 trivial insulators and 1 for TIs (modulo 2). We also note that topological orders can either be intrinsic, where the emergent properties can be robust against any local perturbations, or symmetry-protected, where they are only protected against perturbations that do not break these specific symmetries. The symmetries involved are usually the inversion, time-reversal, or crystalline symmetries.

An important concept in topological materials is the one of band inversion, which describes the local inversion in the usual order of the conduction (empty) and valence (filled) bands, where a gap is opened, usually in a high-symmetry point of the Brillouin zone. This occurs in TIs, and can be explained by a continuity requirement. The wave functions of the filled bands of the topological insulator have a robust topological order, insensitive to continuous deformations, that has to be conserved. At the interface between a TI and the vacuum (or any other trivial insulator), the continuity of the wave function is required. However, it is not possible to continually deform the filled valence band of a TI into a filled valence band of a trivial insulator, which does not possess the same topological order (i.e. the same Z_2 number). What is possible is to transform an empty band of the TI, which does not possess a topological order, into a filled band of the trivial insulator. This results in a twist of the bands at the interface, called band inversion. At the inversion point the bands touch, inducing a metallic character in the interface region, as shown in Figure 1.1 (b). The origin of the band inversion is often attributed to the SOC [63], but the exact mechanisms are still under question, and some other phenomena such as scalar relativistic effects and lattice distortion have been proposed as drivers of the band inversion [67]. Finally, the presence of the time-inversion symmetry in non-centrosymmetric systems can also lead to band inversion [68].

In any case, the presence of SOC is required to open the gap and make a TI [63]. As the size of the spin-orbit is proportional to the fourth power of the effective nuclear charge Z, heavier elements are favoured in the search of large gaps (i.e. measurable at room temperature) in QSH systems, which remains one of the main pursuits in the domain. By comparison, graphene has a SOC induced gap of the order of 10^{-3} meV, which would require an unrealistically low temperature to directly observe the QSH effect. In chapter 5 we present our first results toward the growth of Pb/SiC, as monolayer Pb with hexagonal lattice is expected to be a large gap QSH material [24–29].

While topological insulators were the first class of topological materials widely studied, the concept was soon extended to topological semimetals [69–72], and from 3D materials to 2D ones [73–75], opening the possibilities of smaller and more easily functionalized devices.

1.2.2 Topological semimetals

After the discovery of topological insulators came the discovery of topological semimetals (TSM). Three types of TSMs, Dirac (DSM), Weyl (WSM), and nodal-line semimetals (NLS) have been discovered [72]. These three TSM are schematically represented in Figure 1.2. They have some shared features: a symmetry demanded band crossing, and a linear band dispersion. A DSM, shown in Figure 1.2 (a), is the result of two doubly degenerate bands crossing near the Fermi level at a discrete point in k-space, usually designated as a Dirac point. The Dirac point is demanded by both inversion and time-reversal symmetry. When either inversion symmetry or time-reversal symmetry is broken, the doubly degenerate bands become spin-split (when SOC is considered), separating into two singly degenerate band crossings called Weyl points, shown in Figure 1.2 (b).

At the difference of the DSM and WSM, in nodal-line semimetal (NLS) the bands do not cross at discrete points but rather cross along open lines or closed lines (i.e. loops) in k-space, as shown in Figure 1.2 (c). NLS can be categorized into two types: Dirac nodal line semimetals (DNLS) and Weyl nodal line semimetals (WNLS). The DNLS are found in materials with both inversion symmetry and time-reversal symmetry. When SOC is neglected (or negligible), band inversions happen at one or more high-symmetry points of the Brillouin zone, resulting in two doubly degenerate bands crossing each other to form a fourfold degenerate nodal line [72]. The band crossing can also be enforced by the non-symmorphic space-group symmetry of the system [68], which can help stabilize the DNLs in the presence of SOC [74, 76] that otherwise tends to gap the DNL. WNLS lack either inversion or time-reversal symmetry allowing for spin splitting. Therefore, the otherwise fourfold degenerate nodal lines split into two singly degenerate nodal lines, which are protected by one additional symmetry.

The existence of DNL is strongly tied to the symmetries present in the sys-

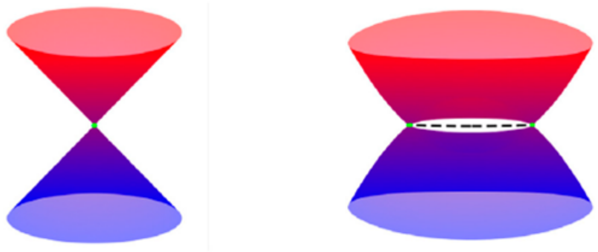

(a) Dirac semimetal (b) Weyl semimetal

(c) Nodal line semimetals

Fig. 1.2 – *Schematic illustration of Dirac node, Weyl node and Nodal line/loop in k-space. (a) A Dirac semimetal, where the bands disperse linearly around the Dirac point, represented by a green dot. (b) A Weyl semimetal, in which the Weyl points with opposite chirality are connected by a Fermi arc. The Weyl points are represented by a green dot and the Fermi arc by a black dotted line. (c) Nodal line semimetals, where the valence and conduction bands cross along an open or closed line, represented by a green circle/line. From [72]*

tem. Three types of crystalline symmetries can generate DNL: inversion plus time-reversal symmetry, mirror reflection symmetry, and non-symmorphic symmetries. Figure 1.3 shows the different topological states, and how symmetries link them together. By the addition or the breaking of symmetries, it is possible to transition from one topological state to another.

1.2.3 2D Nodal-line semimetals

While the concept of NLS was first developed and realized in 3D materials [69, 71, 77, 78] in the search of a 3D analogous to graphene, it was quickly extended to 2D materials as well. Like their 3D counterparts, 2D DNLs have Dirac fermions near the linear band crossing of their valence and conduction bands, and this crossing is

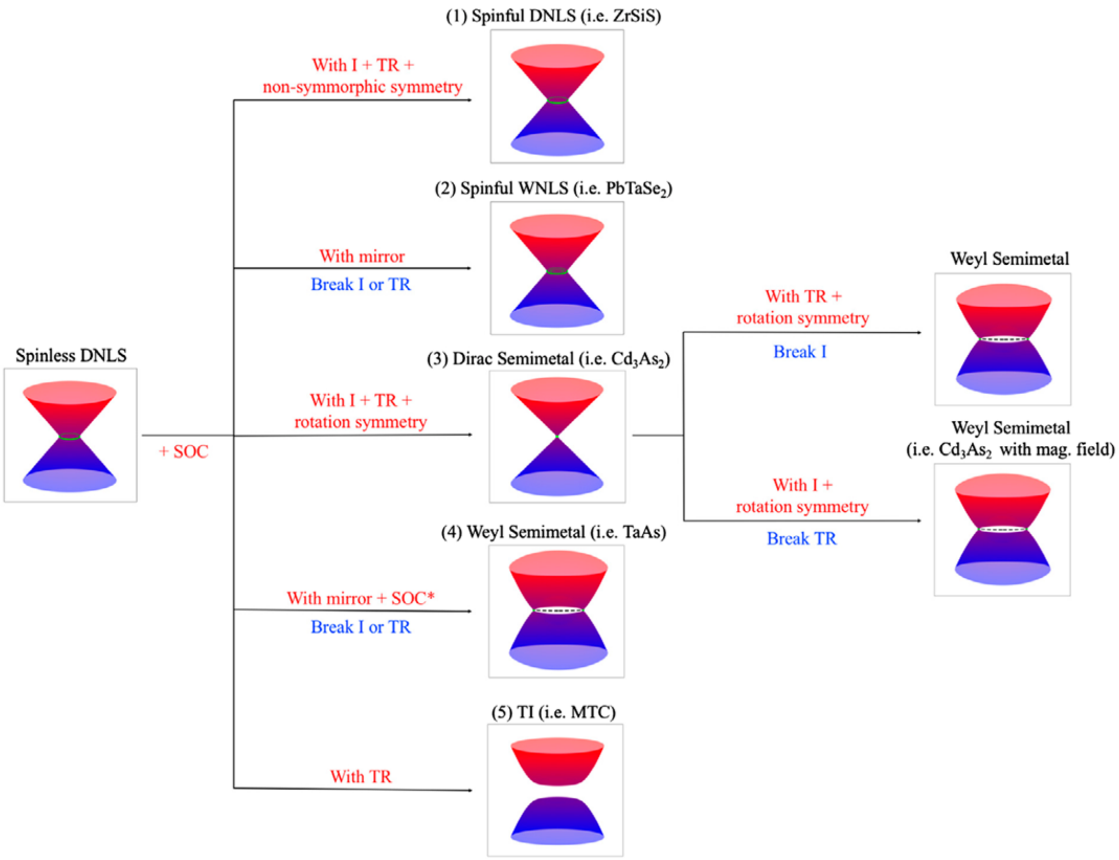

Fig. 1.3 – *Diagram of the different topological states and their relationship with each other. The symmetries in red (blue) captions indicate the global symmetry or spatial/lattice symmetry elements that need to be preserved (broken) to obtain a different topological phase. From [72]*

required from a given set of symmetries. While a recent idea, 2D Dirac nodal lines have been predicted in a growing variety of systems, such as 2D honeycomb kagome lattice [79], in 2D compounds X2Y (X = Ca, Sr, and Ba; Y = As, Sb, and Bi) [80], X_2YZ_4 (X = K, Cs, Rb, Y = Cr, Cu, Z = Cl, F) [81], and MX (M = Pd, Pt; X = S, Se, Te) [82], in 2D Lieb lattices [83], in hydrogenated boron layers [84, 85], MgB_2 [86], MnN [87], B_2C [88], black phosphorous films [89], C_4N_4 [90], ScX (X = P, As) [91], $CuMg_2$ [92], but also in monolayer Cu_2Ge, Fe_2Ge, Fe_2Sn [33] and Cu_2Si [31]. It is interesting to note that while most of these systems have a honeycomb or hexagonal lattice, it is not a requirement. Borophane for instance is constituted of 5- and 7-membered rings [85].

The experimental realizations are sparse so far, with the notable examples of

Cu_2Si [31] which is the first 2D material in which DNLs have been confirmed when grown on Cu(111), followed by Bi/Cu(111) [93], and recently by the exfoliable 2D layers of borophane [94] and $TaNiTe_5$ [95]. We also note that CuSe, despite its band structure similar to Cu_2Si, has been shown to present gaps where the DNLs should cross when prepared on Cu(111) [34]. One of the most pressing issues of the field seems, for now, to increase the number of experimental realizations, with a focus on the choice of substrate or possibility for exfoliation, strategies to get the nodal lines as close to the Fermi level as possible, and air stability. This work focuses on the systems Cu_2Si and Cu_2Ge, belonging to the class of 2D Dirac nodal line (DNL) materials.

Although the interest in 2D DNL systems is often motivated by the attempt to better understand the exotic properties of 2D topological materials and the conditions for their emergence, the possible applications of such materials are fascinating. From a fundamental point of view, they can be good platforms to study topological phase transitions, either towards others TSM or to TI phases [72, 96]. Additionally, TSM with magnetic properties are expected to exhibit topologically non-trivial superconductivity, leading to the elusive Majorana surface states [97]. On more direct applications, the presence of Dirac fermions near the nodal lines offer the possibility of high-speed electronics due to ultrahigh electron mobility, and the possibility of spin-polarized channels offers low-dissipation conduction. Compared to Dirac semimetals, the presence of a crossing line instead of a crossing point could comparatively offer a higher electron density for the conduction. Furthermore, the nodal lines are not necessarily located on high-symmetry points, allowing for an easier manipulation of their properties.

Bibliography of Chapter 1

[1] R. Peierls, “Quelques propriétés typiques des corps solides”, *Annales de l’institut Henri Poincaré*, vol. 5, no. 3, pp. 177–222, 1935 (cited on p. 13).

[2] L. D. Landau, “Zur Theorie der phasenumwandlungen II”, *Phys. Z. Sowjetunion*, vol. 11, pp. 26–35, 1937 (cited on p. 13).

[3] N. D. Mermin, “Crystalline order in two dimensions”, *Phys. Rev.*, vol. 176, pp. 250–254, 1 Dec. 1968. DOI: `10.1103/PhysRev.176.250` (cited on p. 13).

[4] K. S. Novoselov, A. K. Geim, and S. V. Morosov, “Electric Field Effect in Atomically Thin Carbon Films”, *Science*, vol. 306, no. 5696, pp. 666–669, Oct. 2004. DOI: `10.1126/science.1102896` (cited on p. 13).

[5] W. Choi, N. Choudhary, G. H. Han, J. Park, D. Akinwande, and Y. H. Lee, “Recent development of two-dimensional transition metal dichalcogenides and their applications”, *Materials Today*, vol. 20, no. 3, pp. 116–130, Apr. 2017. DOI: `10.1016/j.mattod.2016.10.002` (cited on p. 14).

[6] R. Lv, H. Terrones, A. L. Elías, N. Perea-López, H. R. Gutiérrez, E. Cruz-Silva, L. P. Rajukumar, M. S. Dresselhaus, and M. Terrones, “Two-dimensional transition metal dichalcogenides: clusters, ribbons, sheets and more”, *Nano Today*, vol. 10, no. 5, pp. 559–592, Oct. 2015. DOI: `10.1016/j.nantod.2015.07.004` (cited on p. 14).

[7] Z. Hu, Z. Wu, C. Han, J. He, Z. Ni, and W. Chen, “Two-dimensional transition metal dichalcogenides: interface and defect engineering”, *Chemical Society Reviews*, vol. 47, no. 9, pp. 3100–3128, 2018. DOI: `10.1039/C8CS00024G` (cited on p. 14).

[8] X. Qian, J. Liu, L. Fu, and J. Li, “Quantum spin Hall effect in two-dimensional transition metal dichalcogenides”, *Science*, vol. 346, no. 6215, pp. 1344–1347, Dec. 2014. DOI: `10.1126/science.1256815` (cited on p. 14).

[9] A. Molle, J. Goldberger, M. Houssa, Y. Xu, S.-C. Zhang, and D. Akinwande, “Buckled two-dimensional Xene sheets”, *Nature Materials*, vol. 16, no. 2, pp. 163–169, Feb. 2017. DOI: `10.1038/nmat4802` (cited on p. 14).

[10] L. Tao, E. Cinquanta, D. Chiappe, C. Grazianetti, M. Fanciulli, M. Dubey, A. Molle, and D. Akinwande, "Silicene field-effect transistors operating at room temperature", *Nature Nanotechnology*, vol. 10, no. 3, pp. 227–231, Mar. 2015. DOI: `10.1038/nnano.2014.325` (cited on p. 14).

[11] Y. Sato, Y. Fukaya, M. Cameau, A. K. Kundu, D. Shiga, R. Yukawa, K. Horiba, C.-H. Chen, A. Huang, H.-T. Jeng, T. Ozaki, H. Kumigashira, M. Niibe, and I. Matsuda, "Electronic structure of a (3×3) ordered silicon layer on Al(111)", *Physical Review Materials*, vol. 4, no. 6, p. 064 005, Jun. 15, 2020. DOI: `10.1103/PhysRevMaterials.4.064005` (cited on p. 14).

[12] A. Acun, L. Zhang, P. Bampoulis, M. Farmanbar, A. van Houselt, A. N. Rudenko, M. Lingenfelder, G. Brocks, B. Poelsema, M. I. Katsnelson, and H. J. W. Zandvliet, "Germanene: the germanium analogue of graphene", *Journal of Physics: Condensed Matter*, vol. 27, no. 44, p. 443 002, Nov. 11, 2015. DOI: `10.1088/0953-8984/27/44/443002` (cited on p. 14).

[13] M. E. Dávila, L. Xian, S. Cahangirov, A. Rubio, and G. Le Lay, "Germanene: a novel two-dimensional germanium allotrope akin to graphene and silicene", *New Journal of Physics*, vol. 16, no. 9, p. 095 002, Sep. 9, 2014. DOI: `10.1088/1367-2630/16/9/095002` (cited on p. 14).

[14] F. Reis, G. Li, L. Dudy, M. Bauernfeind, S. Glass, W. Hanke, R. Thomale, J. Schäfer, and R. Claessen, "Bismuthene on a SiC substrate: a candidate for a high-temperature quantum spin hall material", *Science*, vol. 357, no. 6348, pp. 287–290, Jul. 21, 2017. DOI: `10.1126/science.aai8142` (cited on p. 14).

[15] C. R. Ryder, J. D. Wood, S. A. Wells, Y. Yang, D. Jariwala, T. J. Marks, G. C. Schatz, and M. C. Hersam, "Covalent functionalization and passivation of exfoliated black phosphorus via aryl diazonium chemistry", *Nature Chemistry*, vol. 8, no. 6, pp. 597–602, Jun. 2016. DOI: `10.1038/nchem.2505` (cited on p. 14).

[16] H. Liu, A. T. Neal, Z. Zhu, Z. Luo, X. Xu, D. Tománek, and P. D. Ye, "Phosphorene: An Unexplored 2D Semiconductor with a High Hole Mobility", *ACS Nano*, vol. 8, no. 4, pp. 4033–4041, Apr. 2014. DOI: `10.1021/nn501226z` (cited on p. 14).

[17] M. Ezawa, “Triplet fermions and Dirac fermions in borophene”, *Physical Review B*, vol. 96, no. 3, Jul. 20, 2017. DOI: 10.1103/PhysRevB.96.035425 (cited on p. 14).

[18] W. Li, L. Kong, and C. Chen, “Experimental realization of graphene-like borophene”, 2018, Submitted. [Online]. Available: https://arxiv.org/ftp/arxiv/papers/1712/1712.08770.pdf (cited on p. 14).

[19] W.-C. Yi, W. Liu, J. Botana, L. Zhao, Z. Liu, J.-Y. Liu, and M.-S. Miao, “Honeycomb boron allotropes with Dirac cones: a true analogue to graphene”, *The Journal of Physical Chemistry Letters*, vol. 8, no. 12, pp. 2647–2653, Jun. 15, 2017. DOI: 10.1021/acs.jpclett.7b00891 (cited on p. 14).

[20] Y. Jiao, F. Ma, J. Bell, A. Bilic, and A. Du, “Two-dimensional boron hydride sheets: high stability, massless Dirac fermions, and excellent mechanical properties”, *Angewandte Chemie International Edition*, vol. 55, no. 35, pp. 10 292–10 295, Aug. 22, 2016. DOI: 10.1002/anie.201604369 (cited on p. 14).

[21] B. Feng, J. Zhang, S. Ito, M. Arita, C. Cheng, L. Chen, K. Wu, F. Komori, O. Sugino, K. Miyamoto, T. Okuda, S. Meng, and I. Matsuda, “Discovery of 2D Anisotropic Dirac Cones”, *Advanced Materials*, vol. 30, no. 2, p. 1 704 025, Jan. 2018. DOI: 10.1002/adma.201704025 (cited on p. 14).

[22] B. Feng, J. Zhang, R.-Y. Liu, T. Iimori, C. Lian, H. Li, L. Chen, K. Wu, S. Meng, F. Komori, and I. Matsuda, “Direct evidence of metallic bands in a monolayer boron sheet”, *Physical Review B*, vol. 94, no. 4, p. 041 408, Jul. 2016. DOI: 10.1103/PhysRevB.94.041408 (cited on p. 14).

[23] B. Feng, O. Sugino, R.-Y. Liu, J. Zhang, R. Yukawa, M. Kawamura, T. Iimori, H. Kim, Y. Hasegawa, H. Li, L. Chen, K. Wu, H. Kumigashira, F. Komori, T.-C. Chiang, S. Meng, and I. Matsuda, “Dirac fermions in borophene”, *Phys. Rev. Lett.*, vol. 118, p. 096 401, 9 Mar. 2017. DOI: 10.1103/PhysRevLett.118.096401 (cited on p. 14).

[24] Y. H. Lu, D. Zhou, T. Wang, S. A. Yang, and J. Z. Jiang, “Topological properties of atomic lead film with honeycomb structure”, *Scientific Reports*, vol. 6, no. 1, Apr. 2016. DOI: 10.1038/srep21723 (cited on pp. 14, 18).

[25] H. Zhao, C.-W. Zhang, W.-X. Ji, R.-W. Zhang, S.-S. Li, S.-S. Yan, B.-M. Zhang, P. Li, and P.-J. Wang, "Unexpected giant-gap quantum spin hall insulator in chemically decorated plumbene monolayer", *Scientific Reports*, vol. 6, no. 1, Apr. 2016. DOI: `10.1038/srep20152` (cited on pp. 14, 18).

[26] X.-L. Yu, L. Huang, and J. Wu, "From a normal insulator to a topological insulator in plumbene", *Physical Review B*, vol. 95, no. 12, Mar. 9, 2017. DOI: `10.1103/PhysRevB.95.125113` (cited on pp. 14, 18).

[27] A. Visikovskiy, S. Hayashi, T. Kajiwara, F. Komori, K. Yaji, and S. Tanaka, "Computational study of heavy group IV elements (Ge, Sn, Pb) triangular lattice atomic layers on SiC(0001) surface", *arXiv:1809.00829 [cond-mat]*, Sep. 4, 2018. arXiv: `1809.00829` (cited on pp. 14, 18).

[28] J. Yuhara and G. Le Lay, "Beyond silicene: synthesis of germanene, stanene and plumbene", *Japanese Journal of Applied Physics*, vol. 59, SN0801, SN Aug. 1, 2020. DOI: `10.35848/1347-4065/ab8410` (cited on pp. 14, 18).

[29] J. Yuhara, B. He, N. Matsunami, M. Nakatake, and G. Le Lay, "Graphene's latest cousin: plumbene epitaxial growth on a "nano WaterCube"", *Advanced Materials*, vol. 31, no. 27, p. 1 901 017, Jul. 2019. DOI: `10.1002/adma.201901017` (cited on pp. 14, 18).

[30] L.-M. Yang, V. Bačić, I. A. Popov, A. I. Boldyrev, T. Heine, T. Frauenheim, and E. Ganz, "Two-dimensional Cu_2Si monolayer with planar hexacoordinate copper and silicon bonding", *Journal of the American Chemical Society*, vol. 137, no. 7, pp. 2757–2762, Feb. 25, 2015. DOI: `10.1021/ja513209c` (cited on p. 14).

[31] B. Feng, B. Fu, S. Kasamatsu, S. Ito, P. Cheng, C.-C. Liu, Y. Feng, S. Wu, S. K. Mahatha, P. Sheverdyaeva, P. Moras, M. Arita, O. Sugino, T.-C. Chiang, K. Shimada, K. Miyamoto, T. Okuda, K. Wu, L. Chen, Y. Yao, and I. Matsuda, "Experimental realization of two-dimensional Dirac nodal line fermions in monolayer Cu_2Si", *Nature Communications*, vol. 8, no. 1, p. 1007, Dec. 2017. DOI: `10.1038/s41467-017-01108-z` (cited on pp. 14, 21, 22).

[32] L.-M. Yang, I. A. Popov, A. I. Boldyrev, T. Heine, T. Frauenheim, and E. Ganz, "Post-anti-van't Hoff-Le Bel motif in atomically thin germanium–copper alloy film", *Physical Chemistry Chemical Physics*, vol. 17, no. 27, pp. 17 545–17 551, 2015. DOI: `10.1039/C5CP02827B` (cited on p. 14).

[33] L. Liu, C. Wang, J. Li, X.-Q. Chen, Y. Jia, and J.-H. Cho, “Two-dimensional topological semimetal states in monolayer Cu_2Ge, Fe_2Ge, and Fe_2Sn”, *Physical Review B*, vol. 101, no. 16, p. 165 403, Apr. 2020. DOI: `10.1103/PhysRevB.101.165403` (cited on pp. 14, 21).

[34] L. Gao, J.-T. Sun, J.-C. Lu, H. Li, K. Qian, S. Zhang, Y.-Y. Zhang, T. Qian, H. Ding, X. Lin, S. Du, and H.-J. Gao, “Epitaxial growth of honeycomb monolayer CuSe with Dirac nodal line fermions”, *Advanced Materials*, vol. 30, no. 16, p. 1 707 055, Apr. 2018. DOI: `10.1002/adma.201707055` (cited on pp. 14, 22).

[35] Y. Tong, M. Bouaziz, W. Zhang, B. Obeid, A. Loncle, H. Oughaddou, H. Enriquez, K. Chaouchi, V. Esaulov, Z. Chen, H. Xiong, Y. Cheng, and A. Bendounan, “Evidence of new 2D material: Cu_2Te”, *2D Materials*, vol. 7, no. 3, p. 035 010, May 15, 2020. DOI: `10.1088/2053-1583/ab8918` (cited on p. 14).

[36] N. Briggs, S. Subramanian, Z. Lin, X. Li, X. Zhang, K. Zhang, K. Xiao, D. Geohegan, R. Wallace, L.-Q. Chen, M. Terrones, A. Ebrahimi, S. Das, J. Redwing, C. Hinkle, K. Momeni, A. van Duin, V. Crespi, S. Kar, and J. A. Robinson, “A roadmap for electronic grade 2D materials”, *2D Materials*, vol. 6, no. 2, p. 022 001, Jan. 17, 2019, Publisher: IOP Publishing. DOI: `10.1088/2053-1583/aaf836` (cited on pp. 14, 15).

[37] A. D. Franklin, “Nanomaterials in transistors: from high-performance to thin-film applications”, *Science*, vol. 349, no. 6249, aab2750–aab2750, Aug. 14, 2015. DOI: `10.1126/science.aab2750` (cited on pp. 14, 15).

[38] M. Chhowalla, D. Jena, and H. Zhang, “Two-dimensional semiconductors for transistors”, *Nature Reviews Materials*, vol. 1, no. 11, p. 16 052, Aug. 17, 2016, ISSN: 2058-8437. DOI: `10.1038/natrevmats.2016.52` (cited on p. 14).

[39] L. Kou, Y. Ma, Z. Sun, T. Heine, and C. Chen, “Two-dimensional topological insulators: progress and prospects”, *The Journal of Physical Chemistry Letters*, vol. 8, no. 8, pp. 1905–1919, 2017. DOI: `10.1021/acs.jpclett.7b00222` (cited on p. 14).

[40] J. R. Schaibley, H. Yu, G. Clark, P. Rivera, J. S. Ross, K. L. Seyler, W. Yao, and X. Xu, “Valleytronics in 2D materials”, *Nature Reviews Materials*, vol. 1,

no. 11, p. 16 055, Aug. 23, 2016. DOI: 10.1038/natrevmats.2016.55 (cited on p. 14).

[41] M. Ezawa, "Valley-polarized metals and quantum anomalous hall effect in silicene", *Phys. Rev. Lett.*, vol. 109, p. 055 502, 5 Aug. 2012. DOI: 10.1103/PhysRevLett.109.055502 (cited on p. 14).

[42] W. Han, "Perspectives for spintronics in 2D materials", *Apl Materials*, vol. 4, no. 3, p. 032 401, 2016. DOI: 10.1063/1.4941712 (cited on p. 14).

[43] S. Das, D. Pandey, J. Thomas, and T. Roy, "The role of graphene and other 2D materials in solar photovoltaics", *Advanced Materials*, vol. 31, no. 1, p. 1 802 722, Jan. 1, 2019, Publisher: John Wiley & Sons, Ltd. DOI: 10.1002/adma.201802722 (cited on p. 14).

[44] L. Wang, L. Huang, W. C. Tan, X. Feng, L. Chen, X. Huang, and K.-W. Ang, "2D photovoltaic devices: progress and prospects", *Small Methods*, vol. 2, no. 3, p. 1 700 294, Mar. 1, 2018. DOI: 10.1002/smtd.201700294 (cited on p. 14).

[45] L. Chiodo, "Two-dimensional innovative materials for photovoltaics", *Novel materials for energy production and storage*, vol. 17, Jun. 1, 2019. DOI: 10.1016/j.cogsc.2019.04.004 (cited on p. 14).

[46] Q. Ma, Y. Zheng, D. Luo, T. Or, Y. Liu, L. Yang, H. Dou, J. Liang, Y. Nie, X. Wang, A. Yu, and Z. Chen, "Two-dimensional materials for all-solid-state lithium batteries", *Advanced Materials*, vol. 34, no. 16, p. 2 108 079, Dec. 28, 2021, Publisher: John Wiley & Sons, Ltd. DOI: 10.1002/adma.202108079 (cited on p. 14).

[47] S. Bai, M. Yang, J. Jiang, X. He, J. Zou, Z. Xiong, G. Liao, and S. Liu, "Recent advances of MXenes as electrocatalysts for hydrogen evolution reaction", *npj 2D Materials and Applications*, vol. 5, no. 1, p. 78, Sep. 9, 2021. DOI: 10.1038/s41699-021-00259-4 (cited on p. 15).

[48] A. Bhat, S. Anwer, K. S. Bhat, M. I. H. Mohideen, K. Liao, and A. Qurashi, "Prospects challenges and stability of 2d MXenes for clean energy conversion and storage applications", *npj 2D Materials and Applications*, vol. 5, no. 1, p. 61, Jun. 11, 2021. DOI: 10.1038/s41699-021-00239-8 (cited on p. 15).

[49] F. R. Fan, R. Wang, H. Zhang, and W. Wu, “Emerging beyond-graphene elemental 2D materials for energy and catalysis applications”, *Chemical Society Reviews*, vol. 50, no. 19, pp. 10 983–11 031, 2021, Publisher: The Royal Society of Chemistry. DOI: `10.1039/C9CS00821G` (cited on p. 15).

[50] M. Donarelli and L. Ottaviano, “2D materials for gas sensing applications: a review on graphene oxide, mos2, ws2 and phosphorene”, *Sensors*, vol. 18, no. 11, 2018. DOI: `10.3390/s18113638` (cited on p. 15).

[51] J. Zhang, L. Liu, Y. Yang, Q. Huang, D. Li, and D. Zeng, “A review on two-dimensional materials for chemiresistive- and FET-type gas sensors”, *Physical Chemistry Chemical Physics*, vol. 23, no. 29, pp. 15 420–15 439, 2021, Publisher: The Royal Society of Chemistry. DOI: `10.1039/D1CP01890F` (cited on p. 15).

[52] A. Bolotsky, D. Butler, C. Dong, K. Gerace, N. R. Glavin, C. Muratore, J. A. Robinson, and A. Ebrahimi, “Two-dimensional materials in biosensing and healthcare: from in vitro diagnostics to optogenetics and beyond”, *ACS Nano*, vol. 13, no. 9, pp. 9781–9810, Sep. 24, 2019, Publisher: American Chemical Society. DOI: `10.1021/acsnano.9b03632` (cited on p. 15).

[53] N. Rohaizad, C. C. Mayorga-Martinez, M. Fojtů, N. M. Latiff, and M. Pumera, “Two-dimensional materials in biomedical, biosensing and sensing applications”, *Chemical Society Reviews*, vol. 50, no. 1, pp. 619–657, 2021, Publisher: The Royal Society of Chemistry. DOI: `10.1039/D0CS00150C` (cited on p. 15).

[54] K. Liu and J. Wu, “Mechanical properties of two-dimensional materials and heterostructures”, *Journal of Materials Research*, vol. 31, no. 7, pp. 832–844, 2016. DOI: `10.1557/jmr.2015.324` (cited on p. 15).

[55] J. H. Kim, J. H. Jeong, N. Kim, R. Joshi, and G.-H. Lee, “Mechanical properties of two-dimensional materials and their applications”, *Journal of Physics D: Applied Physics*, vol. 52, no. 8, p. 083 001, Feb. 2018. DOI: `10.1088/1361-6463/aaf465` (cited on p. 15).

[56] C. Cui, F. Xue, W.-J. Hu, and L.-J. Li, “Two-dimensional materials with piezoelectric and ferroelectric functionalities”, *npj 2D Materials and Applications*, vol. 2, no. 1, p. 18, Jun. 22, 2018. DOI: `10.1038/s41699-018-0063-5` (cited on p. 15).

[57] K. Khan, A. K. Tareen, M. Aslam, R. Wang, Y. Zhang, A. Mahmood, Z. Ouyang, H. Zhang, and Z. Guo, “Recent developments in emerging two-dimensional materials and their applications”, *Journal of Materials Chemistry C*, vol. 8, no. 2, pp. 387–440, 2020. DOI: `10.1039/C9TC04187G` (cited on p. 15).

[58] K. V. Klitzing, G. Dorda, and M. Pepper, “New method for high-accuracy determination of the fine-structure constant based on quantized Hall resistance”, *Phys. Rev. Lett.*, vol. 45, pp. 494–497, 6 Aug. 1980. DOI: `10.1103/PhysRevLett.45.494` (cited on p. 16).

[59] R. B. Laughlin, “Quantized hall conductivity in two dimensions”, *Phys. Rev. B*, vol. 23, pp. 5632–5633, 10 May 1981. DOI: `10.1103/PhysRevB.23.5632` (cited on p. 16).

[60] G. Cristofano, G. Maiella, R. Musto, and F. Nicodemi, “Topological order in quantum Hall effect and two-dimensional conformal field theory”, *Nucl. Phys. B Proc. Suppl.*, vol. 33, L. Alvarez-Gaume, S. Fubini, C. A. Trugenberger, and A. Devoto, Eds., pp. 119–133, 1993. DOI: `10.1016/0920-5632(93)90377-I` (cited on p. 16).

[61] S. Murakami, N. Nagaosa, and S.-C. Zhang, “Dissipationless quantum spin current at room temperature”, *Science*, vol. 301, no. 5638, pp. 1348–1351, 2003. DOI: `10.1126/science.1087128` (cited on p. 16).

[62] C. L. Kane and E. J. Mele, “Quantum spin Hall effect in graphene”, *Phys. Rev. Lett.*, vol. 95, p. 226 801, 22 Nov. 2005. DOI: `10.1103/PhysRevLett.95.226801` (cited on p. 16).

[63] C. L. Kane and E. J. Mele, “Z_2 topological order and the quantum spin Hall effect”, *Phys. Rev. Lett.*, vol. 95, p. 146 802, 14 Sep. 2005. DOI: `10.1103/PhysRevLett.95.146802` (cited on pp. 16–18).

[64] K. S. Novoselov, Z. Jiang, Y. Zhang, S. V. Morozov, H. L. Stormer, U. Zeitler, J. C. Maan, G. S. Boebinger, P. Kim, and A. K. Geim, “Room-temperature quantum hall effect in graphene”, *Science*, vol. 315, no. 5817, pp. 1379–1379, 2007. DOI: `10.1126/science.1137201` (cited on p. 16).

[65] N. Nagaosa, “A new state of quantum matter”, *Science*, vol. 318, no. 5851, pp. 758–759, 2007. DOI: `10.1126/science.1150199` (cited on p. 17).

[66] M. V. Berry, “Quantal phase factors accompanying adiabatic changes”, *Proceedings of the Royal Society of London. A. Mathematical and Physical Sciences*, vol. 392, no. 1802, pp. 45–57, 1984. DOI: `10.1098/rspa.1984.0023` (cited on p. 17).

[67] Z. Zhu, Y. Cheng, and U. Schwingenschlögl, “Band inversion mechanism in topological insulators: a guideline for materials design”, *Phys. Rev. B*, vol. 85, p. 235 401, 23 Jun. 2012. DOI: `10.1103/PhysRevB.85.235401` (cited on p. 18).

[68] S. Park and B.-J. Yang, “Classification of accidental band crossings and emergent semimetals in two-dimensional noncentrosymmetric systems”, *Physical Review B*, vol. 96, no. 12, Sep. 18, 2017. DOI: `10.1103/PhysRevB.96.125127` (cited on pp. 18, 19).

[69] S. M. Young, S. Zaheer, J. C. Y. Teo, C. L. Kane, E. J. Mele, and A. M. Rappe, “Dirac semimetal in three dimensions”, *Phys. Rev. Lett.*, vol. 108, no. 14, p. 140 405, Apr. 2012, Publisher: American Physical Society. DOI: `10.1103/PhysRevLett.108.140405` (cited on pp. 19, 20).

[70] A. A. Burkov, “Topological semimetals”, *Nature Materials*, vol. 15, no. 11, pp. 1145–1148, Nov. 2016. DOI: `10.1038/nmat4788` (cited on p. 19).

[71] A. A. Burkov and L. Balents, “Weyl semimetal in a topological insulator multilayer”, *Phys. Rev. Lett.*, vol. 107, no. 12, p. 127 205, Sep. 2011, Publisher: American Physical Society. DOI: `10.1103/PhysRevLett.107.127205` (cited on pp. 19, 20).

[72] S.-Y. Yang, H. Yang, E. Derunova, S. S. P. Parkin, B. Yan, and M. N. Ali, “Symmetry demanded topological nodal-line materials”, *Advances in Physics: X*, vol. 3, no. 1, p. 1 414 631, Jan. 2018, ISSN: 2374-6149. DOI: `10.1080/23746149.2017.1414631` (cited on pp. 19–22).

[73] S. Murakami, “Two-dimensional topological insulators and their edge states”, *Journal of Physics: Conference Series*, vol. 302, p. 012 019, Jul. 20, 2011. DOI: `10.1088/1742-6596/302/1/012019` (cited on p. 19).

[74] S. M. Young and C. L. Kane, “Dirac semimetals in two dimensions”, *Physical Review Letters*, vol. 115, no. 12, Sep. 16, 2015. DOI: `10.1103/PhysRevLett.115.126803` (cited on p. 19).

[75] C. Niu, P. M. Buh, H. Zhang, G. Bihlmayer, D. Wortmann, S. Blügel, and Y. Mokrousov, “Topological nodal-line semimetals in two dimensions with time-reversal symmetry breaking”, *arXiv:1703.05540 [cond-mat]*, Mar. 16, 2017. DOI: `10.48550/arXiv.1703.05540` (cited on p. 19).

[76] B. J. Wieder and C. L. Kane, “Spin-orbit semimetals in the layer groups”, *Phys. Rev. B*, vol. 94, no. 15, p. 155 108, Oct. 2016, Publisher: American Physical Society. DOI: `10.1103/PhysRevB.94.155108` (cited on p. 19).

[77] Z. K. Liu, B. Zhou, Y. Zhang, Z. J. Wang, H. M. Weng, D. Prabhakaran, S. K. Mo, Z. X. Shen, Z. Fang, X. Dai, Z. Hussain, and Y. L. Chen, “Discovery of a three-dimensional topological dirac semimetal, Na_3Bi”, *Science*, vol. 343, no. 6173, pp. 864–867, Feb. 21, 2014. DOI: `10.1126/science.1245085` (cited on p. 20).

[78] N. P. Armitage, E. J. Mele, and A. Vishwanath, “Weyl and Dirac semimetals in three-dimensional solids”, *Reviews of Modern Physics*, vol. 90, p. 015 001, 1 Jan. 2018. DOI: `10.1103/RevModPhys.90.015001` (cited on p. 20).

[79] J.-L. Lu, W. Luo, X.-Y. Li, S.-Q. Yang, J.-X. Cao, X.-G. Gong, and H.-J. Xiang, “Two-dimensional node-line semimetals in a honeycomb-kagome lattice”, *Chinese Physics Letters*, vol. 34, no. 5, p. 057 302, May 2017. DOI: `10.1088/0256-307X/34/5/057302` (cited on p. 21).

[80] C. Niu, P. M. Buhl, G. Bihlmayer, D. Wortmann, Y. Dai, S. Blügel, and Y. Mokrousov, “Two-dimensional topological nodal line semimetal in layered X_2Y ($x = Ca$, Sr, and Ba; $y = As$, Sb, and Bi)”, *Phys. Rev. B*, vol. 95, p. 235 138, 23 Jun. 2017. DOI: `10.1103/PhysRevB.95.235138` (cited on p. 21).

[81] T. He, X. Zhang, L. Wang, Y. Liu, X. Dai, L. Wang, and G. Liu, “Ideal fully spin-polarized type-ii nodal line state in half-metals X_2YZ_4 ($X = K$, Cs, Rb, $Y = Cr$, Cu, $Z = Cl$, F)”, *Materials Today Physics*, vol. 17, p. 100 360, 2021. DOI: `10.1016/j.mtphys.2021.100360` (cited on p. 21).

[82] Y.-J. Jin, R. Wang, J.-Z. Zhao, Y.-P. Du, C.-D. Zheng, L.-Y. Gan, J.-F. Liu, H. Xu, and S. Y. Tong, “The prediction of a family group of two-dimensional node-line semimetals”, *Nanoscale*, vol. 9, pp. 13 112–13 118, 35 2017. DOI: `10.1039/C7NR03520A` (cited on p. 21).

[83] B. Yang, X. Zhang, and M. Zhao, "Dirac node lines in two-dimensional Lieb lattices", *Nanoscale*, vol. 9, pp. 8740–8746, 25 2017. DOI: `10.1039/C7NR00411G` (cited on p. 21).

[84] I. Tateishi, N. T. Cuong, C. A. S. Moura, M. Cameau, R. Ishibiki, A. Fujino, S. Okada, A. Yamamoto, M. Araki, S. Ito, S. Yamamoto, M. Niibe, T. Tokushima, D. E. Weibel, T. Kondo, M. Ogata, and I. Matsuda, "Semimetallicity of free-standing hydrogenated monolayer boron from MgB_2", *Phys. Rev. Materials*, vol. 3, p. 024 004, 2 Feb. 2019. DOI: `10.1103/PhysRevMaterials.3.024004` (cited on p. 21).

[85] N. T. Cuong, I. Tateishi, M. Cameau, M. Niibe, N. Umezawa, B. Slater, K. Yubuta, T. Kondo, M. Ogata, S. Okada, and I. Matsuda, "Topological dirac nodal loops in nonsymmorphic hydrogenated monolayer boron", *Physical Review B*, vol. 101, no. 19, 2020. DOI: `10.1103/PhysRevB.101.195412` (cited on p. 21).

[86] K.-H. Jin, H. Huang, J.-W. Mei, Z. Liu, L.-K. Lim, and F. Liu, "Topological superconducting phase in high-tc superconductor MgB_2 with Dirac–nodal-line fermions", *npj Computational Materials*, vol. 5, no. 1, p. 57, May 3, 2019. DOI: `10.1038/s41524-019-0191-2` (cited on p. 21).

[87] S.-S. Wang, Z.-M. Yu, Y. Liu, Y. Jiao, S. Guan, X.-L. Sheng, and S. A. Yang, "Two-dimensional nodal-loop half-metal in monolayer MnN", *Phys. Rev. Materials*, vol. 3, p. 084 201, 8 Aug. 2019. DOI: `10.1103/PhysRevMaterials.3.084201` (cited on p. 21).

[88] P. Zhou, Z. S. Ma, and L. Z. Sun, "Coexistence of open and closed type nodal line topological semimetals in two dimensional B_2C", *Journal of Materials Chemistry C*, vol. 6, no. 5, pp. 1206–1214, 2018. DOI: `10.1039/C7TC05095J` (cited on p. 21).

[89] X. Liu, H. Bao, Y. Li, and Z. Yang, "Prediction of nodal-line semimetals in two-dimensional black phosphorous films", *Scientific Reports*, vol. 10, no. 1, p. 21 351, Dec. 2020. DOI: `10.1038/s41598-020-78451-7` (cited on p. 21).

[90] F. Li, H. Ai, S. Shen, J. Geng, K. Ho Lo, and H. Pan, "Two-dimensional dirac nodal line carbon nitride to anchor single-atom catalyst for oxygen reduction reaction", *ChemSusChem*, vol. 15, e202102537, Feb. 8, 2022, Publisher: John Wiley & Sons, Ltd. DOI: `10.1002/cssc.202102537` (cited on p. 21).

[91] L.-J. Ding, G.-G. Li, C.-W. Zhang, P. Li, and P.-J. Wang, "Prediction of nodal-line semimetals in 2d ScX (x = p, as) with high stability and considerable fermi velocities", *Chemical Physics*, vol. 552, p. 111 375, Jan. 1, 2022. DOI: `10.1016/j.chemphys.2021.111375` (cited on p. 21).

[92] R. Wu, Z.-B. Wu, and I. Božović, "2d mg-cu intermetallic compounds with nontrivial band topology and dirac nodal lines", *Advanced Electronic Materials*, vol. 8, no. 3, p. 2 100 927, Dec. 23, 2021, Publisher: John Wiley & Sons, Ltd. DOI: `10.1002/aelm.202100927` (cited on p. 21).

[93] M. Tian, J. Wang, X. Liu, W. Chen, Z. Liu, H. Du, X. Ma, X. Cui, A. Zhao, Q. Shi, Z. Wang, Y. Luo, J. Yang, B. Wang, and J. G. Hou, "Creation of the Dirac nodal line by extrinsic symmetry engineering", *Nano Letters*, vol. 20, no. 3, pp. 2157–2162, 2020. DOI: `10.1021/acs.nanolett.0c00233` (cited on p. 22).

[94] M. Niibe, M. Cameau, N. T. Cuong, O. I. Sunday, X. Zhang, Y. Tsujikawa, S. Okada, K. Yubuta, T. Kondo, and I. Matsuda, "Electronic structure of a borophene layer in rare-earth aluminum/chromium boride and its hydrogenated derivative borophane", *Phys. Rev. Materials*, vol. 5, p. 084 007, 8 Aug. 2021. DOI: `10.1103/PhysRevMaterials.5.084007` (cited on p. 22).

[95] Z. Hao, W. Chen, Y. Wang, J. Li, X.-M. Ma, Y.-J. Hao, R. Lu, Z. Shen, Z. Jiang, W. Liu, Q. Jiang, Y. Yang, X. Lei, L. Wang, Y. Fu, L. Zhou, L. Huang, Z. Liu, M. Ye, D. Shen, J. Mei, H. He, C. Liu, K. Deng, C. Liu, Q. Liu, and C. Chen, "Multiple dirac nodal lines in an in-plane anisotropic semimetal $\mathrm{TaNiTe_5}$", *Physical Review B*, vol. 104, no. 11, p. 115 158, Sep. 27, 2021. DOI: `10.1103/PhysRevB.104.115158` (cited on p. 22).

[96] L. Li and M. A. N. Araújo, "Topological insulating phases from two-dimensional nodal loop semimetals", *Phys. Rev. B*, vol. 94, p. 165 117, 16 Oct. 2016. DOI: `10.1103/PhysRevB.94.165117` (cited on p. 22).

[97] G. Bednik, A. A. Zyuzin, and A. A. Burkov, "Superconductivity in Weyl metals", *Physical Review B*, vol. 92, p. 035 153, 3 Jul. 2015. DOI: `10.1103/PhysRevB.92.035153` (cited on p. 22).

Chapter 2

Experimental techniques: STM, XPS and ARPES

Chapter 2: Experimental techniques: STM, XPS and ARPES

2.1 The experimental setup

2.1.1 Ultra-high vacuum, why ?

The experimental work presented in this manuscript has been performed on many different setups, all of them under ultra-high vacuum (UHV), i.e. in environments where the pressure is $\leqslant 10^{-9}$ mbar. There are two main reasons for the need for a good vacuum in electron spectroscopy, STM or surface preparation: (1) avoiding **electron scattering** on gas molecules in the path from the sample to the analyzer in the case of spectroscopy, (2) avoiding **surface contamination** by adsorption of unwanted species, which would denature our sample and attenuate and distort spectra. This criterion is especially important when studying the properties of a surface. In the case of STM, unwanted adsorption also concerns the conductive tip of the microscope, which need to remain "clean" for imaging with atomic resolution. Condition (1) is already met by a vacuum of about 10^{-4} mbar. Condition (2) is met when the partial pressures of highly reactive gas are in the order of 10^{-10} mbar. This pressure matches the criterion of having only a few per cent of a monolayer of adsorbed atoms deposited in one hour [1]. By comparison, a vacuum in the order of 10^{-6} mbar leads to approximately one monolayer of residual gas per second. Typically, measurements are realized in chambers with a base pressure in the low 10^{-10} mbar down to a few 10^{-11} mbar.

In order to achieve UHV conditions, different pumping systems are used to obtain different vacuum ranges. Usually, three stages are necessary, each with its own pumping system, and are called: primary vacuum, secondary vacuum and ultra-high vacuum. Primary vacuum (down to 10^{-3} mbar) is commonly achieved using rotary pumps and cryosorption pumps. Secondary vacuum (10^{-3}-10^{-9} mbar) is reached using turbo-molecular or diffusion pumps, and UHV (10^{-9} mbar and below) necessitates ion pumps, often complemented by auxiliary titanium sublimation pumps.

2.1.2 The setup: one of many

A picture of our in-lab setup is shown in Figure 2.1, with its visible equipment annotated. The preparation chamber is equipped with an ion-gun for cleaning by Ar sputtering, a transfer rod with a heating stage for direct current and resistive heating, an e-beam evaporator for monolayer deposition, a quartz micro-balance for calibration, and a low energy electron diffraction (LEED) apparatus for the crystalline characterization of the surface. As the diffraction pattern occurs immediately, LEED is a very convenient tool for quick characterization. In this work, it was used as a first step to determine sample cleanliness (an oxidized Cu crystal will show a very poor LEED pattern, getting sharper as the oxide is removed) before using more time-consuming techniques (XPS, ARPES, STM). It was also used to observe the periodicity of the surfaces synthesized compared to their substrate and adjust the growth parameters in order to optimize the LEED pattern (sharp spots, low background), being in first approximation a good criterion for the local crystalline organization.

In our laboratory, the measurement chamber is equipped with a scanning tunnelling microscope. At synchrotron facilities, where we performed XPS and ARPES, the measurement chamber is equipped with a semi-hemispherical analyzer. More details on these are given below.

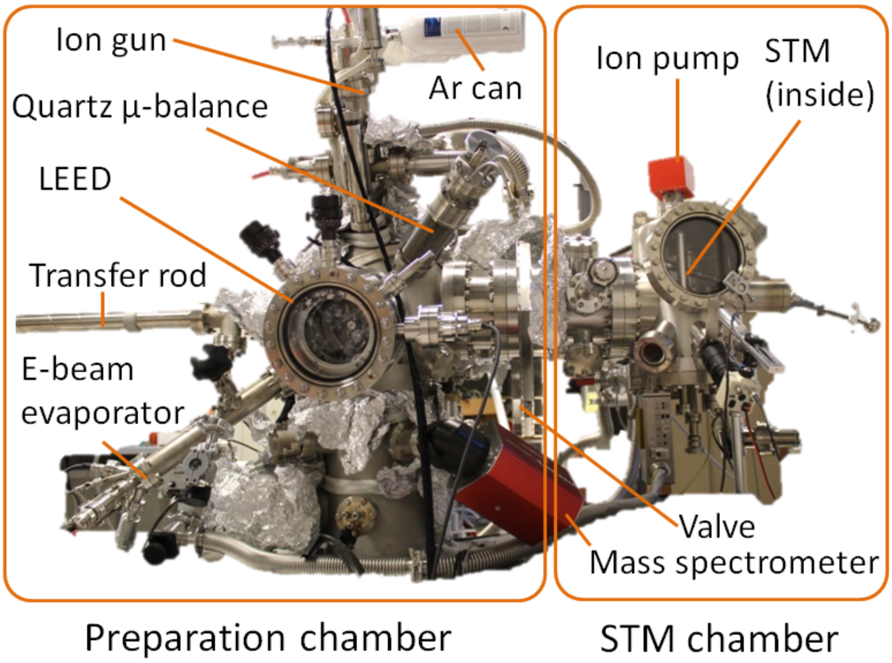

Fig. 2.1 – *Annotated picture of our preparation and STM chambers.*

2.2 Scanning tunnelling microscope (STM)

The scanning tunnelling microscope (STM) is an instrument for imaging surfaces at the atomic level. It has been invented in 1981 by Gerd Binnig and Heinrich Rohrer for which they were awarded the Nobel prize in Physics in 1986 and is now renowned among scientists for its large possibilities. In physics, STM is mainly used for the visualization and manipulation of atoms, to study local electronic properties by scanning tunnelling spectroscopy, and more recently, with the development of the spin-polarized STM, to characterize magnetic properties. Atoms are not imaged directly, instead, STM measures the local density of electronic states. In this work, the STM results presented were obtained using a VT SPM machine from Scienta Omicron.

To understand how an STM works, a brief description of its components is needed. One of its most crucial parts is the probe metallic tip, atomically sharp, usually obtained from chemically etched tungsten or by mechanical cutting. This tip is moved along the sample surface and its displacement is finely controlled by three mutually perpendicular piezoelectric tubes which expand or contract under an applied voltage and are regulated by a feedback loop (see Figure 2.2). As piezoelectric tubes

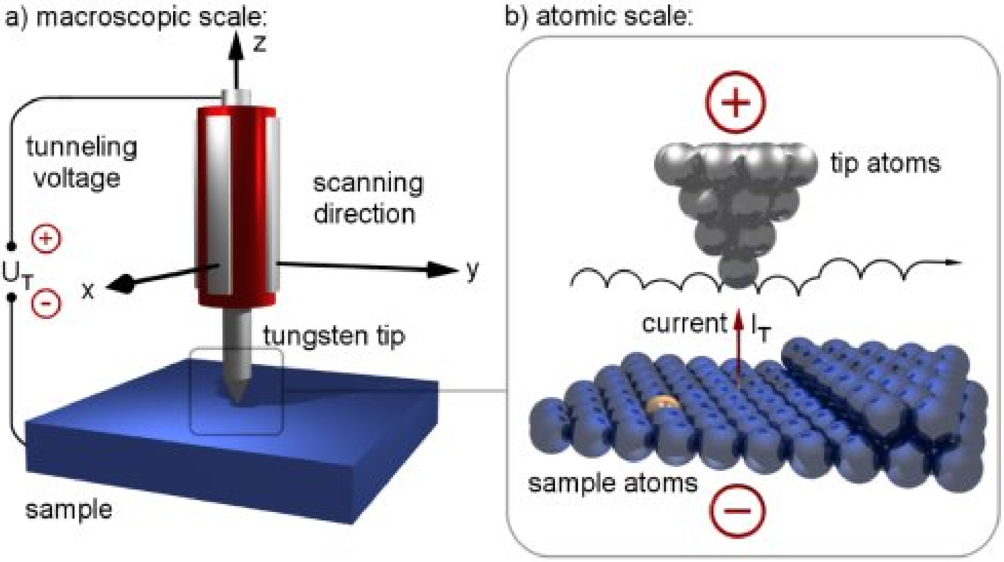

Fig. 2.2 – *Principle of scanning tunnelling microscopy: Applying a negative (positive) voltage to the sample and grounding the tip yields electron tunnelling from occupied (unoccupied) states at the surface into unoccupied (occupied) states of the tip. Keeping the tunnelling current constant while scanning the tip over the surface, the tip height follows a contour of the constant local density of states. Image from [2].*

only allow a small displacement (maximum extension ∼ µm), the coarse approach toward the sample is done by mechanical motors step by step.

2.2.1 The tunnelling effect

The tunnelling effect is the fundamental concept behind STM. In classical mechanics, if an object is trapped in a potential well and does not possess sufficient energy to overcome the depth of the well, it is impossible for it to escape. In quantum mechanics, it is however not the case. Due to the dual description wave/particle for all quantum objects and to the Heisenberg uncertainty principle, the uncertainty in the exact location of particles allows these particles to break rules of classical mechanics and “go through” an energy barrier that would classically be impassable. We show in Figure 2.3 the simplest case of a one-dimensional barrier, of height V_0 and thickness L. On the left side is an incident particle with energy E<V_0 described by the wave function Ψ_I. If the barrier height is not infinite, there exists a probability for the particle to cross the barrier. Inside the barrier, it is described by Ψ_{II}, and by Ψ_{III} afterwards. Ψ_I is a free particle wave function, and must satisfy the Schrödinger equation when reaching the potential barrier:

$$-\frac{\hbar^2}{2m}\frac{d^2}{dx^2}\Psi(x) + (V_0 - E)\Psi(x) = 0 \tag{2.1}$$

Solving this equation for the three different domains, with the help of boundary and continuity conditions, it can be shown that the incident particle can either be reflected by the barrier or cross through it. Ψ_{II} is an evanescent wave: it decays exponentially with the length L of the barrier. A reasonable approximation of the transmission coefficient through the barrier may be obtained by taking the square of the ratio of the amplitudes of Ψ_{III} and Ψ_I. In this case, the probability of tunnelling through the barrier is proportional to:

$$e^{-\frac{2}{\hbar}\sqrt{2m(V_0-E)}L} := e^{-2\kappa L} \tag{2.2}$$

With m the mass of the particle, E its energy in vacuum, V_0 the barrier height (i.e. the sample or tip work function) and L the barrier length (i.e. the distance tip-sample). The transmitted wave Ψ_{III} is again a free particle wave function, with the same energy as the incoming wave Ψ_I. Hence, during tunnelling, no particle is lost.

2.2.2 Working principle of an STM

In an STM experiment, the potential barrier is represented by the vacuum between the tip and the sample, as well as the work function of the sample or the tip (i.e. the energy needed to extract an electron from it). The tunnelling current is given above by $I \sim e^{-\frac{2}{\hbar}\sqrt{2m(V_0-E)}L}$, and varies exponentially with the distance tip-sample. Hence, an increase of the tunnelling distance of only 1 Å changes the tunnelling currents by about one order of magnitude, which underlines the importance of fine control of the tip position and overall stability of the measurement apparatus. For this reason, STM are usually installed at underground level with strong foundations and possess various vibration cancelling systems. In the example above, increasing the voltage bias corresponds to increasing the particle energy E, and to diminishing, by comparison, the height of the barrier, making tunnelling easier.

By applying a negative voltage to the sample and approaching sufficiently close

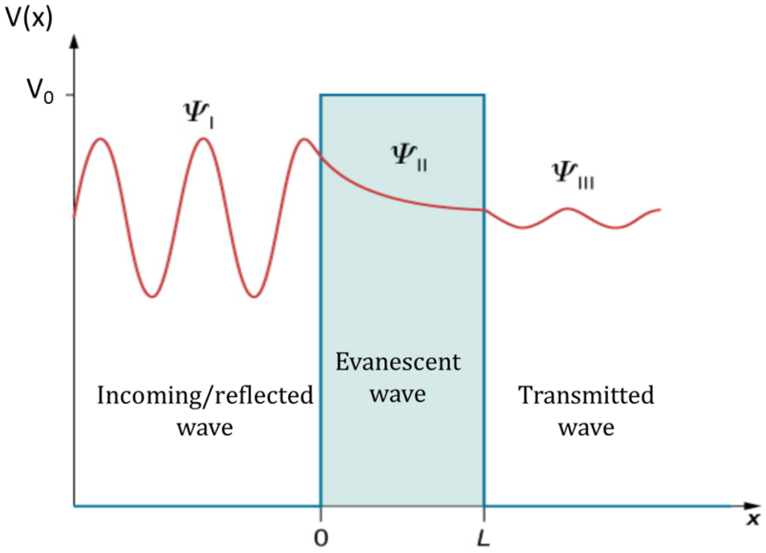

Fig. 2.3 – *The tunnelling effect. On the left side is an incident particle with energy E described by the wave function* Ψ_I*, arriving on a one-dimensional barrier of height* V_0 *(>E) and thickness L. If the barrier height is not infinite, there exists a probability for the particle to cross the barrier. Inside the barrier the particle is described by* Ψ_{II}*, an evanescent wave. After the barrier, it is described by* Ψ_{III}*, which is similar to* Ψ_I *but with a decreased probability.*

the tip (which is grounded), electron tunnelling will occur from the occupied states of the sample towards the unoccupied states of the metallic tip. Conversely, a positive voltage can be applied to the sample to probe its unoccupied states with electrons tunnelling from the tip. It is of course the reverse if the sample is grounded and the tip polarized. A schematic representation of the energy levels of a semiconductor sample and a metallic tip is shown in Figure 2.4. In the case of a semiconductor sample, the bias applied needs to be large enough to overcome the bandgap of the material, otherwise, no electron flow can occur.

Setting a constant tunnelling current while scanning with the tip over the surface will make the tip follow a contour of constant density of states, thus imaging the surface, see Figure 2.2 b. If the tunnelling current exceeds the set value, the feedback control system will increase the distance between the tip and the sample. Conversely, if the tunnelling current is less than the set current value, the feedback control system will bring the tip closer to the surface of the sample. This results in a three-dimensional map of the surface, with the height variation as a function

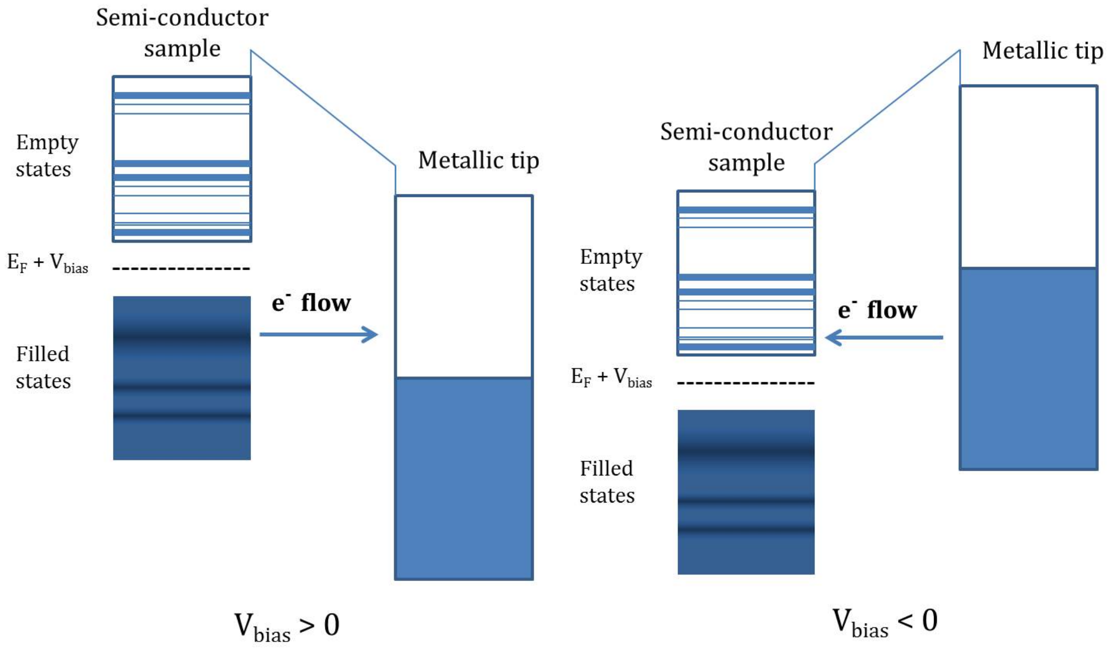

Fig. 2.4 – *Schematic representation of positive and negative STM bias. If the sample bias is higher than the tip bias ($V_{bias}>0$), its Fermi level shifts to higher energy, and the electron will flow from the sample filled states toward the tip. In the reverse case ($V_{bias}<0$) the electrons will flow from the tip toward the sample empty states. This way, both empty and filled states can be mapped by STM.*

of (x, y). This is the model used for the STM images presented in this work. It is important to keep in mind that STM shows the electronic local density of states and not "real" images of atoms.

2.3 X-ray photoelectron spectroscopy (XPS) and Angle-resolved photoelectron spectroscopy (ARPES) Techniques

2.3.1 A Short History of photoelectron spectroscopy

All photoelectron spectroscopy techniques are based on the photoelectric principle, describing the emission of an electron induced upon illumination by photons, as shown in Figure 2.5. But the path from understanding that light could create a current to the use of this property to perform spectroscopy experiments was long, and marked by major steps in the understanding of the underlying physics.

The first account of a photoelectric effect, purely phenomenological, dates from as early as 1839 and is attributed to the French scientist Edmond Becquerel [3]. In 1902 Phillip Lenard, who was awarded a Nobel prize in 1905 “for his work on cathode rays”, discovered that the energy (speed) of the charged particles ejected from a cathode depends only on the wavelength, and not on the intensity of the incident light [4], and that these particles are identical to electrons, which had been described by the British physicist Joseph John Thomson in 1897. This first observation, along with the observed “instantaneity” between the arrival of light and the emission of electrons, and the threshold effect (no electrons are emitted when using light with a wavelength higher than a given threshold) were not explainable in the paradigm of light described purely as an electromagnetic wave through Maxwell’s equations.

A few years later, in 1905, Albert Einstein came up with a corpuscular description of light [5], in which particles of light, photons, carry a quantized amount of energy $E = h\nu$ proportional to their frequency ν and to the quanta of energy h: the Planck constant. Einstein postulated that the photons transferred their energy to the electrons, and by conservation of energy, this reasoning led to the photoelectric equation $E_k = h\nu - \Phi$, where $\mathrm{E_k}$ is the kinetic energy of the emitted electron (the photoelectron), $h\nu$ the incident photon energy, and Φ the energy necessary to move the emitted electron from the surface of its material to the vacuum level (i.e. its work function). In 1921 he obtained the Nobel Prize “for his services to Theoretical Physics, and especially for his discovery of the law of the photoelectric effect”.In 1922 Arthur Compton measured the change in wavelength of x-rays after they interacted with free electrons, and showed that the change could be calculated by treating x-rays as made of photons, thus understanding the true nature of x-ray radiations. This earned him the 1927’s Nobel prize “for his discovery of the effect named after him”.

The next milestone towards experimental applications, was the development in 1957 by Kai Seigbahn of the first x-ray photoemission spectroscopy experiment, allowing the study of electronic core levels for solids [6]. As the founder of the XPS technique, Seigbahn received the Nobel prize in 1981 “for his contribution to the development of high-resolution electron spectroscopy”. Building on this, technical refinements developed XPS and made it an essential tool for physicists and chemists. Further progress made on the detectors and light sources allowed for angle-resolved and spin-resolved experiments, as well as time-resolved ones using pump-probe experiments with pulsed laser sources, multiplying the applications of photoelectron spectroscopy.

2.3.2 Theory of photoelectron spectroscopy (PES)

We will describe here two kinds of PES: X-ray photoelectron spectroscopy (XPS), and angle-resolved photoelectron spectroscopy (ARPES).

X-ray photoelectron spectroscopy (XPS) is a straightforward photon-in electron-out process. A photon of known energy ejects a core-level electron, and by measuring the kinetic energy of this electron, one can deduce its original binding energy level. XPS is a powerful tool to identify a material composition and its chemical structure, as the energy of a core level is affected by its surroundings (chemical shift). The energies of the incident photons typically range from 100 eV to 2000 eV.

ARPES is also a photon-in, electron-out, spectroscopy similar to XPS, at the difference that the angle of emission of the photoelectron is also detected in addition to its kinetic energy, and that it probes the valence electron instead or the core-level ones. It is used to observe the distribution of electrons in the reciprocal space of solids. The incident photon energies typically range from 30eV to 300eV. When using ultraviolet light (30-120eV) instead of x-rays, the term angle-resolved

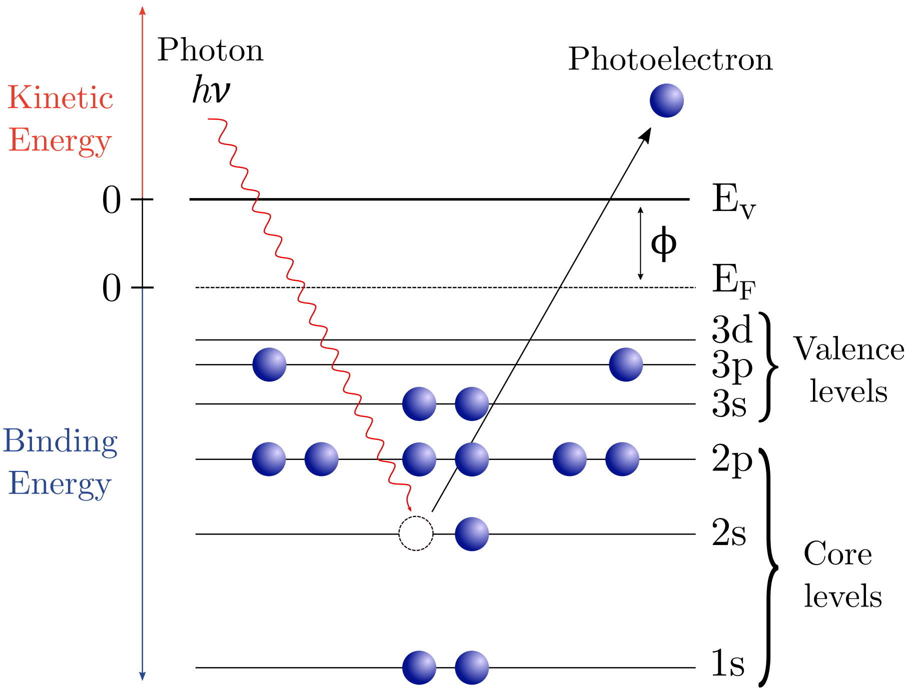

Fig. 2.5 – *A photon transfers its energy* $h\nu$ *to an electron. If this energy allows the electron to reach the vacuum energy level, it is emitted and becomes a photoelectron with a kinetic energy* $E_k = h\nu - |E_b| - \Phi$*, with* E_b *its binding energy and* Φ *the work function of the solid, or of the apparatus collecting the photoelectron.*

ultraviolet photoelectron spectroscopy (ARUPS) is also commonly used.

2.3.2.1 The Three-Step Model

One of the simplest and most used manners to describe the photoemission process is the so-called three-step model, in which the photoemission process is being separated into three independent processes. While purely phenomenological, this model proposed in 1964 by Berglund and Spicer [7] has been very successful when compared to experimental measurements. In the first step, a photon is absorbed by an electron in a solid and excites it. In the second step, the excited electron travels through the solid to its surface. In the third step, the electron escapes through the surface energy barrier (i.e. its work function) into the vacuum, where it is detected and its kinetic energy is measured. All these different energy levels are represented in Figure 2.6.

When a photon of energy $h\nu$ excites an electron, this one goes from a Bloch

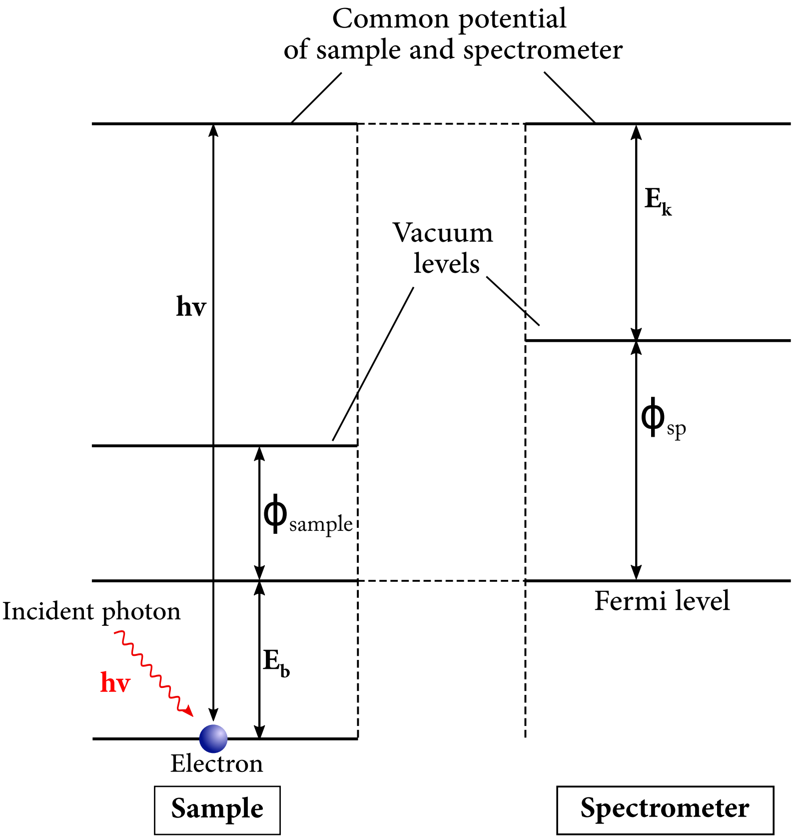

Fig. 2.6 – *Schematic representation of the different energies and energy levels involved in PES. A bound electron of binding energy E_b is excited by a photon of energy $h\nu$ and leaves the sample. The now photoelectron travels in vacuum to the spectrometer, where its kinetic energy E_k is measured by the spectrometer. From energy conservation laws, $E_k = h\nu - |E_b| - \Phi_{sp}$, with Φ_{sp} being the work function of the analyzer.*

state in the crystal towards a free-electron state. The energy of the photon is transferred to the electron, while its momentum can be neglected, being many orders of magnitude smaller than the one of electrons in the UV/soft x-rays range in which we are working here. The transitions allowed by photo-excitation are thus only vertical in k-space. The conservation laws of energy and momentum can thus be written as

$$E_k = h\nu - |E_b| - \Phi_{sp} \tag{2.3}$$

$$\boldsymbol{k_f} = \boldsymbol{k_i} \tag{2.4}$$

where E_k and E_b are the kinetic and binding energies of the photoelectron, $h\nu$

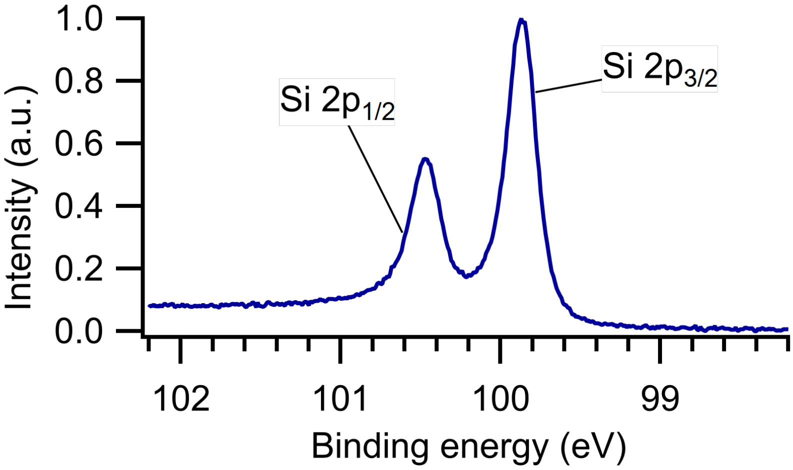

Fig. 2.7 – *Spectrum of the Si 2p core level measured on Si(111) with hv = 150 eV, using a synchrotron light source. Its doublet is clearly resolved.*

the energy of the incident photon, and Φ_{sp} the work function of the spectrometer detector. $\boldsymbol{k_i}$ and $\boldsymbol{k_f}$ are the electron momentum before and after excitation respectively, still inside the crystal. All photoelectrons respecting these equations will contribute to the creation of elastic peaks, while the others (with a non-zero energy loss) will often be considered as a background signal. In some specific cases where those non-zero energy loss interactions are not random but stem from well defined interaction those photoelectrons can create well defined peaks that can also be subject of study. We remark that the law on momentum conservation inside a crystal is only valid modulo a vector of the reciprocal lattice $\boldsymbol{G}$, such as $\boldsymbol{k_f} = \boldsymbol{k_i} + \boldsymbol{G}$.

Figure 2.7 shows an example of XPS spectra: the Si2p core-level of a Si(111) sample was probed by 150 eV photons, resulting in a characteristic doublet shape. The peaks area ratio is determined by the orbital of origin, while the separation between the doublets (the spin-orbit splitting) is core-level and element-specific, and is tabulated. The high energy resolution of the spectrum presented here is due to the synchrotron light-source used (VUV beamline, Elettra) where the energy resolution is the order of 20 meV and allows an excellent distinction between the Si 2p$_{3/2}$ and Si 2p$_{1/2}$ peaks, separated by 0.6 eV. With conventional laboratories sources such as x-ray lamps, the two doublets of the Si2p core-level are usually not separated as the energy resolution is often in the order of 1 eV.

In the second step, the excited electron travels through the solid to its surface.

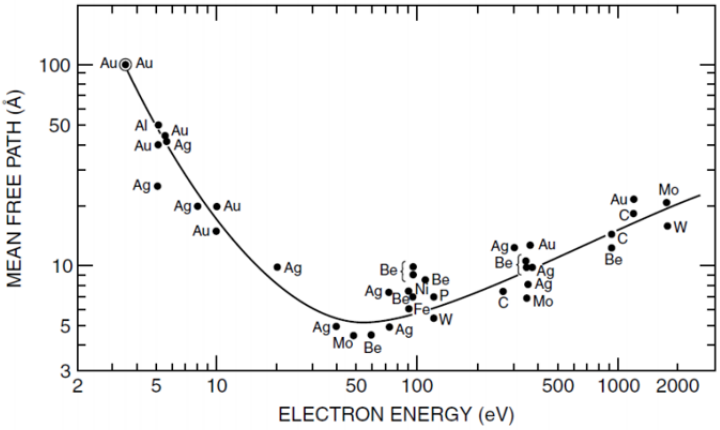

Fig. 2.8 – *"Universal curve" of the inelastic mean free path of an electron in a solid as a function of its kinetic energy, with experimental points. From [11].*

While photoemission can occur up to a few micrometres in the depth of a material, photoelectrons that manage to leave the solid without energy loss usually originate from tens of ångströms below the surface. The average distance an electron can travel inside a material without losing energy is called the inelastic mean free path (IMFP). As a first approximation, the IMFP of photoelectrons follows a "universal curve" [8] depicted in Figure 2.8, with a minimum around 4 Å for 50 eV of kinetic energy, and a general range of 4 Å to 4 nm for kinetic energies in the range 10-5000 eV. This model is however oversimplified and more precise ones have been developed [9]. For up-to-date and precise values, one can refer to the NIST database for instance [10]. We see from Figure 2.8 that varying the incident photon energy, and thus the kinetic energy of the photoelectron, can enable us to collect information at different depths in a material. This property comes in handy to identify the origin of the signal measured. In the case of a layer with different chemical composition than its substrate for example, measuring one core level at different photon energies will allow determining which peaks originate from the layer and which ones come from the substrate. This is one important asset of synchrotron facilities, where photon energy can be tuned at the desire of the experimentalist, which is not the case in more conventional light sources. A similar depth probing can however be achieved by varying the angle of incidence of the photons, with the disadvantage of measuring slightly different cross-sections of the sample for each angle.

During the transmission to the surface, the third step, the symmetry is conserved

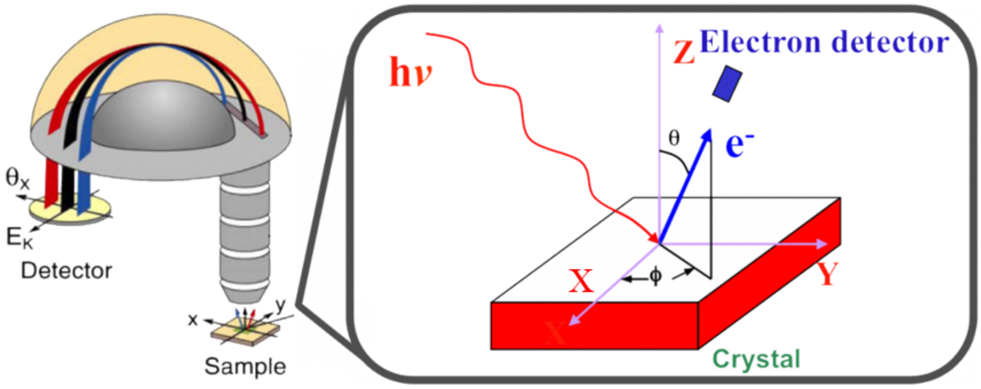

Fig. 2.9 – *Drawing of the ARPES apparatus. The analyzer resolves in energy and angle, giving information on binding energy and momentum. Credits: [12]*

in the surface plane but is broken perpendicularly to the surface: the component of the electron momentum parallel to the surface plane ($\boldsymbol{k}_{||}$) is conserved, but the component perpendicular to the surface ($\boldsymbol{k}_{\perp}$) is not conserved. A schematic representation of the momentum relationship during the surface crossing is represented in Figure 2.10. We note that the momentum transferred by the photon to the electron is neglected, as it is around two orders of magnitude smaller in the UV range. It is then possible to write:

$$k_{||} = \frac{1}{\hbar}\sqrt{2m_e E_k}\sin\theta_{out} \tag{2.5}$$

Where E_k is the photoelectron kinetic energy, m_e its mass, and θ_{out} its emission angle with respect to the surface from which it originates. For ARPES measurements, this formula allows converting the emission angle, which is measured by the analyzer, to a momentum value. A drawing of the PES apparatus is shown in Figure 2.9.

Since the electrons are being projected through the surface, the momentum perpendicular ($k_{\perp}$) to the surface is not conserved. However, when assuming that the final in-crystal states are free-electron-like with a bottom energy $-V_0$, the perpen-

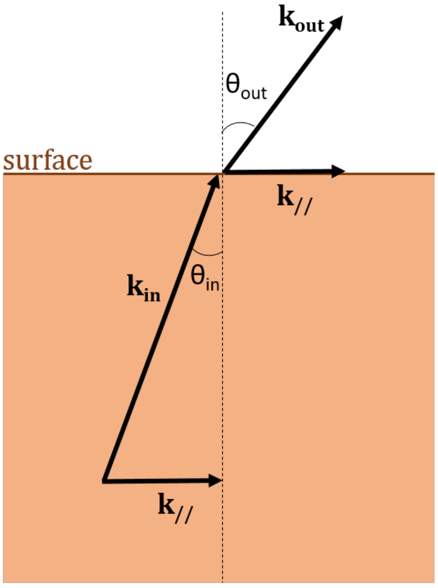

Fig. 2.10 – *Schematic representation of the parallel momentum conservation in PES. While the momentum component parallel to the surface is conversed, the component perpendicular is not.*

dicular momentum can be approximated by

$$k_\perp = \frac{1}{\hbar}\sqrt{2m_e(E_k \cos^2\theta_{out} + V_0)} \tag{2.6}$$

While in XPS only the kinetic energy E_k of the core-level photoelectrons are measured, the use of a two-dimensional detector in ARPES allows measuring conjointly the angle of emission θ_{out}. Using this, it gets possible to obtain two-dimensional images of the valence bands.

We note that in the case of a two-dimensional material, only the parallel momentum $k_{\|}$, which is conserved, is relevant. Conversely, determining if an electronic band disperses with varying photon energy is a good way to determine if the system studied is two-dimensional or three-dimensional, or to determine if the signal observed originates from the surface or the bulk of a material.

We also recall that inside the crystal the momentum is defined to a reciprocal lattice vector $\boldsymbol{G}$ ($\boldsymbol{k_f} = \boldsymbol{k_i} + \boldsymbol{G}$). In the presence of two different lattices, for example a surface layer with different periodicity than the bulk, Umklapp scattering can occur: the G vector involved in the scattering of a surface electron can be the one of the bulk lattice, resulting in an apparent translation of the surface band by a reciprocal lattice vector of the bulk. Despite the words of Rudolph Peierls: "*I used the German term Umklapp (flip-over) and this rather ugly word has remained in use...*", such bands are also sometimes called "shadow", "ghost" or "replicas" bands, and we will see experimental examples of them in chapter 3 and chapter 4.

Finally, the spin is also conserved in the photoemission process. With the suitable detectors, it is then possible to measure the projection of the spin of a photoelectron along three orthogonal directions in space. Combined with ARPES, it is feasible to obtain direct indications on the spin-polarization of electronic bands, even though the process is generally extremely time-consuming due to the low efficiency of the spin detectors.

2.3.2.2 Description of the photoemission intensity

We are here interested in finding an expression for the experimentally measured photoemission intensity.

Upon interaction with light, and taking a mono-electronic approach, the initial state of an electron Ψ_i^N (N =number of electrons) evolves to a final state Ψ_f^N with a transition probability ω_{fi} [13] given by Fermi's golden rule

$$\omega_{fi} = \frac{2\pi}{\hbar} \sum_f |<\Psi_f^N|H_{int}|\Psi_i^N>|^2 \delta(E_f - E_i - h\nu) \tag{2.7}$$

Where E_f, E_i and $h\nu$ are respectively the energies of the final state, initial state and incident photon. The interaction Hamiltonian H_{int} describes the electron-photon interaction, which can be written as

$$H_{int} = -\frac{e}{m_e}\boldsymbol{A}.\boldsymbol{p} \tag{2.8}$$

Where e and m_e are the charge and mass of the electron, $\boldsymbol{A}$ the vector potential of the incident photon, and $\boldsymbol{p}$ the momentum operator of the electron. In this expression of the Hamiltonian, some assumptions are made. First, the Coulomb gauge ($\nabla\boldsymbol{A} = 0$) is chosen. Then, all second or higher orders terms in $\boldsymbol{A}$ are neglected, which assumes that the intensity of the source is not too strong (when using bright synchrotrons sources, second order terms are sometimes to be taken into account). The electric dipole approximation is also made here, which assumes

that $\boldsymbol{A}(\boldsymbol{r}) = \boldsymbol{A}$. This independence on position is justified when the photons wavelength is much larger that the spatial extension of the atom probed, which can then be considered as punctual. In the low energy X-rays (<1000 eV) and UV ranges used in this work, this approximation stands.
Using the same $\boldsymbol{A}$ as above, the intensity $I(\boldsymbol{k}, E_b)$ of the spectral weight is given by

$$I(\boldsymbol{k}, E_b) = I_0|M_{fi}(\boldsymbol{k}, E_b)|^2 f(E_b, T) A(\boldsymbol{k}, E_b) \tag{2.9}$$

With

$$M_{fi}(\boldsymbol{k}, E_b) = \sum_f < \Psi_f^N | H_{int} | \Psi_i^N > \tag{2.10}$$

This intensity $I(\boldsymbol{k}, E_b)$ is what is measured in an ARPES experiment. Additional terms can be added in the form of products of delta functions accounting for all conservation laws stated above. I_0 is a constant, $M(\boldsymbol{k}, E_b)$ describes the matrix elements dependent on incident photon energy. They modulate the intrinsic intensities according to geometric and experimental constraints such as light polarization and emission direction. It enforces the selection rules between initial and final states. More details will be given below. $f(E_b, T)$ is the Fermi-Dirac distribution function, which tells the occupation probability as a function of both temperature and energy. Finally, $\mathrm{A}(\boldsymbol{k}, E_b)$ is the single-particle spectral function (not to be confused with the vector potential), which decides the existence of a peak and its intrinsic width and intensity. It can be thought of as a generalized density of state, and does not depend on experimental conditions. In non-interacting electron systems, it takes the form of delta function at a given momentum and energies. For interacting systems it can be generalized and is written as the imaginary part of Green's function: $A(\boldsymbol{k}, E_b) = -\mathrm{Im}G(\boldsymbol{k}, E_b).$, and can be rewritten as

$$A(k, E_b) = -\frac{1}{\pi} \frac{\sum''(k, E_b)}{[E_b - \varepsilon_k - \sum'(k, E_b)]^2 + [\sum''(k, E_b)]^2} \tag{2.11}$$

Where ε_k is the band energy and $\sum(k, \omega) := \sum'(k, \omega) + i \sum''(k, \omega)$ is the self energy of the system separated into its real and imaginary parts. We remark that the spectral function takes here the form of a Lorentzian.

As said above, the polarization of the incident light can play an important role in the features observed in ARPES, through the transition matrix element. Indeed, the final state obtained will depend on the symmetries of the initial state probed

and of the probe, here the incident photon.
A schematic representation of linear light polarization is shown in Figure 2.11. The linear horizontal (LH) polarization, sometimes called p-polarization, is parallel to the plane of incidence while the linear vertical (LV) polarization, sometimes called s-polarization, is perpendicular to the plane of incidence. In our example, the scattering plane, defined by the incident photon vector and the photoelectron final momentum $\boldsymbol{k_f}$, is a mirror plane of the sample, perpendicular to the sample surface. A combination of linear polarizations results in elliptical or circular light polarizations. The transition matrix element can be written as $M_{fi}(\boldsymbol{k}, E_b) = \sum_f < \Psi_f^N | H_{int} | \Psi_i^N >$ To have non-vanishing intensity, the transition matrix element must be even with respect to the mirror plane of the measured sample. The initial state ψ_i parity with respect to the mirror plane is even for LH (p) polarization and odd for LV (s) polarization. Assuming the final state ψ_f as a free electron, it is always even with respect to the mirror plane.

Therefore, we have two possibilities depending on the light polarization. For LV (s) polarization the initial state ψ_i must be odd with respect to the mirror plane to make the overall space integral $M_{fi}(\boldsymbol{A}) \neq 0$. On the contrary, for LH (p) polarization the initial state ψ_i must be even. We see here that photoemission with different light polarization provides a direct measure of the ground state wave function parities. In the example of Figure 2.11, the lobes of a $d_{x^2-y^2}$ orbital are represented on the surface, with their signs. These lobes have even parity with respect to the mirror plane (scattering plane): LH (p) polarized light will efficiently probe its electronic states, while LV (s) polarized light will result in an overall null matrix element, forbidding the transition thus extinguishing the signal. An experimental example of vanishing matrix element is shown in Figure 2.12 on a Cu(111) crystal surface-state. Mulazzi *et al.* showed that the Shockley surface state of Cu(111), originating mainly from *sp*-orbitals, would emit an intense signal when probed with LH (p) polarized light, while almost vanish when probed with LV (s) polarized light [14]. A summary table of the s, p and d orbital's symmetry with respect to the mirror plane is presented in Table 2.1, along with the light polarization (LV or LH) that is required to probe their electronic states.

We assumed in our example above a geometry where the scattering plane coin-

	Parity / mirror plane	Probed by
s	even	LH (p)
p_x, p_z	even	LH (p)
p_y	odd	LV (s)
$d_{x^2\text{-}y^2}$, d_{z^2}, d_{xz}	even	LH (p)
d_{xy}, d_{yz}	odd	LV (s)

Table 2.1 – Summary table of orbital's polarizations with respect to the mirror plane, with the light polarization type (linear vertical or linear horizontal) adapted to measurement.

cides with a mirror plane of the crystal. When it is not the case, symmetry mixing can be observed, and the matrix element cannot be null. Furthermore, we note that in addition to the symmetry selection rules above, the strength of interaction with light also depends on the shape of the orbitals considered: the signal intensity gets higher the more the spatial extension of the orbital lie in the direction of the $\boldsymbol{E}$-field [15].

To summarize: the observed intensity of measured spectra in a photoemission experiment is heavily dependent on the photon energy, light polarization and geometrical setup of the experiment. One great advantage of synchrotron beamlines is the common possibility to choose light polarization and photon energy, enabling a complete characterization of the band structure, and even observing bands that could have been missed otherwise.

While more complex models than the three-step model will not be discussed in detail here, it is important to know its main limitations. The three-step approach to photoemission ignores the fact that photoemission has to be described as one coherent excitation process. The initial and final states in the photoemission process are assumed to be Bloch states with an infinite lifetime, which does not allow for transitions into evanescent bandgap states, e.g. states that decay exponentially into the solid. Similarly, the assumption of an infinite lifetime for the initial state does not in practice allow the calculation of photoemission spectra that involve surface states. A more detailed model, described in the second quantization formalism, is the so-called one-step model. In it, a Bloch wave electron is excited into a wave that propagates freely in the vacuum but decays away from the surface into the

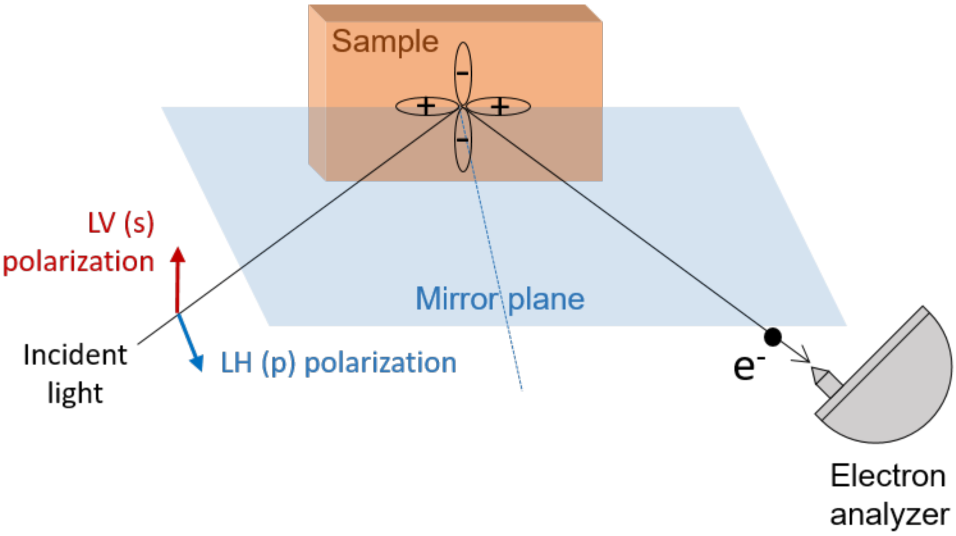

Fig. 2.11 – *Representation of LH (p) and LV (s) light polarization. The linear horizontal (LH) polarization, sometimes called p-polarization, is parallel to the plane of incidence. The linear vertical (LV) polarization, sometimes called s-polarization, is perpendicular to the plane of incidence. Orbitals and their parity with respect to the plane of incidence are schematically represented on the surface of the sample. The lobes of a* $d_{x^2-y^2}$ *are represented.*

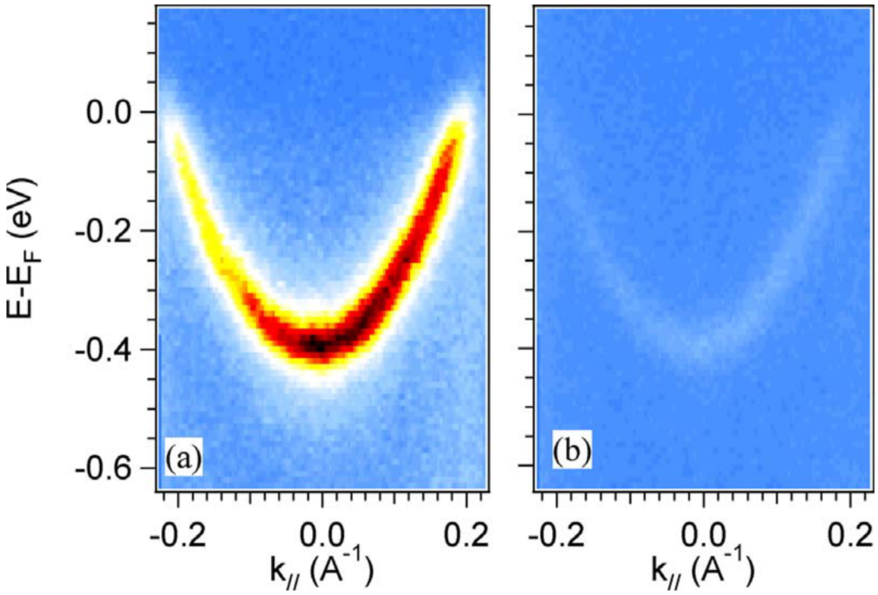

Fig. 2.12 – *ARPES of Cu(111) surface state with different light polarizations, at 30 eV. (a) with linear horizontal (p) polarization and (b) with linear vertical (s) polarization. From [14].*

solid. This decay accounts for the short IMFP of the electron in a solid, and allows for transitions into evanescent bandgap states. It also allows describing the many-body effects accurately, such as the interaction electron-electron, electron-holes and phonon-electron originating from the sudden ejection of an electron from the crystal. The one-step model also allows the calculation of photoemission spectra that involve surface states and to describe correlation effects [16], and is favored for computational ARPES.

2.3.3 Curve fitting in XPS and ARPES data analysis

« *With four parameters I can fit an elephant, and with five I can make him wiggle his trunk* » John von Neumann

In this section, we present what needs to be considered for a proper curve fitting of XPS spectra. Curve fitting is the process by which the analyst will try to obtain a signal matching the experimental one by the use of analytic tools. By using definite peak line shapes and background functions, a fit can be realized (usually by the χ^2 method).

All the XPS fits realized in this work were made using the Igor Pro Paris Photoemission Package [17].

The experimentalist must be wary of the physical reality underlying a fit. Given enough peaks with enough free parameters, anything can be fitted nicely enough. It is important to keep in mind some constraints. A good starting point is to use the binding energy and spin-orbit splitting tables, as these values are quasi constant for all measurements, and to set the branching ratio (i.e. relative areas) of doublets components according to their orbitals (p = 0.5, d = 0.66, f = 0.75). The Lorentzian full width at half maximum (FWHM) is on the first approach similar for all contributions originating from a homogeneous volume of the sample (bulk and surface components might however differ). Then, the choice of peak shapes and background subtraction is crucial.

2.3.3.1 Peak shapes

In a real photoemission experiment, the ground state core electron binding energy cannot be directly probed, because the measured binding energy incorporates both initial state and final state effects, and the spectral linewidth is broadened due to the finite core-hole lifetime (τ). In addition, a Gaussian broadening originating from the experimental setup and its resolution is observed.

Assuming an exponential decay probability for the core hole ($\propto \exp -t/\tau$), the spectral function will have a Lorentzian shape with an intensity given by

$$\begin{aligned} & I_{\text{Lorentz}}\left(E\right) = \frac{1}{\pi}\frac{A\sigma}{\left(E-E_0\right)^2+\sigma^2} \\ & \text{With:} \quad \text{A} = \text{peak area} \\ & \text{Full width at half maximum (FWHM)} \; = 2\sigma \\ & E_0 = \text{peak central value} \end{aligned} \tag{2.12}$$

From the theory of Fourier transforms, σ and τ are linked by the incertitude relation: $\Delta_\sigma \Delta_\tau \geq \hbar$. A short-lived state with small τ will thus lead to a broader peak.

Besides Lorentzian broadening, photoemission spectra are also affected by a Gaussian broadening, whose contribution can be expressed by

$$\begin{gathered} I_{\text{Gauss}}\left(E\right) = \frac{A}{\sigma\sqrt{2\pi}}\exp\left[-\frac{\left(E-E_0\right)^2}{2\sigma^2}\right] \\ \text{with FWHM} \; = 2\sqrt{2\ln(2)}\sigma \end{gathered} \tag{2.13}$$

Three main factors enter the Gaussian broadening of the spectra: the experimental energy resolution, vibrational, and inhomogeneous broadening. The first effect is caused by the imperfect monochromaticity of the photon beam which results in a finite bandwidth, and by the limited resolving power of the analyzer. For comparison, laboratory x-ray sources have energy resolutions of the order of the eV for Mg K_α x-rays and lower for other sources, while synchrotron light has an energy resolution around 10 meV. For UV, it is usually the analyzer that limits the resolution, independently of the light source, and is in the order of the meV for newer commercial analyzers. The vibrational component is produced by the excitation of low energy vibrational modes both in the initial and in the final states, and can be reduced by measuring at low temperature. Finally, inhomogeneous broadening can originate from the presence of unresolved core level components in the spectrum, from differential surface charging of the sample (mitigated by properly grounding the sample), or from the response function of the analyzer.

In order to take into account both the Lorentzian intrinsic peak shape and the Gaussian broadening, **Voigt functions** are commonly used. They are a convolution of Lorentzian and Gaussian line shapes.

$$I_{\text{Voigt}}\left(E\right) = I_{\text{Gauss}}\left(E\right) \otimes I_{\text{Lorentz}}\left(E\right) \tag{2.14}$$

Pseudo-Voigt (weighted sum of Lorentzian and Gaussian) lineshapes have also widely been used in peak fitting, as they are easier to implement. They are however an approximation of a proper Voigt function.

In the case of metallic samples, it has been shown on theoretical grounds that asymmetric profiles should be expected as a result of the many-electron interactions of the metallic conduction electrons with the accompanying deep hole in the final state [18]. While different asymmetrical peak shapes exist, the **Doniach-Sunjic** asymmetrical peak is the only one having a theoretical basis, and is written:

$$I_{\text{D-S}}\left(E\right) = \frac{1}{\pi}\frac{A\,\Gamma[1-\alpha]}{\left[\left(E-E_0\right)^2+\sigma^2\right]^{(1-\alpha)/2}}\cos\left[\frac{\pi\alpha}{2}-(1-\alpha)\arctan\left(\frac{E-E_0}{\sigma}\right)\right] \tag{2.15}$$

With FWHM = 2σ, Γ the gamma function, and α the asymmetry parameter (α = 0 for pure Lorentz function). $0 \leq \alpha < 1$ It is important to note that the Doniach-Sunjic peak shape has an infinite integral, which makes it problematic in quantitative work. Additionally, determining its actual peak position and FWHM is made more difficult by the asymmetrical shape of the peak. In most cases, a Gaussian broadening is applied on the Doniach-Sunjic peak shape, to account for the experimental broadening.

In this thesis, Voigt and Doniach-Sunjic peak shapes have been used for XPS spectra fitting.

2.3.3.2 Background

All photoelectrons arriving on the detector without any energy loss, thus obeying Equation 2.3, make the elastic peaks. By opposition, photoelectrons with a non-quantified energy loss create the background signal.

Experimentally, properly differentiating the background from the peaks is far from trivial, but is crucial for fine analysis, especially quantitative. Many background shapes are commonly used, none of which are physically exact, nor pretend to be. To optimally fit the data, the goal is thus to choose the least wrong type of background.

The background type chosen for our fits is the **Shirley background**. It was designed to account for the difference in background height between the two sides of the peak in a photoelectron spectrum[19]. This is a feature shared by all XPS spectra: a stair-like shape of the general background, each new step appearing on the higher BE side of a core-level peak. This can be observed in the Si 2p spectra shown in Figure 2.7. This asymmetrical distribution is easily understandable: the electrons of a given core-level lose energy through scattering events, appearing on the higher BE side. To appear on the lower BE side, a gain of energy is required, which is comparatively extremely rare. Ideally, each core level peak should possess its own Shirley step, which is what we did in all the XPS fits presented in this thesis, with identical parameters for all components fitted.

More specifically, we used a generalized Shirley background [20] whose shape is given by

$$\begin{aligned} B_{\text{GenShir}}\left(E\right) = S_h \int_{E_0}^{E} I^*\left(E'\right) dE' + S_l \int_{E_0}^{E} dE' \int_{E_0}^{E'} I^*\left(E''\right) dE'' \\ + S_c \int_{E_0}^{E} dE' \int_{E_0}^{E'} dE'' \int_{E_0}^{E''} I^*\left(E'''\right) dE''' \end{aligned} \tag{2.16}$$

$I^*(E) = I(E) - I\left(E_0\right)$, with I(E) the sum of all peaks without background.
E_0 is chosen on the low binding energy side of the peaks. We used an active approach to peak modelling: the background is always assessed during the optimization of the peak parameters, and not beforehand as is sometimes more traditionally done. This was found to always lead to more accurate results [21]. In the case of high-intensity backgrounds, we sometimes used a quadratic background in addition to the Shirley-

step. While not based on any physical phenomena, quadratic backgrounds can be useful to take into accounts Auger, plasmon lines or other peaks in the vicinity of the core-level of interest, and has shown good results when used in combination with a Shirley-step or Tougaard background [20].

The **Tougaard background** [22] is also commonly used to reproduce the stair-like shape of the background, and is comparable to the Shirley-step background in terms of accuracy. It is however more commonly used for large range XPS measurements, and we choose not to use it here.

Various combinations of those backgrounds and of generalized and/or adapted versions have been compared and combined [20, 21, 23, 24], but no generalization can be made as to what is “the best” background shape, as it seems to vary from one set of data to another. However a peak-specific background is always better than a general one, and polynomial backgrounds are best to be avoided if not combined to another type. All in all, the experimenter must keep in mind the limitations of the peak shape and background used, and try their best to preserve the physics behind the spectra.

More can be found in the literature about the use and misuse of curve fitting in the analysis of core X-ray photoelectron spectroscopic data [25, 26].

2.3.3.3 ARPES data analysis

The analysis of ARPES data is mainly a question of image processing, with the goal being to bring out the band structure of the studied material. Basic techniques include Gaussian filtering and normalization of the spectra to compensate asymmetries in the intensity (either induced by a non-constant background or by matrix element effects). It is often fairly common to present second derivative images of ARPES spectra. Here we used in some cases the curvature method [27] (which is actually a Laplacian treatment) to enhance the dispersive features in ARPES spectra, which is an improvement on the second derivative method.

The tools used for ARPES analysis in this work are a combination of different Igor macros collected on the different synchrotron beamlines we have been working on, which were developed by Ryu Yukawa (Photon Factory), Polina Sheverdyaeva (Elettra), Marcin Rosmus (Solaris), and Mathieu Silly (Soleil). These tools have the advantage of being adapted to the way the ARPES data is saved and organized, which is often different from each beamline and acquisition mode.

2.3.4 XPS and ARPES experimental setup

2.3.4.1 The light source: from x-ray tube to synchrotron radiation

To obtain photoelectrons, it is necessary to have a photon source. Historically, the first photon sources used for UPS were plasma discharge lamps. The principle is to introduce a pressurised gas into a small volume, and ionize its molecules by applying an electrical discharge of several kV, creating a plasma. The de-excitation of the atoms leads to emitted photons of strictly defined energies, which can then be used in the photoemission process. Generally, noble gases are used, with He being the most common. As different excited states can be reached, one element can emit on different energies, with intensities depending on the transition probability. One specific energy (amongst the available ones) can then be selected by a monochromator situated between the lamp and the sample.

To obtain x-rays, the conventional sources are x-ray tubes. Inside the tube is a cathode emitting electrons which are accelerated towards an anode (Mg or Al). By transmitting energy to the anode, core-level electrons are ejected. When outer-shell electrons fill the vacancies, x-rays are emitted by fluorescence, with element-specific energies. Those sources are still the most common for in-lab experiments, despite a growing attraction for laser sources, making time-resolved measurements feasible. Some of the experiments presented here, realized at the LPMS in Cergy, and on Tempo, Soleil synchrotron, used these sources. But for most of the work shown here, we used synchrotron radiation as a photon source.

The concept behind synchrotron radiation is that any charged particle (e.g. an electron) will radiate electromagnetic waves when accelerated. The higher the acceleration, the more energetic the emitted photons. When in the ultra-relativist domain ($\gg 0.99\ c$), the radiations are almost tangential to the trajectory, allowing easier gathering, and are channelled through beamlines towards the endstations where the experiments are taking place. Some important characteristics, already stated previously, make synchrotron radiation very attractive as compared to conventional light sources: the extremely high brightness of the excitation and high energy resolution, the tunable photon energy, and the tunable light polarization.

The greater the brightness, the more photons of a given wavelength and direction are concentrated on a given area per unit of time, increasing the signal intensity and signal to noise ratio, allowing to reach higher resolutions than with most in-lab experiments, and with much shorter acquisition times. Energy resolution in synchrotron is in the order of 10 meV compared to the $\sim$ 1 eV in x-ray lamps. The acquisition time for XPS spectra can be easily reduced by a factor of 100 as well due to the high intensity. The choice of photon energy and polarization allows for a complete ARPES characterization and can lead to information of the depth origin of a measured signal in XPS.

2.3.4.2 The hemispherical analyzer

Experimentally, the photoelectrons are gathered by a hemispherical analyzer, schematically represented in Figure 2.9. An array of electrostatic lenses located at the analyzer entrance select photoelectrons arriving from a defined solid angle (angular mode), or from a given region of the sample (spatial mode). This can be done because the trajectory of the electrons is dependent on their kinetic energy and only the ones with a kinetic energy close to the pass energy E_p, following the radius of the central trajectory between the electrodes, will hit the detector situated at the other end. The energy window is determined by the following equation: $\delta E = E_p \frac{S}{2R_0}$ where S is the entrance slit width, R_0 the radius of the analysis. The entrance slits are mechanical slits used to optimize the ratio signal/resolution. A larger opening means more photons, but less focused, inducing a loss of resolution. During a measurement, the pass energy is set to a specific value, but a system of electrostatic lenses placed before the entrance to the hemisphere is used to accelerate or retard the photoelectrons, and their voltage are varied in order to scan over all possible kinetic energies. For each particular energy, the number of electrons hitting the detector are counted and saved, and later integrated into a spectrum. For core level measurements, the angles can be also be integrated (core levels have no dispersion). The detector in itself is usually constituted of multi-channel plates multiplying the signal up to a factor 10^7, which is then measured on a two-dimensional CCD screen (one dimension is for the energy, the second for the angles).

Using the information on both the energy and momentum of photoelectrons two kinds of ARPES measurements are the most widespread: energy dispersion and

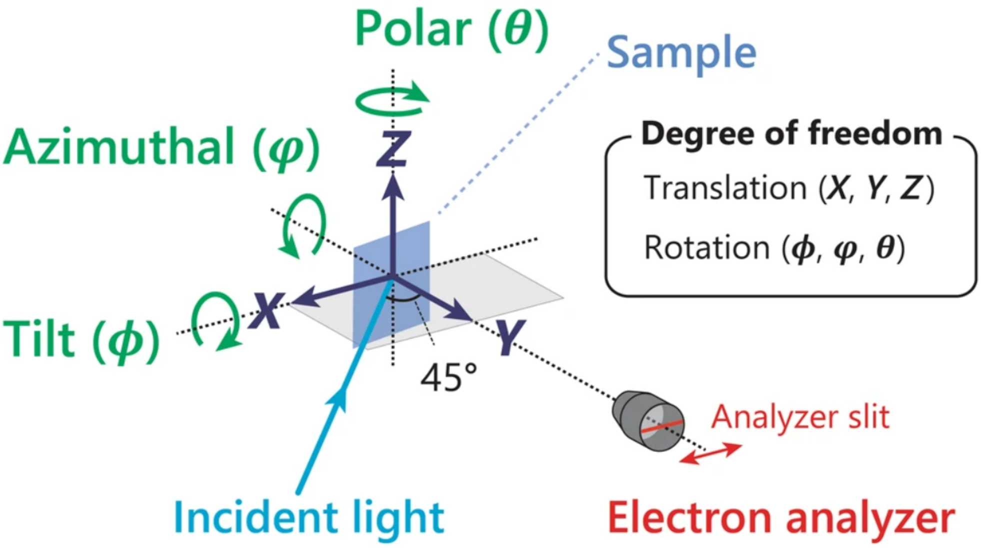

Fig. 2.13 – *Geometry of an ARPES experiment, showing the polar (θ), tilt (ϕ) and azimuthal (φ) angles. Image from [28]*

constant energy maps. To obtain energy dispersion plots, a collection of energy-constant spectra are acquired with an angular acceptance range being physically determined by a lens. Usually, the procedure needs to be repeated many times to obtain a better signal/noise ratio.

The geometry of an ARPES experiment, with all the angles involved, are shown in Figure 2.13. Rotation of the polar angle θ or of the tilt angle φ allow to translate the measurement window in the reciprocal space (see Equation 2.5 for the relationship between θ and the momentum), while the azimuthal angle ϕ is used to align the crystal along the high-symmetry directions. All manipulators can rotate the polar angle θ, but not always the azimuthal and tilt. For mechanical reasons, it is very difficult to have all three rotations on a single manipulator, especially when it needs to have a good thermal contact for low-temperature experiments.

To obtain constant energy maps (k_x-k_y spectrum), different techniques exist. One consists of taking a collection of dispersion plots while rotating the sample along the azimuthal angle. The resulting image is a portion of a disk. This kind of measurement is sometimes called “pizza plots”, and was used on the VUV beamline of Elettra synchrotron.

Another solution would be to rotate the sample along the polar axis. However, a procession of the light beam would occur if the sample was not perfectly aligned. To remedy this issue, many experimental setups use deflectors to be able to map the k-space without physically rotating the sample. Then, a collection of dispersion plots is taken, with the deflector scanning over k-space. This method was used at the Tempo beamline of Soleil synchrotron and UARPES of Solaris synchrotron. In those last two methods, the angular range is determined by the lens selected, while the energy range can be chosen freely.

Finally, another possibility is to make constant energy scans: k_x-k_y maps are directly measured by the analyzer, which scans over the energies. This is faster, but does not average over the detection channels of the analyzer as the previous methods did, and results in a more noisy signal with possible dead spots. Furthermore, the energy range attainable is limited by the selected pass energy and is usually smaller than with the previous methods.

Bibliography of Chapter 2

[1] K. Oura, V. Lifshits, A. Saranin, A. Zotov, and M. Katayama, *Surface Science, An Introduction*. Springer Berlin Heidelberg, 2003, ISBN: 978-3-642-05606-2 (cited on p. 37).

[2] S. Woedtke, PhD thesis, CAU Kiel, 2002. [Online]. Available: `http://www.ieap.uni-kiel.de/surface/ag-kipp/stm/stm.htm#Woedtk98` (cited on p. 40).

[3] E. Becquerel, "Recherche sur les effets de la radiation chimique de la lumière solaire, au moyen des courants électriques", *Comptes rendus des séances de l'Académie des sciences*, vol. 9, pp. 145–149, Jul. 1839 (cited on p. 44).

[4] P. Lenard, "Ueber die lichtelektrische wirkung", German, *Annalen der Physik*, vol. 267, no. 8, pp. 149–198, 1902. DOI: `10.1002/andp.19023130510` (cited on p. 44).

[5] A. Einstein, "Uber einen die erzeugung und verwandlung des lichtes betreffenden heuristischen gesichtspunkt", German, *Annalen der Physik*, vol. 322, no. 6, pp. 132–148, 1905. DOI: `10.1002/andp.19053220607` (cited on p. 44).

[6] C. Nordling, E. Sokolowski, and K. Siegbahn, "Precision method for obtaining absolute values of atomic binding energies", *Phys. Rev.*, vol. 105, pp. 1676–1677, 5 Mar. 1957. DOI: `10.1103/PhysRev.105.1676` (cited on p. 45).

[7] C. N. Berglund and W. E. Spicer, "Photoemission studies of copper and silver: theory", *Phys. Rev.*, vol. 136, A1030–A1044, 4A Nov. 1964. DOI: `10.1103/PhysRev.136.A1030` (cited on p. 46).

[8] M. P. Seah and W. A. Dench, "Quantitative electron spectroscopy of surfaces: a standard data base for electron inelastic mean free paths in solids", *Surface and Interface Analysis*, vol. 1, no. 1, pp. 2–11, 1979. DOI: `10.1002/sia.740010103` (cited on p. 49).

[9] S. Hofmann, *Auger- and X-Ray Photoelectron Spectroscopy in Materials Science*, ser. Springer Series in Surface Sciences. Berlin, Heidelberg: Springer Berlin Heidelberg, 2013, vol. 49, ISBN: 978-3-642-27380-3 (cited on p. 49).

[10] C. J. Powell and A. Jablonski, *NIST Electron Inelastic-Mean-Free-Path Database - Version 1.2*. National Institute of Standards and Technology, Gaithersburg, MD, 2003. DOI: 10.18434/T48C78 (cited on p. 49).

[11] G. A. Somorjai, "Chemistry in two dimensions: surfaces", 1981, ISBN: 0801411793 (cited on p. 49).

[12] *Angle-Resolved Photoemission Spectroscopy | Shen Laboratory*. [Online]. Available: https://arpes.stanford.edu/research/tool-development/angle-resolved-photoemission-spectroscopy (cited on p. 50).

[13] S. Hüfner, *Photoelectron Spectroscopy - Principles and Applications*, ser. Advanced Texts in Physics. Springer Berlin Heidelberg, 2003 (cited on p. 52).

[14] M. Mulazzi, G. Rossi, J. Braun, J. Minár, H. Ebert, G. Panaccione, I. Vobornik, and J. Fujii, "Understanding intensities of angle-resolved photoemission with circularly polarized radiation from a cu(111) surface state", *Phys. Rev. B*, vol. 79, p. 165 421, 16 Apr. 2009. DOI: 10.1103/PhysRevB.79.165421 (cited on pp. 54, 56).

[15] M. A. Valbuena, P. Chudzinski, S. Pons, S. Conejeros, P. Alemany, E. Canadell, H. Berger, E. Frantzeskakis, J. Avila, M. C. Asensio, T. Giamarchi, and M. Grioni, "Polarization dependence of angle-resolved photoemission with submicron spatial resolution reveals emerging one-dimensionality of electrons in nbse$_3$", *Phys. Rev. B*, vol. 99, p. 075 118, 7 Feb. 2019. DOI: 10.1103/PhysRevB.99.075118 (cited on p. 55).

[16] J. Minár, "Theoretical description of ARPES: the one-step model", in *DMFT at 25: Infinite dimensions*, E. Pavarini, E. Koch, D. Vollhardt, and A. Lichtenstein, Eds., vol. 4, Forschungszentrum Jülich GmbH and Institute for Advanced Simulation, Sep. 2014, ch. 13, pp. 385–423 (cited on p. 57).

[17] R. Lazzari, *Igor pro paris photoemission package*. [Online]. Available: http://www.insp.upmc.fr/I4P-Igor-Pro-Paris-Photoemission.html (cited on p. 57).

[18] S. Doniach and M. Sunjic, "Many-electron singularity in X-ray photoemission and X-ray line spectra from metals", *Journal of Physics C: Solid State Physics*, vol. 3, no. 2, pp. 285–291, Feb. 1970. DOI: 10.1088/0022-3719/3/2/010 (cited on p. 59).

[19] D. A. Shirley, “High-resolution x-ray photoemission spectrum of the valence bands of gold”, *Phys. Rev. B*, vol. 5, pp. 4709–4714, 12 Jun. 1972. DOI: `10.1103/PhysRevB.5.4709` (cited on p. 60).

[20] A. Herrera-Gomez, M. Bravo-Sanchez, F. Aguirre-Tostado, and M. Vazquez-Lepe, “The slope-background for the near-peak regimen of photoemission spectra”, *Journal of Electron Spectroscopy and Related Phenomena*, vol. 189, pp. 76–80, Aug. 2013. DOI: `10.1016/j.elspec.2013.07.006` (cited on pp. 60, 61).

[21] A. Herrera-Gomez, M. Bravo-Sanchez, O. Ceballos-Sanchez, and M. O. Vazquez-Lepe, “Practical methods for background subtraction in photoemission spectra: practical methods for background subtraction in photoemission spectra”, *Surface and Interface Analysis*, vol. 46, no. 10, pp. 897–905, Oct. 2014. DOI: `10.1002/sia.5453` (cited on pp. 60, 61).

[22] S. Tougaard, “Inelastic background correction and quantitative surface analysis”, *Journal of Electron Spectroscopy and Related Phenomena*, vol. 52, pp. 243–271, 1990. DOI: `10.1016/0368-2048(90)85022-2` (cited on p. 61).

[23] J. Végh, “The Shirley background revised”, *Journal of Electron Spectroscopy and Related Phenomena*, vol. 151, no. 3, pp. 159–164, May 2006. DOI: `10.1016/j.elspec.2005.12.002` (cited on p. 61).

[24] A. Herrera-Gomez, “The peak-shirley background”, Centro de Investigación y de Estudios Avanzados del Instituto Politécnico Nacional, Tech. Rep., 2012, p. 14. [Online]. Available: `www.qro.cinvestav.mx/~aherrera/reportesInternos/peakShirley.pdf` (cited on p. 61).

[25] P. M. Sherwood, “The use and misuse of curve fitting in the analysis of core X-ray photoelectron spectroscopic data”, *Surface and Interface Analysis*, vol. 51, no. 6, pp. 589–610, Jun. 2019. DOI: `10.1002/sia.6629` (cited on p. 61).

[26] G. H. Major, N. Fairley, P. M. A. Sherwood, M. R. Linford, J. Terry, V. Fernandez, and K. Artyushkova, “Practical guide for curve fitting in x-ray photoelectron spectroscopy”, *Journal of Vacuum Science & Technology A*, vol. 38, no. 6, p. 061 203, 2020. DOI: `10.1116/6.0000377` (cited on p. 61).

[27] P. Zhang, P. Richard, T. Qian, Y.-M. Xu, X. Dai, and H. Ding, “A precise method for visualizing dispersive features in image plots”, *Review of Scientific Instruments*, vol. 82, no. 4, p. 043 712, Apr. 2011. DOI: `10.1063/1.3585113` (cited on p. 61).

[28] H. Iwasawa, H. Takita, K. Goto, W. Mansuer, T. Miyashita, E. F. Schwier, A. Ino, K. Shimada, and Y. Aiura, “Accurate and efficient data acquisition methods for high-resolution angle-resolved photoemission microscopy”, *Scientific Reports*, vol. 8, no. 1, p. 17 431, Nov. 27, 2018. DOI: `10.1038/s41598-018-34894-7` (cited on p. 64).

Chapter 3

A study on Cu_2Si: a two-dimensional Dirac nodal-loop system

Chapter 3: A study on Cu_2Si: a two-dimensional Dirac nodal-loop system

3.1 Introduction to Cu_2Si

3.1.1 Why Cu_2Si?

Cu_2Si is the first two-dimensional material in which Dirac nodal-loops (DNL) have been experimentally evidenced, in a 2017 study by Feng *et al.* [1], were it was synthesized on a Cu(111) substrate. Their work is in line with the topical issue: do three-dimensional topological semimetals have counterparts in two-dimensional materials? While graphene and the x-ene family among others proved good examples of 2D Dirac semimetals, the existence of 2D Dirac nodal-lines semimetals was yet to be experimentally evidenced despite multiple predictions [2–8].

Since the discovery of DNLs in Cu_2Si/Cu(111), the Cu_2Si system attracted further interest, and more interesting properties have been discovered by computational work, opening more possibilities for future applications. The presence of DNLs in a system makes it a good candidate for high-frequency electronic applications due to the possible high-velocity charges carriers arising from the linear band dispersion [1]. Additionally, their higher density of states near the DNLs compared to Dirac cones materials would make them superior for such applications. Cu_2Si is predicted to be a promising candidate for nanoscale electrodes, surpassing graphene [9], or could be used as anode material for lithium and sodium ion batteries [10].

The creation of magnetic moments on the monolayer following adsorption of NO_x and CO_x ($x = 1, 2$) gas molecules indicates good possibilities for the use of Cu_2Si as a discriminant gas sensor [11, 12]. Electroreduction is also envisaged [13]. The surface encapsulation of Cu_2Si with graphene was recently achieved [14], raising new possibilities for the air-stability of the system.

On more fundamental properties, it was shown by simulations that edge states of Cu_2Si could be magnetic, and that carrier doping in a nano-ribbon can induce a transition between ferromagnetic and non-magnetic states [15]. The superconductive nature of free-standing Cu_2Si has also been revealed, being an intrinsic BCS-type superconductor with predicted superconducting temperature T_c being ∼4.1 K [16] or 1.54 K [17]. This T_c is however decreasing with increasing in-plane strain, and superconductivity is expected to be suppressed at strains lower than the one experienced by the Cu_2Si monolayer when prepared on a Cu(111) or Si(111) substrate (6.7% and 9.7% lattice mismatch respectively).

In the following section, we present the existing literature on Cu_2Si, on which we build for the next parts. In section 3.2, we study the impact of Pb deposition on the electronic structure of Cu_2Si/Cu(111). Then, in section 3.3, we characterize Cu_2Si grown on a Si(111) semiconductor substrate and explore how the substrate interacts with the surface layer.

3.1.2 Predictions and first realization of Cu_2Si

The Cu_2Si system is already well present in the literature, and we will regroup below the state of knowledge regarding its structural, growth, and electronic properties.

A Cu_2Si monolayer forms a planar hexacoordinated sheet, composed of a honeycomb Cu lattice and a triangular Si lattice, in which Si and Cu atoms are co-planar, as shown in Figure 3.1. The theoretical lattice constants for the free-standing Cu_2Si monolayer are of a = b = 4.123 Å [18]. It belongs to the space group P63/mmc No. 194. We note here that atomically flat (i.e. not buckled) monolayer are rather rare in the field of 2D materials. First-principle calculations realized in 2015 by L-M. Yang *et al.* [18] have confirmed that the flat Cu_2Si monolayer is the global minimum energy structure in 2D space. It is stabilized by the presence of covalent bonds resulting from the direct overlap of orbitals, and possesses a strong chemical bonding and high in-plane stiffness. The absence of any imaginary phonon modes furthermore demonstrates the local structural stability of the monolayer. Interestingly, despite claiming the prediction of a “new completely flat 2D hexacoordinated structure”, the description of a Cu_2Si surface silicide on Cu(111) can be found in

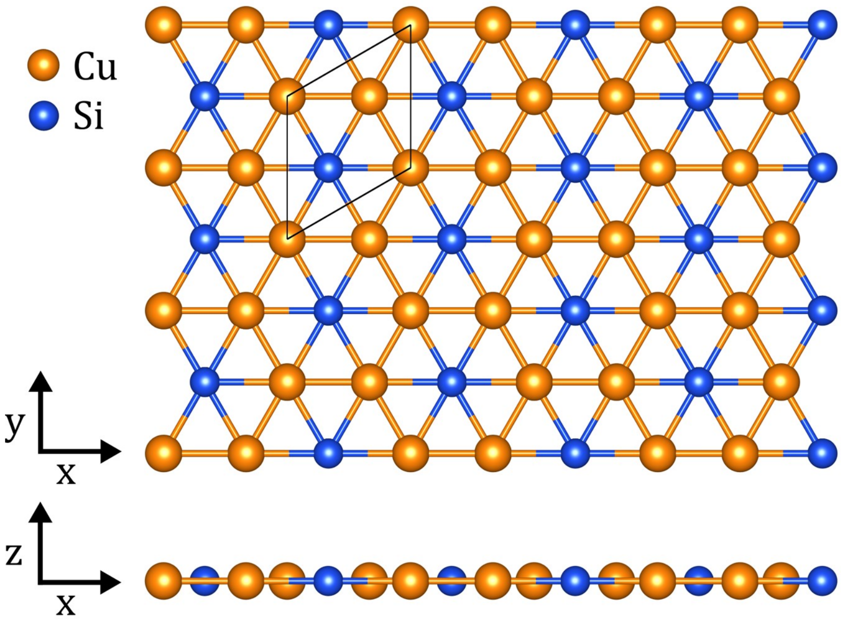

Fig. 3.1 – *Top and side view of a Cu_2Si monolayer are shown. The orange and blue spheres represent Cu and Si atoms respectively. The primitive unit cell of the system is represented by a black lozenge. It has unit vectors rotated 30° and $\sqrt{3}$ times larger than the bulk Cu(111).*

previous work [19–24]. However, those experimental studies were approaching the subject from an interface/surface alloy point of view, rather than from a 2D material one, brought up to date more recently. These studies describe the existence of a $(\sqrt{3} \times \sqrt{3})R30°Cu_2Si$ phase on Cu(111) obtained by decomposition of SiH_4, whose atomic structure might correspond to the one proposed by L - M. Yang *et al.* [18] described above. A normal incidence X-ray standing wave (NIXSW) analysis [22] demonstrated the atomic flatness of the structure (buckling < 0.07 Å), while proposing an atomic model for the surface corresponding to Figure 3.1. Further work [25] showed that the Cu_2Si surface alloy exists in these phases with the Si ion cores occupying FCC:HCP:Bridge sites with ratio 25:25:50 [25]. A schematic view of these three sites is presented in Figure 3.2. It is however the work of Feng *et al.* [1] that unraveled the special electronic properties of Cu_2Si.

They demonstrated, based on combined theoretical calculations and angle-resolved photoemission spectroscopy (ARPES), that the electronic structure of a Cu_2Si

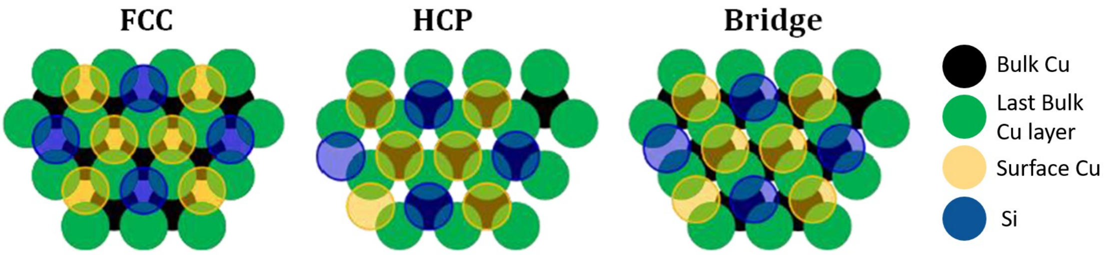

Fig. 3.2 – *The three different phases of monolayer Cu_2Si on Cu(111), with Si atoms occupying the FCC, HCP, and bridge sites. From Feng et al.* [1], *sup. mat.*

monolayer on a Cu(111) substrate displays two concentric nodal loops around the Γ point, arising from the crossing of two hole-like bands (labelled α and β) and one electron-like band (labelled γ) near the Fermi level. The γ band crosses the α and β bands linearly in all directions without opening of energy gaps, forming the DNL. The band structure of freestanding Cu_2Si is shown in Figure 3.3, with the orbital-contribution projection. It is found that the α and β bands are mainly composed of Si p_x/p_y, Cu d_{xy}, Cu $d_{x^2\text{-}y^2}$ and Cu p_x/p_y orbitals, while the γ band is mainly composed of Si p_z and Cu p_z, d_{xz} and d_{yz} orbitals. In the absence of spin orbit coupling (SOC), these DNLs are found to be protected by a mirror reflection symmetry along the xy plane (M_z): the M_z parity of the orbitals forming the band γ are opposite to the ones forming the α and β bands. The opposing M_z parities indicate that the band γ cannot couple with the bands α and β, therefore both Dirac nodal loops remain gapless. When the M_z mirror symmetry is broken, two gapless Dirac points remain along the $\Gamma - M$ and $\Gamma - K$ directions, protected by M_σ and C_2 symmetry respectively. Time-reversal and inversion symmetries do also protect these states. A complete description and discussion of the symmetries involved here was given by Feng *et al.* [1]. In the presence of SOC, gaps ranging from 5 meV to 15 meV are predicted to open. These gaps are rather small, due to the weak intrinsic SOC strength in Cu_2Si, and are not observed by ARPES within the experimental resolution. The absence of folded bulk bands from the Cu(111) substrate in ARPES also indicates a weak interaction between the substrate and the Cu_2Si monolayer, preserving to a large extent the properties expected from a freestanding Cu_2Si monolayer obtained from DFT calculations that do not include any substrate. These results were confirmed in a following study aiming at capping the Cu_2Si/Cu(111) system by graphene [14].

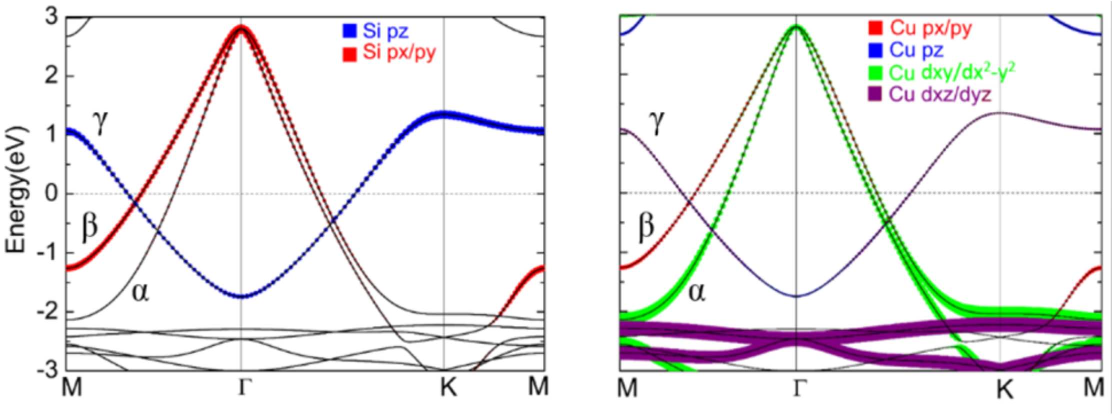

Fig. 3.3 – *Orbital projected band structures of freestanding Cu_2Si. The three bands that cross the Fermi level are labelled as α, β and γ. From Feng et al. [1], sup. mat.*

3.1.3 Cu_2Si on a Si(111) substrate

The successful synthesis of a 2D DNL semimetal is a milestone towards a better understanding of the physical properties of such systems. For practical applications however, being able to grow or transfer it on a non-conductive substrate, instead of a metallic one, would be necessary. Based on the existing literature, it appears that the growth of Cu on a Si(111) substrate can result in an hexagonal lattice with Cu_2Si surface stoichiometry, making Si(111) a substrate worth investigating for the possible existence of DNLs in Cu_2Si/Si(111). As these studies are 20 to 40 years old, they could obviously not adopt this approach at the time, nor compare with the recently predicted properties of Cu_2Si. We will describe here the state of knowledge on this matter.

The deposition of ∼1 monolayer (ML) of Si on Cu(111) was found to result in a superstructure [26], and was shown by Auger electron diffraction to form a planar geometry with sixfold symmetry [27]. The overlayer is discommensurate with the Si substrate (i.e. neither commensurate nor incommensurate) and consists of domains quasi-periodically ordered with a 5.55×5.55 periodicity, with a ±3° rotation with respect to the Si(111) substrate [28–30]. In a study using X-ray standing waves (XSW), Zegenhagen *et al* [31] proposed in 1992 a detailed atomic model of the surface, referred as the $Cu_2Si/Si(111)$ quasi-"5.55×5.55" surface reconstruction. Its atomic model is presented in Figure 3.4, and was later confirmed by numerous studies employing complementary techniques such as x-ray diffraction STM, XPS, and ultra-violet photoelectron diffraction (UVPD) study [32–34]. Those studies also confirmed the Cu_2Si stoichiometry of the surface, CuSi and $CuSi_2$ having been also considered. They furthermore demonstrated that the Si atoms are co-planar with substitutional S_u Cu atoms, while the Cu_2Si layer has a corrugation estimated to 0.27 Å (maximum height difference between Cu atoms occupying S_u and H_3 sites). More recently, it was shown that a $CuSi_2$ precursor phase would exist during the formation of the topmost copper silicide monolayer, due to the yet incomplete substitution of Cu atoms by Si [35].

The atomic model, shown in Figure 3.4, consists of a surface tiled with the $Cu_2Si/Si(111)$ quasi-"5.55×5.55" domains, lacking the long-range order of the free-standing Cu_2Si monolayer, or of $Cu_2Si/Cu(111)$. It worth remarking that in the discommensurate phase the degree of local Si-Si back-bonding depends on the individual sites. Using a He source, Neff *et al.* (2001) [36] performed Fermi surface and band mapping measurements of the $Cu_2Si/Si(111)$ quasi-"5.55×5.55" surface, and observed strong Umklapp bands features, especially in the second Brillouin zone, arising from the different periodicity of the substrate and the bulk material.

3.1.4 Our plans for Cu_2Si

While showing great promises and attracting a lot of new research, the use of Cu_2Si still faces numerous challenges. On a fundamental point of view, the manipulation of the DNLs (shifts, opening, splitting) can be used to study topological phase transitions between different types of Dirac semimetals, and possibly quantum-spin hall insulators [38, 39]. One way to do so is by changing the symmetries of the system, as they are strongly linked to the existence and preservation of the DNL. We have also seen the DNLs could become gaped when intrinsic SOC is taken into account. It has been shown that higher SOC could be induced in a 2D system by heavy-element deposition [40], and experimentally demonstrated to successfully open a gap in graphene's Dirac cones [41, 42] and split bands [43]. Following this, we present in section 3.2 our work on the impact of Pb deposition on the nodal-lines of $Cu_2Si/Cu(111)$.

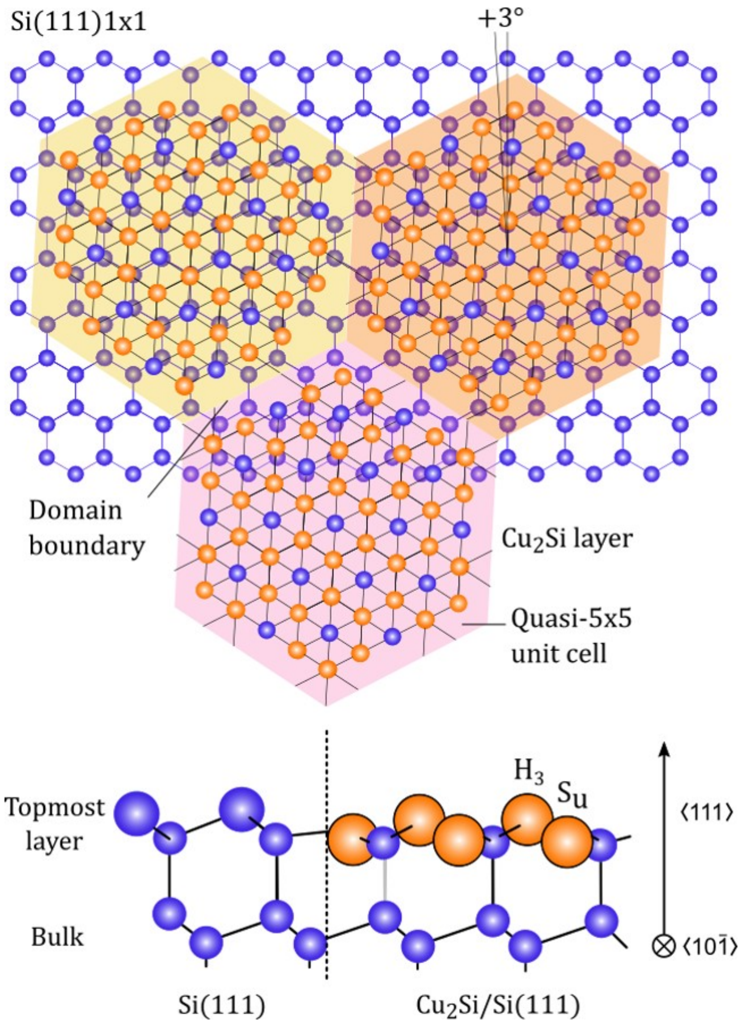

Fig. 3.4 – *Top: Schematic representation of the discommensurate Cu_2Si/Si(111) quasi-"5.55×5.55" surface, as described by Zegenhagen et al [31, 37]. Copper atoms are represented by orange spheres, silicon atoms by blue spheres. The Cu_2Si layer replaces the topmost layer of Si(111)-1x1 surface. The lattice parameter of this topmost Cu_2Si layer is larger by 9.7% compared to the Si(111), and the large lattice misfit leads to a regular dislocation network, creating discommensurate domains, represented here by the large hexagons of variable colours. Complete tiling of the surface requires three types of twisted domains (±3° with respect to the substrate orientation), two of them being rotationally equivalent (here the pink and orange hexagon). Bottom: Side view. The left-hand side of the surface shows the topmost layer of the clean Si(111), while the right-hand part is covered with Cu (orange sphere), showing the positioning of the Cu_2Si layer. The side view show the respective positions of the atoms: Cu atoms on S_u sites are co-planar with their Si neighbours and directly above the center of a Si-formed hexagon, while Cu atoms on H_3 sites lie higher (0.27 Å) [33] and are directly above the previous Si atoms.*

We also discussed the literature treating of Cu_2Si/Si(111), having in mind the importance of non-conductive substrates. Building on this knowledge, we present in section 3.3 our attempt at going further in the band structure characterization, enabled by the use of synchrotron light allowing us to vary the incident photon energies as well as light polarization. We aimed to determine if Dirac nodal lines were present on Cu_2Si/Si(111), whether gapless or not, as a gap opening could be expected from the slight buckling of the layer [44]. Finding a suitable non-conducting substrate would represent a leap towards practical applications.

3.2 Deposition of Pb on $Cu_2Si/Cu(111)$

In this section, we present angle-resolved photoelectron spectroscopy (ARPES) and x-ray photoelectron spectroscopy (XPS) measurements obtained on the system $Pb/Cu_2Si/Cu(111)$. We start by a characterization of the clean Cu(111) substrate, followed by $Cu_2Si/Cu(111)$, and finally moving towards $Pb/Cu_2Si/Cu(111)$.

These results were obtained from different experiments. The clean Cu(111) was studied at the UARPES beamline (Solaris synchrotron, Poland), and by He lamp on Tempo beamline (Soleil synchrotron, France). Results from $Cu_2Si/Cu(111)$ come from the VUV beamline (Elettra synchrotron, Italy), and from the ARPES apparatus of the LPMS (Cergy University, France), where the growth process was optimized. Finally, the results from $Pb/Cu_2Si/Cu(111)$ presented here come from the VUV beamline (Elettra synchrotron, Italy), and from the RGBL-2 beamline (Bessy synchrotron, Germany).

3.2.1 Characterization of a clean Cu(111) single crystal

3.2.1.1 Preparation of Cu(111)

Copper is a widely used substrate, commercially available in the form of a polished single crystal with the desired surface orientation. Our Cu(111) crystal was bought from “Surface preparation laboratory”. The preparation of a Cu(111) monocrystal consists of cycles of ion (Ar^+) sputtering, followed by annealing. From the various setups we used, we observed that any ion gun voltage from 0.6 keV to 3 keV produce a clean surface, with sputtering times ranging from 30 min to 1h at once. A subsequent annealing of 15 min at 450°C allows for proper mobility of the Cu atoms on the surface, and a slow decrease in temperature results in larger terraces. One has to be careful not to exceed 500°C, above which carbon and sulfur start to migrate from the bulk [45, 46].

3.2.1.2 XPS of Cu(111)

We used XPS to evaluate the Cu(111) cleanliness. In Figure 3.5a, an overview scan taken with hv = 650 eV is presented. The peaks identified are Cu 3p (76 eV) and Cu 2s (123 eV), as well as the valence band close to the Fermi energy. While no other element is visible at first, one might be more cautious and focus on expected contaminants, such as oxygen or carbon. In Figure 3.5b is presented a zoom on the energy range at which the C 1s peak should appear. To be more surface sensitive, the spectrum was taken at hv = 334 eV, 50 eV above the binding energy of C 1s (284 eV), which minimizes the photoelectron inelastic mean free path (IMFP). In the absence of any feature emerging from the background noise, the Cu(111) is deemed sufficiently clean.

3.2.1.3 ARPES of Cu(111)

We show in Figure 3.6 the positions of the high-symmetry points Γ, K, and M in the reciprocal hexagonal lattice. The band structure of copper is well studied, from early computational work [47] to state of the art ARPES [48, 49]. Its most preeminent feature is the presence of a parabolic Shockley surface state, originating from the two-dimensional electron gas present at the surface resulting from the broken translational symmetry, in a similar fashion to Au(111) or Ag(111). This Shockley state, shown in Figure 3.7a and Figure 3.7b, is commonly used as a benchmark for ARPES performance and resolution, and its observation and sharpness can be used as a cleanliness indicator when core-level spectroscopy is not available. With high-enough resolution, typically obtainable only from low-energy laser sources, a Rashba spin-splitting can be observed [48].

In addition to this surface state, copper also presents many bulk bands. As some of them are crossing the Fermi level, it is crucial for a proper comparison to measure them on the clean substrate, before any element deposition. Figure 3.8 present wide-angle measurements of Cu(111) Fermi surface and of its band dispersion along the $\Gamma - M$ direction. The first Brillouin zone of Cu(111) is represented on Figure 3.8 (a) by an orange hexagon, with dimensions $\Gamma - K$ = 1.642 Å^{-1} and $\Gamma - M$ = 1.423 Å^{-1}. Additionally to the surface state (SS) band, two other bands are observed, having a hexagonal symmetry and crossing the Fermi level close to the Brillouin zone boundary, and are labelled D and E respectively. A cut along $M - \Gamma - M$ is presented in Figure 3.8 (b). In order to allow the deeper band to be observed alongside the surface Shockley band, a logarithmic colour scale was necessary. Three bands cross the Fermi level: the surface state (SS) at 0.2 Å^{-1}, a diffuse band (D) around 1 Å^{-1}, and another one (E) crossing at 1.22 Å^{-1}. Deeper in energy, below 2 eV, bulk bands are observed.

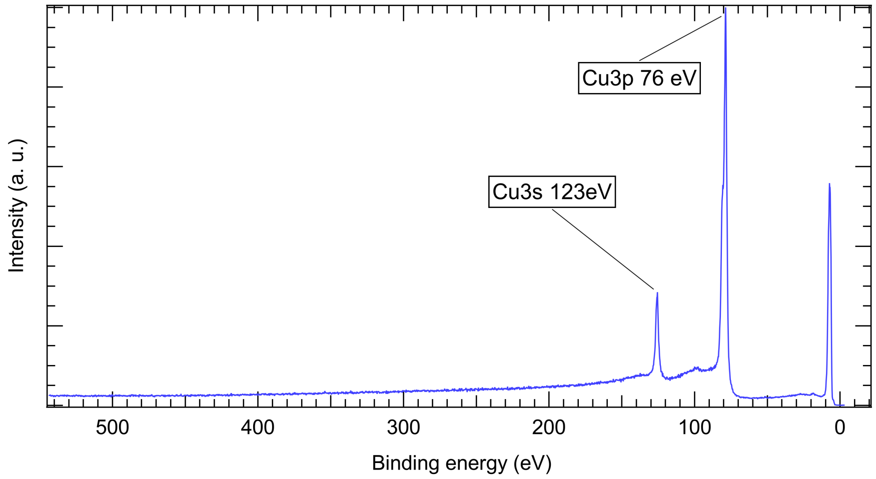

(a)

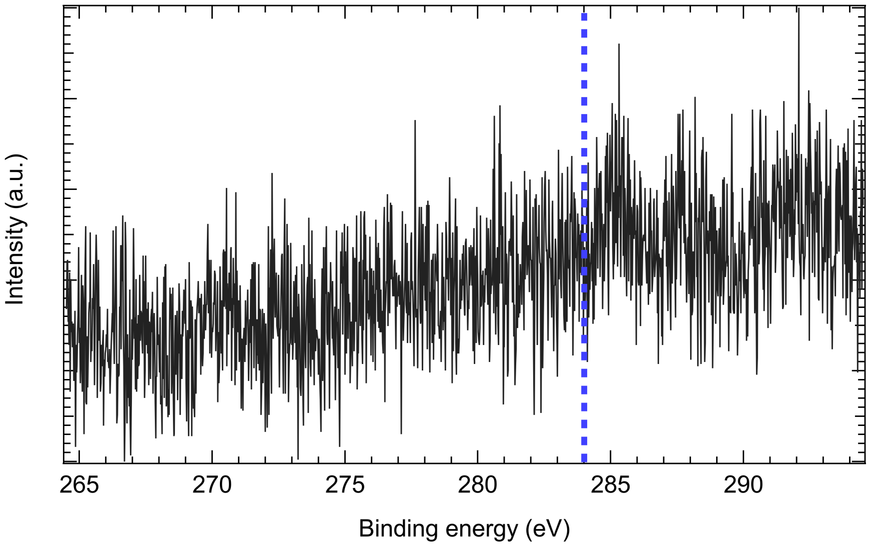

(b)

Fig. 3.5 – *(a) XPS scan at 650 eV of a clean Cu(111) surface. The only visible peaks are attributed to Cu core levels, and to the valence band near the Fermi level. (b) Spectra taken at 330 eV on a clean Cu(111) surface. The position of C 1s is marked by a blue dashed line. The absence of any feature above the noise level indicates complete removal of adventitious carbon.*

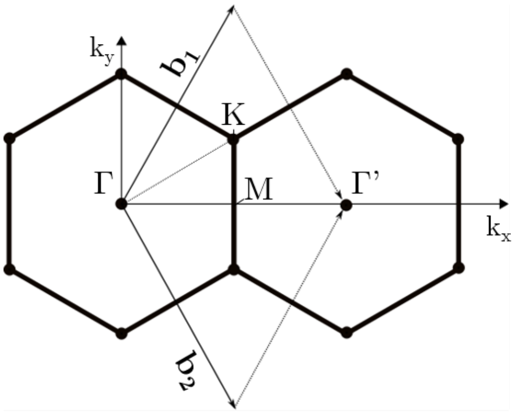

Fig. 3.6 – *Schematic representation of the honeycomb reciprocal lattice with its main high-symmetry points* Γ, *M and K.* $\boldsymbol{b_1}$ *and* $\boldsymbol{b_2}$ *are the lattice reciprocal vectors.*

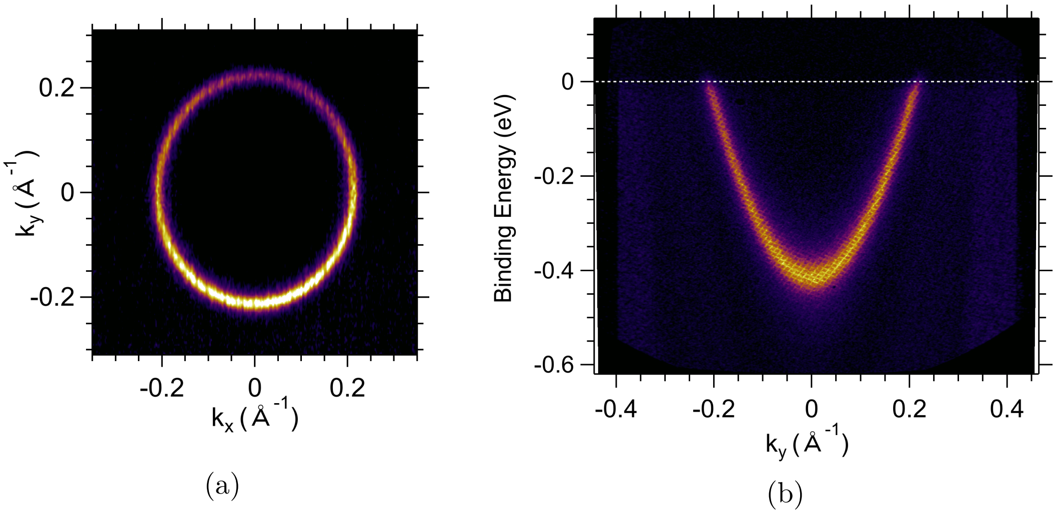

(a) (b)

Fig. 3.7 – *Measurements of the parabolic Shockley surface state of Cu(111), around* Γ*. (a) Fermi surface measured at hv = 100 eV. (b) Band dispersion along* Γ *at hv = 25 eV, showing the parabolic Shockley surface state.*

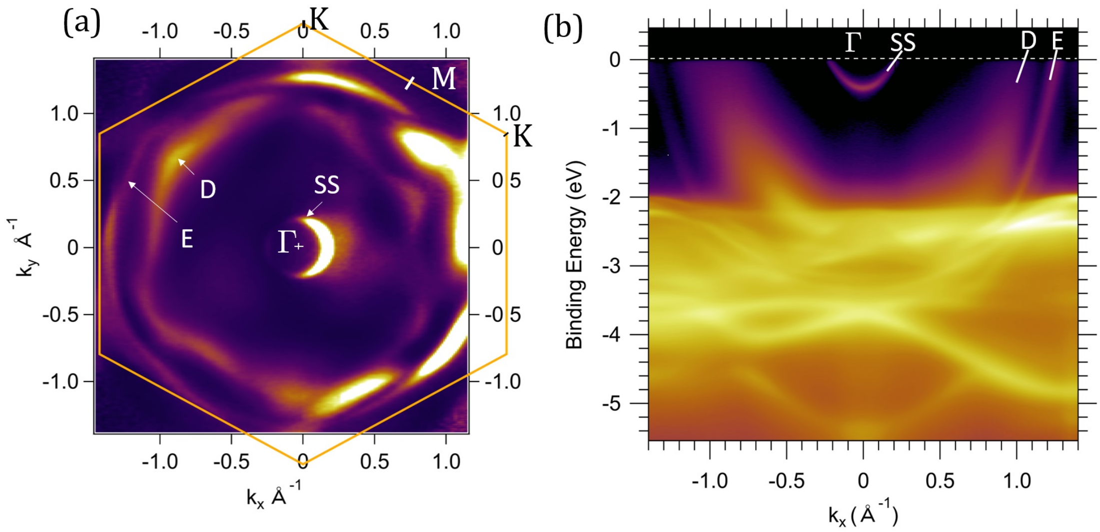

Fig. 3.8 – (*a*) *Fermi surface of Cu(111) at hv = 100 eV, centered around* Γ*. The first Brillouin zone is represented with an orange hexagon. The* $\Gamma - M$ *direction corresponds to* k_x *and the* $\Gamma - K$ *direction corresponds to* k_y*. Three bands are observed, labelled SS, D and E.* (*b*) *Band dispersion of Cu(111) along* $\Gamma - M$*, at hv =75 eV. Three bands are crossing the Fermi level. Their crossing is represented by a white dash on the right side.*

When using a UV lamp as a photon source, He II (hv = 40.8 eV) was preferred to He I (hv = 21.2 eV) despite its lower photon intensity, as He I is ill-suited to measurements involving a Cu substrate. Indeed, as shown in Figure 3.9, when using He I, “shadow” bulk bands are imaged by He I β instead of He I α, occasioning a vertical shift of 1,87 eV ($E_{HeI\beta} - E_{HeI\alpha}$). This results in the Cu bulk bands being duplicated close to -1 eV below the Fermi level, exactly in our energy zone of interest. This phenomenon does not occur using He II, as no other spectral ray is close in energy.

3.2.2 Growth process of Cu_2Si and Pb evaporation

Once a clean Cu(111) single crystal is obtained by the procedure described above, $\sim$ 0.5 monolayer (ML) of Si is evaporated on top of it from a direct current source (a power feed-trough that allows passing current into a piece of Si wafer), with Cu kept at 250°C. The apparition of a $(\sqrt{3} \times \sqrt{3})$R30° surface reconstruction observed

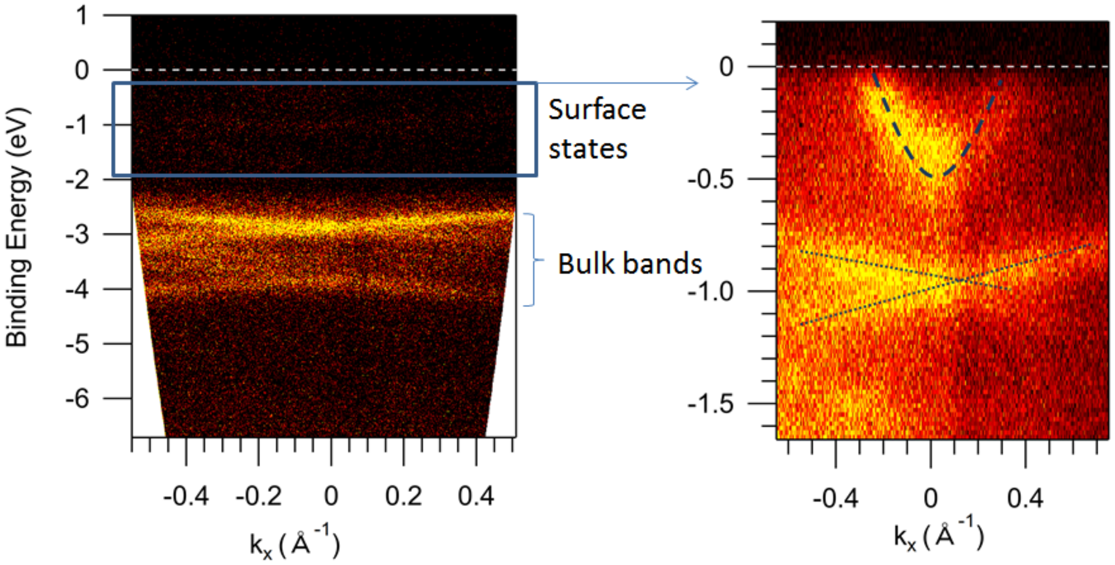

Fig. 3.9 – *Cu(111) band dispersion measured with He I (hv = 21.2 eV). On the left side are shown the bulk bands, much stronger in intensity than the surface states. On the right is presented a spectrum focusing on those surface states. The parabolic Shockley state is visible, as well as low-dispersive features around -1 eV. These features originate from the bulk bands imaged by He I β instead of He I α, occasioning a vertical shift of 1.87* eV *($E_{HeI\beta} - E_{HeI\alpha}$).*

by low energy electron diffraction (LEED) (see Figure 3.10 (b)) is the sign of the formation of Cu_2Si. The evaporation of 1/3-1 ML of Pb on top of the Cu_2Si leads to additional LEED diffraction spots, as shown in Figure 3.10 (c). These spots are aligned with the (1×1) spots and have a periodicity similar to a (4×4), which are all represented on Figure 3.10 (d). These spots could also originates from a triple-domain (4×1) periodicity, as it as been observed on In/Si(11) systems [50, 51].

Above 1 ML of Pb, the $(\sqrt{3} \times \sqrt{3})$R30° diffraction spots disappear and results in the LEED pattern shown in Figure 3.10 (e). The pattern, akin to a (4×4) periodicity, shows however double diffraction spots. The formation of a Pb overlayer on top of Cu(111) described by Meyers *et al.* [52] is identical to the one observed here. It is described as an incommensurate Pb layer, with a lattice constant smaller than that of the commensurate p(4×4) structure and decreasing with increased Pb deposition. They observe it as appearing above 1 ML of Pb, with additional Pb deposition leading to a bulk-like growth: in a layer-by-layer mode at T = 200 K

(Franck van der Merwe) and in 3D islands at T > 300 K (Stranski-Krastanow). It is uncertain if below 1ML the Pb overlayer is commensurate or not with the substrate.

The similarities between Pb growth on Cu(111) and Cu_2Si/Cu(111) can be understood from the similar atomic arrangement of the top surface layer. We note however that no new diffraction spots were observed by Meyer *et al.* below 1 ML of Pb coverage, which is not our case here. Given the LEED observed, we hypothesize that below 1 ML the Pb form discontinuous layers, leaving some areas uncovered.

3.2.3 XPS measurements on Cu_2Si/Cu(111) before and after Pb deposition

XPS overviews of clean samples of Cu_2Si/Cu(111) before and after Pb deposition are shown in Figure 3.11, where all peaks measured belong to Cu, Si or Pb.

Higher-resolution spectra of the Si 2p core level are presented in Figure 3.12 and Figure 3.13, before and after Pb deposition respectively. On Cu_2Si/Cu(111) the Si 2p core level is measured for hv = 150 eV and hv = 250 eV. One main component is observed, corresponding to surface Si. A small shoulder on the lower BE side (-0.24 eV) of the main peak, increasing with photon energy, is attributed to excess Si forming bulk islands on the surface, as already observed in the literature [1] (sup. materials). Doniach-Sunjic peak shapes are used, with an FWHM of 30 meV and Gaussian broadening in the range 60-90 meV, with a fixed $\Delta_{SO} = 0.61$ eV. The asymmetry parameter is 0.07. This picture is coherent with the atomic model of Cu_2Si and with the previous observations of Feng *et al.* [1].

Once Pb is deposited on the surface, a new contribution appears, as shown in Figure 3.13. The position of this new component, relative to the main peak, is dependent on the Pb coverage, as shown in Figure 3.14. For the lower Pb coverage, corresponding to the minimal Pb coverage where the Pb-induced superstructure is observable by LEED ($\sim 1/3$ ML), the shoulder is lying close (0.2 eV) to the main Si 2p peak. When increasing the Pb coverage, this shoulder shifts to 0.27 eV higher binding energy. This is an example of chemical shift, where the electrons of Si atoms are influenced by the presence of Pb atoms, which have a higher electronegativity.

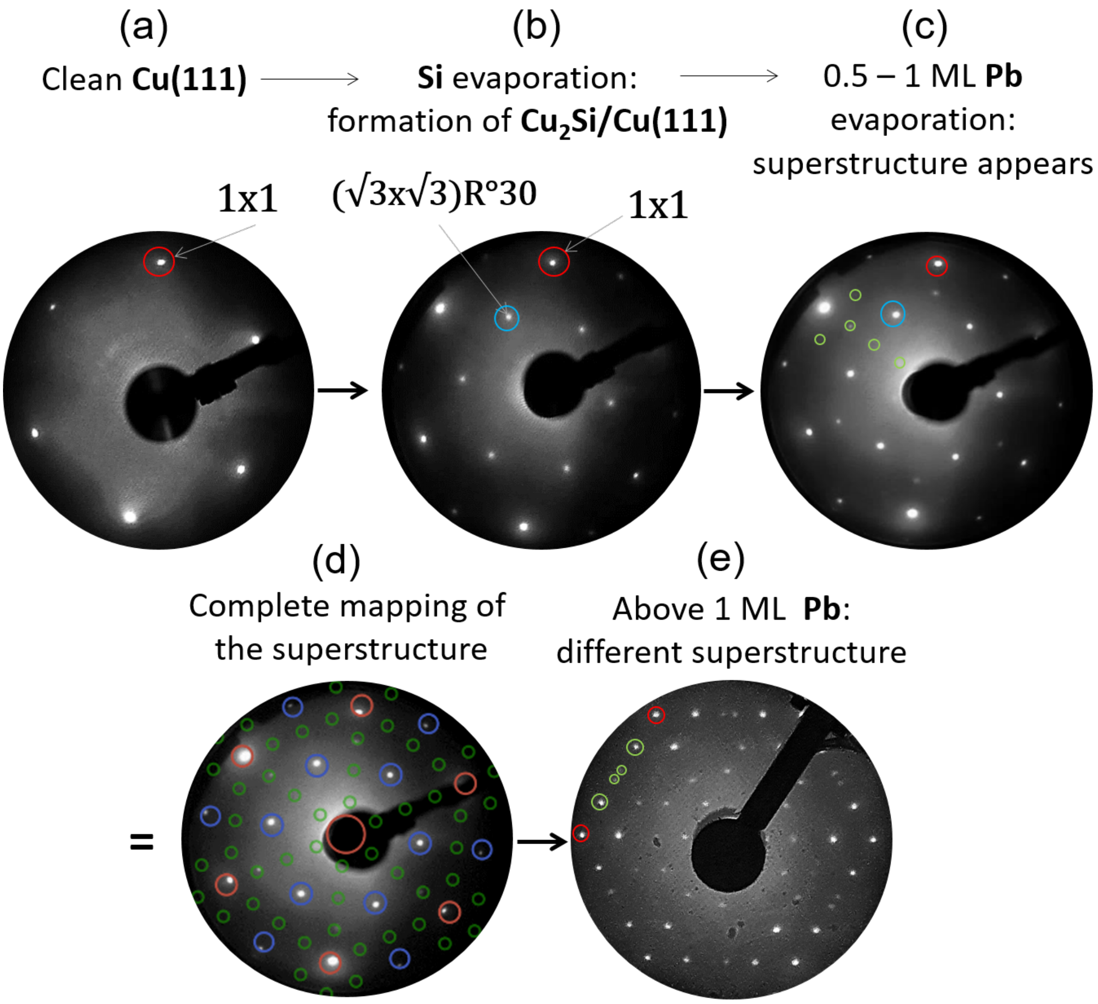

Fig. 3.10 – *Step by step LEED images the Pb/Si/Cu(111) growth process. On (a), a (1×1) spot of the clean Cu(111) crystal are circled in red. (b) After Si evaporation, a* $(\sqrt{3} \times \sqrt{3})R30°$ *surface reconstruction appears, typical of the formation of* $Cu_2Si/Cu(111)$*, and is circled in blue. (c) After Pb evaporation, new diffraction spots appear, circled in green. These spots are aligned with the (1×1) spots and have a periodicity similar to a (4×4) superstructure with missing spots, or to a triple-domain (4×1) periodicity. (d) The LEED image in (c) is entirely mapped with the superposition of (1×1),* $(\sqrt{3} \times \sqrt{3})R30°$*, and (4×4) with missing spots. (e) If more than 1 ML of Pb is deposition, the* $(\sqrt{3} \times \sqrt{3})R30°$ *spots disappear and a double spot appears in the (4×4).*

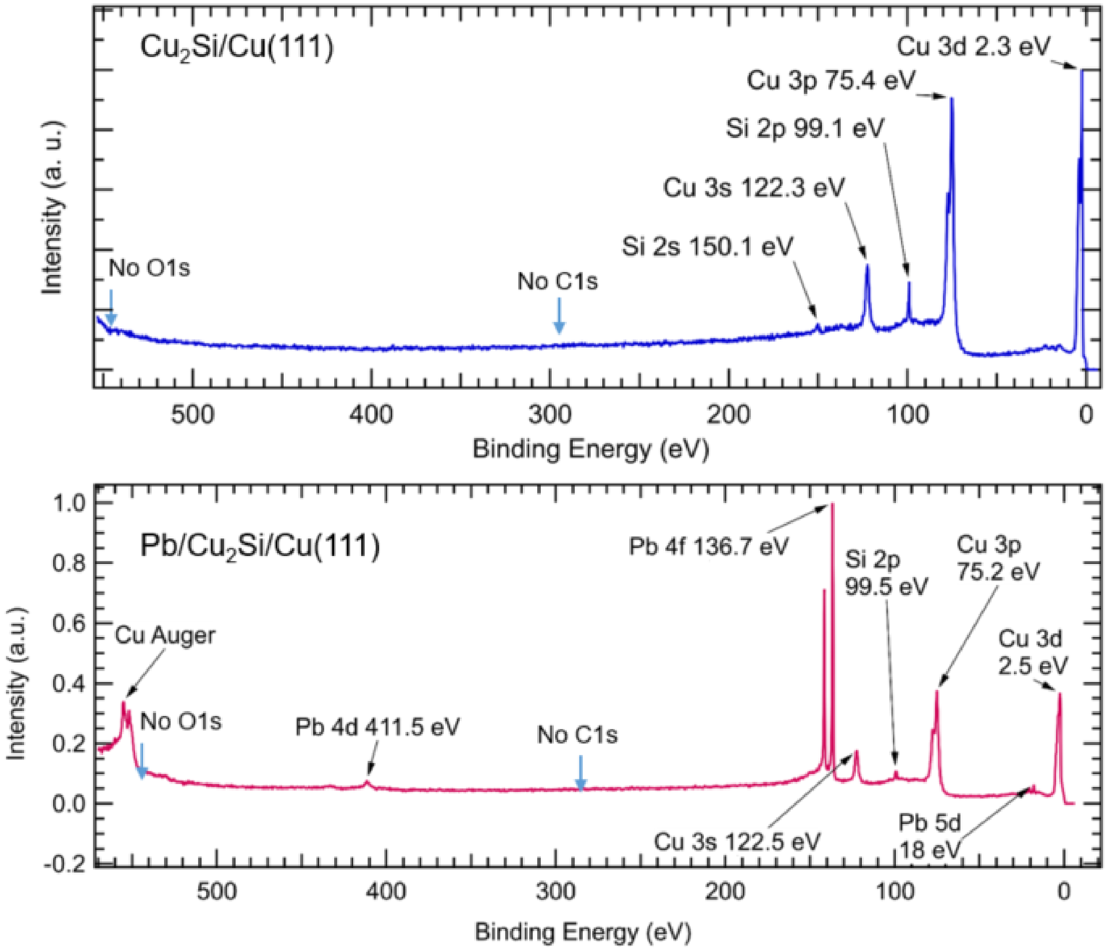

Fig. 3.11 – *XPS overviews of $Cu_2Si/Cu(111)$ before and after Pb deposition. All features observed are labelled, and belong either to Cu, Si or Pb, validating the cleanliness of the surface.*

The “high coverage” presented in the graph corresponds to the optimized coverage determined by LEED (< 1 ML), used for all the data presented here. The position of the Pb-induced Si 2p component can be used as a relative Pb calibration tool, ensuring a better reproducibility of experiments for different samples.

In Figure 3.13b the fits of the Si 2p core level are shown for hν = 150 eV and hν = 250 eV. The parameters used are similar to the ones used before Pb deposition. We find three different contributions. The main doublet, *peak 1*, originates from the surface Si forming the Cu_2Si monolayer, and *peak 3* is attributed to bulk Si forming 3D islands on the surface, as previously already observed before Pb deposition.

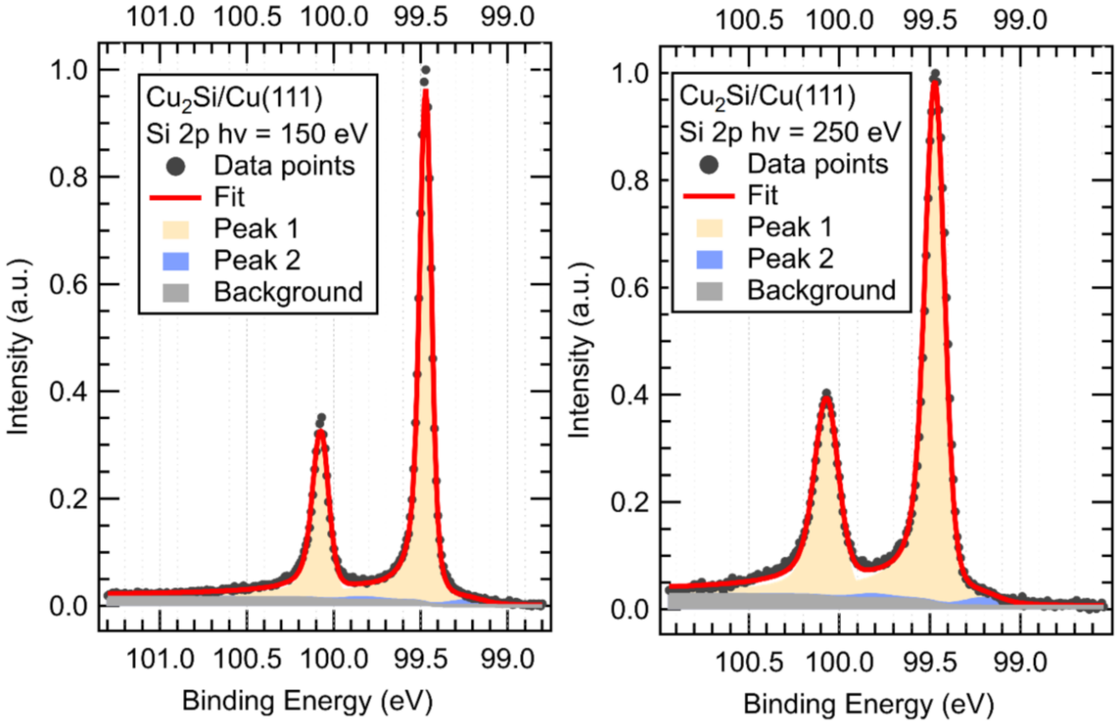

Fig. 3.12 – *Si 2p core level of $Cu_2Si/Cu(111)$ for hv = 150 eV and hv = 250 eV. One main component is observed, corresponding to surface Si. A small shoulder on the lower BE side, increasing with photon energy, is attributed to excess Si forming bulk islands on the surface.*

The new contribution, *peak 2*, thus originates from Si bonding with Pb atoms. It is located 0.44 eV higher in binding energy than the main contribution. This contribution is attributed to Si atoms interacting with the Pb deposited atoms. As the photon energy increase, becoming less surface-sensitive, this new contribution increases in intensity. This signifies that the Si atoms emitting this signal are not on the topmost layer of the system. In other words, this means that the Pb atoms are above the Si atoms, and do not migrate below the Cu_2Si monolayer.

In Figure 3.15 we present the Cu 3p core level of $Cu_2Si/Cu(111)$, for hv = 123 eV (most surface sensitive) and hv = 223 eV (more bulk sensitive). In both cases, one doublet with a branching ratio of 0.5 and a Δ_{SO} of 2.38 eV leads to a good fit. While at least two contributions are expected (bulk Cu and surface Cu), they are not resolved here, possibly due to the large full width at half maximum (FWHM) ($\sim$2 eV) of the Cu 3p peaks, and to the high background surrounding the core level signal for lower photon energies. The same Cu 3p core level is measured after Pb

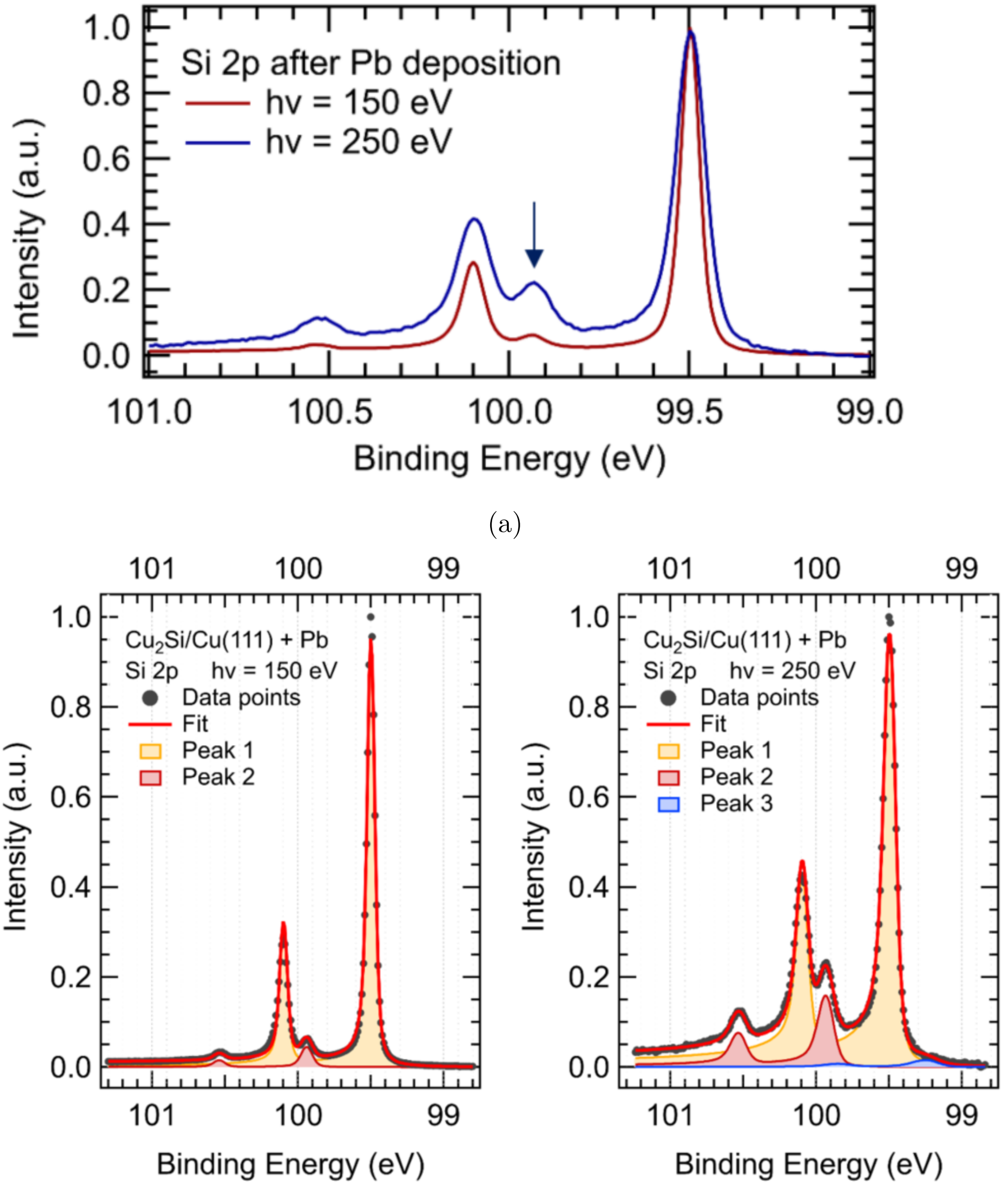

(a)

(b)

Fig. 3.13 – *Si 2p core level of $Cu_2Si/Cu(111)$ after Pb deposition ($\approx$ 1 ML). (a) show the superposition of the core level measured at $h\nu = 150$ eV and $h\nu = 250$ eV, the former one being more surface sensitive and the latter one more bulk sensitive. Compared to before Pb deposition, a new contribution is observed, marked by an arrow. (b) and (c) show the fits of these spectra. Peak 1 corresponds to the surface Si forming the Cu_2Si monolayer, peak 2 is the new contribution originating from Si bonding with Pb atoms, and peak 3 is attributed to bulk Si forming islands on the surface.*

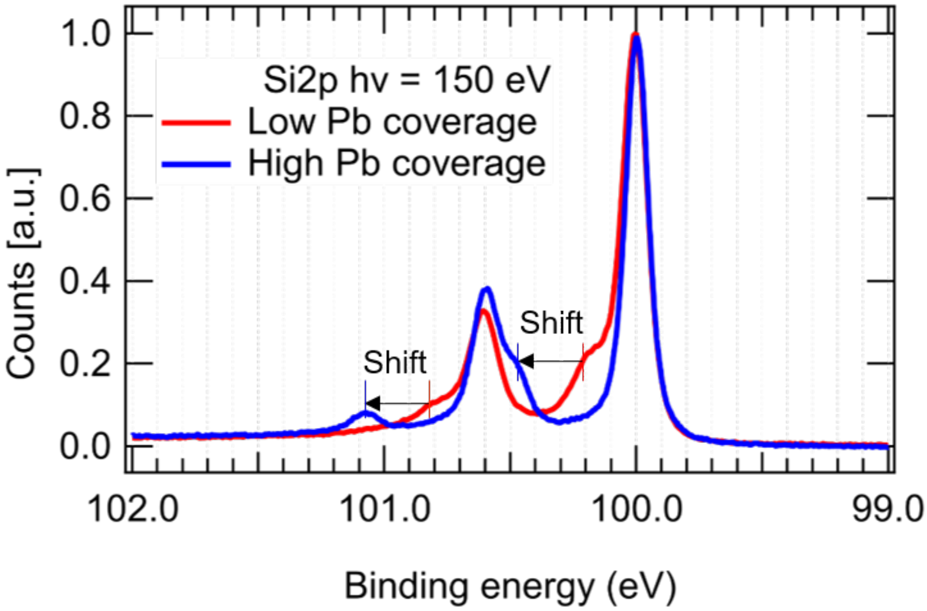

Fig. 3.14 – *Evolution of the Si 2p core level for two Pb coverage. Here, "low coverage" corresponds to the minimal Pb coverage where the Pb-induced superstructure is observable by LEED, while "high coverage" corresponds to the optimized coverage determined by LEED ($\approx$ 1 ML), used for all the data presented here. A shift of +0.27 eV in the Pb-induced XPS component is observed between the two coverages, with the higher binding energy corresponding to the higher Pb deposition.*

deposition, and shown in Figure 3.16. Using the same fitting parameters as above, except for the backgrounds, we obtain similar fits. No new contribution is observed on the surface or as bulk that could be attributable to Pb deposition. This leaves two possibilities: either the Pb atoms do not bond significantly with Cu atoms or the contribution of Cu atoms being influenced by Pb are not resolved from the bulk Cu signal.

Two Pb core levels: Pb 4f and Pb 5d, are presented in Figure 3.17. Each core level is measured for two photon energies, with the lowest one being the more surface sensitive. In all fits, Doniach-Sunjic peaks were used, as is usual for Pb, with Shirley-steps for the background. For Pb 4f, we found a Δ_{SO} of 4.86 eV, and used an FWHM of 0.31 eV with 0.15 eV of Gaussian broadening. The asymmetry parameter is 0.084. For Pb 5d, we found a Δ_{SO} of 2.62 eV, and used an FWHM of 0.20 eV with 0.14 eV of Gaussian broadening. The asymmetry parameter is

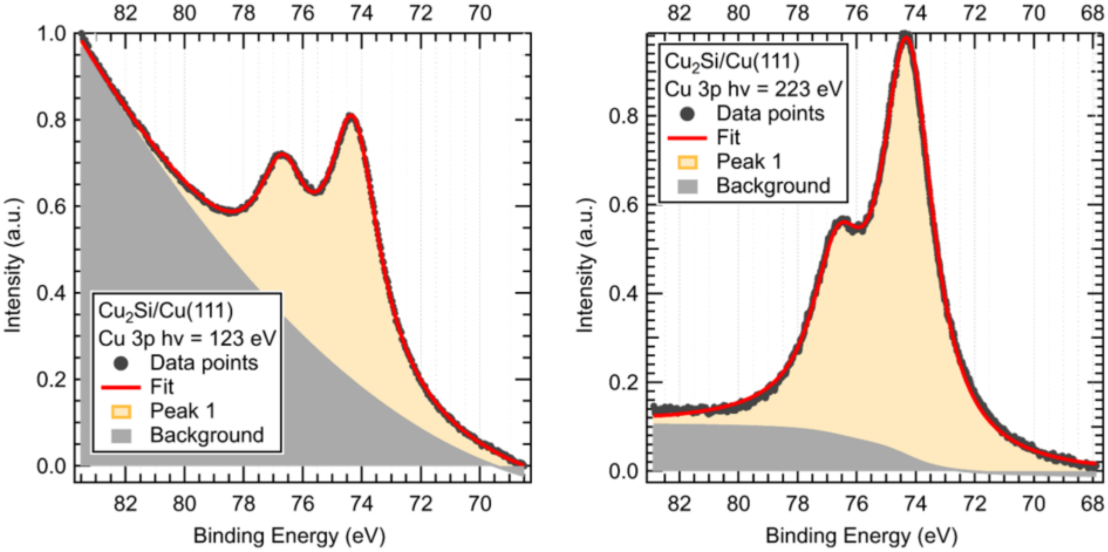

Fig. 3.15 – *Cu 3p core level of* $Cu_2Si/Cu(111)$ *for hv = 123 eV and hv = 223 eV. One doublet is sufficient for fitting the spectrum.*

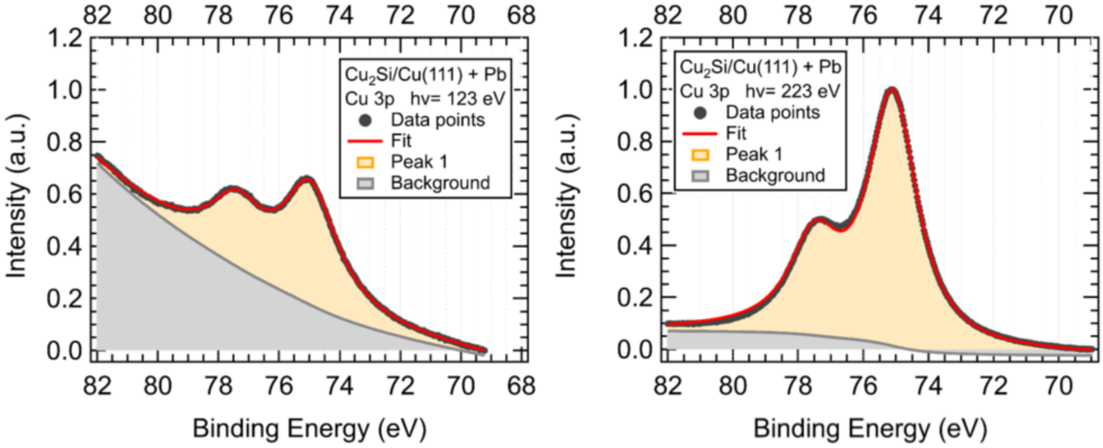

Fig. 3.16 – *Cu 3p core level of* $Cu_2Si/Cu(111)$ *+ Pb, for hv = 123 eV and hv = 223 eV. No new contribution imputable to Pb is observed.*

0.067. We note that in some cases, the branching ratio had to be lowered below the expected 0.75 value to match the spectrum (branching ratio of 0.67 for Pb 4f with hv = 300 eV, and of 0.55 for Pb 5d with hv = 90 eV). In both cases, one doublet is sufficient to obtain a good fit, for both energies. The absence of any bulk-like contribution shows that Pb does not form islands on the surface. This is in good agreement with the proposed growth model where Pb forms first a 2D layer, given that Pb coverage is < 1 ML. As seen above, Pb deposition induces a clear change in the Si 2p XPS spectra, implying some level of interaction between the two elements. As no new contribution is observed in the Cu 3p core levels after Pb deposition, and only one contribution is observed on the Pb core-level spectra, we conclude that Pb atoms evaporated stay on top of the surface and interact with Si atoms only. From the LEED patterns observed and according to previous literature [52], we discussed above the possibility of the Pb overlayer being discommensurate with the substrate, although close to a p(4×4) reconstruction. However, from the XPS only, the discommensuration is not visible, as all Pb atoms appear to share an identical chemical environment. It is possible that below 1ML of Pb (which is our case here), the Pb overlayer is still commensurate with Cu_2Si. We show in Figure 3.18 the atomic model of Cu_2Si, with the (1×1), $(\sqrt{3}\times\sqrt{3})$R30° and (4×4) unit cells represented. We provide an illustration of a possible position for Pb atoms, where all Pb atoms have a similar chemical environment. The possibility of a triple domain (4×1) reconstruction has also been mentioned, but no fitting atomic model has been found. In any cases, STM measurements would be needed to gain a deeper understanding of the atomic structure of the surface.

3.2.4 ARPES measurements on Cu_2Si/Cu(111) before and after Pb deposition

3.2.4.1 ARPES measurements on Cu_2Si/Cu(111)

The band structure of Cu_2Si/Cu(111) along the $\Gamma - M$ direction is shown in Figure 3.19. In total, three bands are observed: two hole-like bands labelled α and β, seen at hv = 41 eV, and a electron-like band labelled γ seen at hv = 60 eV. The γ band crosses the α and β bands around -0.9 eV and -0.4 eV respectively, and all the bands appear continuous (no gap), with a quasi-linear dispersion. Their Fermi vectors were measured as follows: α band: 0.35±0.02 Å^{-1}, β band: 0.48±0.02 Å^{-1},

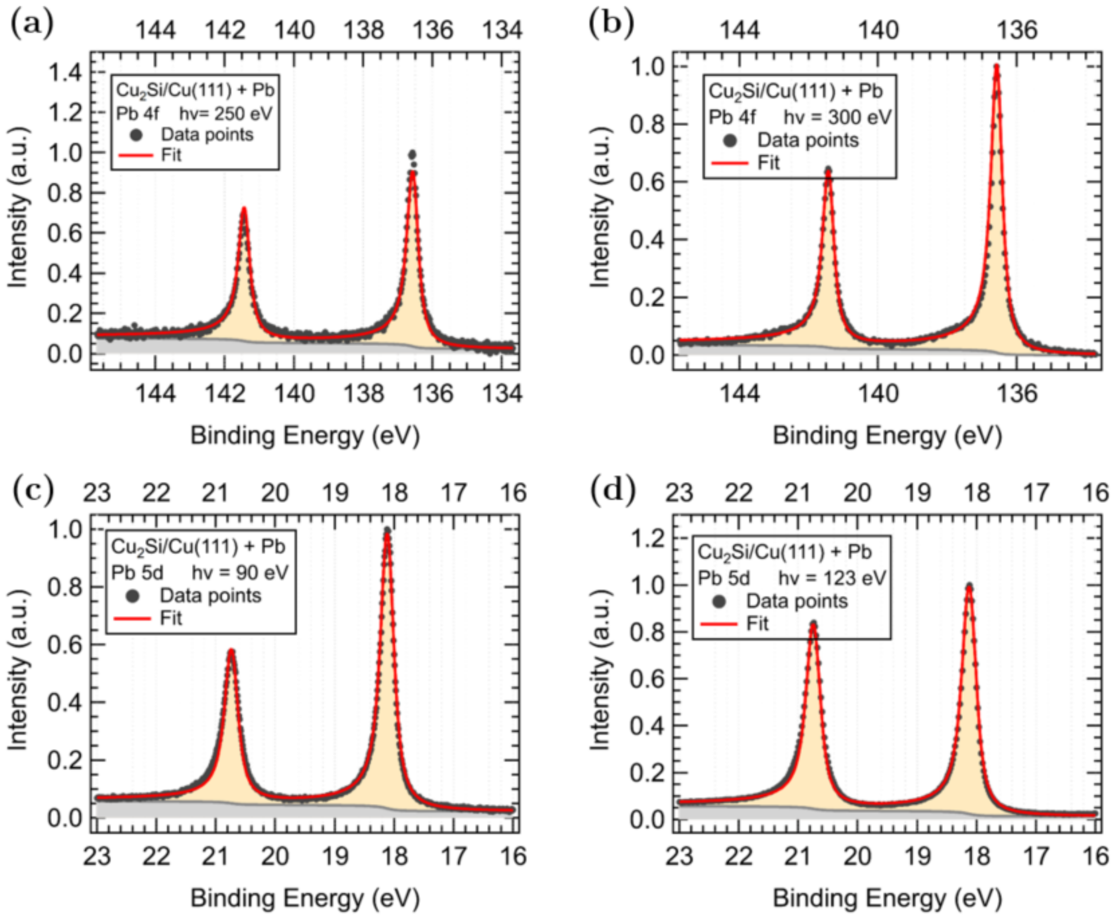

Fig. 3.17 – *Pb 4f and Pb 5d core levels of $Cu_2Si/Cu(111)$ + Pb, for different photon energies. The lowest energies are more sensitive to the surface. Only one contribution is observed in all cases.*

and γ band: 0.65±0.05 Å^{-1}. The γ band being more diffuse than the others, an exact determination of its position is more difficult, and the curvature method can induce some shifts in the scale, the error in its position is thus larger. A schematic representation of those three bands is shown in Figure 3.19 (e), and can be compared to the DFT calculation of Feng *et al.* obtained for the freestanding Cu_2Si monolayer [1], shown in Figure 3.19 (f).

The main conclusion is that the ARPES measurements are in good agreement with the band structure predicted for the freestanding Cu_2Si monolayer, with an upward shift in the Fermi level (the band crossings lie 0.3 eV below the predictions). The presence of the two concentric Dirac nodal loops centred around Γ appear to be present in the experimental system by confronting the ARPES measurements.

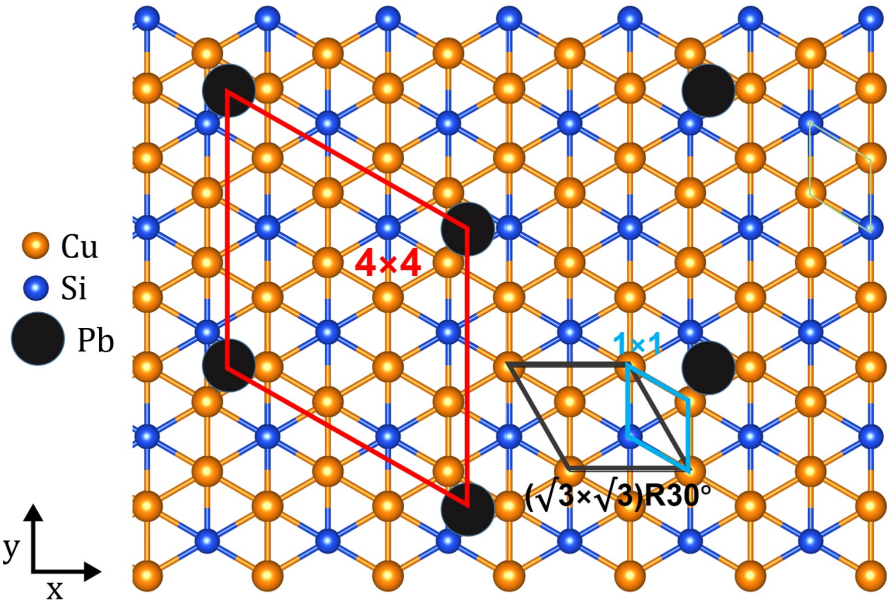

Fig. 3.18 – *Atomic model of Cu_2Si, with the (1×1), $(\sqrt{3} \times \sqrt{3})R30°$ and (4×4) unit cells represented. We provide an illustration of a possible position for Pb atoms, where all Pb atoms have a similar chemical environment.*

These results match those obtained from the two previous experimental studies involving Cu_2Si [1, 14], confirming the reproducibility of the ARPES measurements of Cu_2Si grown on a Cu(111) substrate.

3.2.4.2 ARPES measurements on Pb/Cu_2Si/Cu(111)

We are now interested in the effect of Pb evaporation on top of Cu_2Si/Cu(111). As described above, a superstructure is observed by LEED, corresponding to the formation of an incommensurate Pb overlayer. The diffraction spots of Cu_2Si remain visible, implying that the crystalline periodicity of the monolayer is conserved. We want to determine if the bands observed above (α, β and γ) are still present, if they still cross (i.e. if DNLs are still present), and if different features are observed.

Constant energy ARPES spectra (k_x-k_y maps) measured with hv = 30 eV are shown in Figure 3.20, and their curvature image in Figure 3.21. Three bands are observed, labelled as α, α' and β. The α and β bands are similar to the ones observed on Cu_2Si/Cu(111), while the α' is new. Its dispersion follows the one of

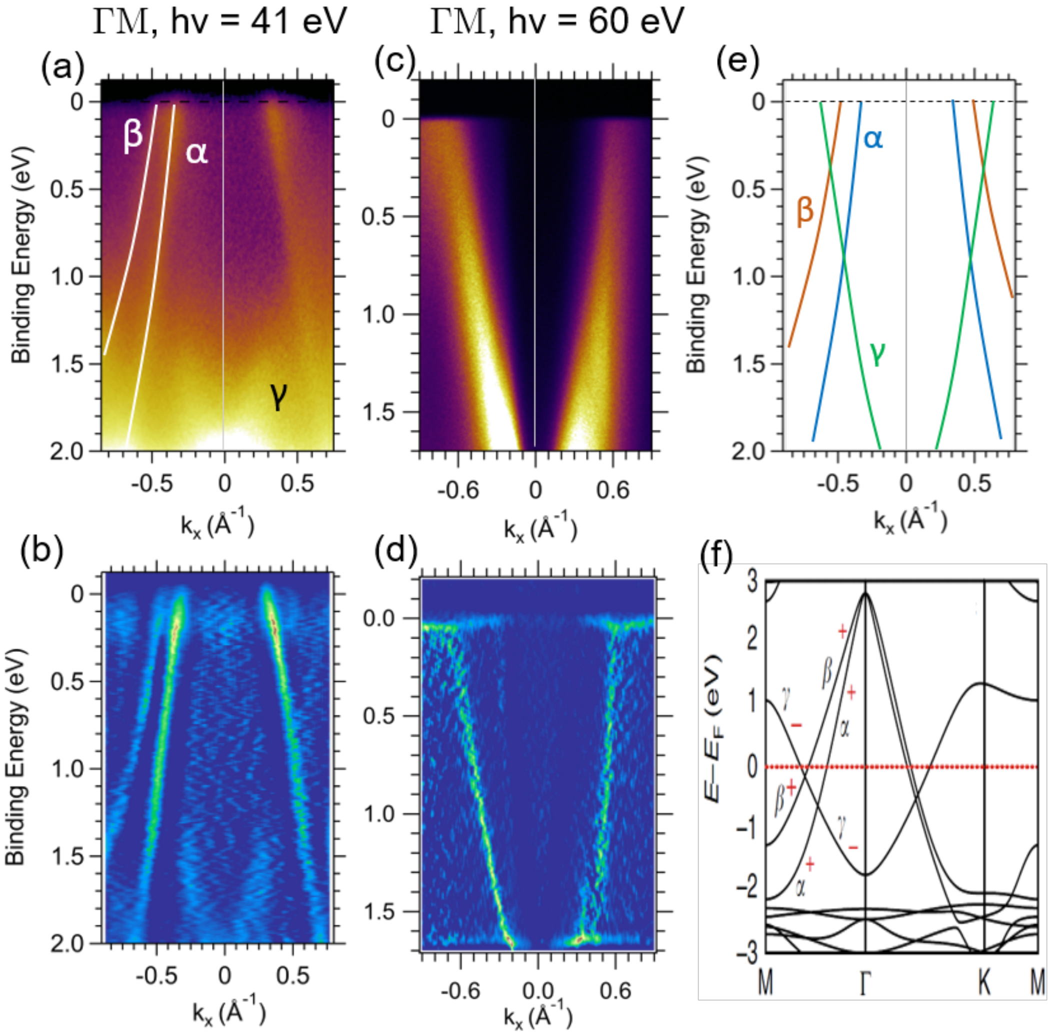

Fig. 3.19 – *ARPES on $Cu_2Si/Cu(111)$, before any Pb deposition, along the $\Gamma - M$ direction with LV-polarized light, centered around Γ. (a) and (b) show the spectrum measured with hv = 41 eV and its curvature image. Two hole-like bands are identified on the left-hand side of the images, labelled α and β. A third band (electron-like) labelled γ is faintly distinguishable. It is better seen on (c) where the same region is measured with hv = 60 eV, and on (d), which shows the curvature of (c). (e) shows schematically the three bands observed. These are in good agreement with the DFT calculations for the free-standing Cu_2Si shown in (f) (from [1])*

the α band, and its shape is also hexagonal, hence its denomination of α'. These bands are schematically represented in Figure 3.21, along with the DFT prediction of the Fermi surface for the freestanding Cu_2Si monolayer, as well as the size of its Brillouin zone and the position of the high symmetry points M and K.

In order to better observe the dispersion of these bands, E-k_x cuts are shown in Figure 3.22 (Γ-M direction) and Figure 3.23 (Γ-K direction). Figure 3.22 (a) is a cut taken at hv = 30 eV, as the k_x-k_y maps shown before, along the Γ-M direction. Here again, the bands α, α' and β are identified and labelled, and better seen in (b) which is the curvature image of (a). The similarity in the dispersion of α and α' is evident here. While the electron-like band γ is perceived, its intensity is weak at this photon energy. Figure 3.22 (c) and (d) is measured at hv = 60 eV. Here, only the γ band is observed. From the curvature images, no gap in the bands is observed within our experimental resolution.A schematic representation of the bands observed is presented in Figure 3.22 (e). To complete the picture, Figure 3.23 shows E-k_x cuts along the Γ-K direction, with hv = 30 eV. In this direction, the β band is not visible, and only α and α' are identified.

Further experiments allowed us to measure farther into the reciprocal space. Constant energy spectra (k_x-k_y maps) are presented in Figure 3.24, reaching up to the second Brillouin zone (2BZ). For better visualization, the first and second Brillouin zones (1BZ and 2BZ) of Cu_2Si are represented as well as the first Brillouin zone of Cu(111), $\sqrt{3}$ times larger and rotated 30°. The K point of Cu(111) 1BZ thus corresponds to the centre of Cu_2Si 2BZ (Γ'). Compared to the previous k_x-k_y maps showed, two more bands are observed. One of them, that we label δ, is hexagonal, rotated 30° compared to the α band, and curves when going deeper in energy. Its dispersion is hole-like, meaning that the further down we go in energy, the more distant from Γ it will be, ensuring that it is not confused with the γ band, which disperses in the opposite direction. We attribute its origin to the Pb layer. Another band, labeled Cu_{bulk}, is very intense and lies after the 1BZ of Cu_2Si. This band originates the Cu(111) bulk and corresponds well to the one described in subsection 3.2.1. We note here that the α' band is barely visible due to a lower resolution compared to Figure 3.20, and to the different photon energy used. A schematic representation of all the bands originating from the system Pb/Cu_2Si observed at

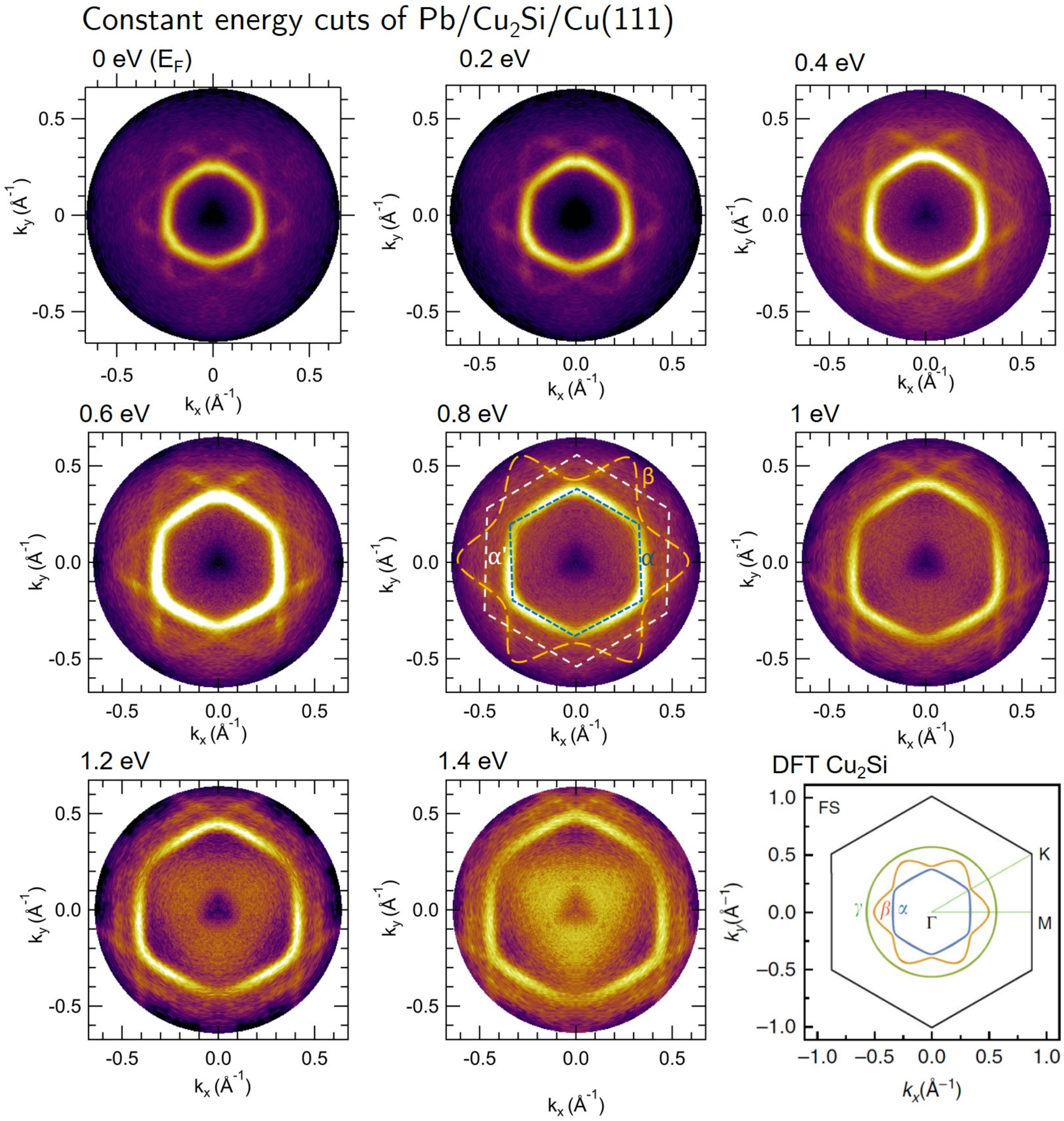

Fig. 3.20 – *Constant energy maps of Pb/Cu₂Si/Cu(111) at 30 eV, LV polarisation, 20 K. Eight constant energy maps are shown, ranging from the Fermi level to -1.4 eV below it. In the bottom right corner is shown the DFT calculation of the Fermi surface for the freestanding Cu₂Si monolayer, as well as the size of its Brillouin zone and the position of the high symmetry points M and K. Three bands are observed, which are drawn over the central image, and labelled as α, α' and β. The bands α and α' are hexagonal, while β is a hexagram with rounded corners. Curvature images of these spectra are shown in Figure 3.21*

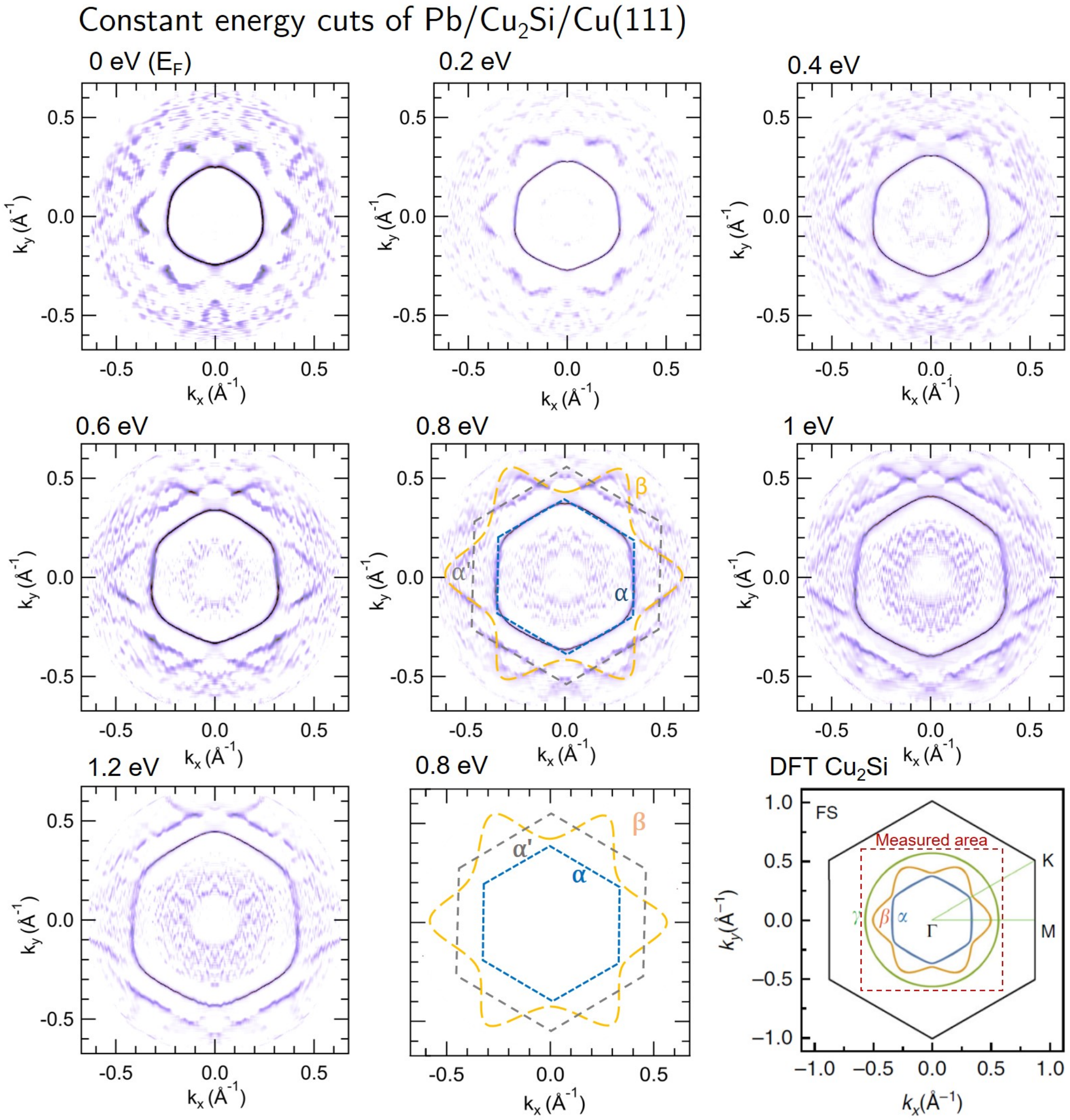

Fig. 3.21 – *Curvature images of the constant energy maps shown in Figure 3.20. A schematic representation of the three bands observed is added.*

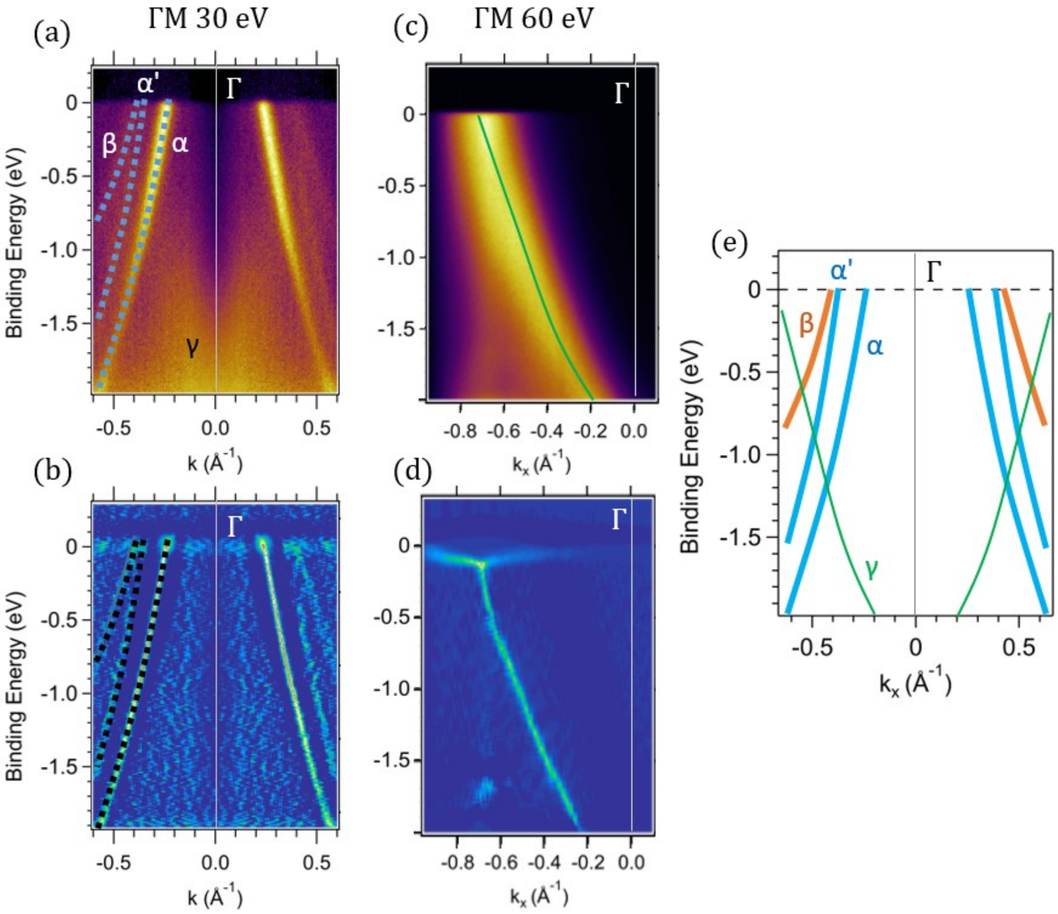

Fig. 3.22 – *ARPES 2D cuts along the M-Γ-M direction in of $Pb/Cu_2Si/Cu(111)$. (a) and (b) show the measured spectra with hv = 30 eV and its curvature image respectively. The images are centred on Γ. Three bands are observed, labelled α, α' and β by identification with the band structure before Pb deposition. (c) and (d) show the measured spectra with hv = 60 eV and its curvature image respectively. Only one band, γ, is observed here. (e) represents schematically all the bands observed.*

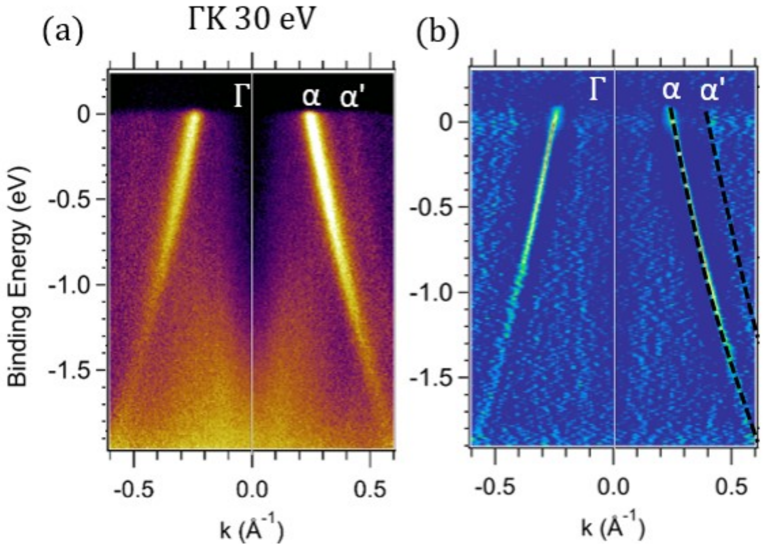

Fig. 3.23 – *ARPES 2D cuts along K-Γ-K direction in of Pb/Cu_2Si/Cu(111). In this direction, only the α and α' bands are visible.*

the Fermi surface is shown in Figure 3.25.

Two E-k_x cuts are labelled in Figure 3.24: both along the Γ-M direction, "cut 1" is in Cu_2Si 2BZ, while "cut 2" is in Cu_2Si 1BZ. The resulting images are shown in Figure 3.26. Cut 1 is centred on the M high symmetry point, allowing us to see the α and β bands entirely. The Cu(111) bulk band is here labelled as ϵ. Being close to the K point of Cu(111), where Cu does never have states, allows for an increase in the signal/noise ratio near Γ' compared to measurements near Γ in the 1BZ. The high intensity of α and β bands makes it clear that they are not gaped. In the second picture (cut 2), the signal is not as good but the bands are also visible. At this photon energy, the γ band is barely visible and is discernible almost only in the lower binding energies.

The Fermi vectors of the bands observed are regrouped in Table 3.1, measured in the Γ-M and Γ-K directions. By comparison to before Pb deposition, the Fermi vectors of the hole-like bands α and β are smaller, while the Fermi vector of the electron-like band γ is larger. This indicates a rigid shift of the Fermi level towards higher binding energy. The Cu_2Si layer thus transfers charges to the Pb layer. If we look at the position of the band crossing, the same shift is observed. The crossing

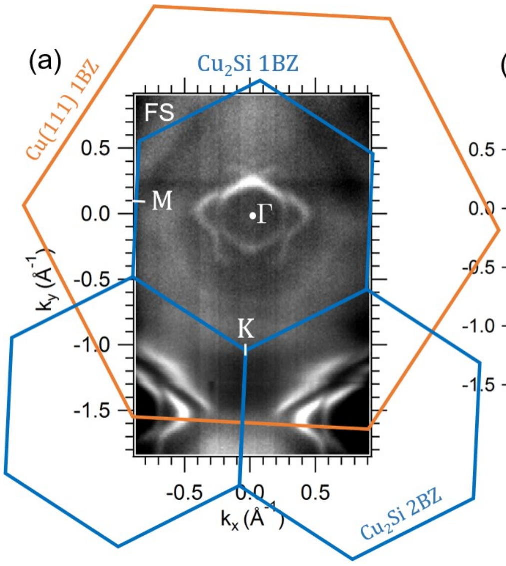

Fig. 3.24 – *Constant energy maps of Pb/Cu_2Si/Cu(111) measured with hv = 45 eV and at T° = 40 K. (a) shows the Fermi surface. The first and second Brillouin zones (1BZ and 2BZ) of Cu_2Si are represented by blue hexagons, with the high symmetry points Γ, M and K labelled in white. The first Brillouin zone of Cu(111) is represented by an orange hexagon. (b) shows a constant-energy cut 0.8 eV below the Fermi level. Two new bands are labelled: δ, originating from the Pb layer, and Cu_{bulk}. (c) shows a constant-energy cut 1.4 eV below the Fermi level. Two cuts are labelled, the resulting images are displayed in Figure 3.26*

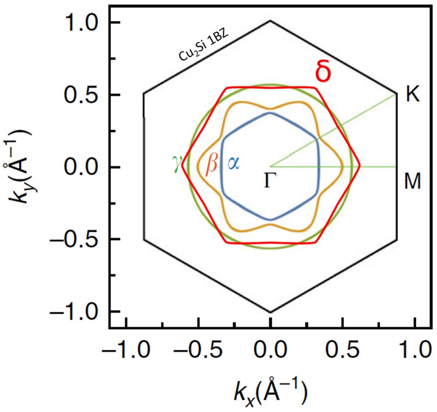

Fig. 3.25 – *Schematic representation of all bands observed on the Fermi surface as shown in Figure 3.24*

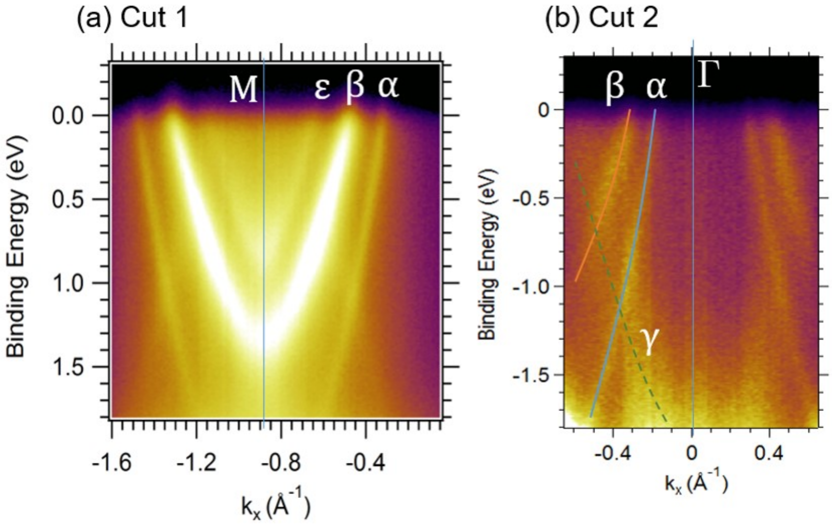

Fig. 3.26 – *E-k_x cuts along the Γ-M direction as shown in Figure 3.24. (a) is centered on M, and (b) on Γ.*

of the γ band with the α and β bands takes place around -1.2 eV and -0.65 eV respectively. This is a change in the binding energy of 0.25-0.3 eV compared to before Pb deposition. The γ band also crosses the new α' band around - 0.9 eV.

Fermi vectors, in Å^{-1}

Band name	Γ-M direction	Γ-K direction
α	0.23	0.23
α'	0.35	0.39
β	0.40	-
γ	0.69	0.68
δ	0.75	0.68

Table 3.1 – Fermi vectors of all bands from Pb/Cu_2Si/Cu(111). Precision is given at ± 0.02 Å^{-1}.

The splitting of the α band into α and α' most likely originates from the Pb deposition, as such phenomenon has been observed in graphene [41–43]. According to calculations from Brey *et al.* [40] on Pb deposition on graphene, two different kinds of SOC can be induced. A periodic and commensurate Pb atoms disposition should induce spin-conserving intrinsic-like SOC, whereas a random distribution of Pb adatoms should result in a spin-flipping Rashba-like SOC. In both cases, the intensity of the induced SOC is expected to be proportional to the amount of Pb deposited. In our system, the Pb sheet is crystalline and appears to be commensurate with Cu_2Si for a Pb coverage below 1 ML. One question naturally arises: what is the spin polarization of the α and α' bands?

We tried to answer this question by performing Spin-ARPES measurements on the RGBL-2 beamline at Bessy synchrotron, equipped with a Mott detector. Figure 3.27 shows the resulting measurements. The spin component of the photoelectrons can only be measured along a constant-momentum line. To understand better where in the reciprocal space this measure was taken, Figure 3.27 (a) shows the E-k_x position where the classical ARPES was measured. This cut is shown in (b). Three bands, the α, α' and β are visible. At this position, the spin polarization of the bands was measured along a constant-momentum line, around 0.4 $Å^{-1}$, as represented on the image. The resulting spin measurements are shown in Figure 3.27 (c) and (d), for the in-plane and out-of-plane spin components respectively, with a zoom-in on the surface bands in (e) and (f). While the signal for the bulk bands (below -2 eV) is reasonable, the one for the surface bands (above -2 eV), in which we are interested here, is of low-intensity and noisy: the bands observed in ARPES cannot be distinguished here, even less their possible spin-polarization. The difference between spin up and spin down is plotted alongside each graph, and no distinctive feature is observed within our experimental resolution, despite acquisition times of several hours.

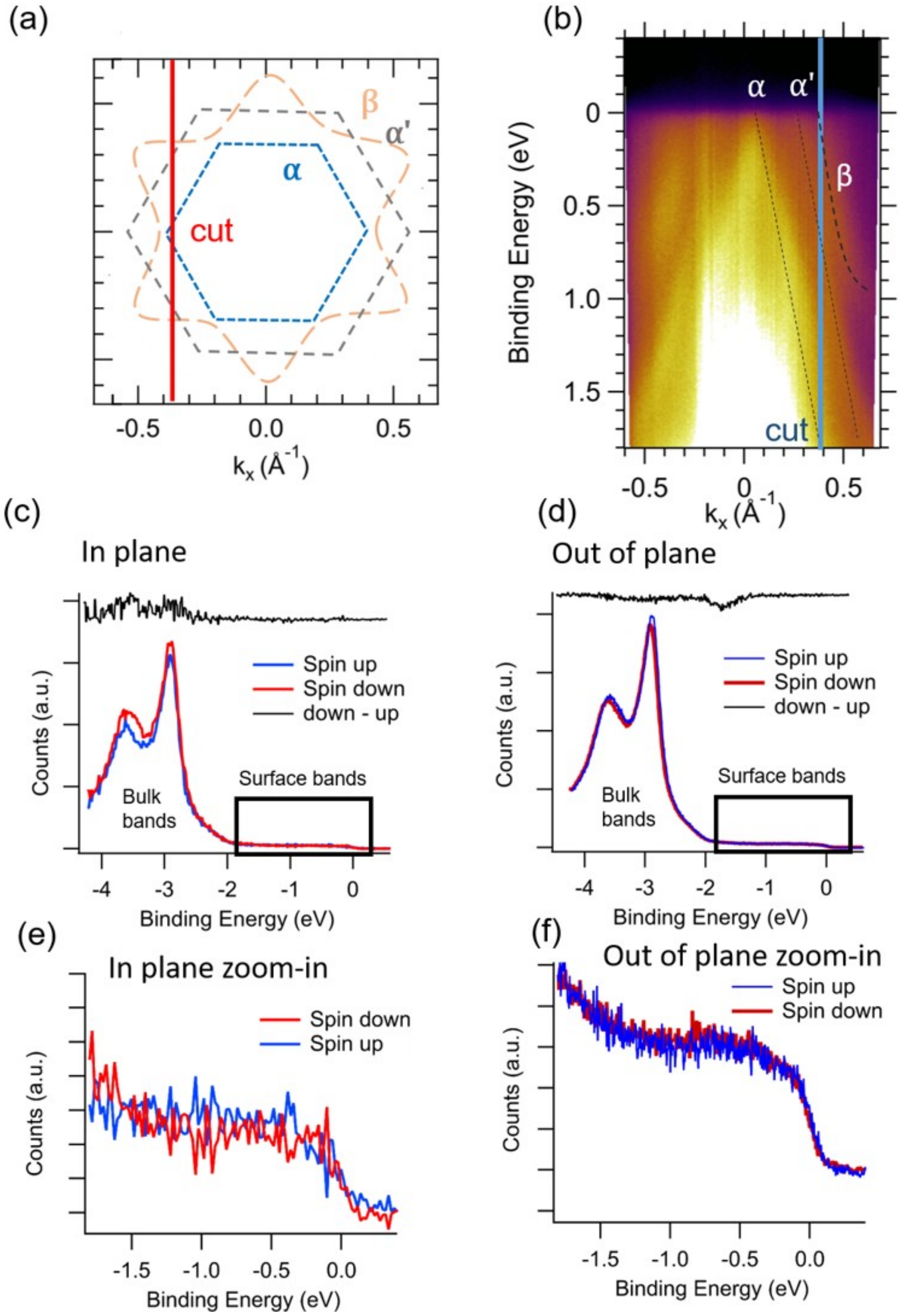

Fig. 3.27 – *Spin-ARPES on Pb/Cu_2Si/Cu(111) split bands.(a) and (b) show where the constant-momentum line for spin measurement was taken. (c) and (d) are the resulting spin spectrum, measured at hv = 30 eV, in the in-plane and out of plane directions respectively.*

3.2.5 Conclusion

We have successfully synthesized a Cu_2Si monolayer on a Cu(111) substrate, with XPS and ARPES results in agreement with the few previous experimental works on this system [1, 14]. ARPES measurements especially confirmed the presence of two concentric Dirac nodal loops centred around Γ, and the close similarity between the band structure of the experimental system and the predictions for the freestanding Cu_2Si monolayer.

We then took interest in the effects of Pb deposition of Cu_2Si/Cu(111), as a heavy element can induce SO splitting in 2D materials [40, 41, 43]. The LEED pattern would correspond to a (4×4) periodicity, or to a triple domain (4×1). It would be interesting to perform STM experiments on this system, to determine more accurately the atomic organisation of the Pb atoms. The XPS found that the Pb atoms adsorbed on top of the Cu_2Si monolayer, and interacted only with Si atoms, with a peak shift in a Si 2p component dependent on the amount of Pb deposited. ARPES measurements showed the preservation of the band structure of Cu_2Si, with the addition of a Pb band, and more remarkably of a split of one of the Cu_2Si band, characteristic of an increase of SO coupling in the system. Spin-resolved measurements however were inconclusive and failed to provide more information on the properties of this SO increase, due to a too poor signal/noise ratio. This could be attempted again on a surface of higher quality and freshly prepared, with sufficient acquisition time. We underline that the DNLs and the linear dispersion of the bands are preserved and that no gap was detected within our experimental resolution, indicating strong robustness of the nodal lines: neither the induced SO coupling nor the symmetry breaking at the surface was sufficient to gap them. This would prove useful for applications where Cu_2Si monolayers might not be as pristine as in lab conditions. This would however require the growth or transfer onto a non-conductive substrate.

In this optic, we focus our attention in the following section on the study of the growth of Cu_2Si on a Si(111) substrate and in its characterization by XPS and ARPES.

3.3 Of the influence of a semiconducting substrate: $Cu_2Si/Si(111)$

We present in this section our work on the characterization of the Cu_2Si/Si(111) (“5.55×5.55”) surface reconstruction by ARPES, XPS and DFT calculations. This work has been the subject of a publication [53], from which part of the information presented here is adapted.

3.3.1 Cu_2Si/Si(111): sample preparation

Clean Si(111) surfaces, showing a (7×7) surface reconstruction, were prepared by flashing the sample to 1150-1200°C and annealing with reducing the temperature from 850°C to 600°C over the course of 5 minutes, under UHV. An evaporator was prepared using a tungsten filament and a copper wire (99.999% purity) as a source of Cu atoms. The deposition rate was evaluated at 0.5 $Å.min^{-1}$ by the means of a quartz micro-balance. This corresponds to $\sim$ 0.2$ML.min^{-1}$ as one monolayer (ML) of Cu(111) = 2.6 Å. 1 ML was deposited on the Si substrate held at 630°C and annealed at the same temperature for 2 minutes after deposition. As for the Si(111) (7×7), the Cu_2Si incommensurate (“5.55×5.55”) surface reconstruction was checked by low energy electron diffraction (LEED) , as shown in Figure 3.28, and reproduces accurately what is expected [31, 33, 36]. It is interesting to note that it is possible to recover the Si(111) (7×7) with a flashing procedure, one sample can thus be used or “refreshed" multiple times.

Two samples were prepared following this procedure: the first cut along the Si(111) Γ-M direction and the second cut along the Si(111) Γ-K direction. In the following, the samples will be referred to by their cut orientation.

3.3.2 ARPES characterization

All ARPES measurements presented in this section were taken at the beamline BL-2A MUSASHI of Photon Factory, KEK, Japan. Measurements of angle-resolved photoemission spectroscopy were performed at 20 K, and XPS overview showed no other elements than Si and Cu.

Figure 3.29 (a) shows the photoemission Fermi surface map of the Cu_2Si surface, taken at a photon energy of 70 eV and with linear-horizontal (LH) polarization.

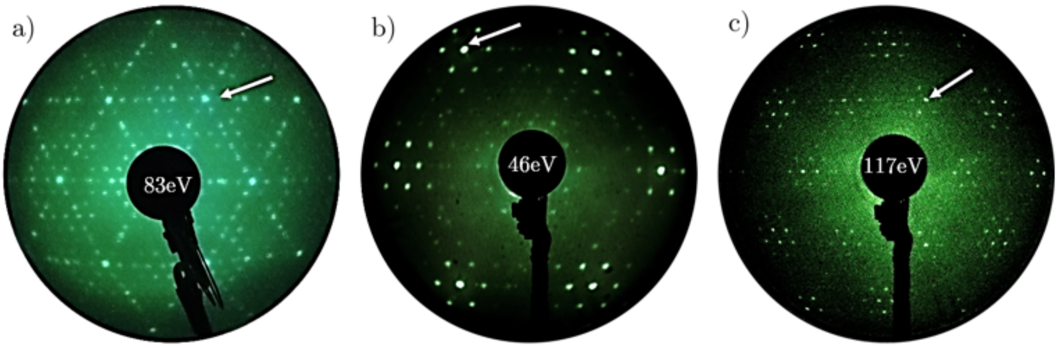

Fig. 3.28 – *LEED images.* ***a)*** *Si(111) 7×7 reconstruction* ***b)*** *and* ***c)*** *Cu_2Si "5.55×5.55" reconstruction for electron energy of 46 eV and 117 eV. The white arrows indicates the position of one of the six first-order Si(111) spots*

These parameters were experimentally determined as the optimal ones for a high resolution of the electronic bands. Contours of the Fermi surface are composed of a hexagon, exhibiting large photoemission intensity, and lower intensity structures. The photoemission bands are composed of the surface bands and their Umklapp scattering replicas associated with the quasi-"5.55×5.55" periodicity. The map of the Fermi surface is reproduced by taking into account two types of Fermi surfaces (hexagonal and flower-shaped) with ±3° rotations and by tiling with the Umklapp scattering vectors, as shown in Figure 3.29 (b-d). We note that the hexagonal and flower-shaped Fermi surfaces match with the energy contours of the α and β bands of the Cu_2Si layer [1, 18]. The tiling of the hexagonal (α) band is consistent with the previous band-mapping of the Si(111)quasi-"5×5"-Cu surface [36]. The observation and subsequent tiling of the β band is a novelty.

The electronic band structure was also measured along two directions in the reciprocal space: Γ-K and Γ-M of the Si(111) 1×1 Brillouin zone surface. The results are shown in Figure 3.30, using 70 eV LH-polarized photons, along with the curvature image of both spectra. The presence of bands crossing the Fermi level indicates that the surface is metallic.

On both spectra, one can recognize the Si(111) bulk bands [54, 55] around the Γ point. The bulk bands are composed of many sub-bands that are generated due to the quantum confinement by the narrow space charge layer at the surface of Si [56]. The white dotted line in the figures traces the edge of the bulk bands and, within

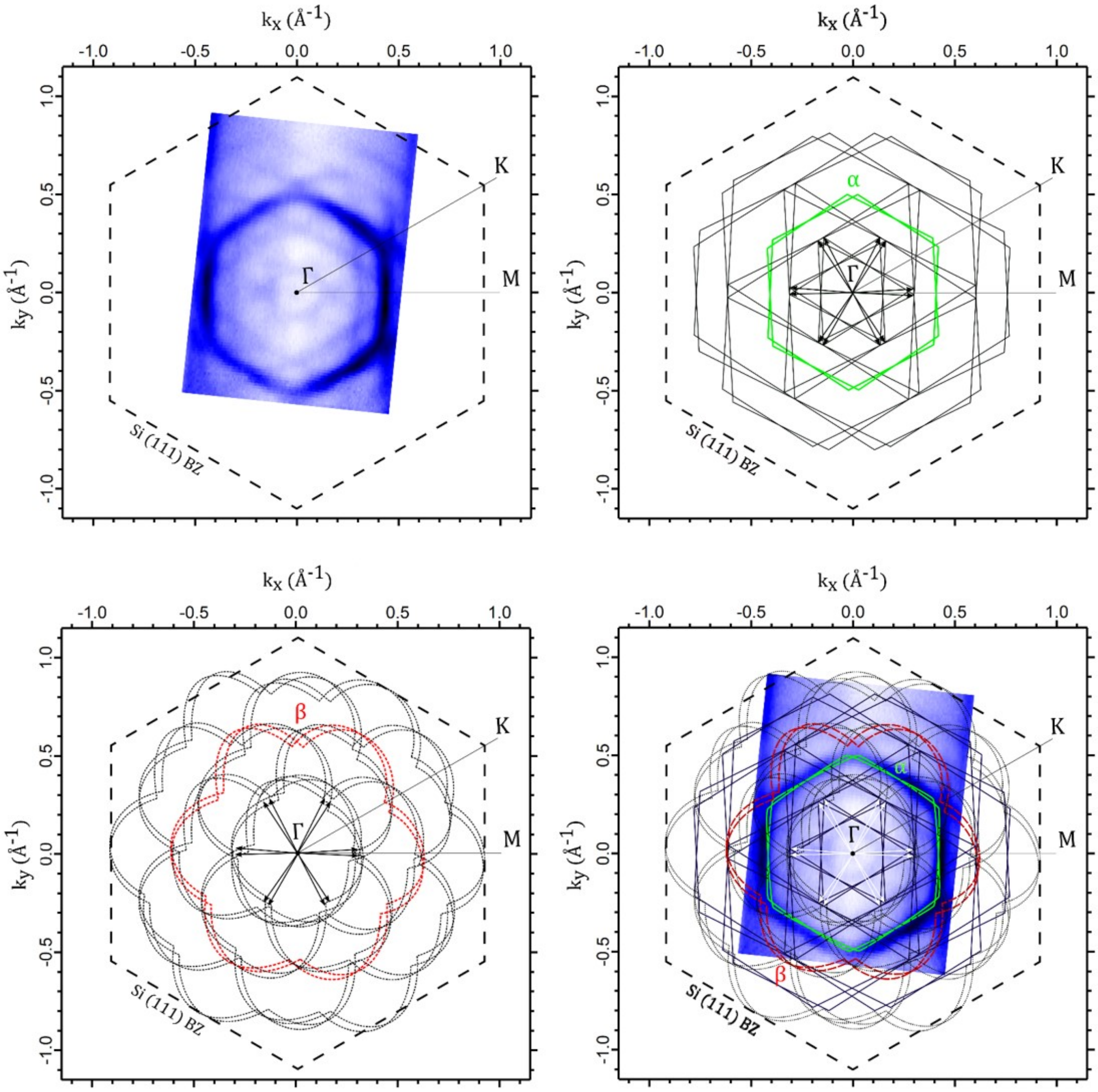

Fig. 3.29 – *Study of the Fermi surface of* Cu_2Si*. Top left: Constant energy contour map measured using 70 eV linear horizontal polarized photons at the Fermi level. Two bands, one hexagonal (*α*) and one flower-shaped (*β*), are observed, as well as lighter patterns arising from Umklapp scattering. Top right: Schematic representation of the hexagonal* α *band, in green, and its Umklapp tiling, in black. The Umklapp vectors, by which the* α *band is translated, are represented by the arrows centred on* Γ*, and the Si(111) Brillouin zone is represented by the dashed hexagon. Bottom left: Schematic representation of the flower-shaped* β *band, in red, and its Umklapp tiling, in black. Bottom right: Superposition of the three precedent images, creating the complete quasi-"5×5" Umklapp scattering of the Fermi surface.*

the bulk bandgap, one can identify dispersion curves of the α band that crosses the Fermi level (E_F). The Fermi vector of the α band along the Γ-M direction is 0.42 Å^{-1}, which is similar to the previously reported value [36], and 0.48 Å^{-1} along the Γ-K direction. The metallic β band is also identified for the first time (it was not resolved in the previous studies), and is better seen in the Γ-K direction. Its Fermi vectors are measured as 0.65 Å^{-1} along the Γ-M direction, and 0.54 Å^{-1} along the Γ-K direction. The Fermi vectors are given within a ±0.02 Å^{-1} error. Other bands, indicated by arrows in Figure 3.30, correspond to replica bands by the quasi-“5.55×5.55” Umklapp scattering of the α and β bands. We confirm the observation of no other band at the Fermi level for different photon energy (hv = 35, 40, 50, 60, 80, 100 and 105 eV), and with LH and LV polarized light, which are not shown here.

The α and β bands observed in the present research are hole-like and also have similar dispersion curves (Fermi surfaces) to those of the α and β bands in the work of Feng *et al.* [1], we thus find it natural to equate them. A comparison between Fermi vectors for three different systems is presented in Table 3.2. Taking parameters of the freestanding Cu_2Si as a reference, the wave vectors show opposite shifts between the Cu and Si substrates. The k_F values become smaller on Cu(111) but larger on Si(111), indicating a lower and higher shift in the energy of the α and β bands, respectively. In the case of Cu(111), the substrate transfers charges to the monolayer, while it is the opposite with Si(111).

Concerning the γ band in the free-standing Cu_2Si layer, it was not observed under the present experimental conditions at the Fermi level for the $Cu_2Si/Si(111)$ quasi-“5.55×5.55” surface, at the difference of the α and β bands. We infer that this difference is due to the orbital symmetry.

Indeed, as discussed earlier, the α and β bands have the mixed Si p_x/p_y and Cu p_x/p_y characters. On the other hand, the γ band originates from Si p_z and Cu p_z orbitals [1]. Looking at the orbitals occupation in space, this means that in the surface layer the α and β bands distribute in-plane, while the γ band extends out-of-plane. It can then be expected that the p_z states in the Cu_2Si layer make interactions with Si dangling-bond (p_z) states of the Si(111) substrate, resulting in the formation of the bonding-states. This picture is consistent with the structure model of the $Cu_2Si/Si(111)$ (“5.55×5.55”) surface presented in Figure 3.4. In order to verify this hypothesis, DFT calculations were made on the $Cu_2Si/Si(111)$ system.

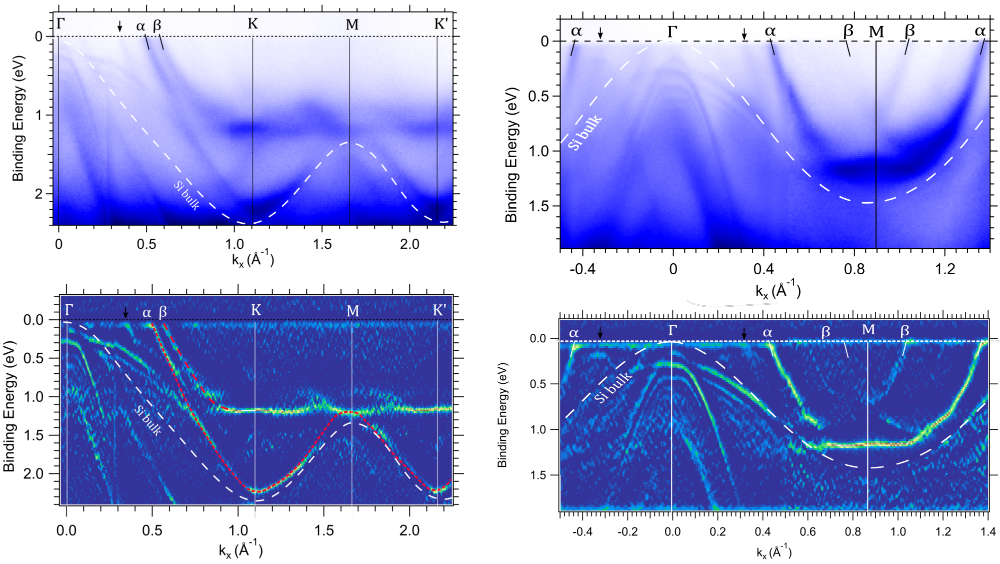

(a) (b)

Fig. 3.30 – *Photoelectron dispersion plot of Cu_2Si monolayer on a Si(111) substrate along the Γ-K* (**a**) *and Γ-M* (**b**) *directions, using 70 eV LH-polarized photons. The white dotted line represents the projected bulk states of Si(111)[54, 55]: everything above it originates from the Cu_2Si monolayer. Two metallic bands are observed, labelled as α and β, as well as Umklapp replica bands denoted by black arrows. Curvature images of both spectra are presented for better visualization of the main bands' positions. The thinner features, such as Umklapp bands, might better be seen on the original spectra.*

Direction	band	Free-standing Cu_2Si	Cu_2Si Cu(111)	Cu_2Si Si(111)
	α	0.37	0.23	0.48
$\overline{\Gamma}$-$\overline{\mathrm{K}}$	β	0.39	0.27	0.54
	α	0.34	0.21	0.42
$\overline{\Gamma}$-$\overline{\mathrm{M}}$	β	0.50	0.31	0.65

Table 3.2 – Fermi vectors k_F in the three systems: free-standing Cu_2Si, Cu_2Si/Cu(111) and Cu_2Si/Si(111), for the bands α and β, along the $\overline{\Gamma}$-$\overline{\mathrm{K}}$ and $\overline{\Gamma}$-$\overline{\mathrm{M}}$ directions. The unit is Å^{-1}. Values of the free-standing layer are obtained from the DFT calculation, while those of the Cu_2Si/Cu(111) and Cu_2Si/Si(111) are experimentally determined, with accuracy of ±0.02 Å^{-1}. The values for Cu_2Si/Cu(111) are comparable to the ones already published [1].

3.3.3 DFT calculations on Cu_2Si/Si(111)

To understand the differences between the band structure observed and the one predicted for free-standing Cu_2Si, first-principles calculations taking into account the substrate were realized. These simulations are the work of H.-T. Jeng (National Tsing-Hua University and Academia Sinica, Taiwan), C.-H. Chen and A. Huang (National Tsing-Hua University, Taiwan)

Those first-principles calculations were performed using the projected augmented wave method (PAW) [57, 58] as implemented in the Vienna Ab initio Simulation Package (VASP) [59–62] based on density functional theory (DFT) with the Perdew-Burke-Ernzerhof (PBE) type of generalized gradient approximation (GGA). A 12 × 12 × 1 Monkhorst-Pack k-mesh with a cutoff energy of 400 eV is used in the self-consistent field calculations. The geometry of all the systems are optimized with the total energies converged within 10^{-4} eV. To study the substrate effect in the Cu_2Si/Si(111) systems, we put Cu_2Si 1x1 monolayer on top of a 12-layer Si 1x1 substrate with the Cu_2Si lattice constant of 4.09 Å.

In Figure 3.31, the calculated band structures of a Cu_2Si monolayer are presented, for the freestanding layer and for the layer grown on a Si(111) substrate. For the free-standing Cu_2Si, the band structure is consistent with the previous report [1]. Three metallic bands are labelled: two hole-like bands, α_+ and β_+, and one electron-like band, γ_-, at the $\overline{\Gamma}$ point. The bands cross each other in regions with linear dispersion and generate two loops of the nodal lines [1]. Wave functions of the α_+ and β_+ bands have even-parity, while that of the γ_- band has odd-parity with respect to the mirror symmetry M_z. On the Si substrate, the discommensurate Cu_2Si/Si(111)-("5.55×5.55") reconstruction was modelled by a commensurate structure with similar atomic structure parameters. Despite its simplicity, the model is sufficient to capture electronic change coming from the back-bond formation between the overlayer and the substrate as observed by ARPES. The band structure for different relative positions of the Cu_2Si monolayer with respect to the Si(111) substrate were also tried, leading to results in poorer agreement with the ARPES experimental results. As shown in Figure 3.31 (b), the α and β bands remain almost unchanged, while the γ band changes significantly. Furthermore, comparing Figure 3.31 (a) and (b) (free-standing and with Si substrate respectively), one can recognize additional bands around K point at binding energy of 1-2 eV in (b), as observed by ARPES and shown in Figure 3.30a. The calculation supports our experimental results, evidencing that the γ band is much more strongly influenced by the Si(111) substrate than the α and β bands.

Another recent experimental work on this system [63] proposes that the γ band is shifted to higher energies and would cross the α and β bands ~1 eV above the Fermi level . The authors do not however explain why this shift would impact only the γ band, nor provide computational work backing up this claim. We suppose that the band they observed, showing a weak intensity, does not have the same origin as the γ band of the Cu_2Si monolayer.

3.3.4 XPS characterization

To complement the ARPES results, XPS spectra of the Si 2p and Cu 3p core levels were measured on the Cu_2Si/Si(111)-("5.55×5.55") surface, on the VUV beamline of Elettra synchrotron, Trieste, Italy.

The Cu 3p spectra are presented in Figure 3.32 for two photon energies (123 eV and 223 eV), with higher energy being more bulk-sensitive. In both cases, only one Voigt doublet is sufficient to fit the experimental points. The best fits are obtained for a $\Delta_{SO} = 2.52$ eV, a branching ratio fixed at 0.5, and a Lorentzian width $W_L =$ 0.92 eV. The Gaussian widths used are 1.49 eV and 1.96 eV for the photon energies of 123 eV and 223 eV respectively. The absence of any other contributions shows that the Cu is present only on the surface and does not migrate in the bulk, at least not in detectable proportions. According to the atomic model presented above, Cu atoms should occupy two adsorption sites (S_u and H_3), whose contributions are not resolved here.

The Si 2p spectra are presented in Figure 3.33. Two photon energies (150 eV and 250 eV) are shown with their fits. Here, lower photon energy (150 eV) is most surface-sensitive, while higher photon energy (250 eV) will be more bulk-sensitive. We find the existence of five doublets with the same relative positions for the two photon energies, as given in Table 3.3. Voigt functions were used, with a fixed Lorentzian width W_L of 40 meV as is commonly found in the literature [64, 65]. The fitting parameters used are regrouped in Table 3.4 for easier readability.

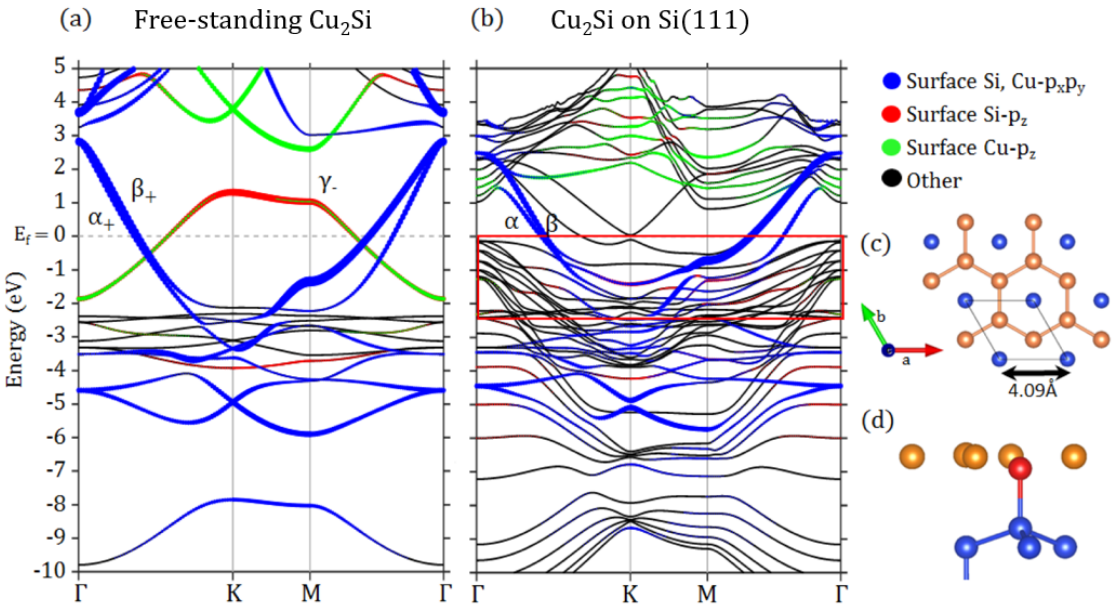

Fig. 3.31 – *Calculated band structure for a monolayer of* Cu_{Si}*, in its free-standing form and with a Si(111) substrate.* ***(a)*** *Freestanding. Three metallic bands are clearly identified, namely* α_+*,* β_+*, and* γ_-*, with the sign corresponding to their parity with respect to the mirror symmetry* M_z*.* ***(b)*** *On* Cu_2Si *on Si(111), following the atomic model in (c,d). The contributions of the different orbitals is represented as follows: red from the surface Si-*p_z*, green from the surface Cu-*p_z*, blue from the surface Si and surface Cu* p_x *and* p_y*, and black for other sources. The red rectangle in* ***(b)*** *represents the extent of the ARPES experiment.* ***(c)*** *Top view of the* Cu_2Si *structure.* ***(d)*** *Side view of the* $Cu_2Si/Si(111)$ *structure, based on the model shown in Figure 3.4, used for the DFT calculation. Blue and red spheres are Si atoms, orange spheres are Cu atoms.*

One component, S_1, is directly attributed to the surface as its area decrease with increasing photon energy. Its contribution is attributed to the Si-Cu bonds formed on the surface layer. All other contributions increase in relative area with increased depth probing and are attributed to bulk contributions (B_1 to P_3). The most intense bulk contribution, B_1, is attributed to bulk Si(111) and is used as a reference for relative peak positions. The observation of only one surface contribution is coherent with the atomic model proposed, where all surface Si atoms are equivalent. S_1 is located at a lower binding energy (-0.28 eV) than B_1. Santis *et al.* [33] also attributed a lower binding energy peak to the (“5.55×5.55”) surface, with a relative

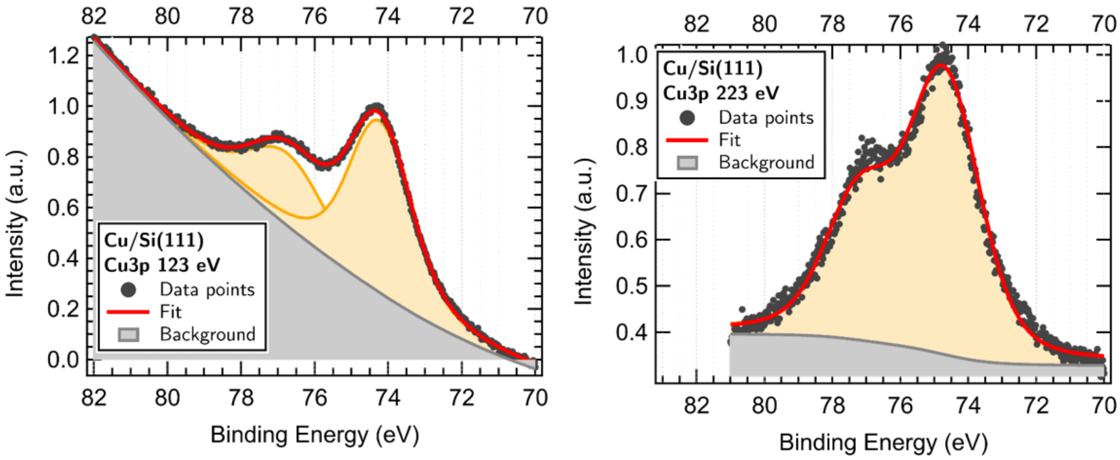

Fig. 3.32 – *Cu3p XPS spectra of Cu_2Si/Si(111) for hv = 123 eV and hv = 223 eV. One doublet is sufficient for a fit. Its important width could however hide more than one contribution.*

position of -0.5 to -0.6 eV however.

We attribute all other observed components (P_1, P_2, P_3)to the presence of Si-(7×7) on the surface. Indeed, the Si-(7×7) and Cu/Si(111)-("5.55×5.55") phases have been shown to coexist [66], and is in agreement with Santis *et al.* [33]. By comparing the measured spectra to published work on the Si-(7×7) [67], we find that all remaining components match the peak positions and energy dependence of the (7×7) doublets, once aligned on the bulk peak. P_1 would then originate from the rest atoms, P_2 from the atoms binding to the adatoms, and P_3 would originate from the adatoms.

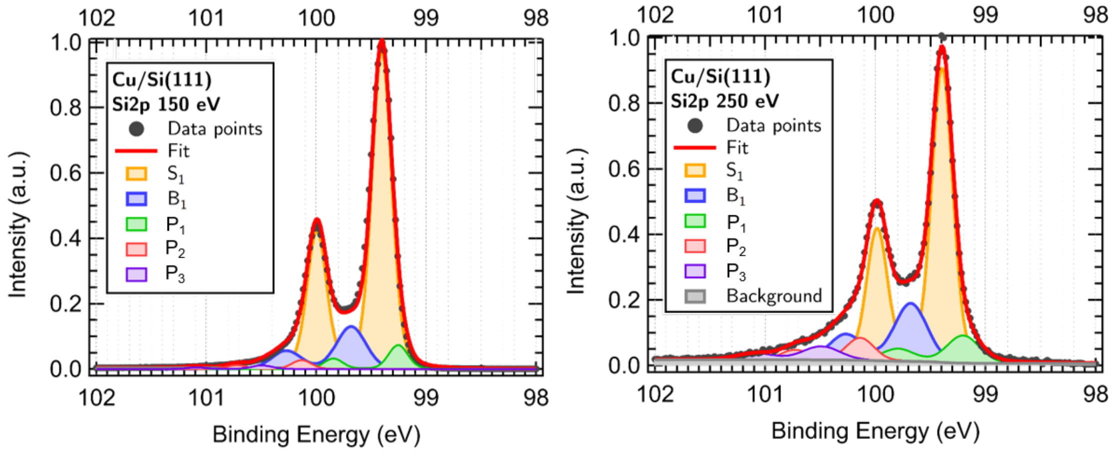

Fig. 3.33 – *Si2p XPS spectra of $Cu_2Si/Si(111)$ at hν = 150 eV and hν = 250 eV. Five Voigt doublets are used to obtain a good fit. One surface component is identified. Fit parameters are given in Table 3.4 and Table 3.3.*

	Distance to bulk peak B_1	Part of tot. area 150 eV	Part of tot. area 250 eV
Peak B_1	-	0.15	0.20
Peak S_1	- 0.28 eV	0.77	0.59
Peak P_1	- 0.43 eV	0.06	0.10
Peak P_2	+ 0.46 eV	0.02	0.06
Peak P_3	+ 0.83 eV	0.01	0.05

Table 3.3 – Peak positions relative to the main bulk peak (B_1) are presented, in binding energy, as well as the part of the total peaks area. The precision on the relative energy difference is given at ±0.01 eV, and the relative area at 10% of the given value.

Fitting parameters	
W_L	0.04 eV
Δ_{SO}	0.59±0.01 eV
Branching ratio	0.44±0.01

Gaussian widths W_G for the different photon energies		
Peak	hv = 150 eV	hv = 250 eV
B_1	0.29 eV	0.36 eV
S_1	0.19 eV	0.20 eV
P_1	0.18 eV	0.33 eV
P_2	0.19 eV	0.31 eV
P_3	0.20 eV	0.41 eV

Table 3.4 – Fitting parameters for the Cu/Si(111) Si 2p core-level. Peak positions relative to the bulk peak are presented, in binding energy. The precision on the relative energy difference is given at ±0.01 eV. Lorentzian FWHM (W_L) and Gaussian broadening (W_G) are given for all photon energies, along with spin-orbit splitting (Δ_{SO}) and branching ratio. The precision of Gaussian broadening is ±0.02 eV.

3.3.5 Conclusion

In summary, we mapped the Fermi surface and band dispersion curves of a Cu_2Si layer on Si(111), forming a quasi-"5.55×5.55" surface reconstruction, by angle-resolved photoemission spectroscopy. This is to date the most detailed band-structure measured on this system, with the observation of two bands (α and β) crossing the Fermi level compared to only one band being resolved in the previous works [36]. The possibility to change photon energy and polarization allowed us to rule out the presence of any other band with strong intensity. The complex structure of the Fermi surface is completely explained by its tiling by the observed bands and their Umklapp replicas originating from the difference of periodicity between the bulk and the surface layer. XPS measurements were realized, showing good agreement with the established structural model.

By comparing the experimental results with DFT band calculations, we found that electronic states originating from x-y (in-plane) orbitals remained unchanged but those originating from z- (out-of-plane) orbitals are modified when the overlayer is prepared on a Si substrate. One of the bands predicted for the free-standing system then strongly hybridizes with the substrate, forbidding the preservation of nodal lines in this system.

This work links the theoretically predicted free-standing monolayer to the one prepared on a Si(111) substrate, and the evolution of its electronic structure. We show that calculations on free-standing layers are an important first step, but that the substrate chosen and dramatically impact the electronic properties of the monolayer. Indeed, for Cu_2Si, a Cu(111) substrate results in minimal interactions, but a Si(111) substrate strongly interacts.

Bibliography of Chapter 3

[1] B. Feng, B. Fu, S. Kasamatsu, S. Ito, P. Cheng, C.-C. Liu, Y. Feng, S. Wu, S. K. Mahatha, P. Sheverdyaeva, P. Moras, M. Arita, O. Sugino, T.-C. Chiang, K. Shimada, K. Miyamoto, T. Okuda, K. Wu, L. Chen, Y. Yao, and I. Matsuda, "Experimental realization of two-dimensional Dirac nodal line fermions in monolayer Cu_2Si", *Nature Communications*, vol. 8, no. 1, p. 1007, Dec. 2017. DOI: `10.1038/s41467-017-01108-z` (cited on pp. 73, 75–77, 87, 95–97, 107, 109, 111–113).

[2] L. Liu, C. Wang, J. Li, X.-Q. Chen, Y. Jia, and J.-H. Cho, "Two-dimensional topological semimetal states in monolayer Cu_2Ge, Fe_2Ge, and Fe_2Sn", *Physical Review B*, vol. 101, no. 16, p. 165 403, Apr. 2020. DOI: `10.1103/PhysRevB.101.165403` (cited on p. 73).

[3] C. Niu, P. M. Buh, H. Zhang, G. Bihlmayer, D. Wortmann, S. Blügel, and Y. Mokrousov, "Topological nodal-line semimetals in two dimensions with time-reversal symmetry breaking", *arXiv:1703.05540 [cond-mat]*, Mar. 16, 2017. DOI: `10.48550/arXiv.1703.05540` (cited on p. 73).

[4] C. Niu, P. M. Buhl, G. Bihlmayer, D. Wortmann, Y. Dai, S. Blügel, and Y. Mokrousov, "Two-dimensional topological nodal line semimetal in layered X_2Y (x = Ca, Sr, and Ba; y = As, Sb, and Bi)", *Phys. Rev. B*, vol. 95, p. 235 138, 23 Jun. 2017. DOI: `10.1103/PhysRevB.95.235138` (cited on p. 73).

[5] Y.-J. Jin, R. Wang, J.-Z. Zhao, Y.-P. Du, C.-D. Zheng, L.-Y. Gan, J.-F. Liu, H. Xu, and S. Y. Tong, "The prediction of a family group of two-dimensional node-line semimetals", *Nanoscale*, vol. 9, pp. 13 112–13 118, 35 2017. DOI: `10.1039/C7NR03520A` (cited on p. 73).

[6] J.-L. Lu, W. Luo, X.-Y. Li, S.-Q. Yang, J.-X. Cao, X.-G. Gong, and H.-J. Xiang, "Two-dimensional node-line semimetals in a honeycomb-kagome lattice", *Chinese Physics Letters*, vol. 34, no. 5, p. 057 302, May 2017. DOI: `10.1088/0256-307X/34/5/057302` (cited on p. 73).

[7] S. Park and B.-J. Yang, "Classification of accidental band crossings and emergent semimetals in two-dimensional noncentrosymmetric systems", *Physical*

Review B, vol. 96, no. 12, Sep. 18, 2017. DOI: `10.1103/PhysRevB.96.125127` (cited on p. 73).

[8] L. Gao, J.-T. Sun, J.-C. Lu, H. Li, K. Qian, S. Zhang, Y.-Y. Zhang, T. Qian, H. Ding, X. Lin, S. Du, and H.-J. Gao, "Epitaxial growth of honeycomb monolayer CuSe with Dirac nodal line fermions", *Advanced Materials*, vol. 30, no. 16, p. 1 707 055, Apr. 2018. DOI: `10.1002/adma.201707055` (cited on p. 73).

[9] K. M. Yam, N. Guo, and C. Zhang, "Two-dimensional Cu_2Si sheet: a promising electrode material for nanoscale electronics", *Nanotechnology*, vol. 29, no. 24, p. 245 704, Jun. 2018. DOI: `10.1088/1361-6528/aabb45` (cited on p. 73).

[10] X. Sun, S. Wu, K. N. Dinh, and Z. Wang, "Metallic two-dimensional cu2si monolayer as promising anode materials for lithium and sodium ion batteries, a first principles study", *Journal of Solid State Chemistry*, vol. 274, pp. 265–269, 2019. DOI: `https://doi.org/10.1016/j.jssc.2019.03.041` (cited on p. 73).

[11] H.-H. Zhu, X.-J. Ye, C.-S. Liu, and X.-H. Yan, "Monolayer Cu_2Si as a potential gas sensor for NO_x and CO_x (x = 1, 2): A first-principles study", *Surface Science*, vol. 668, pp. 42–46, Feb. 2018. DOI: `10.1016/j.susc.2017.10.021` (cited on p. 73).

[12] R. N. Somaiya, Y. Sonvane, and S. K. Gupta, "Adsorption of toxic gas molecules on the pre-oxidized Cu_2Si nanosheet – a DFT study", *Computational Materials Science*, vol. 173, p. 109 414, Feb. 15, 2020. DOI: `10.1016/j.commatsci.2019.109414` (cited on p. 73).

[13] M. Tang, H. Shen, Y. Qie, H. Xie, and Q. Sun, "Edge-state-enhanced CO_2 electroreduction on topological nodal-line semimetal Cu_2Si nanoribbons", *The Journal of Physical Chemistry C*, vol. 123, no. 5, pp. 2837–2842, Jan. 2019. DOI: `10.1021/acs.jpcc.8b08871` (cited on p. 73).

[14] S. Roth, G. Gatti, A. Crepaldi, and M. Grioni, "The growth and band structure of a graphene-encapsulated two-dimensional nodal line semimetal: Cu_2Si", *Electronic Structure*, vol. 1, no. 1, p. 014 001, Feb. 2019. DOI: `10.1088/2516-1075/ab02a3` (cited on pp. 73, 76, 96, 107).

[15] M. Zhu, H. Yao, L. Jiang, and Y. Zheng, “Magnetism in Cu_2Si zigzag nanoribbon”, *Computational Materials Science*, vol. 161, pp. 119–126, Apr. 2019. DOI: `10.1016/j.commatsci.2019.01.038` (cited on p. 74).

[16] L. Yan, P.-F. Liu, T. Bo, J. Zhang, M.-H. Tang, Y.-G. Xiao, and B.-T. Wang, “Emergence of superconductivity in a Dirac nodal-line Cu_2Si monolayer: ab initio calculations”, *Journal of Materials Chemistry C*, 2019. DOI: `10.1039/C9TC03740C` (cited on p. 74).

[17] X. Wang and J. Chen, “Dynamical stability and superconductivity in two-dimensional nodal line semimetal CuSe and Cu_2Si”, *Journal of Superconductivity and Novel Magnetism*, vol. 34, no. 9, pp. 2229–2237, Sep. 2021. DOI: `10.1007/s10948-021-05924-9` (cited on p. 74).

[18] L.-M. Yang, V. Bačić, I. A. Popov, A. I. Boldyrev, T. Heine, T. Frauenheim, and E. Ganz, “Two-dimensional Cu_2Si monolayer with planar hexacoordinate copper and silicon bonding”, *Journal of the American Chemical Society*, vol. 137, no. 7, pp. 2757–2762, Feb. 25, 2015. DOI: `10.1021/ja513209c` (cited on pp. 74, 75, 109).

[19] T. Asahi, S. Yagi, H. Aga, Y. Takata, Y. Kitajima, T. Yokoyama, and T. Ohta, “Adsorption and decomposition of silane on Cu(111)”, *Japanese Journal of Applied Physics*, vol. 32, p. 380, 1993. DOI: `10.7567/JJAPS.32S2.380` (cited on p. 75).

[20] T. Kanazawa, Y. Kitajima, T. Yokoyama, S. Yagi, A. Imanishi, and T. Ohta, “Adsorption and decomposition of SiH_4 and surface silicide formation on Cu(111) studied by x-ray absorption fine structure spectroscopy”, *Surface Science*, vol. 357-358, pp. 160–164, 1996. DOI: `10.1016/0039-6028(96)00080-5` (cited on p. 75).

[21] N. J. Curson, H. G. Bullman, J. R. Buckland, and W. Allison, “Interaction of silane with Cu(111): surface alloy and molecular chemisorbed phases”, *Phys. Rev. B*, vol. 55, pp. 10 819–10 829, 16 Apr. 1997. DOI: `10.1103/PhysRevB.55.10819` (cited on p. 75).

[22] I. G. Shuttleworth, C. J. Fisher, J. J. Lee, R. G. Jones, and D. P. Woodru, “A NIXSW structural investigation of the $(\sqrt{3}\times\sqrt{3})$R30°-Cu_2Si surface alloy phase formed by SiH_4 reaction with Cu(111)”, *Surface Science*, p. 6, 2001. DOI: `10.1016/S0039-6028(01)01384-X` (cited on p. 75).

[23] M. J. Spencer, G. L. Nyberg, A. W. Robinson, and A. P. Stampfl, “Adsorption of SiH_4 on copper (110) and (111) surfaces”, *Surface Science*, vol. 505, pp. 308–324, 2002. DOI: 10.1016/S0039-6028(02)01378-X (cited on p. 75).

[24] H. Ménard, A. B. Horn, and S. P. Tear, “Methylsilane on Cu(111), a STM study of the R30°-Cu_2Si surface silicide”, *Surface Science*, vol. 585, no. 1-2, pp. 47–52, Jul. 2005. DOI: 10.1016/j.susc.2005.04.008 (cited on p. 75).

[25] I. Shuttleworth, “Deduction of a three-phase model for the $(\sqrt{3}\times\sqrt{3})$R30°-Cu_2Si/Cu(111) surface alloy”, *Applied Surface Science*, vol. 256, no. 3, pp. 636–639, Nov. 2009. DOI: 10.1016/j.apsusc.2009.08.032 (cited on p. 75).

[26] F. Ringeisen, J. Derrien, E. Daugy, J. M. Layet, P. Mathiez, and F. Salvan, “Formation and properties of the copper silicon(111) interface”, *Journal of Vacuum Science & Technology B: Microelectronics Processing and Phenomena*, vol. 1, no. 3, pp. 546–552, 1983. DOI: 10.1116/1.582596 (cited on p. 77).

[27] S. A. Chambers, S. B. Anderson, and J. H. Weaver, “Atomic structure of the Cu/Si (111) interface by high-energy core-level Auger electron diffraction”, *Physical Review B*, vol. 32, no. 2, p. 581, 1985. DOI: 10.1103/PhysRevB.42.1674 (cited on p. 77).

[28] R. J. Wilson, S. Chiang, and F. Salvan, “Examination of the Cu/Si(111) 5×5 structure by scanning tunneling microscopy”, *Phys. Rev. B*, vol. 38, pp. 12 696–12 699, 17 Dec. 1988. DOI: 10.1103/PhysRevB.38.12696 (cited on p. 77).

[29] J. E. Demuth, U. K. Koehler, R. J. Hamers, and P. Kaplan, “Phase separation on an atomic scale: the formation of a novel quasiperiodic 2D structure”, *Phys. Rev. Lett.*, vol. 62, pp. 641–644, 6 Feb. 1989. DOI: 10.1103/PhysRevLett.62.641 (cited on p. 77).

[30] K. Mortensen, “Frustration in the si(111) “pseudo 5×5” Cu structure directly observed by scanning tunneling microscopy”, *Phys. Rev. Lett.*, vol. 66, pp. 461–464, 4 Jan. 1991. DOI: 10.1103/PhysRevLett.66.461 (cited on p. 77).

[31] J. Zegenhagen, E. Fontes, F. Grey, and J. R. Patel, “Microscopic structure, discommensurations, and tiling of Si (111)/Cu-“5x5””, *Physical Review B*, vol. 46, no. 3, p. 1860, Jul. 1992. DOI: `10.1103/PhysRevB.46.1860` (cited on pp. 77, 79, 108).

[32] S. Nakatani, Y. Kuwahara, H. Kuramochi, T. Takahashi, and M. Aono, “Study of the Si(111) “5×5”-Cu Surface Structure by X-Ray Diffraction and Scanning Tunneling Microscopy”, *Japanese Journal of Applied Physics*, vol. 40, no. Part 2, No. 7A, pp. L695–L697, Jul. 2001. DOI: `10.1143/JJAP.40.L695` (cited on p. 78).

[33] M. D. Santis, M. Muntwiler, J. Osterwalder, G. Rossi, F. Sirotti, A. Stuck, and L. Schlapbach, “Electronic and atomic structure of the Cu/Si(111) “quasi-5×5” overlayer”, *Surface Science*, no. 477, pp. 179–190, Apr. 2001. DOI: `10.1016/S0039-6028(01)00708-7` (cited on pp. 78, 79, 108, 115, 116).

[34] P. Mutombo and V. Cháb, “Theoretical STM images of Cu atoms on a Si surface”, *Surface Science*, vol. 532-535, pp. 645–649, Jun. 2003. DOI: `10.1016/S0039-6028(03)00180-8` (cited on p. 78).

[35] L. Zhu, Z. Wei, G. Shi, B. Shang, M. Li, W. Wan, and W.-X. Tang, “Coverage-driven phase transition of copper silicide monolayer on Si (111)”, *Ultramicroscopy*, vol. 200, pp. 39–42, May 1, 2019. DOI: `10.1016/j.ultramic.2019.02.019` (cited on p. 78).

[36] H.-J. Neff, I. Matsuda, M. Hengsberger, F. Baumberger, T. Greber, and J. Osterwalder, “High-resolution photoemission study of the discommensurate (5.55 ×5.55) Cu/Si(111) surface layer”, *Physical Review B*, vol. 64, no. 23, p. 235 415, Nov. 27, 2001. DOI: `10.1103/PhysRevB.64.235415` (cited on pp. 78, 108, 109, 111, 119).

[37] J. Zegenhagen, P. Lyman, M. Bohringer, and M. Bedzyk, “Discommensurate Reconstructions of (111)Si and Ge Induced by Surface Alloying with Cu, Ga and In”, *physica status solidi (b)*, vol. 204, no. 2, pp. 587–616, Dec. 1997. DOI: `10.1002/1521-3951(199712)204:2<587::AID-PSSB587>3.0.CO;2-Y` (cited on p. 79).

[38] S.-Y. Yang, H. Yang, E. Derunova, S. S. P. Parkin, B. Yan, and M. N. Ali, “Symmetry demanded topological nodal-line materials”, *Advances in Physics:*

X, vol. 3, no. 1, p. 1 414 631, Jan. 2018, ISSN: 2374-6149. DOI: `10.1080/23746149.2017.1414631` (cited on p. 78).

[39] L. Li and M. A. N. Araújo, "Topological insulating phases from two-dimensional nodal loop semimetals", *Phys. Rev. B*, vol. 94, p. 165 117, 16 Oct. 2016. DOI: `10.1103/PhysRevB.94.165117` (cited on p. 78).

[40] L. Brey, "Spin-orbit coupling in graphene induced by adatoms with outer-shell p orbitals", *Physical Review B*, vol. 92, no. 23, p. 235 444, Dec. 29, 2015. DOI: `10.1103/PhysRevB.92.235444` (cited on pp. 78, 104, 107).

[41] I. I. Klimovskikh, M. M. Otrokov, V. Y. Voroshnin, D. Sostina, L. Petaccia, G. Di Santo, S. Thakur, E. V. Chulkov, and A. M. Shikin, "Spin–orbit coupling induced gap in graphene on Pt(111) with intercalated Pb monolayer", *ACS Nano*, vol. 11, no. 1, pp. 368–374, Jan. 24, 2017. DOI: `10.1021/acsnano.6b05982` (cited on pp. 78, 104, 107).

[42] D. A. Estyunin, I. I. Klimovskikh, V. Y. Voroshnin, D. M. Sostina, L. Petaccia, G. Di Santo, and A. M. Shikin, "Formation of a quasi-free-standing graphene with a band gap at the dirac point by Pb atoms intercalation under graphene on Re(0001)", *Journal of Experimental and Theoretical Physics*, vol. 125, no. 5, pp. 762–767, Nov. 2017. DOI: `10.1134/S1063776117100065` (cited on pp. 78, 104).

[43] D. Ma and Z. Yang, "First-principles studies of Pb doping in graphene: stability, energy gap and spin–orbit splitting", *New Journal of Physics*, vol. 13, no. 12, p. 123 018, Dec. 9, 2011. DOI: `10.1088/1367-2630/13/12/123018` (cited on pp. 78, 104, 107).

[44] B. Feng, J. Zhang, R.-Y. Liu, T. Iimori, C. Lian, H. Li, L. Chen, K. Wu, S. Meng, F. Komori, and I. Matsuda, "Direct evidence of metallic bands in a monolayer boron sheet", *Physical Review B*, vol. 94, no. 4, p. 041 408, Jul. 2016. DOI: `10.1103/PhysRevB.94.041408` (cited on p. 80).

[45] L. Jenkins and M. Chung, "LEED and Auger investigations of Cu(111) surface", *Surface Science*, vol. 24, no. 1, pp. 125–139, 1971. DOI: `10.1016/0039-6028(71)90223-8` (cited on p. 81).

[46] R. Musket, W. McLean, C. Colmenares, D. Makowiecki, and W. Siekhaus, “Preparation of atomically clean surfaces of selected elements: A review”, *Applications of Surface Science*, vol. 10, no. 2, pp. 143–207, Jan. 1982. DOI: 10.1016/0378-5963(82)90142-8 (cited on p. 81).

[47] G. A. Burdick, “Energy band structure of Copper”, *Phys. Rev.*, vol. 129, pp. 138–150, 1 Jan. 1963. DOI: 10.1103/PhysRev.129.138 (cited on p. 82).

[48] A. Tamai, W. Meevasana, P. D. C. King, C. W. Nicholson, A. de la Torre, E. Rozbicki, and F. Baumberger, “Spin-orbit splitting of the Shockley surface state on Cu(111)”, *Phys. Rev. B*, vol. 87, p. 075 113, 7 Feb. 2013. DOI: 10.1103/PhysRevB.87.075113 (cited on p. 82).

[49] C. Chen, Z. Tao, A. Carr, P. Matyba, T. Szilvási, S. Emmerich, M. Piecuch, M. Keller, D. Zusin, S. Eich, M. Rollinger, W. You, S. Mathias, U. Thumm, M. Mavrikakis, M. Aeschlimann, P. M. Oppeneer, H. Kapteyn, and M. Murnane, “Distinguishing attosecond electron–electron scattering and screening in transition metals”, *Proceedings of the National Academy of Sciences*, vol. 114, no. 27, Jul. 2017. DOI: 10.1073/pnas.1706466114 (cited on p. 82).

[50] S. Mizuno, Y. O. Mizuno, and H. Tochihara, “Structural determination of indium-induced Si(111) reconstructed surfaces by LEED analysis: (3×3)R30° and (4×1)”, *Physical Review B*, vol. 67, no. 19, p. 195 410, May 2003. DOI: 10.1103/PhysRevB.67.195410 (cited on p. 86).

[51] O. Bunk, G. Falkenberg, J. H. Zeysing, L. Lottermoser, R. L. Johnson, M. Nielsen, F. Berg-Rasmussen, J. Baker, and R. Feidenhans’l, “Structure determination of the indium-induced Si(111)-(4×1) reconstruction by surface x-ray diffraction”, *Physical Review B*, vol. 59, no. 19, pp. 12 228–12 231, May 1999. DOI: 10.1103/PhysRevB.59.12228 (cited on p. 86).

[52] G. Meyer, M. Michailov, and M. Henzler, “LEED studies of the epitaxy of Pb on Cu(111)”, *Surface Science*, vol. 202, pp. 125–141, 1988. DOI: 10.1016/0039-6028(88)90065-9 (cited on pp. 86, 94).

[53] M. Cameau, R. Yukawa, C.-H. Chen, A. Huang, S. Ito, R. Ishibiki, K. Horiba, Y. Obata, T. Kondo, H. Kumigashira, H.-T. Jeng, M. D’angelo, and I. Matsuda, “Electronic structure of a monoatomic Cu_2Si layer on a Si(111) substrate”, *Physical Review Materials*, vol. 3, no. 4, p. 044 004, Apr. 2019. DOI: 10.1103/PhysRevMaterials.3.044004 (cited on p. 108).

[54] O. Madelung and M. Rössler U.and Schulz, Eds., *Silicon (Si), band structure: Datasheet from Landolt-Börnstein - Group III Condensed Matter - Volume 41A1β: "Group IV Elements, IV-IV and III-V Compounds. Part b - Electronic, Transport, Optical and Other Properties"*. Springer-Verlag Berlin Heidelberg, 2002. DOI: 10.1007/10832182_432 (cited on pp. 109, 112).

[55] G. G. Guzmán-Verri and L. C. Lew Yan Voon, "Electronic structure of silicon-based nanostructures", *Phys. Rev. B*, vol. 76, p. 075 131, 7 Aug. 2007. DOI: 10.1103/PhysRevB.76.075131 (cited on pp. 109, 112).

[56] S. N. Takeda, N. Higashi, and H. Daimon, "Visualization of in-plane dispersion of hole subbands by photoelectron spectroscopy", *Physical Review Letters*, vol. 94, no. 3, p. 037 401, Jan. 24, 2005. DOI: 10.1103/PhysRevLett.94.037401 (cited on p. 109).

[57] P. E. Blöchl, "Projector augmented-wave method", *Phys. Rev. B*, vol. 50, pp. 17 953–17 979, 24 Dec. 1994. DOI: 10.1103/PhysRevB.50.17953 (cited on p. 113).

[58] G. Kresse and D. Joubert, "From ultrasoft pseudopotentials to the projector augmented-wave method", *Phys. Rev. B*, vol. 59, pp. 1758–1775, 3 Jan. 1999. DOI: 10.1103/PhysRevB.59.1758 (cited on p. 113).

[59] G. Kresse and J. Hafner, "Ab initio molecular dynamics for liquid metals", *Phys. Rev. B*, vol. 47, pp. 558–561, 1 Jan. 1993. DOI: 10.1103/PhysRevB.47.558 (cited on p. 113).

[60] G. Kresse and J. Hafner, "Ab initio molecular-dynamics simulation of the liquid-metal–amorphous-semiconductor transition in germanium", *Phys. Rev. B*, vol. 49, pp. 14 251–14 269, 20 May 1994. DOI: 10.1103/PhysRevB.49.14251 (cited on p. 113).

[61] G. Kresse and J. Furthmüller, "Efficiency of ab-initio total energy calculations for metals and semiconductors using a plane-wave basis set", *Computational Materials Science*, vol. 6, no. 1, pp. 15–50, 1996. DOI: 10.1016/0927-0256(96)00008-0 (cited on p. 113).

[62] G. Kresse and J. Furthmüller, "Efficient iterative schemes for ab initio total-energy calculations using a plane-wave basis set", *Phys. Rev. B*, vol. 54,

pp. 11 169–11 186, 16 Oct. 1996. DOI: 10.1103/PhysRevB.54.11169 (cited on p. 113).

[63] H.-J. Joo, C. Hwang, and K. Kim, “The low-energy electron band structure of a two-dimensional Dirac nodal-line semimetal grown on a silicon surface”, *Journal of the Korean Physical Society*, vol. 78, no. 1, pp. 34–39, Jan. 2021. DOI: 10.1007/s40042-020-00016-8 (cited on p. 114).

[64] F. Jolly, F. Rochet, G. Dufour, C. Grupp, and A. Taleb-Ibrahimi, “Oxidized silicon surfaces studied by high resolution Si 2p core-level photoelectron spectroscopy using synchrotron radiation”, *Journal of Non-Crystalline Solids*, vol. 280, no. 1, pp. 150–155, 2001. DOI: 10.1016/S0022-3093(00)00370-7 (cited on p. 114).

[65] K. Hricovini, R. Günther, P. Thiry, A. Taleb-Ibrahimi, G. Indlekofer, J. E. Bonnet, P. Dumas, Y. Petroff, X. Blase, X. Zhu, S. G. Louie, Y. J. Chabal, and P. A. Thiry, “Electronic structure and its dependence on local order for H/Si(111)-(1×1) surfaces”, *Phys. Rev. Lett.*, vol. 70, pp. 1992–1995, 13 Mar. 1993. DOI: 10.1103/PhysRevLett.70.1992 (cited on p. 114).

[66] S. Tosch and H. Neddermeyer, “Nucleation of Cu on Si(111) 7 ×7 and atomic structure of the Cu/Si(111) interface”, *Surface Science*, vol. 211-212, pp. 133–142, 1989. DOI: 10.1016/0039-6028(89)90763-2 (cited on p. 116).

[67] C. J. Karlsson, E. Landemark, Y.-C. Chao, and R. I. G. Uhrberg, “Atomic origins of the surface components in the si 2_p core-level spectra of the Si(111)-7×7 surface”, *Physical Review B*, vol. 50, no. 8, pp. 5767–5770, Aug. 15, 1994, ISSN: 0163-1829, 1095-3795. DOI: 10.1103/PhysRevB.50.5767 (cited on p. 116).

Chapter 4

Toward the experimental realization of Cu_2Ge: a new Dirac nodal-loop material

Chapter 4: Towards the experimental realization of Cu_2Ge: a new Dirac nodal-loop material

4.1 Introduction to Cu_2Ge

4.1.1 Cu_2Ge: a planar hexacoordinate material with two concentric DNLs

Amongst the theoretically predicted two-dimensional nodal-loop semimetals, Cu_2Ge appears a promising candidate to experimental realization, as it bears many similarities to the previously studied system Cu_2Si. This system was first presented by L.-M. Yang *et al.* in 2015 [1], where it is described as the first stable planar hexacoordinate germanium material in 2D space, presenting a metallic and non-magnetic character. Its atomic structure consists of a superposition of a honeycomb lattice of Cu atoms, with a triangular lattice of Ge atoms located at the centre of the honeycombs, as illustrated in Figure 4.1, forming a sheet belonging to the *P6/mmm* space group symmetry. Each Cu atom has three Cu and three Ge atoms as neighbours, while Ge atoms are surrounded by six Cu atoms. This Cu_2Ge is atomically flat, with all its atoms resting on the same plane and forming bond angles of 60°. The unit cell of the Cu_2Ge monolayer consists of two Cu atoms and one Ge atom, with lattice constants of a = b = 4.214 Å, and Ge–Cu and Cu–Cu bond lengths of 2.433 Å. The structural stability was demonstrated by the absence of imaginary phonon mode and attributed to the presence of multi-centre σ bonds (covalent bonds resulting from the direct overlap of orbitals). Furthermore, ab-initio calculations showed that this atomic configuration was the global energy minimum amongst other stable Cu_2Ge isomers. Molecular dynamics simulations also showed that the structure is overall maintained upon annealing up to 1200 K during 10 ps, but we will see later that on experimental time scales of a few seconds, the structure obtained deteriorates above 500°C.

While the electronic structure of Cu_2Ge was already presented by L.-M. Yang

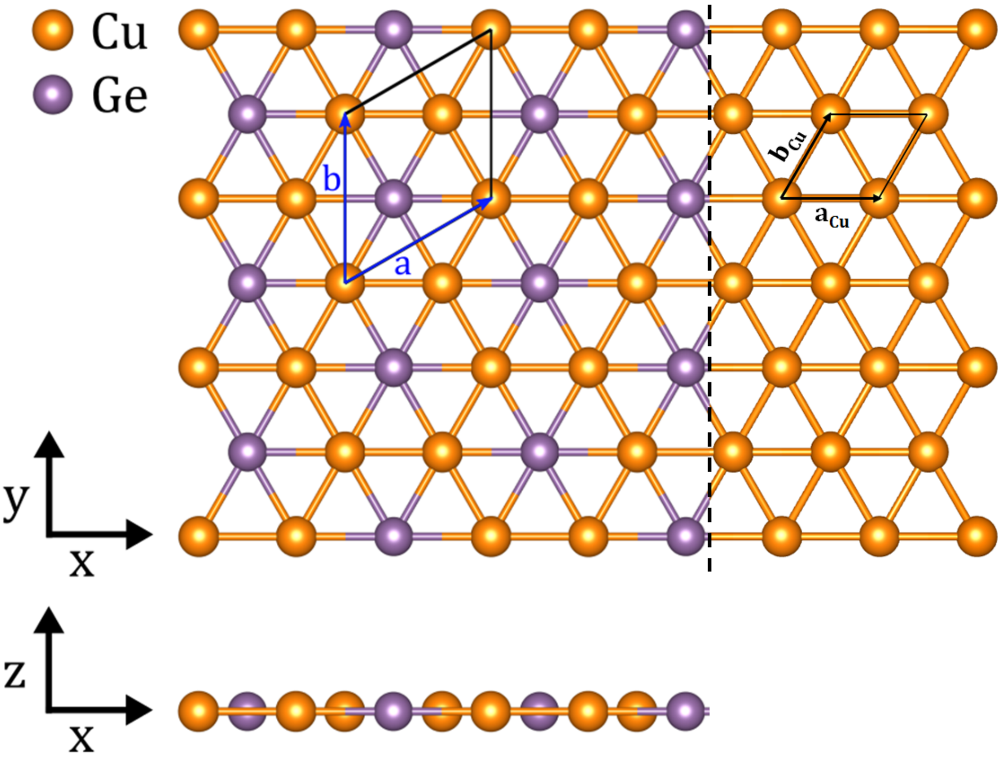

Fig. 4.1 – *Top and side view of a Cu_2Ge monolayer are shown on the left side of the image. The orange and purples spheres represent Cu and Ge atoms respectively. The unit vectors* **a** *and* **b** *are represented by blue arrows and form a diamond-shaped primitive unit cell of the system. The right side shows the (1×1) Cu surface with its unit vectors. It can be seen that the unit vectors of Cu_2Ge are $\sqrt{3}$ times longer than the ones of Cu(111), and rotated by 30°, thus forming a $(\sqrt{3} \times \sqrt{3})R30°$ surface reconstruction. The position of the Cu_2Ge layer with respect to the substrate might not reflect the reality. It is drawn here as if the monolayer only occupies top sites, whereas its atoms could also occupy HCP, FCC or bridge sites, as for Cu_2Si, see Figure 3.2.*

et al. [1], it was not until a study by L. Liu *et al.* (2020) [2] that its topological properties were investigated, and the Dirac nodal-lines were revealed. They demonstrated the existence of two concentric DNLs around Γ, protected by the M_z mirror reflection symmetry. Three bands are involved in the existence of the DNLs: two hole-like and one electron-like, respectively labelled α, β and γ, as presented in Figure 4.2a. From band projection calculations, it is shown that the α and β bands are mainly composed of the Cu $d_{xy}/dx^2 - y^2$ and Ge p_x/p_y orbitals, while the γ band is composed of the Cu d_{xz} and Ge p_z orbitals. Therefore, the α and β bands have even-parity $(+)$ eigenvalues of M_z while the γ band has odd-parity $(-)$ eigenvalues of M_z, forbidding hybridization with each other and thus ensuring gapless DNLs in the absence of SOC. The two DNLs, shown in Figure 4.2b along with their projection on the Fermi surface, form two loops and are located within 0.8 eV of the Fermi surface. Once the SOC is taken into account, band openings are observed along the Γ-M and Γ-K directions as presented in Figure 4.2c. The innermost nodal-line (points A and A') shows gaps of 47.2 meV and 45.1 meV along the directions Γ-M and Γ-K respectively, while the outermost (with point B and B') shows gaps of 63 meV and 59.3 meV along those directions. These gaps are larger than the ones expected in Cu_2Si from the same types of calculations, ranging from 5 meV to 15 meV. [3], probably due to the stronger SOC induced by Ge, heavier than Si.

There are yet too few 2D DNLs materials experimentally evidenced, and expanding the list is crucial for a better understanding of their general properties. The importance of synthesizing such materials is manifold. From a fundamental point of view, Cu_2Ge could be used as a platform to study possible topological phase transitions, by changing the symmetries of the system either intrinsically (e.g. by physical deformation) or by an external field. For example from DNL semimetal to topological insulator, topological crystalline insulator and Chern insulator [4]. If a topological insulator state can be reached, it would open the way to Quantum-spin Hall effect materials (dissipationless devices), and if WNLs are obtained, the possibility of exotic superconductive states such as Majorana surface states is open [5]. On more direct applications, the presence of DNLs close to the Fermi level with no other state close to it should ensure high electronic mobility due to the linear dispersion. Adding to that, DNLs system could have a higher carrier density than

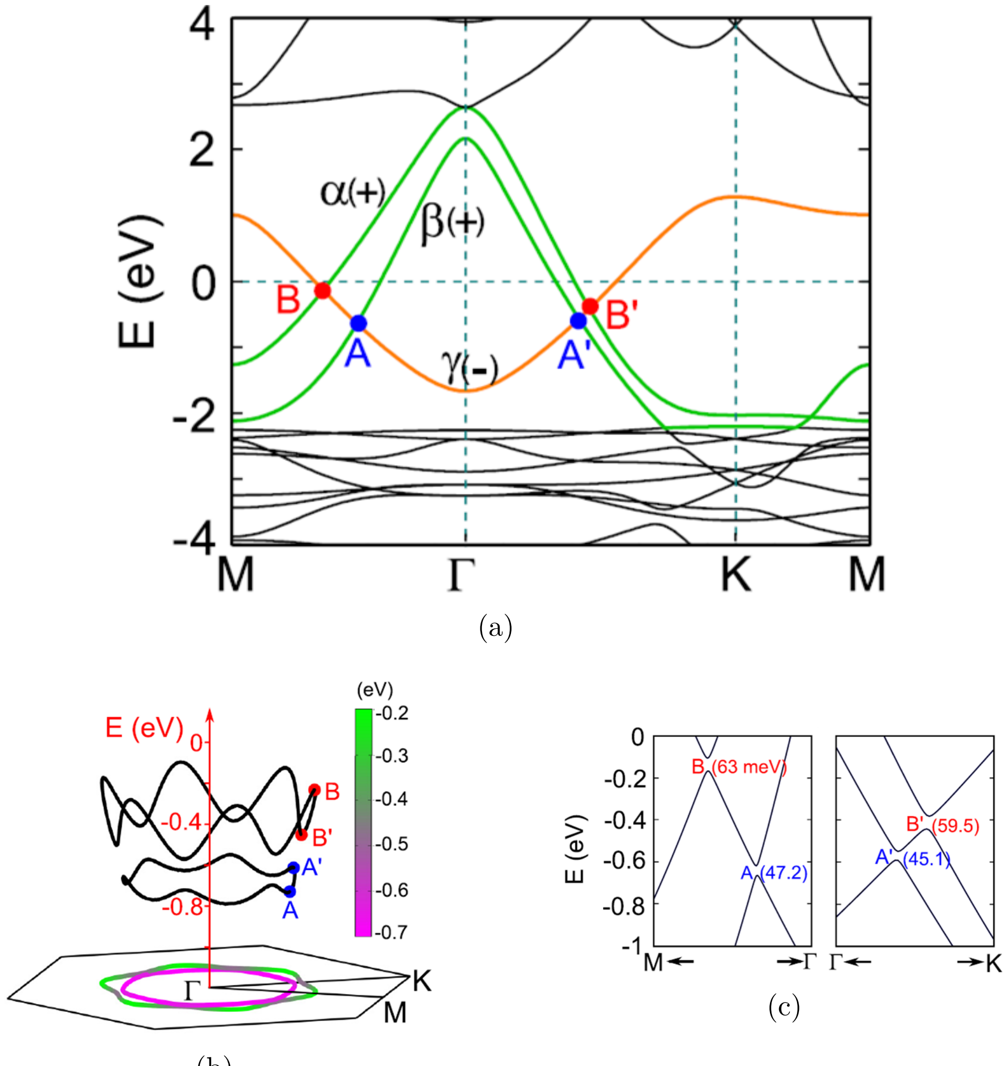

(a)

(b)

(c)

Fig. 4.2 – *(a) Calculated band structure of the Cu_2Ge monolayer in the absence of SOC. The three bands labelled α, β and γ cross in four points along the Γ-M and Γ-K lines: A, A', B, and B'. For the α, β and γ bands, the parity of mirror symmetry is labelled by the plus or minus sign in parentheses. (b) Energy dispersion of the two DNLs passing through the A and A' (B and B') points, together with their projections onto the first Brillouin zone using the colour scale. (c) Zoom-in band structures around the A and B (A' and B') points, obtained by including SOC. The numbers represent the gaps (in meV) at the A, A', B, and B' points. Figures and caption from [2].*

systems with Dirac cones, due to the band crossing happening along a 2D line and not only at discrete points. Those properties would lead to uses in high-frequency 2D heterostructure devices. Despite the interesting properties predicted in Cu_2Ge, there is no experimental realization of it reported in the literature to the best of our knowledge. We thus decided to attempt to remedy this problem. We adopted a two-fold approach: on one hand pursuing the synthesis of Cu_2Ge on a Cu(111) substrate, optimistic from the results obtained with Cu_2Si/Cu(111), and on the other hand, explore the electronic properties of Cu on Ge(111) in an attempt to determine if a Cu_2Ge monolayer could be obtained on a non-conductive substrate.

4.1.2 Experimental approach to Cu_2Ge realization

While no synthesis of a planar hexacoordinate Cu_2Ge is mentioned in the literature, growth studies of both Ge on Cu(111) and Cu on Ge(111) exist, with a focus oriented towards the growth mode and atomic structure of interfaces and surfaces rather than on their possible electronic properties. We will discuss in the following paragraphs the experimental work on which our work took support.

4.1.2.1 Growth of Ge/Cu(111): state of the art

There exist few reports on the growth of Ge on Cu(111), possibly because the first accounts did not augur anything exciting or at least different than Si on Cu(111), more studied. It is in one study comparing those two types of interfaces that most of the information can be found. In 1990, R. Dudde *et al.* [6] studied by angle-resolved direct and inverse photoemission the growth of Ge on Cu(111) for thickness ranging from 3 Å to 25 Å, reporting only a diffuse LEED background signal before annealing, and a (1×1) LEED pattern after a 3 min anneal at 420 K for thin films (< 5 Å). For thicker films, the spectroscopic measurements show a continuous transition toward bulk Ge states. In a more recent study (2003) [7], using low-energy electron diffraction (LEED) and Auger electron spectroscopy (AES) it has been observed that the Ge/Cu(111) system shows a (1×1) structure up to 5 monolayers deposited at 300 K, that interdiffusion of Ge/Cu(111) films occurs as soon as 375 K, and that the Auger peaks were restored to their original kinetic energy upon annealing above 500 K.

Finally, in 2017 the successful preparation of bi-layer islands of Ge on Cu(111) have been shown to host Dirac cones in an STS study [8], where the proposed periodicity of the islands with respect to Cu(111) is a $(\sqrt{3} \times \sqrt{3})$R30°. In this study, the annealing temperatures were kept below 500 K to avoid intermixing leading to the formation of a surface alloy, and the islands are thought to be composed only of Ge atoms.

It is however the surface alloy Cu_2Ge that interests us in this work, and we will discuss in section 4.2 our attempt to realize it.

4.1.2.2 Growth of Cu/Ge(111): state of the art

A detailed study of the surface reconstructions of monolayer Cu on Ge(111) was conducted by M. Börhinger et al. [9], in which they describe a discommensurate, hexagonal domain superlattice, with a ("8.88×8.88")R30° periodicity with respect to the substrate. Atomic resolution STM images show that these domains are constituted of a local (1×1) geometry with a 5% lattice mismatch with the substrate, with the domain walls forming an ordered zigzag pattern allowing for a relaxation of the surface stress. The locally commensurate domains exhibit a slight buckling, with some of the atoms resting on a higher plane than their neighbours. A precise measurement of this height difference was deemed too difficult, due to the different electronic contributions of atoms of different elements inducing a too large uncertainty.

They proposed three possible atomic models, with respective surface stoichiometries of Cu_2Ge, CuGe and $CuGe_2$, further x-ray standing waves measurements (XSW) [10] leaning in favour of the last two models. All these models have a buckled surface. A later x-ray photoelectron diffraction (XPED) study [11] is also reporting a Cu/Ge(111)-("8.8×8.8")R30° structure, and confirms the buckling of the layer, giving a 12° bond angle between the lower and higher atoms. This time only two possible atomic models are proposed, with Cu_2Ge and $CuGe_2$ stoichiometries, in order to agree with the forward scattering peaks observed. These models, differing only from the element occupying a given site, are presented in Figure 4.3. We note that the diagram is not to scale and that the last three atomic plans should be seen as one buckled layer.

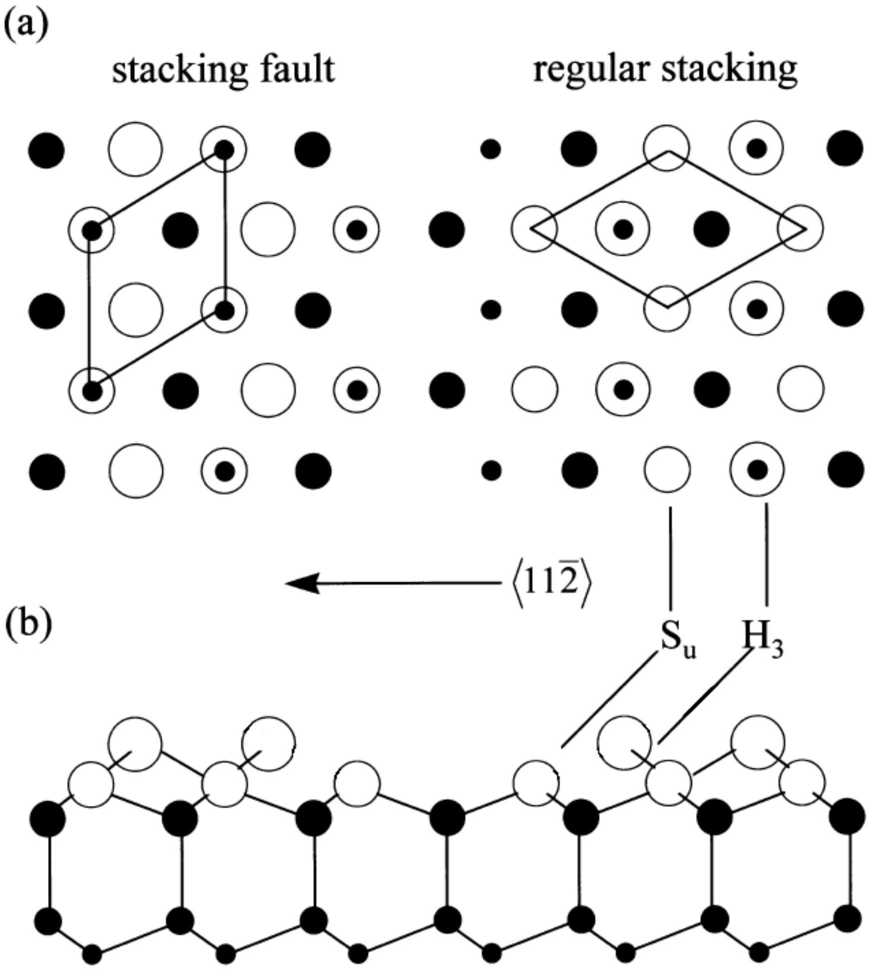

Fig. 4.3 – *Structural model for the local atomic structure within the Cu/Ge(111) discommensurate domains in (a) top view and (b) side view. The black filled circles correspond to the substrate Ge atoms, with the last Ge layer being taken into account for the surface stoichiometry. The white circles correspond to the Cu atoms in the Cu_2Ge model, while in the $CuGe_2$ model the topmost atoms (H_3 sites) are replaced by Ge atoms. The left-hand side of the pictures (a) and (b) suggest a stacking fault. In it, there is an hcp-stacking instead of fcc-stacking of the substitutional Cu atoms (S_u) with respect to the underlying substrate lattice. These two coexistent stacking models explain the STM images obtained [9]). The estimated height between the S_u and H_3 sites is estimated at 0.5 Å [11]. The last three atomic plans: last Ge layer, S_u and H_3 sites should be seen as a buckled surface rather than distinct atomic layers. Figure and caption adapted from [11].*

The first model, resulting in a $CuGe_2$ stoichiometry, consists of Cu atoms substituting for Ge atoms on the surface (S_u sites), and Ge atoms adsorbing above in H_3 sites. At room temperature, the Cu atoms may be randomly distributed over the substitutional S_u or the H_3 positions, while the respective other site is occupied by a Ge atom. Interchange of the two species may be permitted, resulting in an internal atomic structure difficult to resolve (it was not managed until now). At low temperature, the Cu and Ge would reach their energy minimum configuration: Cu in the surface layer and Ge on top.

The second model, resulting in a Cu_2Ge stoichiometry, is a limit case of the first, in which all the topmost Ge layer is replaced by Cu, resulting in a double Cu layer. In both models, the alternation of stacking fault and regular fault from domain to domain would explain the shift of the atomic rows observed in STM [9]. Due to the very similar scattering strengths of Cu and Ge, a differentiation between the two appears difficult, and a possible transition from one to another with increasing Cu coverage is not excluded either. The determination of the stoichiometry of the surface alloy Cu/Ge(111) is still an open question, and the possibility of a a phase coexistance is not excluded [11], as it is the case on Cu/Si(111) [12].

It is worth remarking that these studies disagree with the first experimental work on Cu/Ge(111) [13] which, using valence-band and core level measurements, describes a commensurate and ordered (5×5)R30° reconstruction at low coverage, from 0.27 monolayer (ML) to 1 ML, and the formation of bulk-like Cu for higher coverage, from 1 ML up to 12 ML. Their LEED patterns do not however display all the spots expected in a (5×5) R30° surface reconstruction, and while the authors acknowledge this, they compare it to the (5×5)Cu/Si(111), which was later better understood as a discommensurate surface reconstruction [6, 14, 15]. A discommensurate surface would furthermore explain the LEED pattern they observed. The quality of LEED measurements of this time, alongside the will to identify similarities with Cu/Si(111) might explain an imprecise conclusion.

We should note here that the possibility of a buckled Cu_2Ge monolayer is worthwhile to investigate, as it could host gaped Dirac nodal-loops if its electronic coupling to the substrate is sufficiently weak [2], as a buckling would break the M_z

mirror reflection symmetry protecting the DNLs in the absence of SOC.

4.2 The first experimental realization of Cu_2Ge on Cu(111)

4.2.1 Clean Cu(111)

For a description of the cleaning procedure and cleanliness characterization of Cu(111), see subsection 3.2.1.

4.2.2 Growth process of Ge on Cu(111)

After the Cu(111) sample was cleaned, Ge was evaporated from an e-beam evaporator, within a UHV chamber with base pressure in the low 10^{-10} mbar range. The Ge evaporated originates from pieces of bulk Ge crystal. We aimed at depositing 0.5 monolayer (ML) over a few minutes, with the Cu(111) substrate kept at 300±50°C. Uncertainty on the substrate temperature is mainly due to uncertainty on the emission coefficient of Cu (we used $\epsilon = 0.1$). Once evaporation is done, prolonging the anneal for 5 more minutes yields a better low energy electron diffraction (LEED) pattern. The determination of the optimal growth process was done by optimization of the observed $(\sqrt{3} \times \sqrt{3})$R30° LEED pattern, which is presented in Figure 4.4. This reconstruction is consistent with what is expected from the crystalline Cu_2Ge monolayer described above. No other surface reconstruction was observed by LEED, with a surface coverage of Ge ranging from 0.1 ML to 1 ML, and at varying temperatures of deposition and of anneal. Annealing above 500°C results in a degradation of the structure, followed by a disappearance of the $(\sqrt{3} \times \sqrt{3})$R30° diffraction pattern.

Through the remainder of this section, we will refer to the surface obtained as Ge/Cu(111), and show that its characteristics conform to what is expected of Cu_2Ge.

4.2.3 XPS results

Characterization of the sample obtained was done using XPS. A first step to verify the quality of the surface is to check for impurities. Figure 4.5 shows an overview scan taken at hν = 330 eV. All peaks present are assigned either to Ge or Cu. A

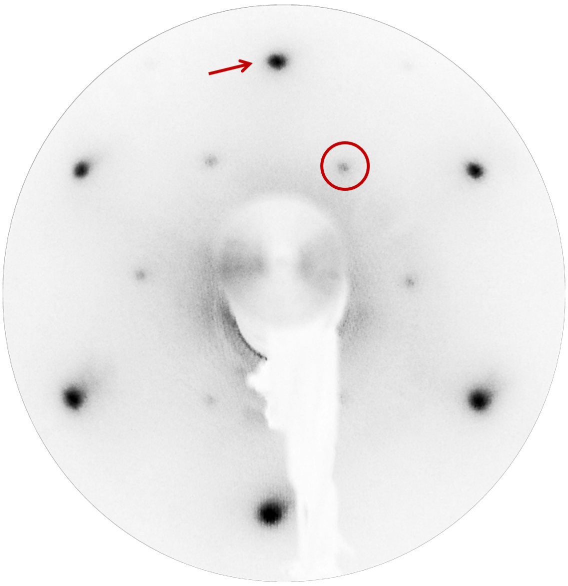

Fig. 4.4 – $(\sqrt{3} \times \sqrt{3})$*R30° surface reconstruction observed by LEED after evaporation of Ge on Cu(111), of which one spot is circled in red. The red arrow shows a spot of the substrate (1x1). Picture taken at 100 eV*

scan with a finer resolution was taken around 284 eV of binding energy, where C 1s should be observed in the presence of carbon. It was measured at hv = 330 eV making it the most surface sensitive possible for the detection of C 1s. The absence of any feature above noise level (i.e. in the detection limit) demonstrates the absence of adventitious carbon on the surface, and thus the cleanliness of the surface.

Once that cleanliness has been checked, we focused our attention on the core-level spectra of Cu and Ge. Figure 4.6 shows the Ge 2p core level measured at three different photon energies (hv = 1290 eV, 1330 eV and 1400 eV), the lower energies being the most surface sensitives. For hv = 1290 eV, only the Ge $2p_{3/2}$ peak was measured. Doniach-Sunjic peak-shapes were used to account for the asymmetry of the peaks as is usual for Ge core levels, as well as a Shirley-type background. Using the Fermi level for binding energy calibration, the position of the Ge $2p_{3/2}$ peak is found at 1215.1 eV of binding energy, with a spin-orbit splitting of 30.97 eV. For all photon energies we used an FWHM of 1.36 eV with a Gaussian broadening of 0.22 eV. The asymmetry parameter used was 0.055 in all three cases, and the branching ratio was constrained to 0.5. In all cases, only one contribution is identified, in good agreement with the atomic model proposed for Cu_2Ge in which all Ge atoms have

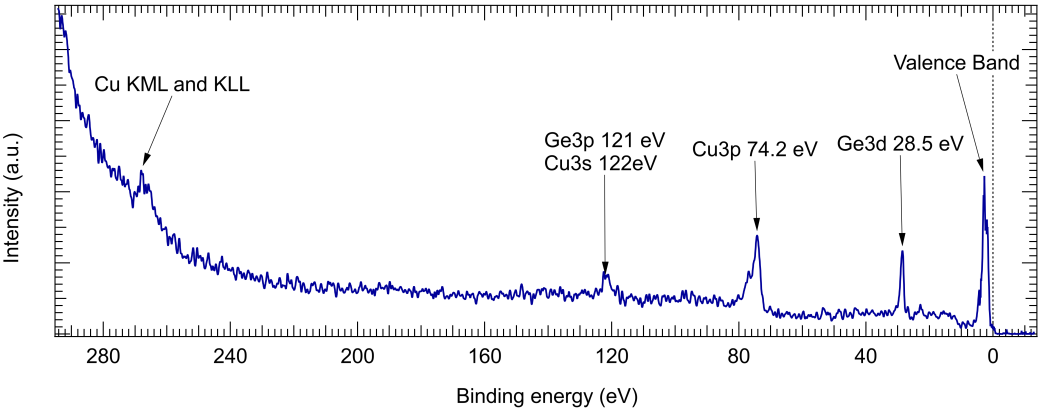

(a)

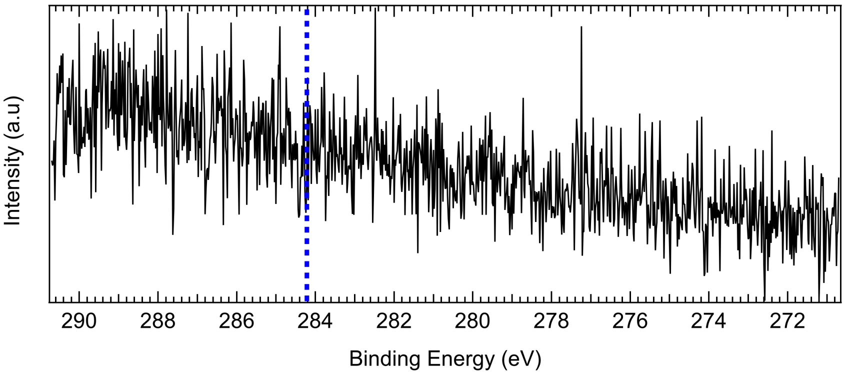

(b)

Fig. 4.5 – *(a) shows an overview spectra taken at hv = 330 eV, where all peaks observed belong either to Cu or Ge. KML and KLL are two Auger peaks of Cu. (b) a finer spectrum measured at hv = 330 eV around the expected position of C 1s, represented by a blue dashed line, demonstrates the absence of adventitious carbon on the surface in the detection limit of our experiment.*

an identical chemical environment.

The Ge 3d core level was also measured with three different photon energies, hv = 80 eV, 130 eV and 180 eV , where lower energy increases surface sensitivity, and is presented in Figure 4.7. As for Ge 2p, all the fits were realized using Doniach-Sunjic peak shapes to account for the asymmetry of the peaks, and the background was fitted using a Shirley step for each peak. Doublets relative areas were fixed at a ratio of 0.66 as required for *d* orbitals, and spin-orbit splitting was 0.55 eV in all three fits. Peak width was fixed for all peaks measured at a given photon energy, but was allowed to change from one spectrum to another, increasing with photon energy, to account for the experimental loss of resolution resulting in broadening at higher photon energies.

We found that two pairs of doublets account satisfyingly to the signal measured. Those two contributions are separated by 0.40 eV in all spectra. We attribute the main contribution (Peak 1, largest area) to the Ge atoms residing in the topmost layer, resulting in the periodic reconstruction $(\sqrt{3} \times \sqrt{3})R30^\circ$ observed by LEED. We attribute the smaller contribution (Peak 2) to small Ge islands formed by excess Ge evaporation, residing on top of the surface. This argument is supported by the evolution of the relative areas of the two components with increasing photon energy. Looking at the ratio between the area of the two contributions, we determined that the smaller one represented 7%, 4% and 2% of the larger one, for photon energies of 80 eV, 130 eV and 180 eV respectively. By looking at the highest variations in area ratio that could result in fits of adequate quality, we estimate the precision of relative areas at ±1%. The decreasing sensitivity to the smaller component with increasing energy (i.e. increasing probing depth) suggests that the atoms emitting those photoelectrons are located above the ones of the larger component. This can also be explained by the preparation method, which aims at depositing Ge in excess and uses the diffusion of Ge atoms by heating to form the largest crystalline monolayer possible.

The absence of a second contribution in the Ge 2p spectra can be explained by a surface of better prepared than the one measured above, as those measurements were taken on different surfaces and with different equipment. It is also possible

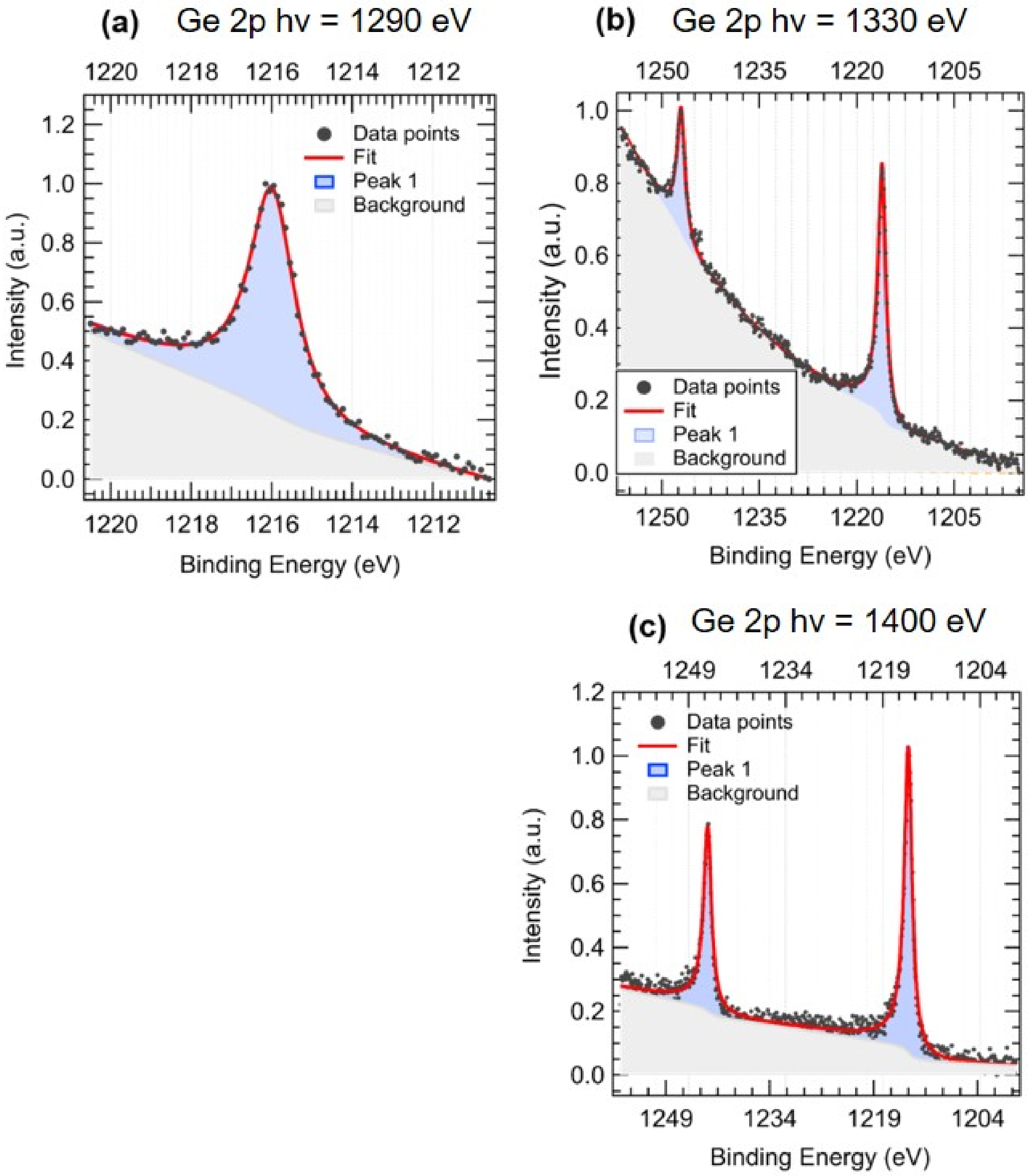

Fig. 4.6 – *Ge 2p core level measured on Ge/Cu(111) at different photon energies. In all cases, a single asymmetric doublet provides a good fit. (a) Measured at hv = 1290 eV, only the Ge* $2p_{3/2}$ *peak is shown here. (b) hv = 1330 eV. (c) hv = 1400 eV.*

that a small second contribution to Ge 2p is hidden in the asymmetrical shape of the peak or in the background and cannot be resolved. The addition of a second contribution does not however lead to better fits.

Finally, we present the Cu2p core level. Figure 4.8 shows a spectrum taken at hv = 1100 eV, where $Cu2p_{3/2}$ and $Cu2p_{1/2}$ are identified. The presence of satellite features following the peaks induces some difficulty to perform a proper background fit, we thus decided to fit only the $Cu2p_{3/2}$ peak, as is often found in the literature. The weakness of the satellite features is however a good indicator of the absence of oxidized copper species, as they get intense when oxides are present [16]. The fitted spectra are presented in Figure 4.9. Voigt functions were used for the fits, with an equal share of Gaussian and Lorentzian, as is usual in the literature. Total FWHM was found to be 0.9 eV. In both spectra, two components are found, separated by 0.81 eV. The main peak, labelled *peak 1*, resides at 932.5 eV of binding energy. The smaller component, labelled *peak 2*, forms a shoulder on the lower binding-energy side and increases in relative area with increasing photon energy. At hv = 1050 eV, the smaller component area represents 4% of the larger one, while at hv = 1100 eV it represents 18%. As increasing energy increases probing depth, we attribute the larger component to surface Cu, bonded to Ge, and the smaller component to bulk Cu. At those energies, the inelastic mean free path (the average distance that an electron with a given energy travels between successive inelastic collisions) is around 5.5 Å[17] corresponding to between two and three atomic layers.

We conclude from the XPS data that the Ge involved in the crystalline structure resides on one main site of adsorption, with an equal chemical environment for those Ge atoms, and that the copper atoms have two distinct chemical environments: bulk and surface. This is all in good agreement with the proposed atomic model for Cu_2Ge on Cu(111).

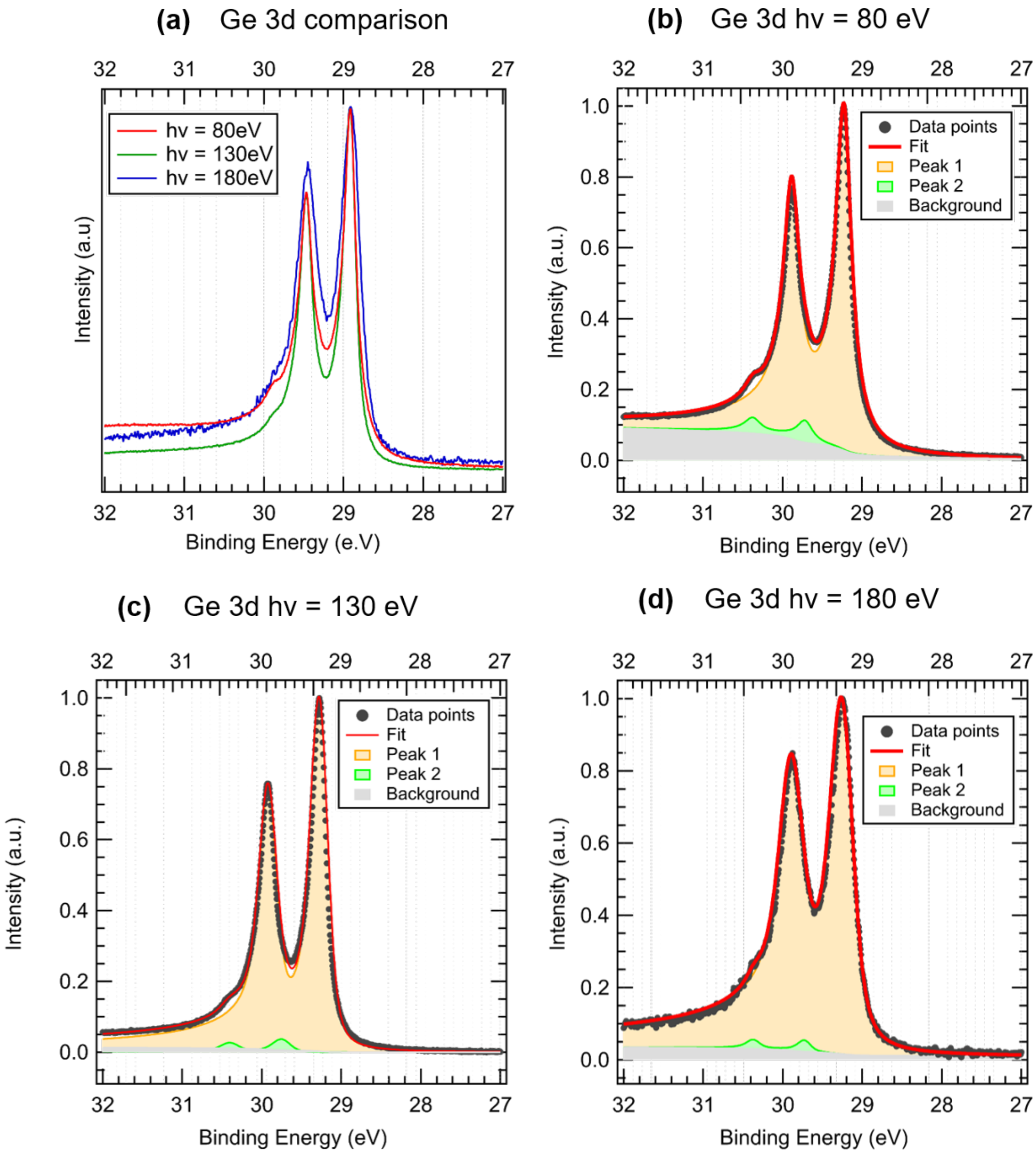

Fig. 4.7 – *The Ge 3d core level of Ge/Cu(111) was measured for three different photon energies (80 eV, 130 eV and 180 eV), to obtain information on the depth dependence of the components. (a) presents the superposition of the three spectra. (b), (c) and (d) show the spectra fitting. Two contributions are found: we attribute the main one (peak 1, in orange) to Ge adsorbed on the topmost layer and the smaller (peak 2, in green) one to islands formed from excess Ge. The background, obtained from Shirley steps, is in grey.*

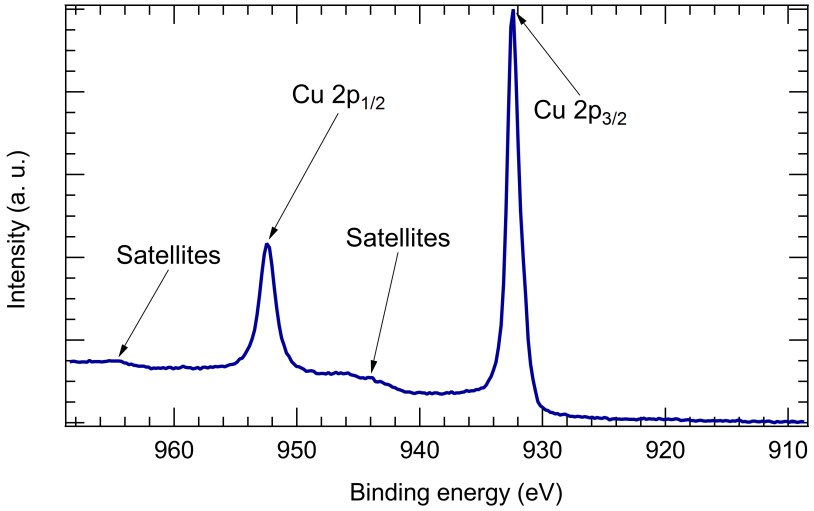

Fig. 4.8 – *Cu2p core level at hv = 1100 eV. The weakness of satellite features indicates the absence of oxidized copper species [16].*

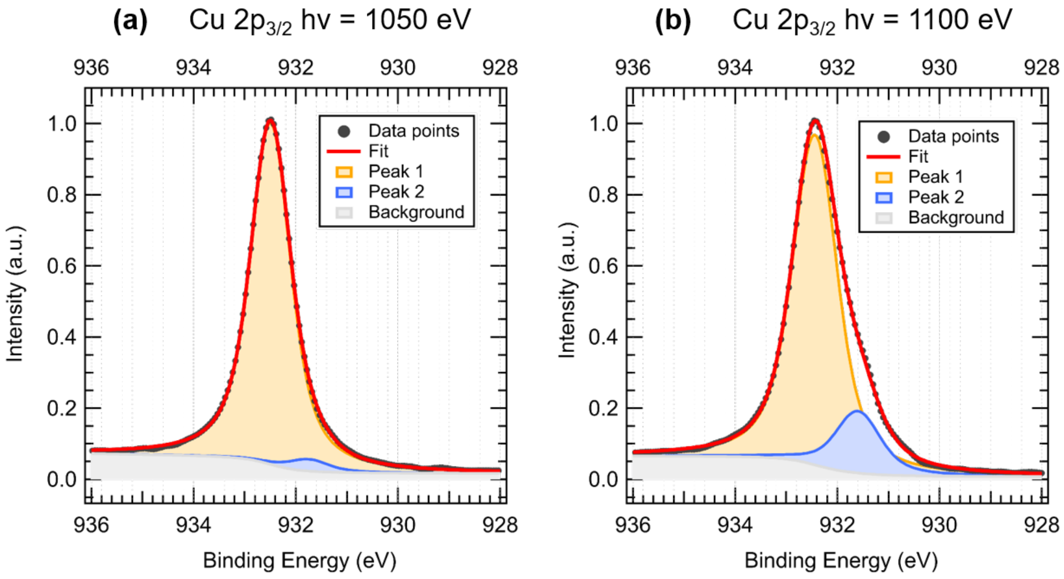

Fig. 4.9 – *Cu $2p_{3/2}$ for Ge/Cu(111). (a) hv = 1050 eV, (b) hv = 1100 eV. Two components are observed. Peak 1 is attributed to the surface contribution and peak 2 to the bulk contribution, as its relative area increases with increasing photon energy (i.e. probing depth).*

4.2.4 ARPES study

Before getting to the ARPES measurements, we show a schematic representation of the Brillouin zones (BZ) of Cu_2Ge and Cu(111) with their high-symmetry points in Figure 4.10, for the reader to get a better understanding of the geometry of the problem, and better locate the direction of measurement. As Cu_2Ge forms a $(\sqrt{3} \times \sqrt{3})$R30° surface reconstruction, its BZ is $\sqrt{3}$ times smaller and with a 30° rotation compared to the BZ of Cu(111), leading to the centre of the second Brillouin zone (Γ_2) of Cu_2Ge coinciding with a K point of Cu(111).

We measured the band dispersion of the Ge/Cu(111) surface around Γ for varying photon energies and light polarization to observe all the electronic bands of the system, and to determine the best experimental conditions to measure them. The measurements, made along the direction Γ-K and ranging from 20 eV to 100 eV are presented in Figure 4.11 and Figure 4.12, for linear horizontal and vertical horizontal polarization respectively. We observe a strong intensity variation in the bands with energy and polarization. The intensity variation of these bands originates from the matrix element effects in the photoemission process. However, looking at all 2D spectra, three bands can be identified as originating from the Cu_2Ge surface, as they

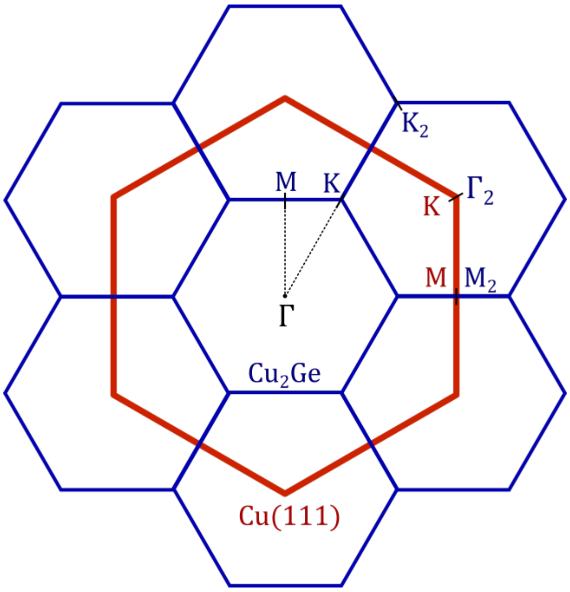

Fig. 4.10 – *Schematic representation of the Brillouin zones of* Cu_2Ge *in blue and Cu(111) in red. As the* Cu_2Ge *form a* $(\sqrt{3} \times \sqrt{3})R30°$ *surface reconstruction, its BZ is* $\sqrt{3}$ *times smaller and with a 30° rotation compared to the BZ of Cu(111).*

do not correspond to any band measured on clean Cu(111), see subsection 3.2.1. These three bands are superposed to the first image of Figure 4.11, and presented with a larger scale in Figure 4.13. Two of them have hole-like dispersion (their maxima are at Γ above the Fermi level). The closest to Γ is labelled as α band, while the further to Γ is labelled as β band. Those two bands are better seen at lower photon energies (hv$\leq$ 50 eV, LH polarization). The third band has an electron-like dispersion (its minimum is on Γ, below the Fermi level), and is labelled as γ. Less defined as the other two, this band is better seen at higher photon energies (hv$\geq$ 50 eV), and especially at 70 eV with LH polarization or at 80 eV with LV polarization. At high photon energies (hv = 100 eV for example), a band can be observed crossing the Fermi level with higher Fermi vector (1.3 Å^{-1}). This band, very wide, corresponds well to the closest band to Γ of the clean Cu(111) metal and is not of interest to us here. We remark that the bands' intensity seems more dependent on the photon energy than on the light polarization: the orbitals contributing to the bands must then have different parities with respect to the mirror plane (scattering plane), which seems in agreement with the projected band calculations made by Liu *et al.* [2] (supplementary materials).

Curvature images of selected spectra (LH polarization, hv = 20 eV, 50 eV and 70 eV) are shown in Figure 4.14. From them, it appears that the three bands observed (α, β and γ) are all continuous, and that no gap is present at the crossings, or at least not within our experimental resolution. According to the DFT calculations, the DNLs in Cu_2Ge are protected by mirror reflection symmetry (M_z), and should be gaped if this symmetry is broken. Here, the presence of a Cu(111) substrate on one side of the surface and of the vacuum on the other side results in a M_z symmetry breaking, but the absence of any sign of a detectable gap opening in our ARPES measurements indicates a weak, or negligible, interaction between the topmost layer and the Cu(111) substrate. Another argument in favour of the weak interaction with the substrate is the absence of folded bands of Cu(111). We could indeed expect Umklapp scattering with the $(\sqrt{3} \times \sqrt{3})$R30° superlattice leading to a folding of the Cu(111) bands into the first Brillouin zone.

The Fermi vectors along the Γ-K direction (with respect to the Cu_2Ge Brillouin zone) were measured for the three bands α, β and γ. We found that they cross the

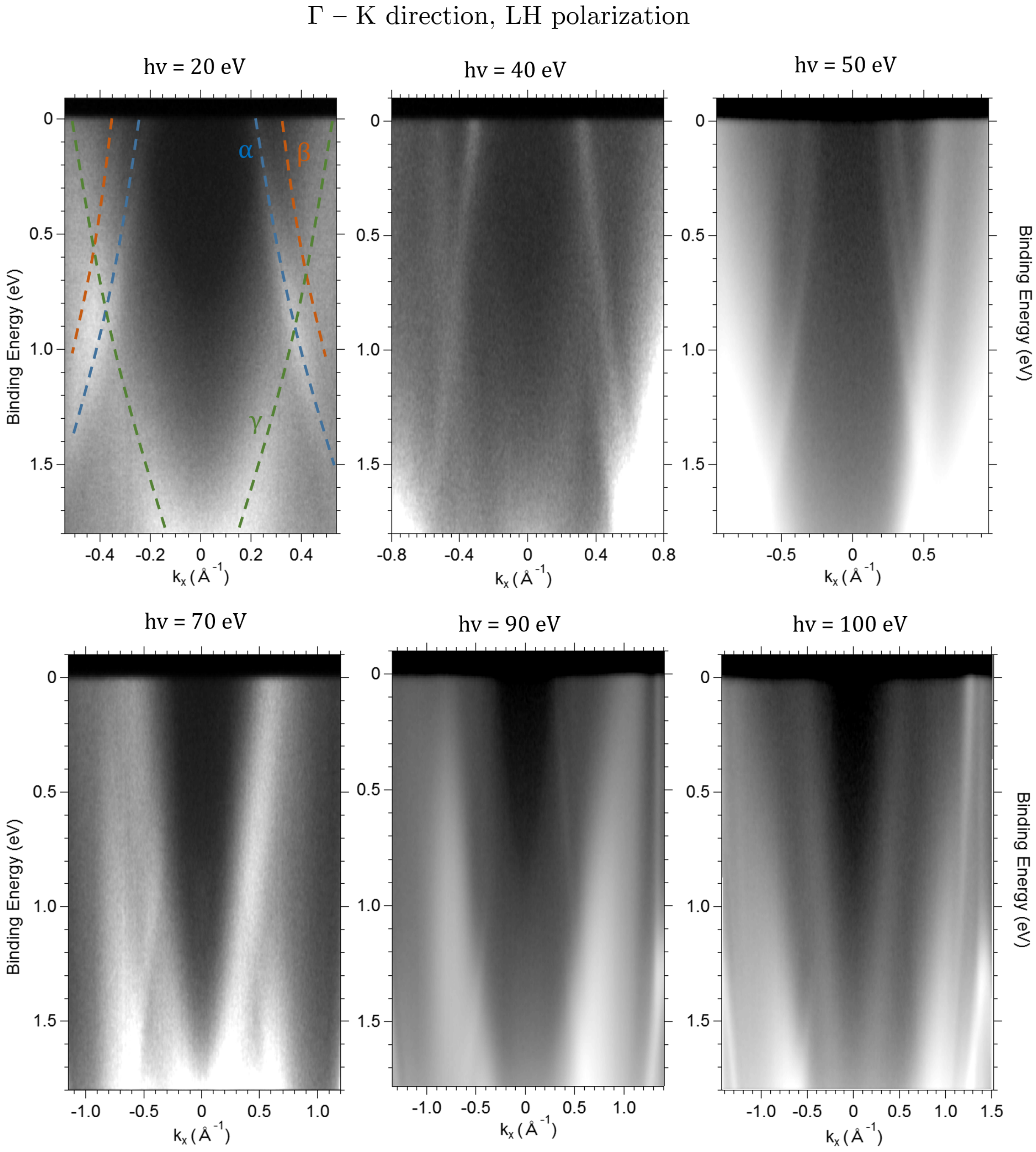

Fig. 4.11 – *ARPES of Ge/Cu(111) for photon energies ranging from 20 eV to 100 eV, along the* Γ*-K direction, with linear horizontal light polarization. The relative band intensities vary strongly with photon energy. A higher intensity corresponds to a whiter hue. The three main observed bands attributed to the surface are represented on the first image by green, blue and orange dashed lines respectively.*

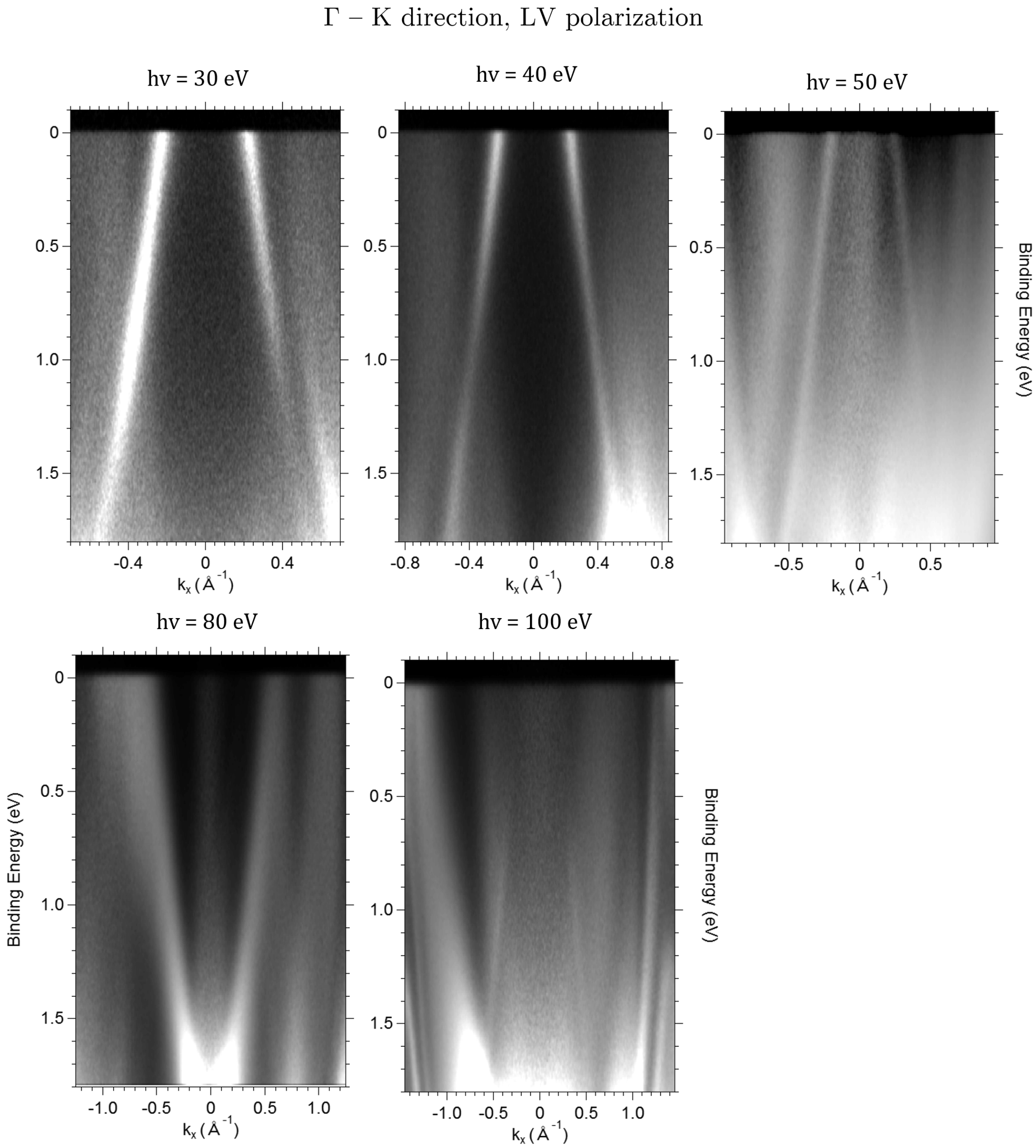

$\Gamma - K$ direction, LV polarization

hv = 30 eV

hv = 40 eV

hv = 50 eV

hv = 80 eV

hv = 100 eV

Fig. 4.12 – *ARPES of Ge/Cu(111) for photon energies ranging from 30 eV to 100 eV, along the* Γ*-K direction, with linear vertical light polarization. The relative band intensities vary strongly with photon energy. A higher intensity corresponds to a whiter hue.*

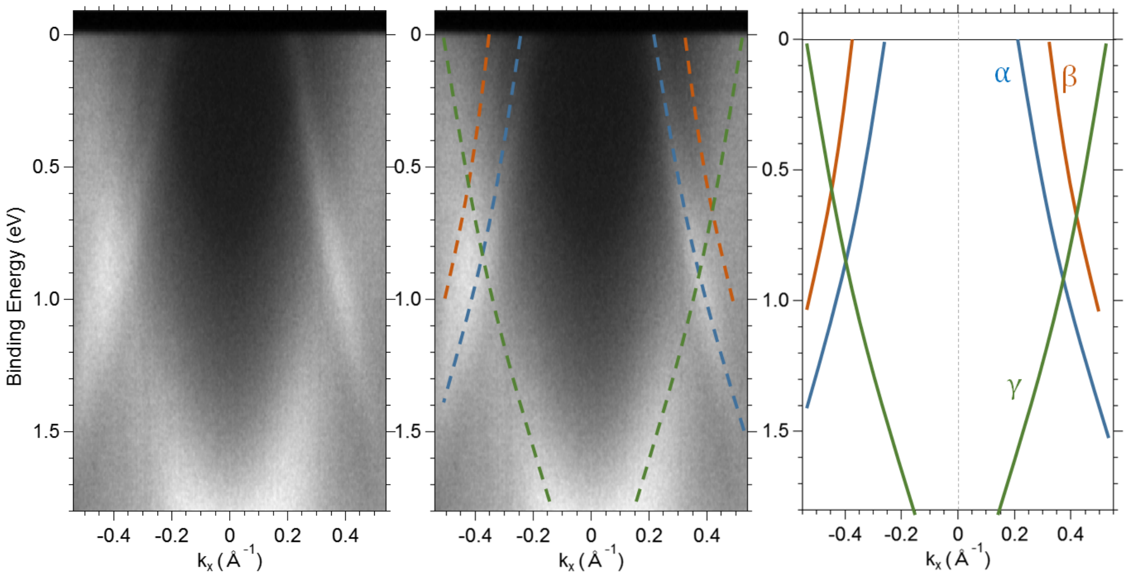

Fig. 4.13 – *The ARPES spectrum of Ge/Cu(111) at hv = 20 eV with LH polarized light is presented again. Left: as is. Middle: with a schematic representation of the three bands observed attributed to the surface drawn over. The bands are labelled* α, β *and* γ *and are represented by a blue, orange and green line respectively, and are presented alone on the right.*

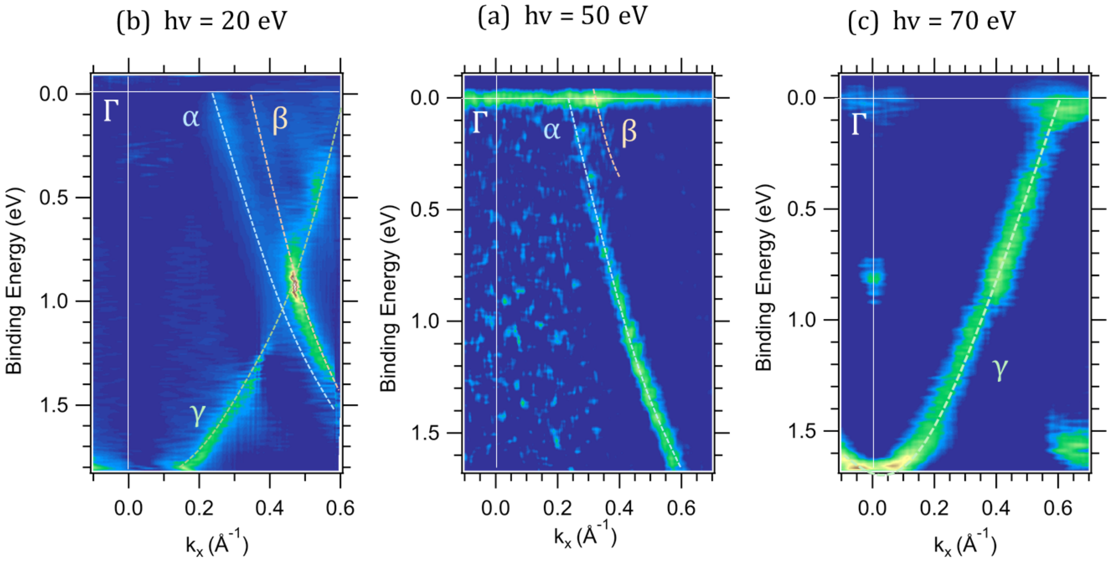

Fig. 4.14 – *2D curvature images from selected spectra presented in Figure 4.11, along the* Γ-*K direction. The plots have been resized for a better visualization of the bands continuity. (a) hv = 20 eV. All three bands* α, β *and* γ *are seen. (b) hv = 50 eV, the* α *band is clearly observed.*
(c) hv = 70 eV, here only the γ *band is seen. From these images, it appears that all bands are continuous (non-gaped).*

Fermi level at $\alpha : 0.22 \pm 0.01$ Å^{-1}, $\beta : 0.32 \pm 0.02$ Å^{-1} and $\gamma : 0.55 \pm 0.05$ Å^{-1}. All these bands lie in the first Brillouin zone of Cu_2Ge, which forms a hexagon with dimensions Γ-M = 0.861 Å^{-1} and Γ-K = 0.994 Å^{-1}, using the theoretical lattice parameters. The varying uncertainties come from the observed sharpness of the bands, the γ band being much larger than the other two. The measurement of the Fermi vectors led to similar results at every photon energy where the α, β, γ bands could be identified, with the variations of values showing no trend and being within the error margin. Equivalent values are also found from the measurement of the Fermi surface. Two Fermi surfaces, one measured with hv = 50 eV and the other measured with a He II source (hv = 40.8 eV), are presented in Figure 4.15 and Figure 4.16 respectively. The use of He II was favoured over He I for the reasons explained in subsection 3.2.1. On those two figures, bands corresponding to DFT calculations for freestanding Cu_2Ge are superposed to the ARPES spectra. In both cases, the α and β bands are nicely replicated by the experiment, while the γ band is either not observed or out of the measurement range.

The absence of dispersion with varying photon energy is equivalent to having a null k_z dispersion, indicating a truly 2D system (see Equation 2.6). The observed bands are in excellent agreement with the DFT calculations of freestanding Cu_2Ge [2], strengthening again the evidence of the experimental realization of Cu_2Ge. The main difference is the energy at which these bands cross: we observe the crossing of the α and γ bands around 0.75±0.1 eV and the crossing of the β and γ bands around 0.55±0.1 eV, while the DFT predicts 0.6 eV and 0.4 eV respectively. We should note the large uncertainty regarding the precise crossing point of the bands, mainly due to the lack of sharpness of the γ band, and to the small asymmetry observed between the right-hand side and left-hand side of the spectra. Even taking into account those uncertainties, it appears that the bands cross each other 0.15 eV deeper in energy compared to the predictions. Noticing that the distance separating the two crossings is coherent with the DFT calculations, we explain those discrepancies by a vertical shift of the bands, induced by a charge transfer from the Cu(111) substrate to the surface layer. The same phenomenon was observed for $Cu_2Si/Cu(111)$ [3] and reproduced in our experiments.

The measurements from this chapter were obtained from two synchrotron beam-

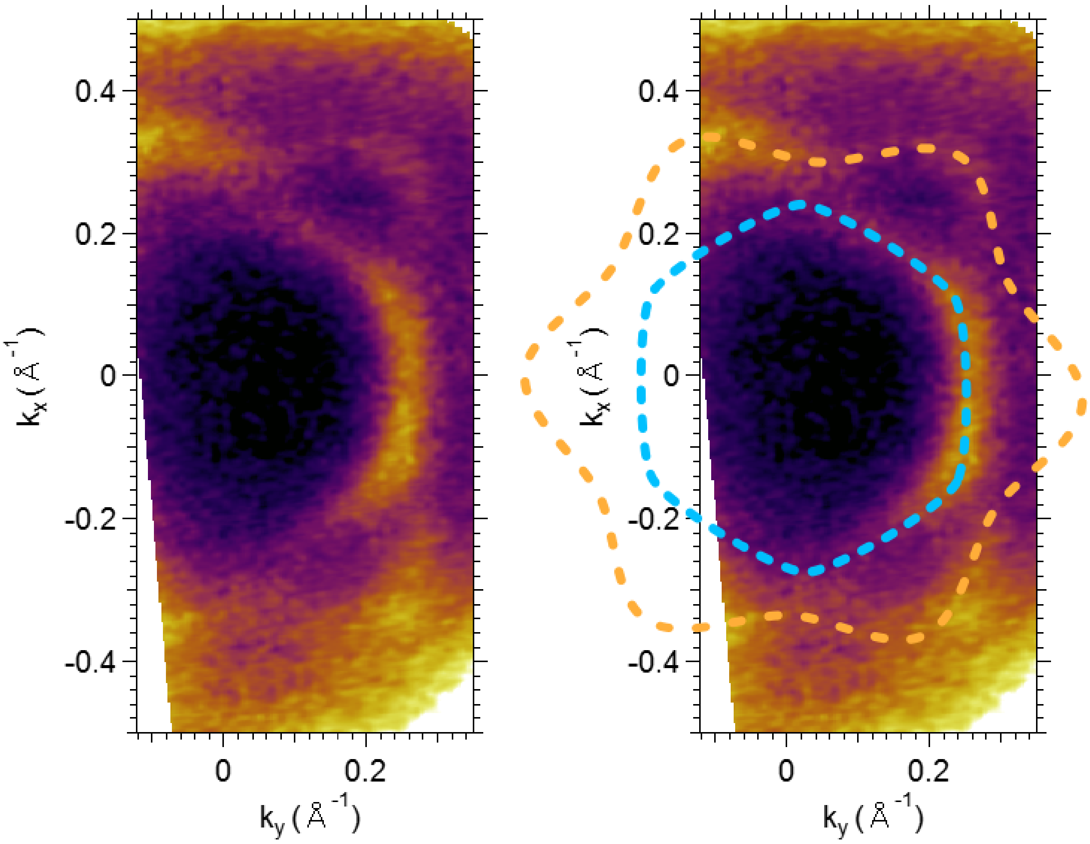

Fig. 4.15 – *Fermi surface of* Cu_2Ge *on Cu(111) measured with hv = 50 eV, in the first Brillouin zone, centered on* Γ *and LV polarized light. The schematic of* α *and* β *bands predicted for freestanding* Cu_2Ge *are superposed to the spectrum in the right image. The* α *forms a blue hexagon, the* β *band an orange hexagram. While the* γ *band does not seem to be visible at this photon energy, the measured spectrum shows an excellent match with* α *and* β *bands, both in shape and Fermi vectors. The* Γ*-K direction correspond here to* k_y *axis, and the* Γ*-M direction to the* k_x *axis.*

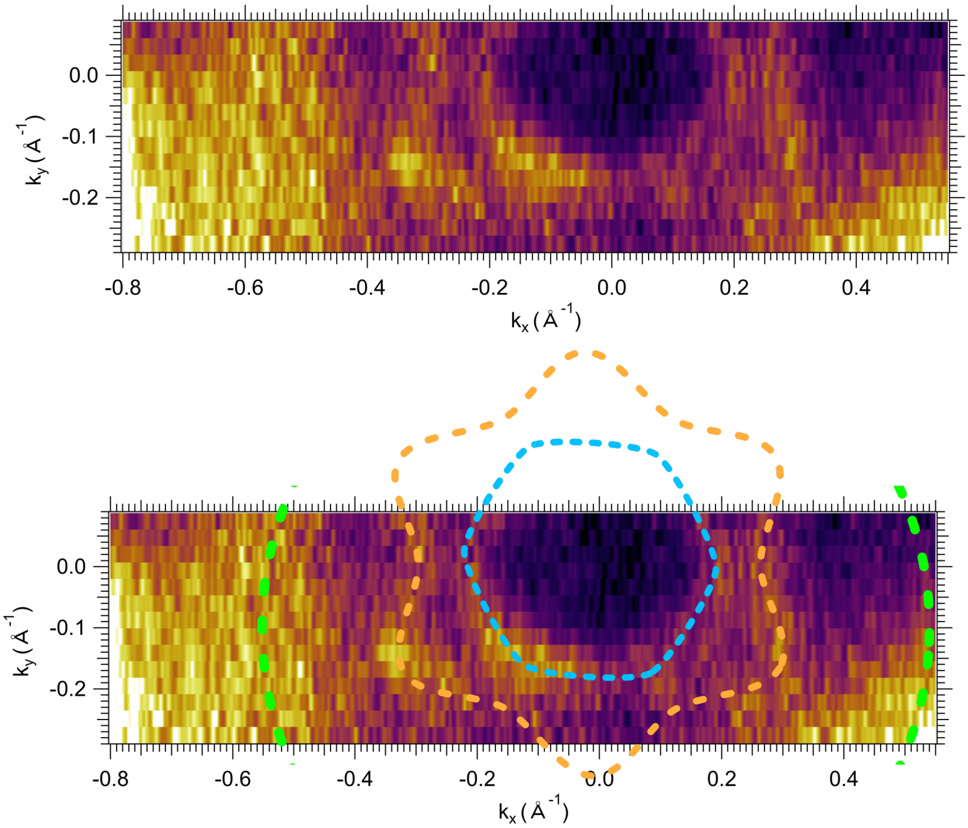

Fig. 4.16 – *Fermi surface of Cu_2Ge on Cu(111) measured with He II, in the first Brillouin zone, with* Γ *at (0,0). The schematic of* α, β *and* γ *bands predicted in freestanding Cu_2Ge are superposed to the spectrum in the bottom image. The* α *forms a blue hexagon, the* β *band an orange hexagram and the* γ *band a green circle (truncated to two arcs here). While the* γ *band does not seem to be distinguishable at this photon energy, possibly due to the high background, the measured spectrum shows an excellent match with* α *and* β *bands, both in shape and position. The* Γ*-K direction correspond here to* k_y *axis, and the* Γ*-M direction to the* k_x *axis.*

lines. Cu 2p, Ge 2p and He II measurements were made on the Tempo beamline of Soleil synchrotron, while Ge 3d and all the other ARPES spectra were acquired on the UARPES beamline of Solaris synchrotron.

4.2.5 DFT comparison between $CuGe_2$, Cu_2Ge and CuGe

While all previous experimental results are in agreement with what is expected of a freestanding Cu_2Ge monolayer, the absence of stoichiometric characterization of the surface raises an important issue: can we be certain that the surface is indeed Cu_2Ge, or could it be $CuGe_2$, pure Ge, or any other alloys of Ge and Cu?

The possibility of pure Ge is dismissed from the outset. Indeed, monolayer Ge (i.e. germanene) is predicted to be a buckled sheet exhibiting Dirac cones [18], and bi-layer Ge islands grown on Cu(111) also exhibit Dirac cones [8], which is not what we observe here by ARPES. The XPS spectra Cu 2p also showed that we have Cu on the surface. More complicated alloys in the form of Cu_xGe_y with x or $y \neq 2$ do not appear in the literature, but we can safely assume that they would not result in a $(\sqrt{3} \times \sqrt{3})$R30° reconstruction as observed by LEED, and might additionally display more complex XPS spectra. The possibility of $CuGe_2$ is however worth investigating, especially as we will see in the next part that it is one proposed stoichiometry for the growth of Cu/Ge(111). Additionally, a CuGe honeycomb structure would also fit the criteria derived from LEED and XPS.

First-principles calculations were realized on these structures, resulting in the band structure presented in Figure 4.17 along their atomic model, with the Cu_2Ge band structure given as a comparison, reproducing with good precision the work of Liu *et al.* [2].. For the hexagonal $CuGe_2$ monolayer, the band dispersion obtained is very different from the one of monolayer Cu_2Ge. Focusing on the first 2 eV below the Fermi level, we notice the presence of only two bands, both having a local maximum at Γ close to the Fermi level and one of them having almost flat dispersion in the Γ-M direction. These bands are reminiscent of the band structure of clean Ge(111), as presented in the next section, or in the existing literature [19–22]. No band with a local minimum at Γ is observed, as is the case of the γ band in Cu_2Ge and in our experimental observations. From this, we can exclude $CuGe_2$ as a system potentially characterized in the above experiment. Interestingly, the honeycomb monolayer CuGe shows a closer resemblance to Cu_2Ge. The α, β and γ bands are identified and cross each other. The relative positions of the α and β bands is however dissimilar. Indeed, in the case of Cu_2Ge, they are close to each other and parallel in the direction $\Gamma - K$, in agreement with the ARPES measurements. However for CuGe, their separation is larger, especially in the $\Gamma - M$ direction, and does not match the E-k_x maps or Fermi surface measurements. The existence of nodal lines in honeycomb CuGe appears worth investigating, as well as its growth, as it does not appear in the literature.

The first-principle calculations were done using the software *Winmostar^{TM} V10* (X-Ability Co. Ltd.), providing tools to run Quantum Espresso [23, 24]. The $CuGe_2$ monolayer is modelled by a P6/mmm space group crystal, with vector sizes a = b = 4.214 Å similar to the ones found for Cu_2Ge, and the vertical spacing between plans is set as c = 30 Å, which is a suitable distance for simulating two-dimensional materials. For the honeycomb CuGe, the same lattice parameters were used. A plane-wave basis is employed with a kinetic energy cutoff of 100 Ry, a charge density cutoff of 400 Ry, and the k-space integration was done using 17x17 meshes in the 2D Brillouin zone. To determine the optimal lattice parameters, all atoms were allowed to relax along with the calculated forces with a total energy convergence threshold of 10^{-6} Ry and a force convergence threshold of 10^{-6} Ry. A Gaussian smearing of 0.011 was used. Within the generalized gradient approximation of the PBE exchange-correlation potential [25], we chose the projector augmented wave method Ge-PBE-kjpaw and Cu-PBE-kjpaw potentials, available from PSlibrary [26].

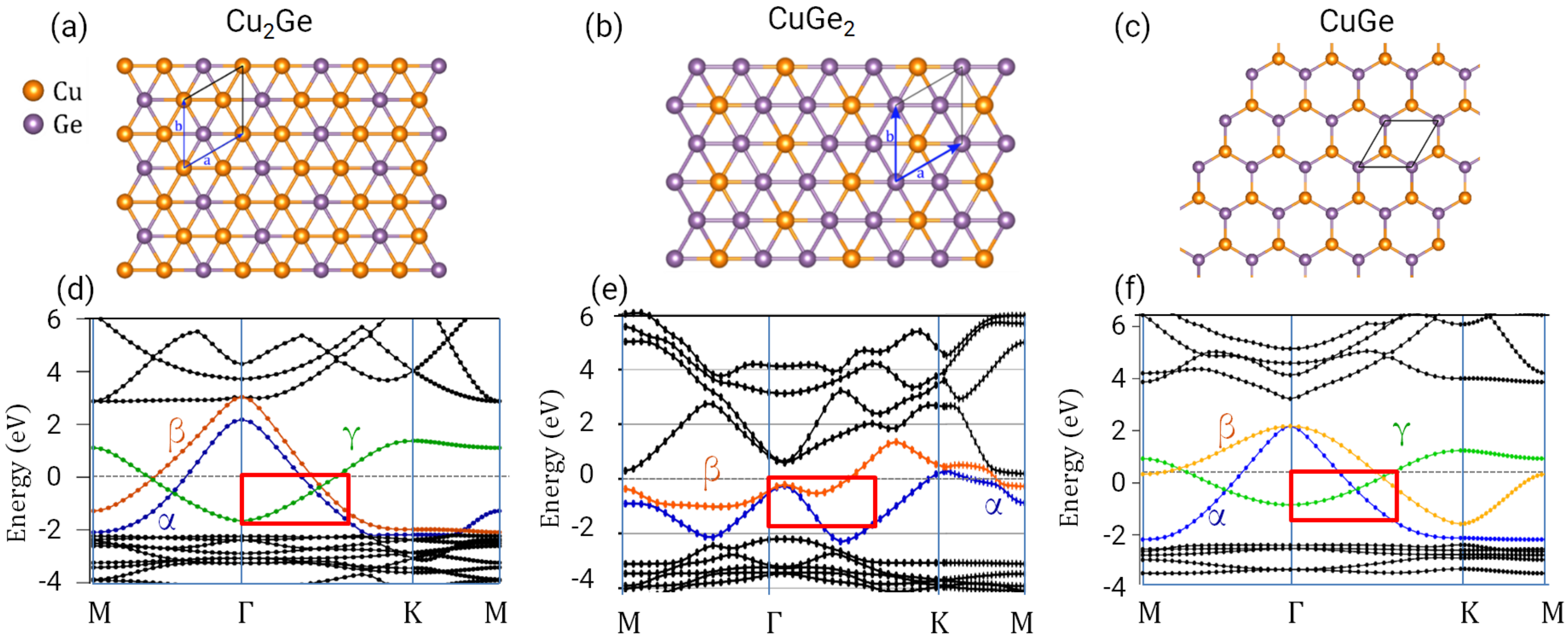

Fig. 4.17 – *(a)-(c) Atomic structure of Cu_2Ge, $CuGe_2$ and CuGe monolayers and their associated band structure (d)-(f) obtained from DFT calculations. The red rectangle represents the area measured by ARPES presented earlier.*

4.2.6 Conclusions about Cu_2Ge on Cu(111)

The growth of Ge on Cu(111) has been studied in an attempt to make the first experimental realization of the Dirac nodal loop semimetal Cu_2Ge. In the previous pages, we described the observation of a $(\sqrt{3} \times \sqrt{3})$R30° LEED pattern and of a single adsorption site of Ge atoms by XPS, which is coherent with the Cu_2Ge monolayer atomic model. More importantly, the presence of the three electronic bands α, β and γ by ARPES, none of them being gaped within our experimental resolution, are in good agreement with the band structure calculated from DFT for a freestanding Cu_2Ge monolayer. We also ruled out the possibility of a Ge, CuGe or $CuGe_2$ layer.

By comparing our experimental results to the expected properties of freestanding Cu_2Ge obtained from simulations [2], we posit to have successfully synthesized Cu_2Ge, with interactions with its Cu(111) substrate weak enough to not disturb or gap the DNLs. This is one of the few two-dimensional DNLs experimentally observed.

It is also the experimental realization of one of the newly predicted 2D binary compounds with copper. For now, three amongst them have been predicted to host Dirac nodal-lines: Cu_2Si, Cu_2Ge and CuSe. The first two appear to preserve their DNL structure when using a Cu(111) substrate, while CuSe/Cu(111), presenting a honeycomb structure, has been shown to display gaps at the DNLs [27]. To pursue towards applications, the main challenge to overcome is now the preparation (or transfer) of Cu_2Ge on a non-conductive substrate. It is with this aim in mind that we will present in the next section a study mirroring this one, focusing on the growth of Cu/Ge(111) and the characterization of the surface obtained.

4.3 Atomic and electronic structure of the discommensurate (“8.88 x 8.88”) R30° phase of Cu/Ge(111)

4.3.1 The growth process of Cu/Ge(111)

Germanium is one of the most used and abundant semiconductor element after silicon. It can be commercially bought in the shape of wafers and cut along the desired crystallographic orientation. For this study, we used hexagonal Ge(111) wafers. All preparations were realized in UHV with a base pressure in the low 10^{-10} mbar range. In order to remove the native oxide layer and clean the surface of Ge(111), cycles of Ar^+ sputtering followed by annealing were performed, as is common in the literature [28–32]. One cycle consists of 20 min of Ar^+ sputtering at 1 kV with the Ge(111) kept at 450°C, followed by a 10 min annealing up to 750°C and a slow cooling down ($\approx$ 15 min) to room temperature. 5 cycles of sputtering/annealing are necessary to remove most of the native oxide when the wafer is new, one cycle is sufficient to refresh the surface once the sample has already been prepared and stayed in UHV. This method of preparation leads to the well-known c(2×8) surface reconstruction of Ge(111), already identified since 1981 [33], and determined to be the most stable surface reconstruction of Ge(111), before the (2×2) and c(4×2) with which it can coexist. The LEED picture of the c(2×8) surface reconstruction of Ge(111) is shown in Figure 4.18a, and agrees with the expected diffraction pattern [29]. To optimize the diffraction pattern, the most important parameter is the temperature reached during annealing: too low and the LEED pattern is not clearly resolved, too high and the Ge might melt.

Once the Ge(111)-c(2×8) surface is obtained, copper is evaporated on top from an e-beam evaporator, while keeping the Ge substrate at 250°C, until a (“8.88×8.88”)R30° LEED pattern is observed, as shown in Figure 4.18b. From the e-beam evaporator calibration, the maximum amount of Cu deposited on the surface for a LEED optimized image corresponds to 0.5 ML. This would hint towards a $CuGe_2$ surface stoichiometry, in line with the saturation coverage observed by Zengenhagen *et al.* [10].

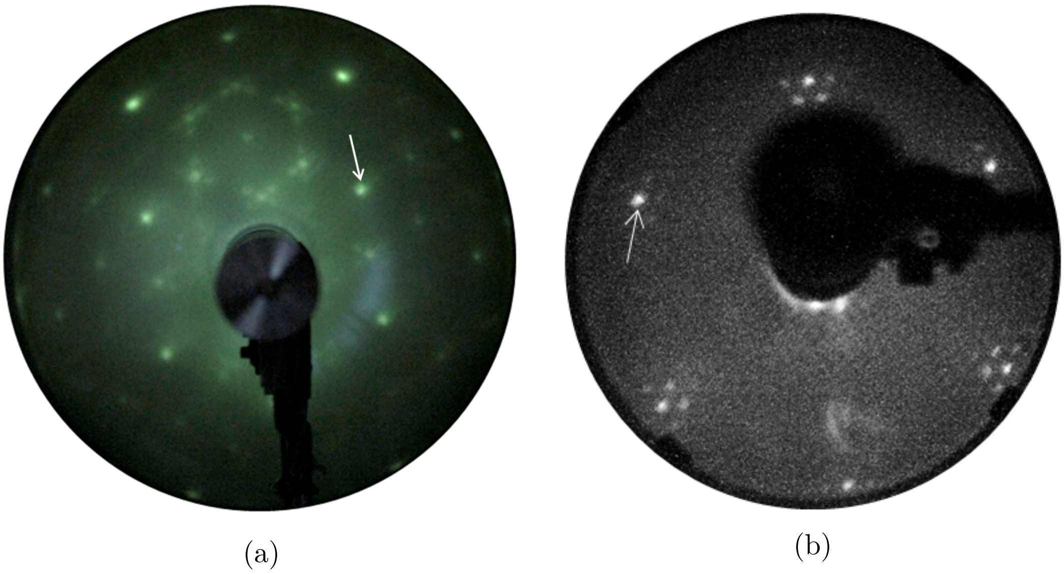

(a) (b)

Fig. 4.18 – *(a) LEED picture of Ge(111)-c(2×8) surface reconstruction, taken at 120 eV. (b) Discommensurate ("8.88 × 8.88")R30° surface reconstruction of Cu/Ge(111), taken at 150 eV. The white arrows points to a (1×1) diffraction spot of the Ge bulk.*

4.3.2 Atomic structure characterization by STM

The Ge(111)-c(2×8) and the Cu/Ge(111)-("8.88×8.88")R30° surface reconstructions were studied by scanning tunnelling microscopy. In our setup, a positive voltage means that the electrons flow from the tip to the sample, mapping the empty electronic states. All measurements were made at room temperature. The clean Ge(111) surface and the c(2×8) reconstruction have already been extensively studied by STM with excellent results [28, 34, 35]. The consensual atomic model, consisting of adatoms and rest atoms (i.e. surface layer atoms not bonded to adatoms), is presented in Figure 4.19. Domains of (2×2) surface reconstruction have also been observed coexisting with the c(2×8) and disordered domains. We present in Figure 4.20 images of the c(2×8) surface reconstruction, at 2 V and 250 pA (empty states). On the larger scale image, we see the characteristic rows of dimers forming different domains separated by disorganised borders. The smaller-scale images show the adatoms, with a c(2×8) unit cell measuring 8 Å×30 Å, represented by a parallelogram overlayed. Two different phases are observed: in Figure 4.20b adatoms present an asymmetric form, with some higher than others, while in Figure 4.20c they all show the same height. Those two phases are already described in the literature [34] and can coexist on a surface. The observation of the Ge(111) surface was used to check the cleanliness and crystalline organisation of the sample surface to further optimize the preparation parameters. It was also used to calibrate the STM x-y-z scales, ensuring an adequate calibration for the following measurements of less well-known structures.

After evaporation of Cu on the surface, a hexagonal superstructure starts to appear, corresponding to the (“8.88×8.88”)R30° surface reconstruction. We observed that the (“8.88×8.88”)R30° domains grow at the foot of the steps and as flat islands first, as illustrated by Figure 4.21 which shows a surface on which the amount of Cu deposited is not sufficient to cover entirely the Ge terraces. We measured the height of the different domains, which we will label as “Ge” for the Ge terraces and as “CuGe” for the superstructure domains. We found $\Delta_{Ge-CuGe} = 1.9 \pm 0.1$ Å, and $\Delta_{CuGe-Ge} = 1.4 \pm 0.1$ Å , with a sum of height being in agreement with the theoretical size of an atomic Ge step of 3.26 Å. The error bars were determined as the standard deviation on many step height measurements. The superstructure induced by Cu deposition adds height to the Ge terrace, but stays lower than a full atomic plan. While most islands have a height of 0.19 Å above the surrounding Ge terrace, some islands have been observed to lie one or two atomic plans above the Ge terrace. Some domains with the superstructure can be seen residing lower than the surrounding Ge terrace, and often near higher superstructure islands. As the superstructure is an alloy made of Cu and Ge atoms, we suspect that the formation of superstructured islands can “drain” surrounding Ge atoms, thus creating holes in which Cu atoms will deposit and form their own superstructure there.

Increasing the Cu surface coverage leads to large areas covered by the superstructure. We show in Figure 4.22a an almost entirely covered surface, with a zoom-in in Figure 4.22b, both measured at 2 V, 250 pA. The unit lattice of the superstructure is drawn on top, and its measured dimension is 35±1 Å in both directions. The lattice parameter of Ge(111) being of 4 Å, the superstructure measured is in agreement with the (“8.88×8.88”)R30° model proposed by Böhringer *et al.* [9] presented in section 4.1, which should lead to a 35.5Å lattice parameter. We recall here that this superstructure is quasi-commensurate domains of Cu and Ge atoms separated by domain walls. With a bias below 2 V and at smaller scales, it is possible to obtain the atomic resolution of those domain walls, as shown in Figure 4.23. Those domain walls form double rows, arranged in zig-zag patterns.

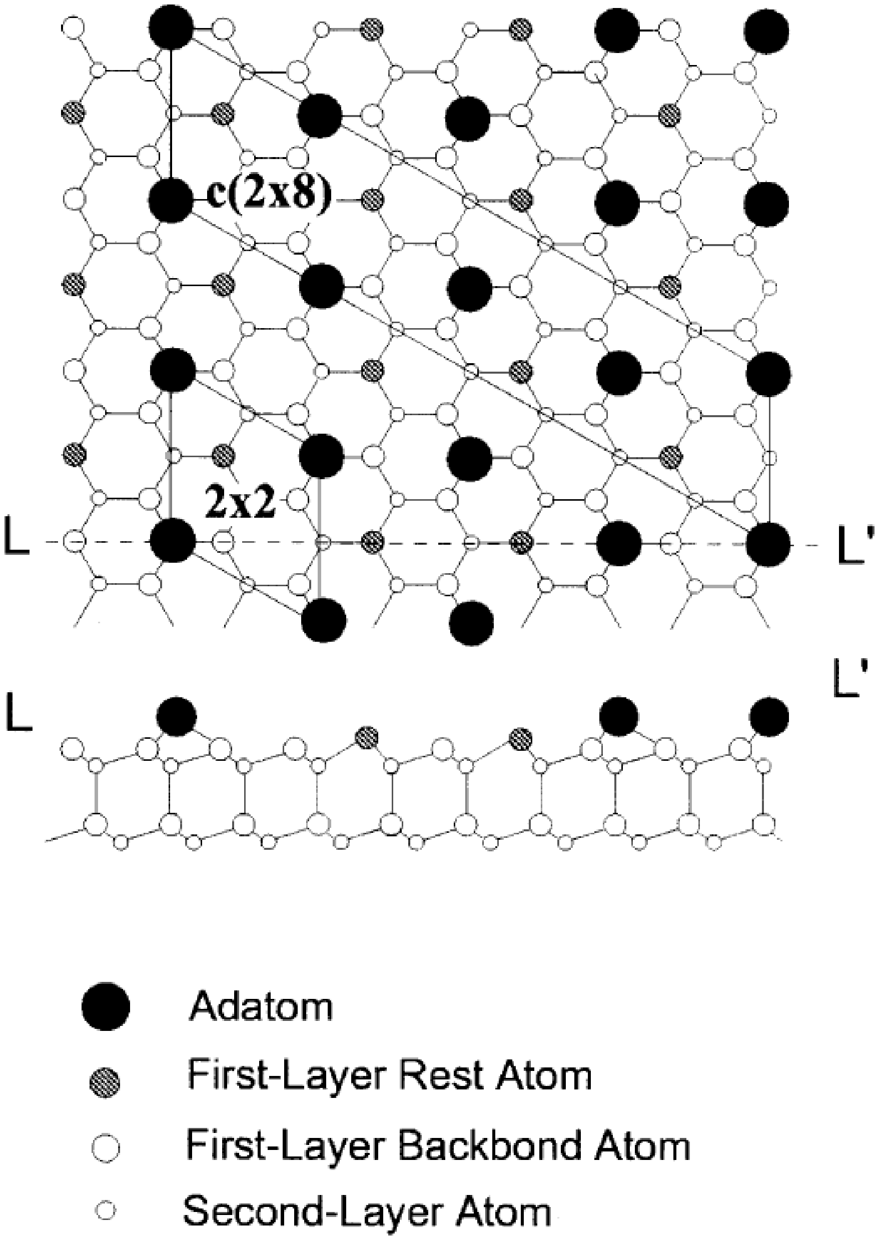

Fig. 4.19 – *Ball-and-stick model of the* $\mathrm{Ge}(111) - c(2\times8)$ *surface in the top view and side view (cut along the line LL’). Adatoms, first-layer atoms, and second-layer atoms are shown by large black circles, medium-sized circles (shaded for rest atoms, whites for backbond atoms) and small white circles, respectively. A* (2×2) *and a conventional* $c(2\times8)$ *unit cells are also drawn. Figure and caption from [35].*

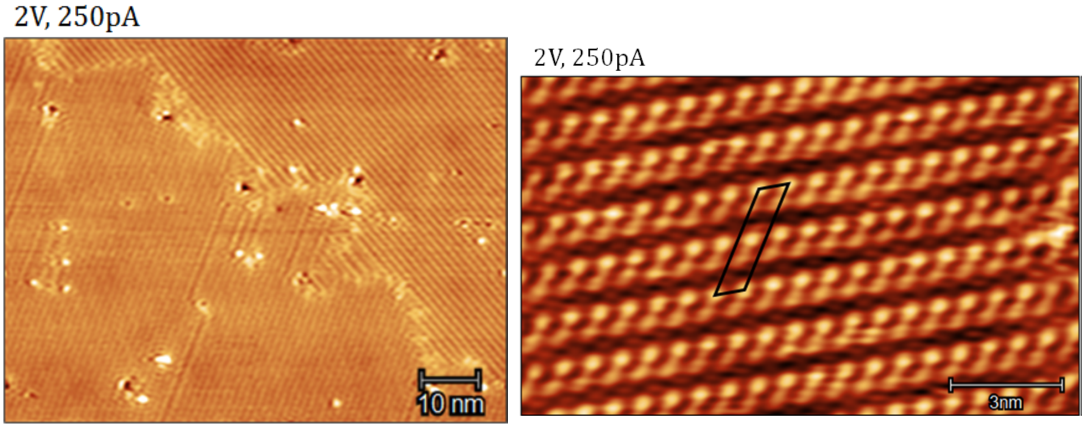

(a) *Large scale image of the Ge(111)-c(2×8) surface*

(b) *Asymmetric c(2×8)*

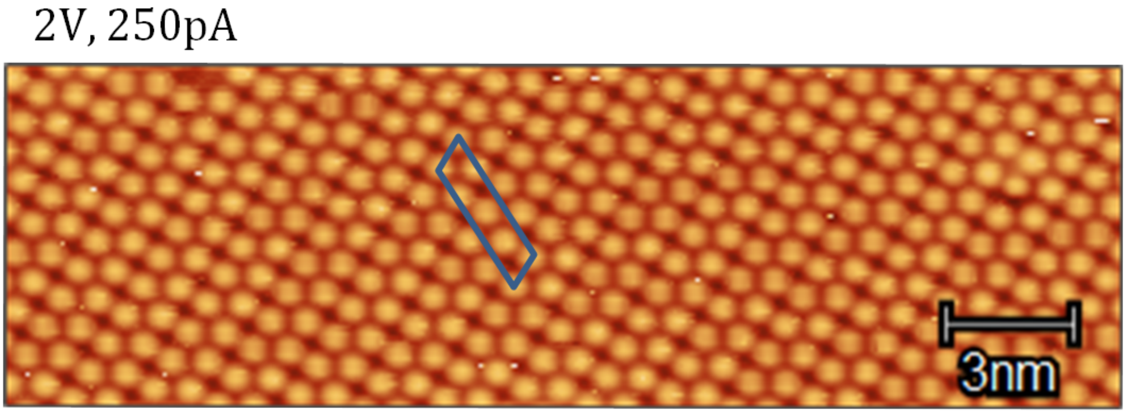

(c) *Symmetric c(2×8)*

Fig. 4.20 – *Ge(111)-c(2×8) surface, measured at 2 V, 250 pA (empty states). (a) 90 nm×60 nm. The characteristic rows are well visible, and different domains are seen. (b) Asymmetric phase of the c(2×8), where all adatoms do not have the same apparent height. 15 nm×9 nm. (c) Symmetric phase of the c(2×8), where all adatoms have the same apparent height. 26 nm×8 nm. In (b) and (c), the c(2×8) unit cell is drawn on top, and measures 8 Å×30 Å.*

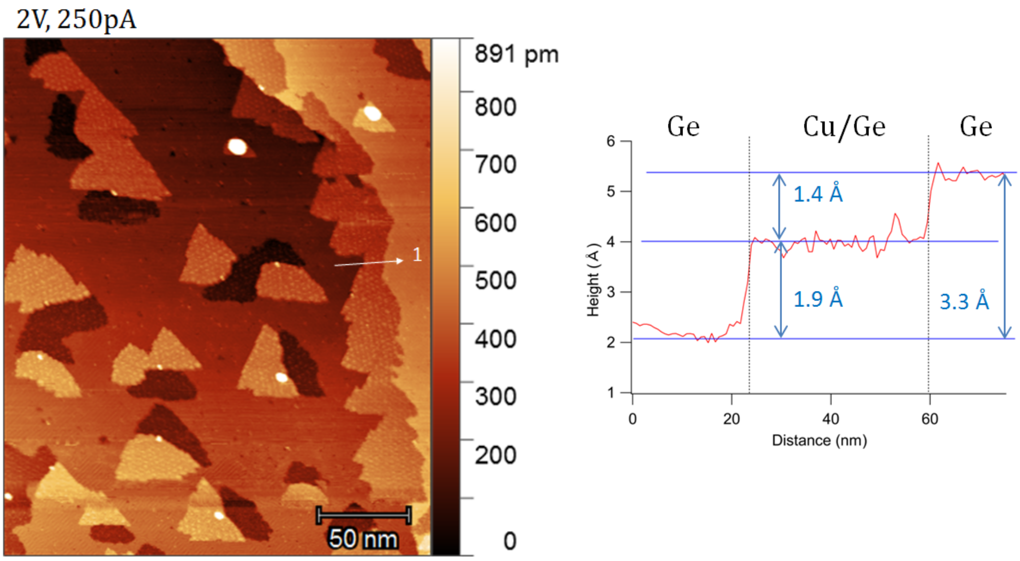

Fig. 4.21 – *For low Cu coverage, the hexagonal superstructure corresponding to the (“8.88×8.88”)R30° reconstruction forms preferentially at the foot of atomic steps, or forms islands, leaving parts of the Ge terraces uncovered. From the cut indicated by a white arrow whose profile is on the right, the apparent height of the superstructure is 1.9 Å above the Ge terrace and 1.4 Å below the next.*

In Figure 4.23 (a), on the top right of the image we can see a Ge terrace, with an intermixing of c(2×8), (2×2) and disordered areas. The others areas are covered by the superstructure. Once again, the superstructure unit cell is represented. In Figure 4.23 (b) is presented a zoom-in insert from (a) of the domain walls, where the zig-zag arrangement is visible. In Figure 4.23 (c), the atomic resolution inside of the superstructure is achieved, measured at 150 mV and 1 nA (empty states). Despite being noisy, the periodicity observed, measured using a fast Fourier transform (Figure 4.24) is 4.3±0.1 Å, in good agreement with the 5% expansion compared to Ge(111) (1×1) described by Böhringer *et al.* [9], resulting in a 4.2 Å parameter.

This STM work confirmed the previous observations of Böhringer *et al.* [9] of the Cu induced (“8.88×8.88”)R30° surface reconstruction on Ge(111). A discommensurate superstructure forms with an overall periodicity 8.88 larger than the Ge(111) unreconstructed surface. This superstructure is locally quasi-commensurate, and forms domains separated by walls. We note that it is the first time that the domains are resolved atomically at room temperature, even though it was not expected

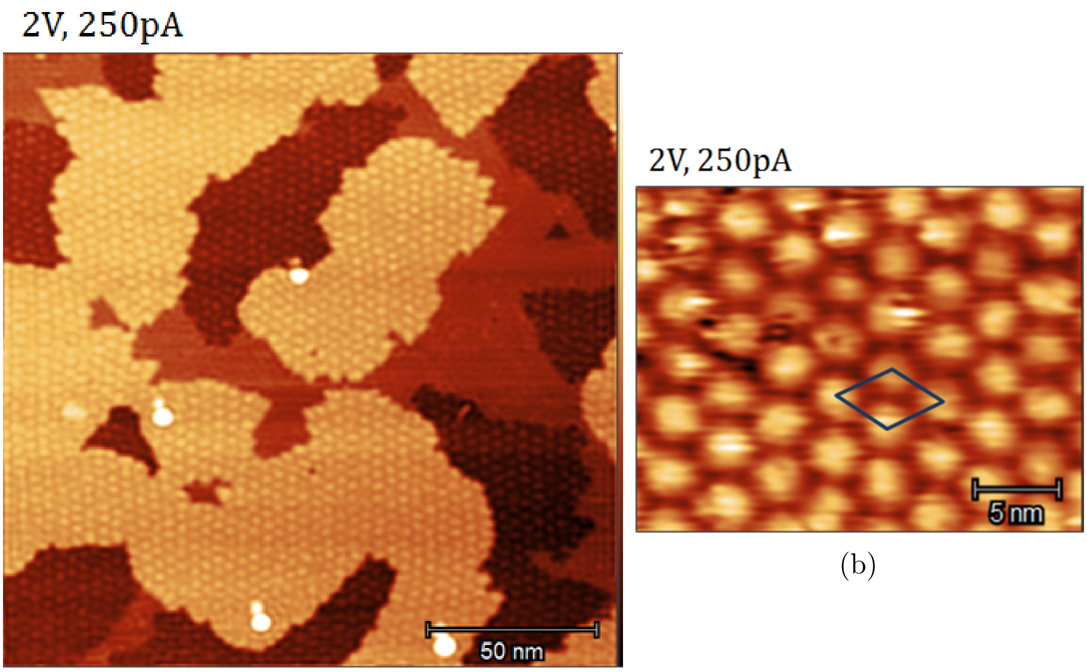

(a)

(b)

Fig. 4.22 – *STM images of the ("8.88×8.88")R30° superstructure. (a) The surface is almost entirely covered by the Cu induced superstructure. The islands formed at lower coverage merged together forming terraces. 175 nm×170 nm. (b) Detailed image of the superstructure. In these conditions, the internal atomic arrangement cannot be resolved. The unit lattice of the superstructure is drawn on top, and measures 35 ±1 Å in both directions, in good agreement with the proposed 8.88 periodicity. 26 nm×20 nm, empty states.*

to be possible at room temperature due to the high atomic mobility and possible site exchanges of the Ge and Cu atoms forming the reconstruction. We remark however the difficulty to obtain stable images in those conditions. Now that the atomic structure of our system is understood, it would be interesting to study its electronic properties. Furthermore, the surface stoichiometry is still undetermined, with Cu_2Ge and $CuGe_2$ being the main contenders, making it difficult to predict its electronic properties.

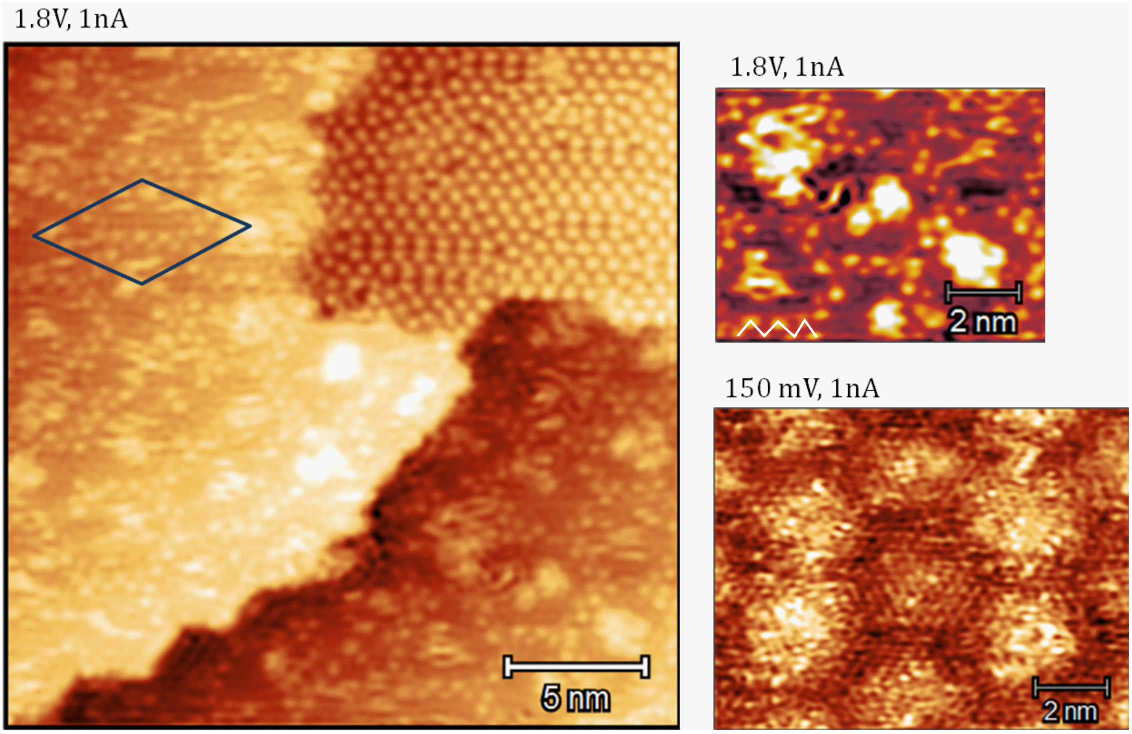

Fig. 4.23 – *STM images of the Cu/Ge-(“8.88× 8.88”)R30° surface. Left: the walls separating each domain of (“8.88×8.88”)R30° are visible. They are formed of double rows with an alternating arrangement (i.e. a zig-zag pattern). The unit cell is drawn on top, with its corners on the centers of domains. On the top right corner of the image, a Ge terrace is visible, with mixed phases of (2×2), c(2×8) and disorganized areas. 25×25 nm, 1.8 V, 1 nA. Top right: insert from the left image, focusing on the domain walls contrast. One of the domain walls is drawn over with a white zig-zag line. The inside of the domains is not resolved. Bottom right: atomic resolution inside the superstructure, for the first time resolved at room temperature. The atomic distance is measured at 4.3±0.1 Å. 10×8 nm, 150 mV, 1 nA. All three images probe the empty states.*

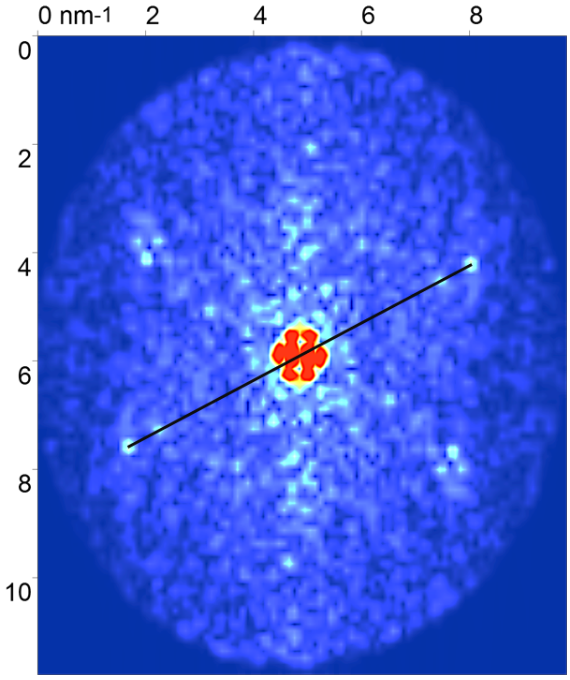

Fig. 4.24 – *2D fast Fourier transform of the atomically-resolved ("8.88×8.88")R30° superstructure shown in Figure 4.23 (c). The distance between the most intense points indicates a periodicity of 4.3±0.1 Å, slightly higher (5-10%) than bulk Ge (1×1).*

4.3.3 XPS study

4.3.3.1 XPS on clean Ge(111)-c(2×8)

We start by measuring the core levels spectra of the clean Ge(111) substrate. The Ge 3d core-level of the clean Ge(111)-c(2×8) was measured at three different photon energies (hv = 80 eV, 180 eV and 280 eV). The fitted spectra are presented in Figure 4.25, with the contributions observed attributed to the atomic model presented above. All spectra were analyzed with four spin-orbit doublets, one of which corresponds to the bulk Ge (labelled B), and three others to surface components (labelled S1, S2, S3), none of which can be attributed to an oxide species. The assignation of the bulk component is justified by the increase of relative area with probed depth (i.e. photon energy) compared to the relative area diminution of the other components. The positions of the surface peaks, relative to the bulk peak, are as follows: ΔB-S1 = -0.26 eV, ΔB-S2 = -0.75 eV, ΔB-S3 = +0.17 eV. Those relative positions are given at ±0.01 eV, corresponding to the variation observed between the peaks' relative positions in the different fits. The spin-orbit splitting between the $3d_{5/2}$ and $3d_{3/2}$ peaks is found to be $\Delta_{SO} = 0.58$ eV in agreement with the tabulated values, and the branching ratio was fixed at 0.66. As the surface does not appear metallic (see ARPES results in subsubsection 4.3.4.1), all peak shapes used are Voigt functions, with a FWHM of 0.12 eV and a Gaussian broadening of 0.31 eV with variations of the order of ± 0.02 eV depending on the photon energy (without any noticeable trend). The background was fitted using an individual Shirley-step function with the same parameters for each peak. Peak width, peak area and Shirley-step height were the only parameters allowed to vary from one spectrum to another, resulting in a very robust fit. This fit is also in good agreement with the existing literature [32, 36]. Each surface component can then be attributed to distinct atomic sites. A model of the atomic structure of Ge(111)-c(2×8) surface is presented in Figure 4.19, consisting of adatoms and rest atoms (i.e. first-layer atoms not bonded to adatoms). Using the work of Göthelid *et al.* [36], the S1 peak can be attributed to first-layer backbond atoms (wide white circles), the S2 peak to the rest atoms (shaded circles) and the S3 peak to the adatoms (large black circles). In the model structure presented above, the second layer atom signal is indistinguishable from the bulk.

4.3.3.2 XPS on the ("8.88 x 8.88")R30° phase of Cu/Ge(111)

XPS spectra of the Ge 3d core level of Cu/Ge(111) are presented in Figure 4.26. The surface, already described above and schematically presented in Figure 4.3, is rather complex and presents many different chemical environments for the Ge atoms. A proper fitting of the spectra recorded is thus rather delicate and was made possible only due to the high-resolution of synchrotron light. We measured the Ge 3d core level for three different photon energies (hv = 80 eV, 180 eV and 330 eV) to gain insight on the origin of the signal and obtain more robust fits. For all cases, the best fit was obtained using six asymmetric Doniach-Sunjic doublets. To ensure a physical grounding of the fits, an array of precautions and constraints were taken. For a given photon energy, Lorentzian FWHM (W_L), Gaussian broadening (W_G) and the Shirley-step background were constrained to be the same for all peaks, with starting parameters based on the clean Ge(111) Ge 3d fits. A broadening of all peaks is observed at hv = 330 eV, explained by a decrease in experimental resolution. The asymmetry parameter used was identical for all peaks (0.026). Those

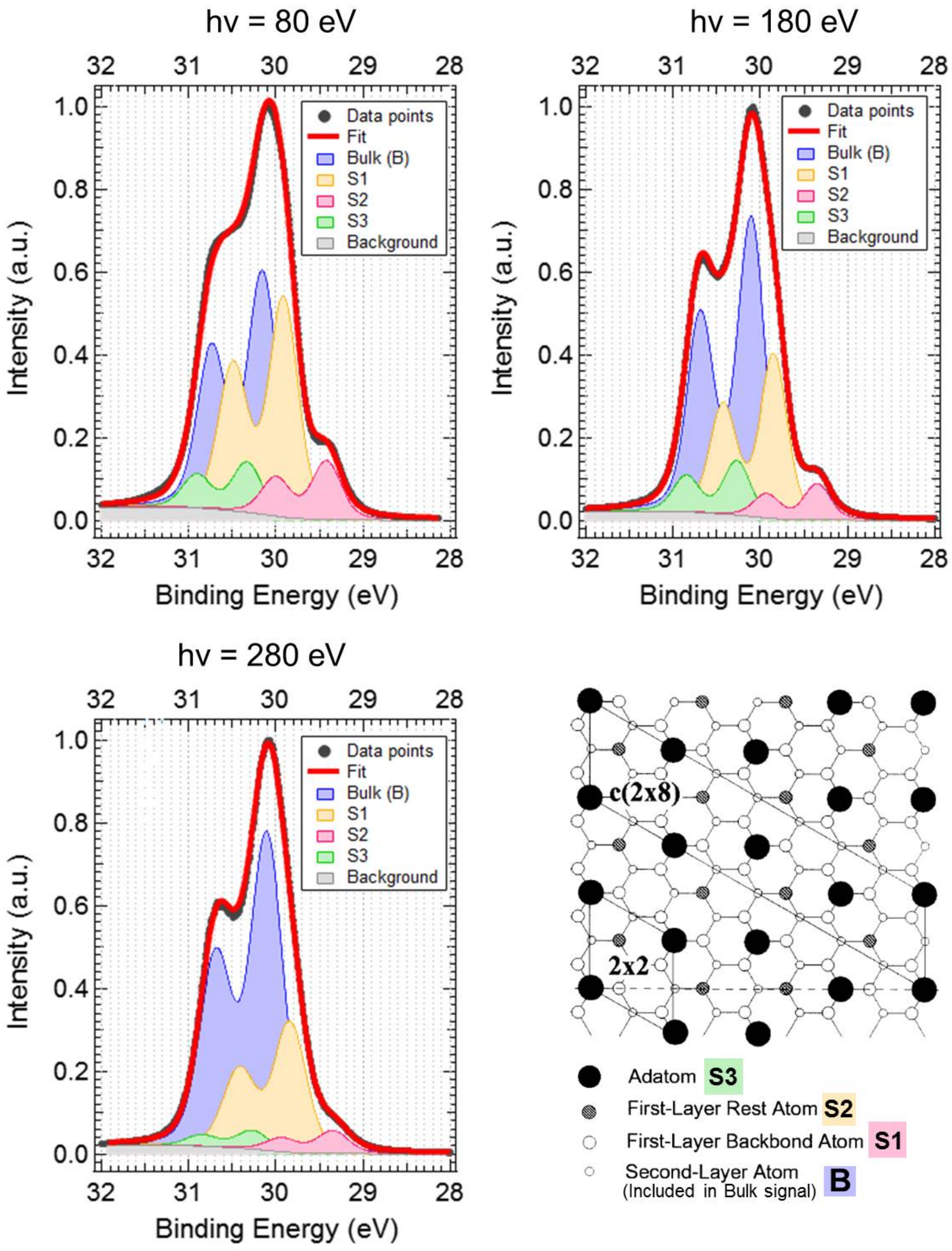

Fig. 4.25 – *XPS spectra of the Ge 3d core level of clean Ge(111)-c(2x8) surface reconstruction, measured at different photon energies. All spectra are fitted by four spin-orbit doublets, one of which corresponds to the bulk (B) and three others to surface components (S1, S2, S3). These contributions are linked to the atomic model of Ge(111)-c(2x8), image from [35].*

parameters are all gathered in Table 4.1a. Finally, we made sure that the relative peak positions were the same for all spectra. These positions are given with respect to the peak labelled as *Peak 1*, in binding energy. The FWHM and relative peak positions are given with a precision of 0.01 eV, corresponding to the variations observed on the different fits.
We will now discuss the origin of the different spectroscopic contributions, some being shown directly on the atomic model in Figure 4.26. We present in Table 4.2 the percentage of the total fitted area occupied by each doublet, for every photon energy used, and comment on their variation for increasing photon energy. Totals might not be of 100% due to rounding errors. We should note that the precision in the determination of peak area is subject to caution, especially with the use of Doniach-Sunjic peaks which extend up to infinity and thus have an area which depends on the energy range selected for the fit window. We estimate the precision to a few % of a given peak own’s area at best.

From 4.2 it is clear that *Peak 1* increases the most with photon energy (i.e. with depth sensitivity). We thus attribute it to the bulk Ge, laying below the three atomic layers forming the surface. *Peak 6*, located at -0.19 eV from *Peak 1*, also increases in area with photon energy. This peak thus does not originates from the topmost atomic layer. Three components (*Peak 2*, *Peak 3* and *Peak 4*) show a decreasing relative area with increasing photon energy, and are thus attributed to surface components. The last component, *Peak 5*, has a too-small relative area change to see a clear variation trend. If we look at the atomic model shown in Figure 4.3, we can identify at least three different chemical environments for Ge atoms in the case of a $CuGe_2$ surface stoichiometry: bulk, last Ge layer (taken into account in the surface stoichiometry), and topmost layer (H_3 sites). In the case of a Cu_2Ge surface stoichiometry, the topmost layer is entirely populated by Cu atoms, there is thus one less chemical environment for Ge atoms. To this we can add the domain walls, even though it is not sure from what element they are constituted. Furthermore, they are not structurally described, so we have no information on a possible multiplicity of contributions. The two different stacking models could also lead to different contributions, however with all first- and second-neighbours being the same for all Ge in both stacking configurations we find it more likely that those differences might not be resolved.

Photon energy	W_L	W_G
80 eV	0.12	0.21
180 eV	0.12	0.24
330 eV	0.12	0.33
Δ_{SO}	0.58 eV	
Branching ratio	0.66	
Asymmetry	0.026	

(a)

	Distance to Peak 1
Peak 2	- 0.41 eV
Peak 3	- 0.66 eV
Peak 4	+ 0.23 eV
Peak 5	+ 0.52 eV
Peak 6	- 0.19 eV

(b)

Table 4.1 – Fitting parameters used for the Cu/Ge(111) Ge 3d core-level. (a) Lorentzian FWHM (W_L) and Gaussian broadening (W_G) are given for all photon energies, along with spin-orbit splitting (Δ_{SO}), branching ratio and Doniach-Sunjic asymmetry parameters that are kept identical for all fits. (b) Peak positions relative to peak 1 are presented, in binding energy.

% of total area	Peak 1	Peak 2	Peak 3	Peak 4	Peak 5	Peak 6
80 eV	15	31	12	6	2	34
180 eV	19	29	9	4	1	38
330 eV	28	22	8	3	1	38
Variation	Increase	Decrease	Decrease	Decrease	Stable	Increase

Table 4.2 – Percentage of the total fit area occupied by each peak for each photon energy. A decrease of area with increasing energy indicates an origin at the surface, while an increase of area indicates an origin in the bulk/below the surface.

Using this information we can attribute *Peak 1* to the bulk and *Peak 6* to the last Ge layer. Looking at the peaks' relative areas, we then attribute *Peak 2* to the topmost layer as its area is the largest of the surface contributions and should originate from the atomic sites hosting more atoms. This assumes a surface stoichiometry of $CuGe_2$. The second-largest area surface contribution is *Peak 3*, and is attributed to the domain walls. We are left with two small contributions, *Peak 4* from the surface, and *Peak 5*, that could be attributed to Ge atoms substituting Cu atoms on the lower surface layer (S_u sites), patches of clean Ge left uncovered, or Ge surface clusters. We note that this attribution of the peaks observed to the atomic structure could be greatly improved by a definitive atomic model and the determination of the surface stoichiometry of this system.

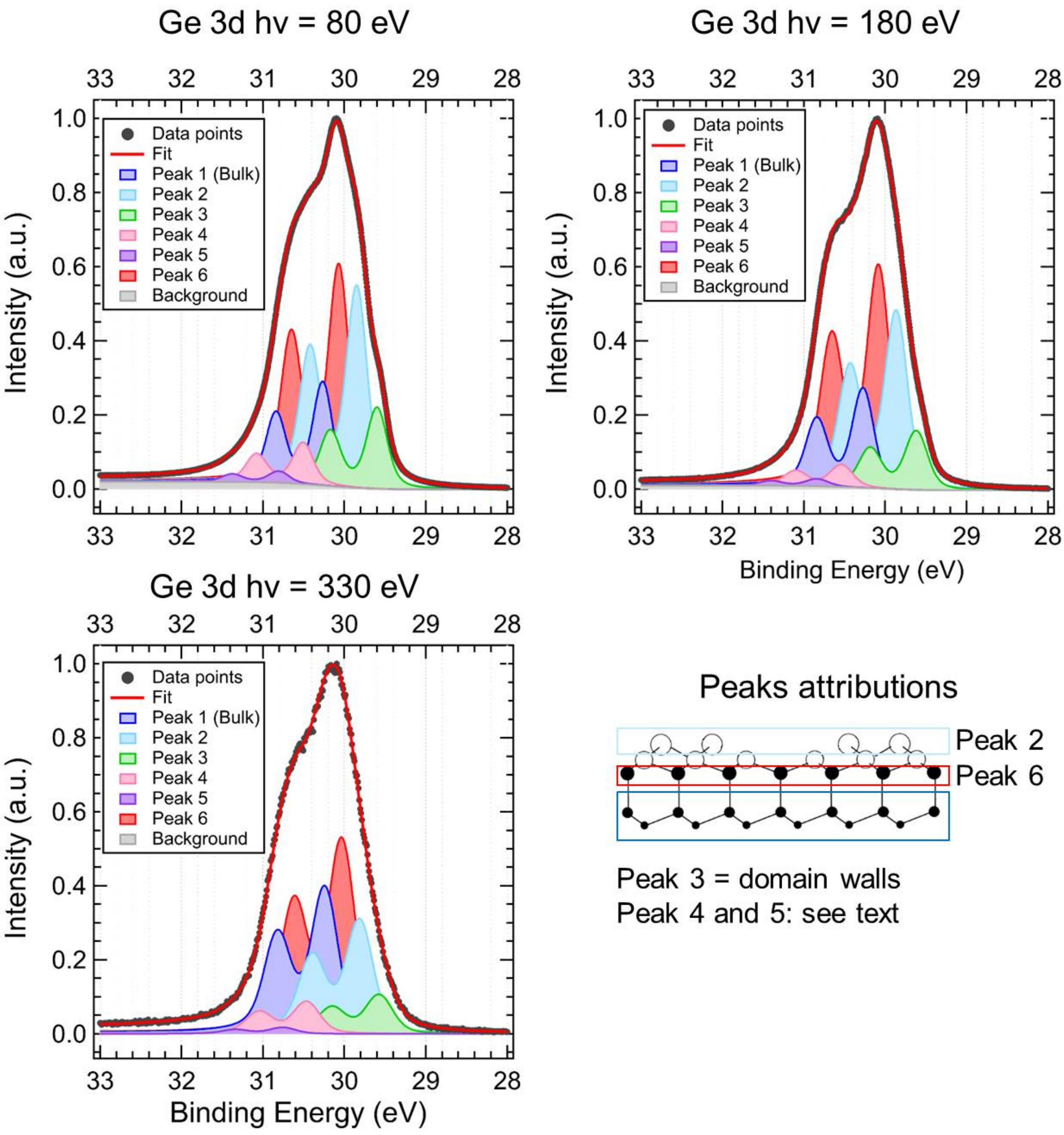

Fig. 4.26 – *XPS spectra of the Ge 3d core level of Cu/Ge(111) at different photon energies: hv = 80 eV, 180 eV and 330 eV. Six asymmetric Doniach-Sunjic doublets are used for all fit, with constrained parameters described in the text. On the bottom right is recalled the proposed atomic structure, with a partial attribution of the XPS components.*

4.3.4 ARPES study

4.3.4.1 ARPES on clean Ge(111)-c(2 × 8)

There exist a few ARPES studies dating from the eighties describing the band structure of Ge(111)-c(2×8) [19–22], from the time where the c(2×8) atomic structure was still to be fully determined. All of these studies do not fully agree on band assignment and existence, mainly due to the limited resolution and acquisition of the 1D detectors used at the time, but the work of J. Aarts *et al.* [22] provides an excellent comparison and discussion of all those results, and was here used extensively for the analysis. It is worth remarking that purely computational work, while more recent, tends to obtain a metallic character of the surface due to difficulty in determining an accurate bandgap [29, 37], despite experimental observations showing the existence of a non-null bandgap [38]. We could not find contemporary ($\leq$ 20 years) ARPES work on Ge(111)-c(2×8), even though it has been used as a substrate for 2D systems such as Pb/Au [39], Sn [34], In/Pb [40] or Pb [41], all studied by ARPES.

We present in Figure 4.27 and Figure 4.28 the band dispersion of Ge(111)-c(2×8) at hv = 50 eV and hv = 20 eV respectively. Both spectra are measured along the Γ-K direction with respect to Ge(111), using LH polarized light. In both cases, a 2D curvature of the spectrum is presented to determine more accurately the bands' shape and position. The observed bands are labelled on the curvature images. Three dispersive features with a strong signal between -2.5 eV and -4 eV are observed on the spectra taken at hv = 20 eV, and are labelled A, B and C. We can remark an asymmetry of intensities between the right and left sides of Γ, which was already observed in previous works and accurately modelled by calculations [21]. On the hv = 50 eV spectra, only the A feature is observable, with its minimum (not observed in this angular range) below -8 eV, in good agreement with Wachs *et al.* [20] whereas other sources do not observe any features below -4 eV [19, 22]. All experimental work until now only observed two of these bands (A, B or C), but they are all expected from the calculations and can be assigned to bulk band transitions [21]. On Figure 4.27 (hv = 20 eV), three features are observed between -0.5 eV and -2 eV, labelled S1, S2 and S3. All of them can be attributed to surface states [22]. S1 and S2 are again observed in Figure 4.28 (hv = 50 eV), along with

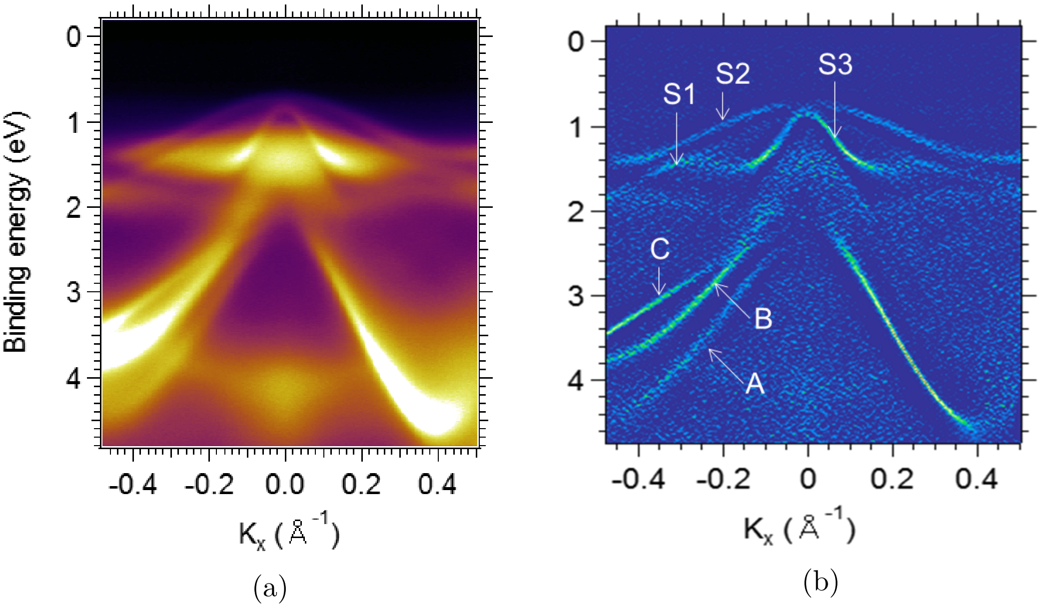

Fig. 4.27 – *(a) Band dispersion of Ge(111)-c(2×8) at hv = 20 eV, along Γ-K/Ge(111), and LH polarized light. (b) 2D curvature image of (a).*

a non-dispersive pair of bands labelled S4 and S4’. Despite not being predicted by calculations, this non-dispersive feature has been observed in most work on Ge(111)-c(2×8) [19, 20, 22] but not on cleaved surfaces (which do not display the c(2×8) surface reconstruction), and is thus attributed to a surface state. In previous works, only one band was seen, and we attribute the presence of two here to the higher energy resolution of our experiment. We also remark the presence of a bandgap, none of the bands reaching the Fermi level. Careful calibration of the Fermi level was made using the sample holder as a reference and assuming no sample charging as none was observed during XPS measurements.

4.3.4.2 ARPES on Cu/Ge(111)

The Fermi surface of Cu/Ge(111), measured at hv = 50 eV, is presented in Figure 4.29a. Multiple bands are observed. As the surface is discommensurate, Umklapp scattering is strongly expected similarly to Cu_2Si/Si(111). The aim here is to identify the main bands and their Umklapp replicas, corresponding to a translation by a vector of the reciprocal lattice of the overlayer. The bands close to Γ will be discussed later below. The whole identification process is shown step by step through Figure 4.29b to Figure 4.29g. We start with two bands: one hexagon shown

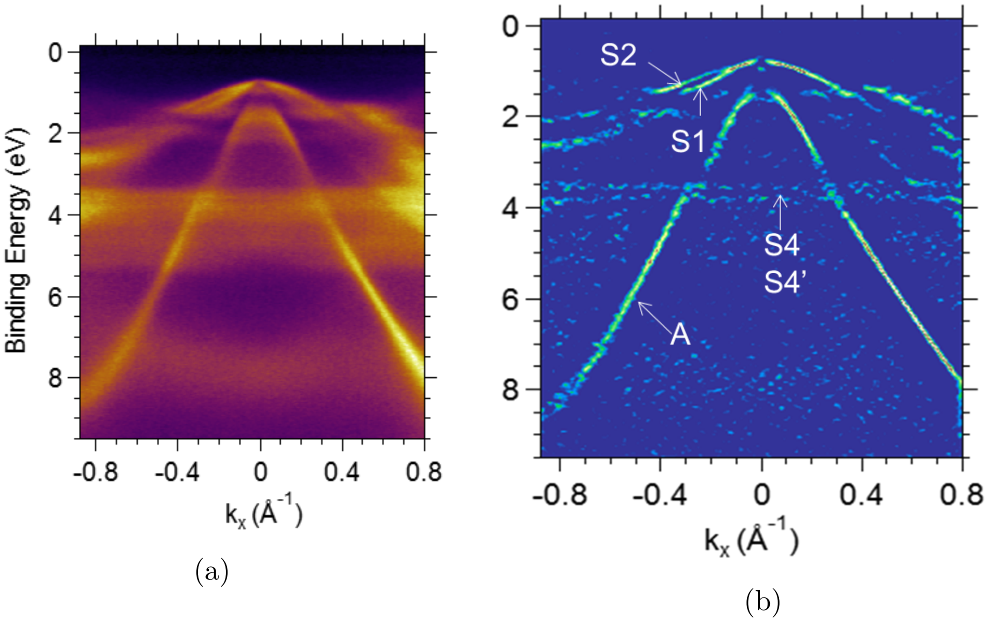

(a)

(b)

Fig. 4.28 – *(a) Band dispersion of Ge(111)-c(2×8) at hv = 50 eV, along Γ-K/Ge(111), and LH polarized light. (b) 2D curvature image of (a).*

in blue, and a hexagram inscribed in the hexagon, shown in orange. The replicas must preserve the sixfold symmetry, each band must then be replicated six times. All translating vectors must also have the same norm. Taking those constraints into account, we show in the following figures the patterns obtained by translation of the two main bands, and overlay them to the spectrum, first individually and then together. While the measured intensity of the bands varies strongly with the measured region in k-space, all observed features are nicely superimposed to the bands drawn. The size of the translation vectors, determined based on the spectra, is 0.19 Å^{-1}. From 2D scans at higher photon energy, we determined $\Gamma - K = 0.974$ Å^{-1}, leading to a reciprocal lattice vector of 1.69 Å^{-1}, for Ge(111). The periodicity to the surface being 8.88 larger than the bulk, we expect Umklapp vectors of size $1.69/8.88 = 0.19$ Å^{-1}, in excellent agreement with our measurement.

ARPES spectra along the $\Gamma - K$ direction for selected photon energies are presented in Figure 4.30 and Figure 4.31, with LV and LH polarized light respectively. The relative intensity of the bands observed is strongly dependent on the measurement parameters, especially concerning the bands close to Γ, which can almost be suppressed with LV light depending on the photon energy. By comparison to the ARPES spectra obtained previously on the clean Ge(111)-c(2×8) substrate, we assign those bands to bulk states. On the figures, they correspond to all bands encompassed by the black dotted lines. It is worth remarking that some of those bands cross the Fermi level, implying a vertical shift in the bands (i.e. a charge transfer) compared to the clean substrate of approximately 0.7 eV. These bulk bands near Γ are also well seen along the $\Gamma - M$ direction, shown for hv = 50 eV in Figure 4.32. The other bands, best seen on Figure 4.30 bottom (hv = 50 eV, LV polarization) are marked by white lines, and are attributed to the surface as they do not correspond to anything observed on clean Ge(111). We confirm that their Fermi vectors are identical to the ones from the Fermi surface spectrum.

The spectroscopic measurements from this chapter were all obtained at the UARPES beamline of Solaris synchrotron.

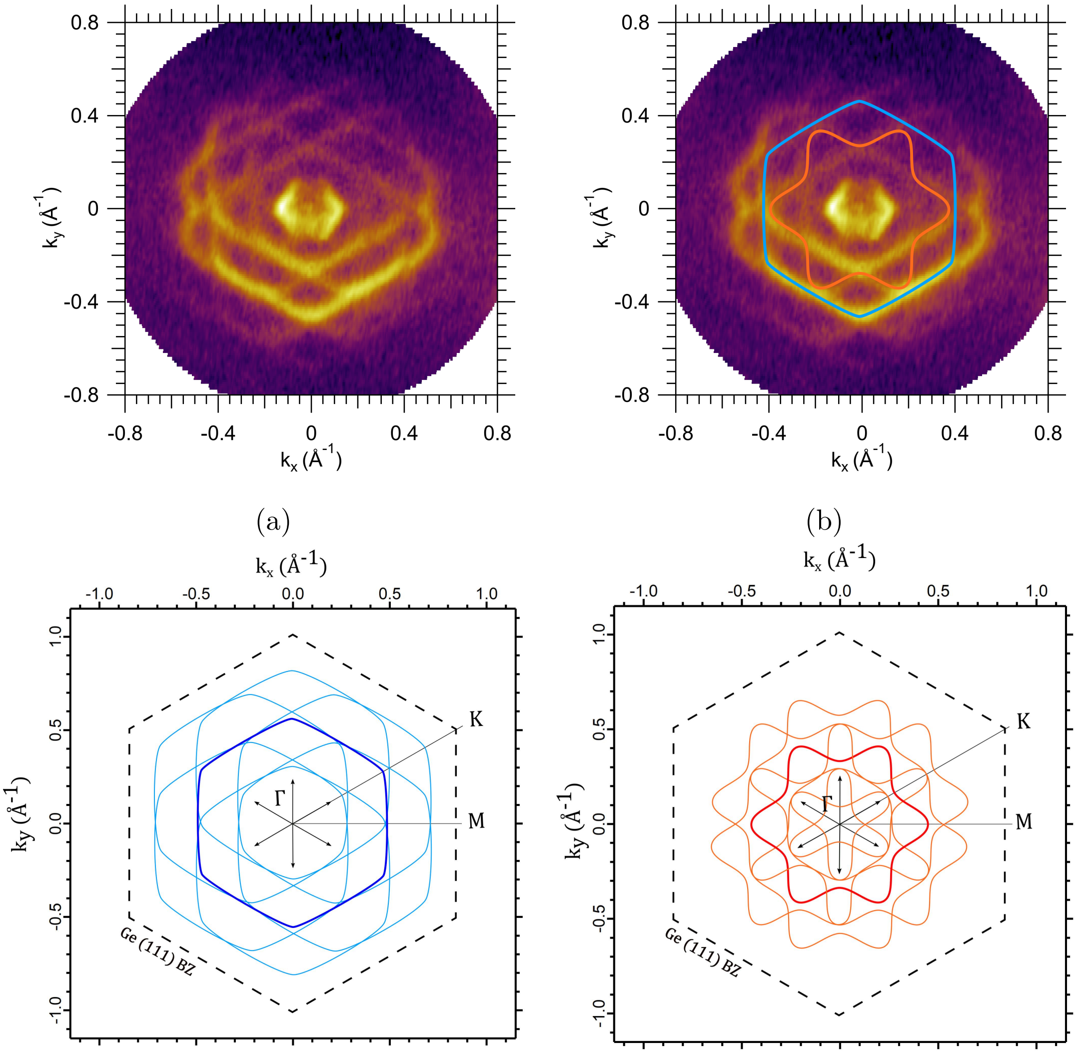

(a) (b)

(c) (d)

Fig. 4.29 – *First part - (a) Fermi surface of Cu/Ge(111) at hv = 50 eV, with LV polarized light. Many bands are observed, and Umklapp scattering is expected due to the discommensurate surface. (b) Two main bands are proposed, one hexagonal (blue) with an inscribed hexagram (orange). (c) and (d) Duplication of the band by six translations. Vector sizes are all identical and determined from the spectrum.*

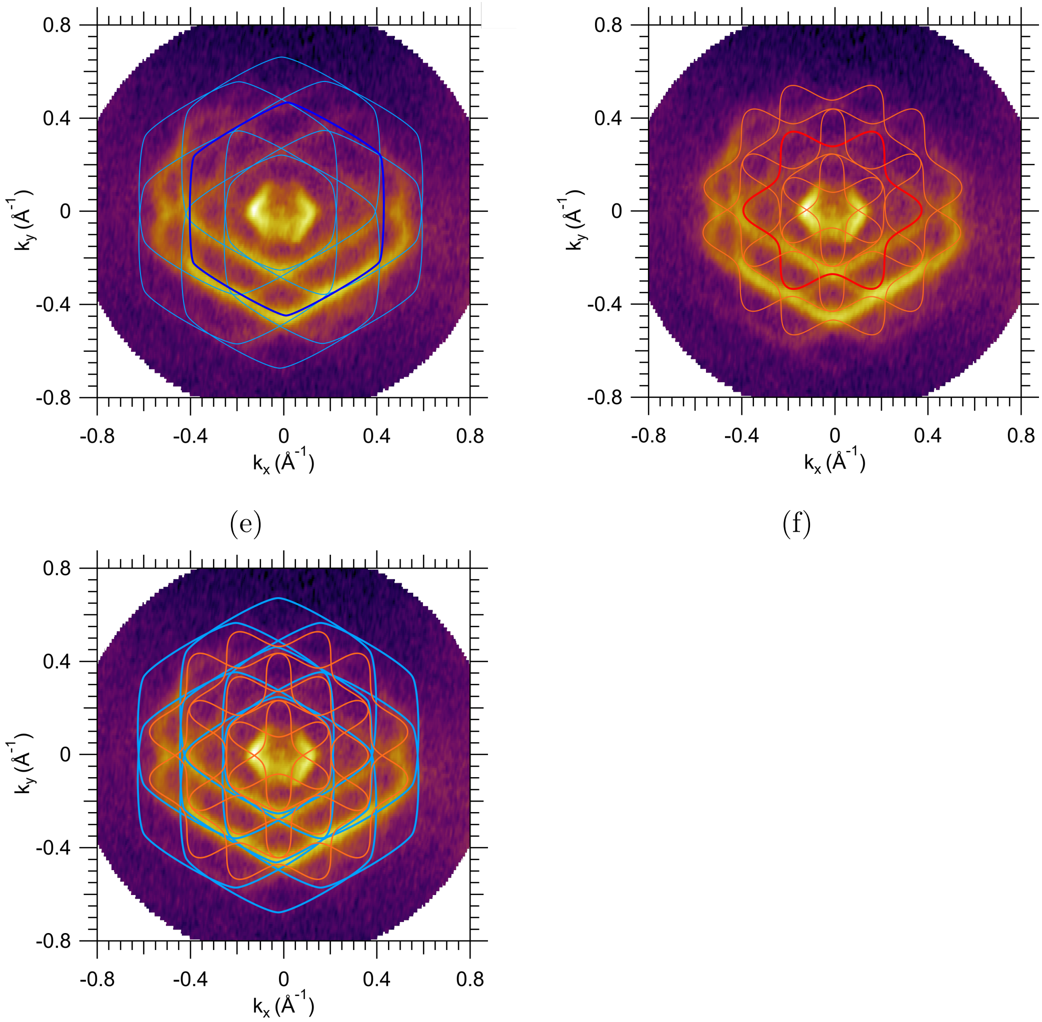

(e)

(f)

(g)

Fig. 4.29 – *Second part - (e) and (f) superposition to the spectrum of the patterns obtained from the translation of the hexagonal and hexagram bands respectively. (g) superposition of both patterns to the original spectrum. All features measured are superposed to the bands drawn.*

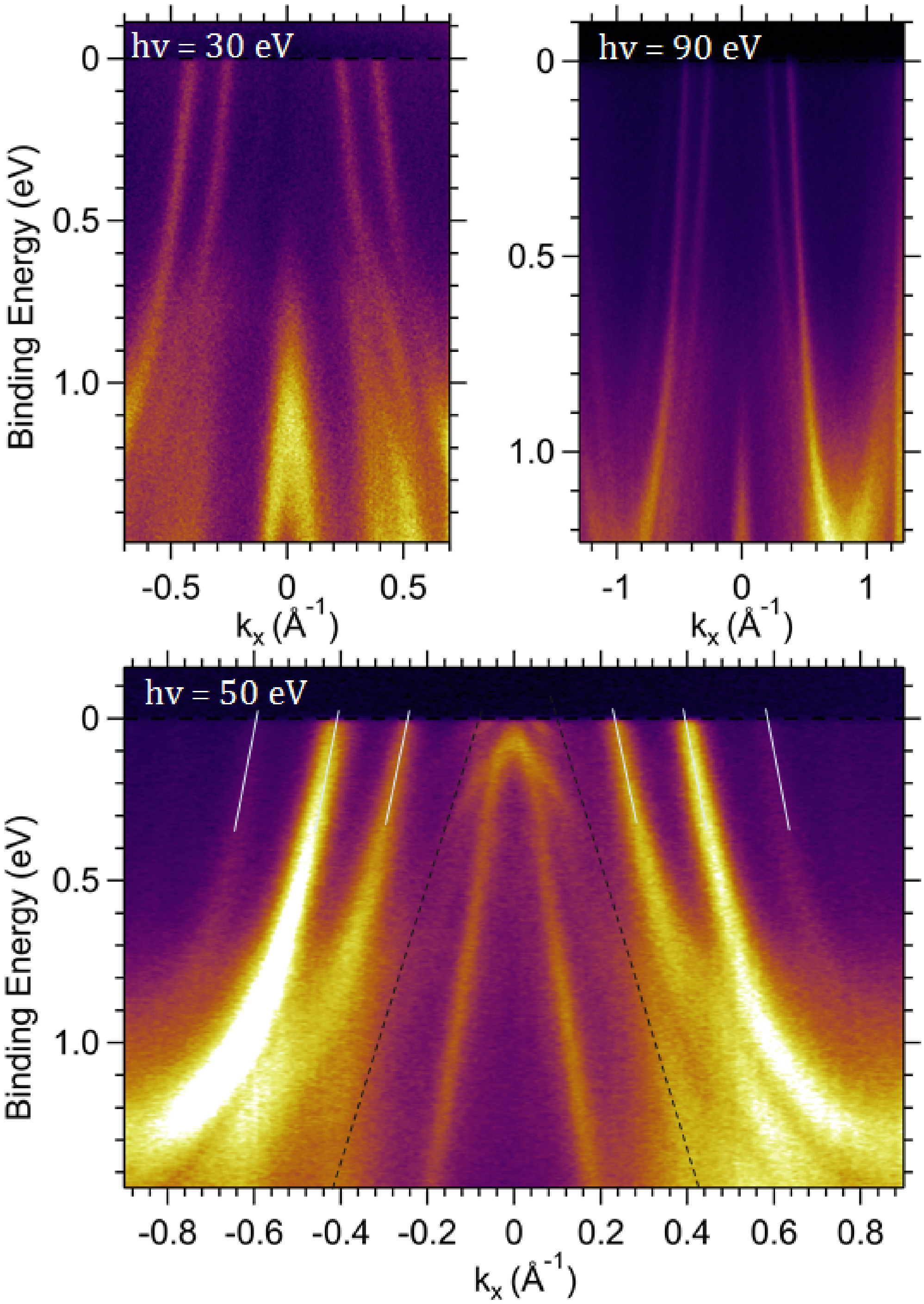

Fig. 4.30 – *ARPES spectra of Cu/Ge(111) along the* $\Gamma - K$ *direction, with LV polarized light, for different photon energies. All features around* Γ *encompassed by the dashed black lines are attributed to bulk bands. Surface bands are indicated on the bottom image by white lines.*

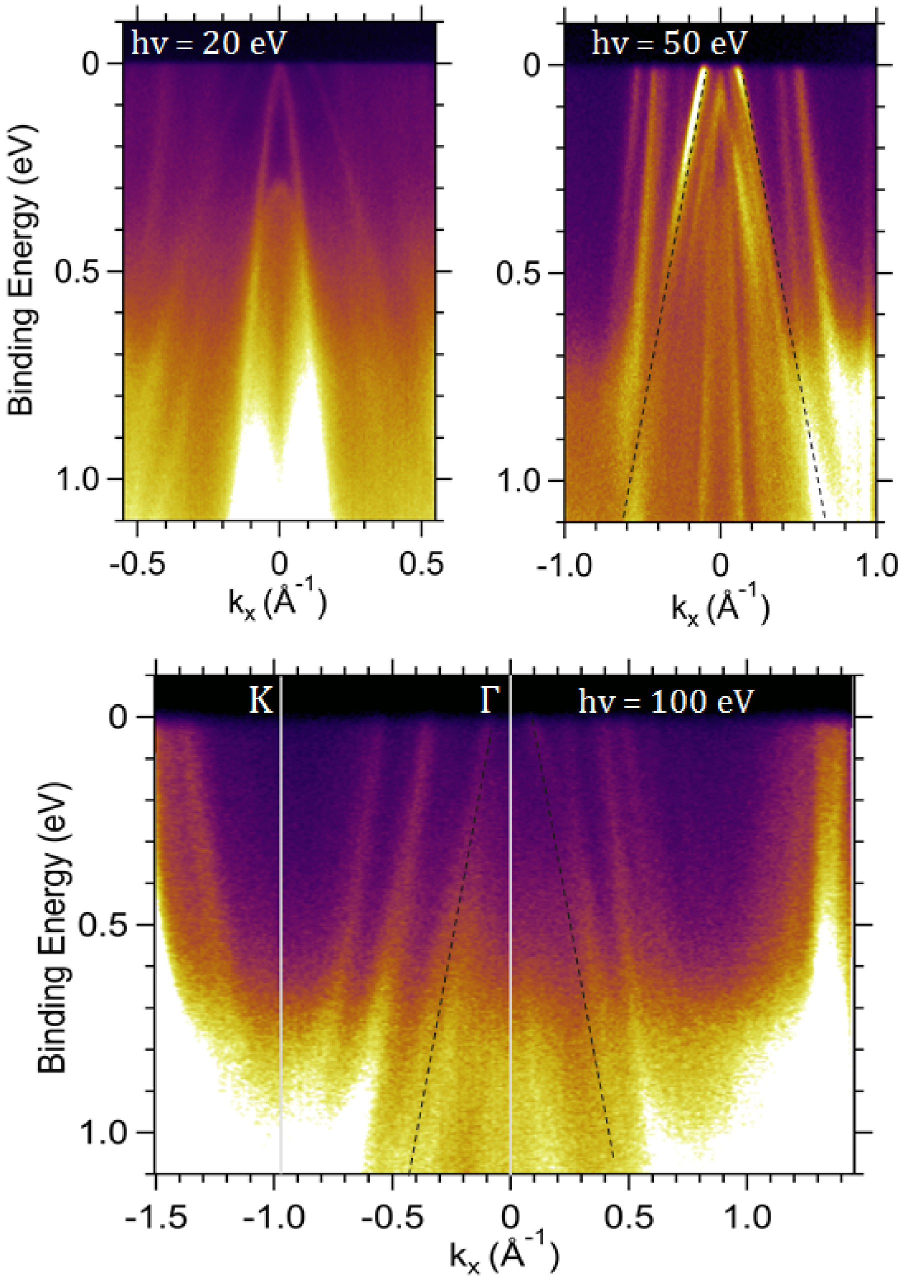

Fig. 4.31 – *ARPES spectra of Cu/Ge(111) along the* $\Gamma - K$ *direction, with LV polarized light, for different photon energies. All features around* Γ *encompassed by the dashed black lines are attributed to bulk bands. Further, many bands are observed crossing the Fermi level. On the bottom image, at hv = 100 eV, the* K *high-symmetry point is visible and denoted by a vertical white line.*

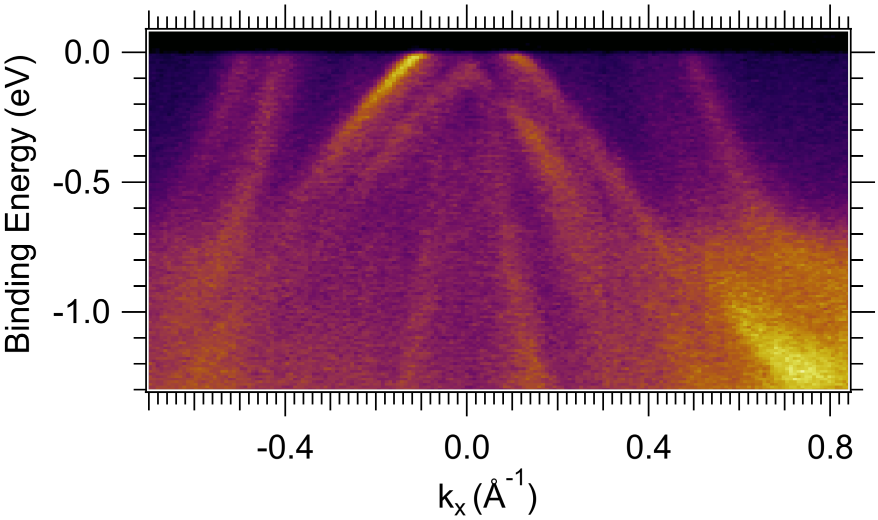

Fig. 4.32 – *Cut along the* $\Gamma - M$ *direction, at 50 eV, with LV polarized light. The bands close to* Γ*, attributed to the bulk, are well visible here.*

4.3.5 Conclusions about Cu/Ge(111)

If we compare the band structure of Cu/Ge(111) to the one of Ge/Cu(111), we quickly realize they are very different. The first difference lies in the presence of strong bands near Γ reaching up to the Fermi surface and originating from the substrate, while in Ge/Cu(111) all the bands involved in the conduction originated from the surface layer. The second, in the absence of any electron-like band that could cross the others bands and induce a DNL. Here, on Cu/Ge(111), no band crossing is observed. Thirdly, the relative positions of the two surface bands observed are exchanged as compared to Cu_2Ge: the hexagonal band is the outer one, while the hexagram becomes the inner one. Finally, the presence of strong Umklapp features are observed.

Those differences can be explained by two main causes. The first one, most obvious, is the difference in the atomic structure. From the existing literature and our results, it appears clearly that Cu/Ge(111) does not form a planar hexacoordinate surface, and could have a different stoichiometry than Cu_2Ge, resulting in a system entirely different from the theoretical Cu_2Ge or the experimental Cu_2Ge/Cu(111) that we presented. We nevertheless remark that the band structure observed does not correspond either to the one computed for a flat $CuGe_2$ monolayer, presented in Figure 4.17.

However, the atomic structure in itself was not a deterrent for this experiment, as a buckled Cu_2Ge surface could have led to gaped DNL states. The second cause is the substrate’s influence. Indeed, the Ge(111) substrate presents dangling bonds and forms strong bonds with the Cu evaporated on top, making it impossible in this case to obtain a surface decoupled from the substrate as in the case of Cu_2Ge/Cu(111), which also leads to the discommensuration and thus the Umklapp replicas. By analogy with Cu_2Si/Si(111), we also hypothesize that the absence of an electron-like band might originate from the hybridization of out-of-plane orbitals of the substrate with the surface. Indeed, the *gamma* band of Cu_2Ge originates mainly from the Ge p_z orbital [2] (SM), which is out-of-plane, and is the one most strongly impacted here by the substrate change.

This system presents many similarities to Cu_2Si/Si(111): discommensurate domains leading to Umklapp states, intense substrate states near Γ, and a buckled surface. In both cases, the surface cannot be considered independent from its substrate and its electronic band structure is different from what is expected from the corresponding 2D free-standing monolayer. This highlights the importance of experimental realizations, needed to observe the full complexity of physical systems, which is not available in initial computational results.

This work is, to the best of our knowledge, the first complete electronic structure characterization of the (“8.88×8.88”)R30° surface reconstruction of Cu/Ge(111).

Bibliography of Chapter 4

[1] L.-M. Yang, I. A. Popov, A. I. Boldyrev, T. Heine, T. Frauenheim, and E. Ganz, "Post-anti-van't Hoff-Le Bel motif in atomically thin germanium–copper alloy film", *Physical Chemistry Chemical Physics*, vol. 17, no. 27, pp. 17 545–17 551, 2015. DOI: `10.1039/C5CP02827B` (cited on pp. 131, 133).

[2] L. Liu, C. Wang, J. Li, X.-Q. Chen, Y. Jia, and J.-H. Cho, "Two-dimensional topological semimetal states in monolayer Cu_2Ge, Fe_2Ge, and Fe_2Sn", *Physical Review B*, vol. 101, no. 16, p. 165 403, Apr. 2020. DOI: `10.1103/PhysRevB.101.165403` (cited on pp. 133, 134, 138, 149, 153, 156, 159, 183).

[3] B. Feng, B. Fu, S. Kasamatsu, S. Ito, P. Cheng, C.-C. Liu, Y. Feng, S. Wu, S. K. Mahatha, P. Sheverdyaeva, P. Moras, M. Arita, O. Sugino, T.-C. Chiang, K. Shimada, K. Miyamoto, T. Okuda, K. Wu, L. Chen, Y. Yao, and I. Matsuda, "Experimental realization of two-dimensional Dirac nodal line fermions in monolayer Cu_2Si", *Nature Communications*, vol. 8, no. 1, p. 1007, Dec. 2017. DOI: `10.1038/s41467-017-01108-z` (cited on pp. 133, 153).

[4] L. Li and M. A. N. Araújo, "Topological insulating phases from two-dimensional nodal loop semimetals", *Phys. Rev. B*, vol. 94, p. 165 117, 16 Oct. 2016. DOI: `10.1103/PhysRevB.94.165117` (cited on p. 133).

[5] Y. Li and F. D. M. Haldane, "Topological nodal Cooper pairing in doped Weyl metals", *Phys. Rev. Lett.*, vol. 120, p. 067 003, 6 Feb. 2018. DOI: `10.1103/PhysRevLett.120.067003` (cited on p. 133).

[6] R. Dudde, H. Bernhoff, and B. Reihl, "Growth of silicon and germanium on Cu(111) studied by angle-resolved direct and inverse photoemission", *Physical Review B*, vol. 41, no. 17, pp. 12 029–12 034, Jun. 1990. DOI: `10.1103/PhysRevB.41.12029` (cited on pp. 135, 138).

[7] J. S. Tsay, L. W. Chang, and A. B. Yang, "Formation and annealing effect for close-packed Ge/Cu(111) layers", *Journal of Vacuum Science & Technology A: Vacuum, Surfaces, and Films*, vol. 21, no. 6, pp. 1892–1894, Nov. 2003. DOI: `10.1116/1.1615972` (cited on p. 135).

[8] Z. Qin, J. Pan, S. Lu, Y. Shao, Y. Wang, S. Du, H.-J. Gao, and G. Cao, "Direct Evidence of Dirac Signature in Bilayer Germanene Islands on Cu(111)", *Advanced Materials*, vol. 29, no. 13, p. 1 606 046, Apr. 2017. DOI: `10.1002/adma.201606046` (cited on pp. 136, 156).

[9] M. Böhringer, Q. Jiang, R. Berndt, W.-D. Schneider, and J. Zegenhagen, "Discommensurations, epitaxial growth and island formation in Ge(111):Cu", *Surface Science*, vol. 367, no. 3, pp. 245–260, Dec. 1996. DOI: `10.1016/S0039-6028(96)00874-6` (cited on pp. 136–138, 162, 165).

[10] J. Zegenhagen, P. Lyman, M. Bohringer, and M. Bedzyk, "Discommensurate Reconstructions of (111)Si and Ge Induced by Surface Alloying with Cu, Ga and In", *physica status solidi (b)*, vol. 204, no. 2, pp. 587–616, Dec. 1997. DOI: `10.1002/1521-3951(199712)204:2<587::AID-PSSB587>3.0.CO;2-Y` (cited on pp. 136, 160).

[11] T. Suzuki, S. Omori, and Y. Nihei, "X-ray photoelectron diffraction study of discommensurate Cu/Ge(111)", *Surface Science*, vol. 440, no. 3, pp. 881–886, Oct. 1999. DOI: `10.1016/S0039-6028(99)00868-7` (cited on pp. 136–138).

[12] L. Zhu, Z. Wei, G. Shi, B. Shang, M. Li, W. Wan, and W.-X. Tang, "Coverage-driven phase transition of copper silicide monolayer on Si (111)", *Ultramicroscopy*, vol. 200, pp. 39–42, May 1, 2019. DOI: `10.1016/j.ultramic.2019.02.019` (cited on p. 138).

[13] J. C. Hansen, B. J. Knapp, R. de Souza-Machado, M. K. Wagner, and J. G. Tobin, "Column 1B metal adsorption on Ge(111): The growth mode of Cu", *Journal of Vacuum Science & Technology A: Vacuum, Surfaces, and Films*, vol. 7, no. 3, pp. 2083–2086, May 1989. DOI: `10.1116/1.575975` (cited on p. 138).

[14] D. D. Chambliss and T. N. Rhodin, "Electronic and atomic structure of the Cu/Si(111) quasi-5x5 overlayer", *Physical Review B*, vol. 42, no. 3, p. 13, Jul. 1990. DOI: `10.1103/PhysRevB.42.1674` (cited on p. 138).

[15] J. Zegenhagen, E. Fontes, F. Grey, and J. R. Patel, "Microscopic structure, discommensurations, and tiling of Si (111)/Cu-"5x5"", *Physical Review B*, vol. 46, no. 3, p. 1860, Jul. 1992. DOI: `10.1103/PhysRevB.46.1860` (cited on p. 138).

[16] M. C. Biesinger, L. W. Lau, A. R. Gerson, and R. S. Smart, "Resolving surface chemical states in xps analysis of first row transition metals, oxides and hydroxides: Sc, Ti, V, Cu and Zn", *Applied Surface Science*, vol. 257, no. 3, pp. 887–898, Nov. 2010. DOI: `10.1016/j.apsusc.2010.07.086` (cited on pp. 145, 147).

[17] C. J. Powell and A. Jablonski, *NIST Electron Inelastic-Mean-Free-Path Database - Version 1.2*. National Institute of Standards and Technology, Gaithersburg, MD, 2003. DOI: `10.18434/T48C78` (cited on p. 145).

[18] X.-S. Ye, Z.-G. Shao, H. Zhao, L. Yang, and C.-L. Wang, "Intrinsic carrier mobility of germanene is larger than graphene's: first-principle calculations", *RSC Adv.*, vol. 4, pp. 21 216–21 220, 41 Apr. 2014. DOI: `10.1039/C4RA01802H` (cited on p. 156).

[19] T. Yokotsuka, S. Kono, S. Suzuki, and T. Sagawa, "Study of electronic structures of Ge(111) 7×7-Sn and Ge(111) "2×8" surfaces by Angle-Resolved UPS", *Journal of the Physical Society of Japan*, vol. 53, no. 2, pp. 696–701, 1984. DOI: `10.1143/JPSJ.53.696` (cited on pp. 156, 174, 175).

[20] A. L. Wachs, T. Miller, T. C. Hsieh, A. P. Shapiro, and T.-C. Chiang, "Angle-resolved photoemission studies of Ge(111)-c(2×8), Ge(111)-(1×1)H, Si(111)-(7×7), and Si(100)-(2×1)", *Physical Review B*, vol. 32, no. 4, pp. 2326–2333, Aug. 1985. DOI: `10.1103/PhysRevB.32.2326` (cited on pp. 156, 174, 175).

[21] R. D. Bringans, R. I. G. Uhrberg, and R. Z. Bachrach, "Surface and bulk electronic structure of Ge(111) c(2×8) and Ge(111):As 1×1", *Physical Review B*, vol. 34, no. 4, pp. 2373–2380, Aug. 1968. DOI: `10.1103/PhysRevB.34.2373` (cited on pp. 156, 174).

[22] J. Aarts, A. J. Hoeven, and P. K. Larsen, "Electronic structure of the Ge(111)-c(2×8) surface", *Physical Review B*, vol. 37, no. 14, pp. 8190–8197, May 1988. DOI: `10.1103/PhysRevB.37.8190` (cited on pp. 156, 174, 175).

[23] P. Giannozzi, S. Baroni, N. Bonini, M. Calandra, R. Car, C. Cavazzoni, D. Ceresoli, G. L. Chiarotti, M. Cococcioni, I. Dabo, A. Dal Corso, S. de Gironcoli, S. Fabris, G. Fratesi, R. Gebauer, U. Gerstmann, C. Gougoussis, A. Kokalj, M. Lazzeri, L. Martin-Samos, N. Marzari, F. Mauri, R. Mazzarello, S. Paolini, A. Pasquarello, L. Paulatto, C. Sbraccia, S. Scandolo, G. Sclauzero, A. P. Seitsonen, A. Smogunov, P. Umari, and R. M. Wentzcovitch, "Quantum

espresso: a modular and open-source software project for quantum simulations of materials", *Journal of Physics: Condensed Matter*, vol. 21, no. 39, 395502 (19pp), 2009. DOI: 10.1088/0953-8984/21/39/395502 (cited on p. 157).

[24] P. Giannozzi, O. Andreussi, T. Brumme, O. Bunau, M. Buongiorno Nardelli, M. Calandra, R. Car, C. Cavazzoni, D. Ceresoli, M. Cococcioni, N. Colonna, I. Carnimeo, A. Dal Corso, S. de Gironcoli, P. Delugas, R. A. J. DiStasio, A. Ferretti, A. Floris, G. Fratesi, G. Fugallo, G. Gebauer, U. Gerstmann, F. Giustino, T. Gorni, J. Jia, M. Kawamura, H.-Y. Ko, A. Kokalj, E. Küçükbenli, M. Lazzeri, M. Marsili, N. Marzari, F. Mauri, N. L. Nguyen, H.-V. Nguyen, A. Otero-de-la-Roza, L. Paulatto, S. Poncé, D. Rocca, R. Sabatini, B. Santra, M. Schlipf, A. P. Seitsonen, A. Smogunov, I. Timrov, T. Thonhauser, P. Umari, N. Vast, X. Wu, and S. Baroni, "Advanced capabilities for materials modelling with quantum espresso", *Journal of Physics: Condensed Matter*, vol. 29, no. 46, p. 465 901, 2017. DOI: 10.1088/1361-648x/aa8f79 (cited on p. 157).

[25] J. P. Perdew, K. Burke, and M. Ernzerhof, "Generalized gradient approximation made simple", *Phys. Rev. Lett.*, vol. 78, pp. 1396–1396, 7 Feb. 1997. DOI: 10.1103/PhysRevLett.78.1396 (cited on p. 157).

[26] A. Dal Corso, "Pseudopotentials periodic table: from H to Pu", *Computational Materials Science*, vol. 95, pp. 337–350, 2014. DOI: 10.1016/j.commatsci.2014.07.043 (cited on p. 157).

[27] L. Gao, J.-T. Sun, J.-C. Lu, H. Li, K. Qian, S. Zhang, Y.-Y. Zhang, T. Qian, H. Ding, X. Lin, S. Du, and H.-J. Gao, "Epitaxial growth of honeycomb monolayer CuSe with Dirac nodal line fermions", *Advanced Materials*, vol. 30, no. 16, p. 1 707 055, Apr. 2018. DOI: 10.1002/adma.201707055 (cited on p. 159).

[28] R. S. Becker, B. S. Swartzentruber, J. S. Vickers, and T. Klitsner, "Dimer adatom stacking-fault (DAS) and non-DAS (111) semiconductor surfaces: a comparison of Ge(111)-c(2×8) to Si(111)-(2×2), -(5×5), -(7×7), and -(9×9) with scanning tunneling microscopy", *Physical Review B*, vol. 39, no. 3, p. 1633 1647, Jan. 1989. DOI: 10.1103/PhysRevB.39.1633 (cited on pp. 160, 161).

[29] I. Razado-Colambo, J. He, H. M. Zhang, G. V. Hansson, and R. I. G. Uhrberg, “Electronic structure of Ge(111) c(2×8) : STM, angle-resolved photoemission, and theory”, *Physical Review B*, vol. 79, no. 20, p. 205 410, May 2009. DOI: `10.1103/PhysRevB.79.205410` (cited on pp. 160, 174).

[30] R. S. Becker, J. A. Golovchenko, and B. S. Swartzentruber, “Tunneling images of germanium surface reconstructions and phase boundaries”, *Phys. Rev. Lett.*, vol. 54, pp. 2678–2680, 25 Jun. 1985. DOI: `10.1103/PhysRevLett.54.2678` (cited on p. 160).

[31] A. Selloni, N. Takeuchi, and E. Tosatti, “Reconstructions and phase transitions at semiconductor surfaces: Ge(111)”, *Surface Science*, vol. 331-333, pp. 995–1001, 1995. DOI: `10.1016/0039-6028(95)00102-6` (cited on p. 160).

[32] P. De Padova, J.-M. Mariot, L. Favre, I. Berbezier, B. Olivieri, P. Perfetti, C. Quaresima, C. Ottaviani, A. Taleb-Ibrahimi, P. Le Fèvre, F. Bertran, O. Heckmann, M. Richter, W. Ndiaye, F. D’Orazio, F. Lucari, C. Cacho, and K. Hricovini, “Mn_5Ge_3 films grown on Ge(111)-c(2×8)”, *Surface Science*, vol. 605, no. 5, pp. 638–643, Mar. 2011. DOI: `10.1016/j.susc.2011.01.002` (cited on pp. 160, 169).

[33] D. J. Chadi and C. Chiang, “New c2×8 unit cell for the ge(111) surface”, *Phys. Rev. B*, vol. 23, pp. 1843–1846, 4 Feb. 1981. DOI: `10.1103/PhysRevB.23.1843` (cited on p. 160).

[34] K. Higashiyama, S. Lewis, R. Ynzunza, E. Tober, Y. Kim, and C. Fadley, “Asymmetry of adatoms on Ge(111) observed by scanning tunneling microscopy: the clean c(2×8) and Sn-induced (7×7) structures”, *Surface Science*, vol. 291, no. 1, pp. 47–56, Jul. 1993. DOI: `10.1016/0039-6028(93)91475-5` (cited on pp. 161, 162, 174).

[35] G. Lee, H. Mai, I. Chizhov, and R. Willis, “Charged defects on Ge(111)-c(2×8): characterization using STM”, *Surface Science*, vol. 463, no. 1, pp. 55–65, 2000. DOI: `10.1016/S0039-6028(00)00596-3` (cited on pp. 161, 163, 170).

[36] M. Göthelid, T. M. Grehk, M. Hammar, U. O. Karlsson, and S. A. Flodström, “Adatom and rest-atom contributions in Ge(111)c(2×8) and Ge(111)-Sn(7×7) core-level spectra”, *Phys. Rev. B*, vol. 48, pp. 2012–2015, 3 Jul. 1993. DOI: `10.1103/PhysRevB.48.2012` (cited on p. 169).

[37] P. V. Smith, M. W. Radny, and G. A. Shah, “Density functional study of the Ge(111)c(2×8) surface using the modified Becke-Johnson exchange potential with LDA correlation and spin–orbit interactions”, *RSC Advances*, vol. 4, pp. 48 245–48 253, 89 2014. DOI: 10.1039/C4RA05636A (cited on p. 174).

[38] R. M. Feenstra, S. Gaan, G. Meyer, and K. H. Rieder, “Low-temperature tunneling spectroscopy of Ge(111)c(2×8) surfaces”, *Phys. Rev. B*, vol. 71, p. 125 316, 12 Mar. 2005. DOI: 10.1103/PhysRevB.71.125316 (cited on p. 174).

[39] W.-C. Chen, T.-R. Chang, S.-T. Tsai, S. Yamamoto, J.-M. Kuo, C.-M. Cheng, K.-D. Tsuei, K. Yaji, H. Lin, H.-T. Jeng, C.-Y. Mou, I. Matsuda, and S.-J. Tang, “Significantly enhanced giant Rashba splitting in a thin film of binary alloy”, *New Journal of Physics*, vol. 17, no. 8, p. 083 015, Aug. 2015. DOI: 10.1088/1367-2630/17/8/083015 (cited on p. 174).

[40] H. M. Sohail and R. I. G. Uhrberg, “Experimental studies of an In/Pb binary surface alloy on Ge(111)”, *Surface Science*, vol. 649, pp. 146–151, 2016. DOI: 10.1016/j.susc.2016.02.016 (cited on p. 174).

[41] H. Morikawa, I. Matsuda, and S. Hasegawa, “Absence of charge-density waves on the dense Pb/Ge(111)-β-$\sqrt{3}\times\sqrt{3}$ surface”, *Phys. Rev. B*, vol. 77, p. 193 310, 19 May 2008. DOI: 10.1103/PhysRevB.77.193310 (cited on p. 174).

Chapter 5

First steps on Pb/SiC, a good candidate for quantum spin Hall effect

Chapter 5: First steps on Pb/SiC, a good candidate for quantum spin Hall effect

5.1 Pb/SiC, a system full of promise

As discussed in subsection 1.2.1, possible candidates for the QSHE are honeycomb-lattice structures with two sublattices, similar to graphene, according to the Kane and Mele model [1, 2]. We also mentioned that a larger gap was more likely to be obtained in systems with high SOC, i.e. in systems with heavy elements. It is then only natural to look for candidates in the X-ene family: mono-elemental systems exhibiting the same 2D honeycomb structure as graphene, usually chemically close, and preferentially towards the heaviest elements, such as Pb or Bi.

Recently, a new candidate for room-temperature QSH insulator was proposed, consisting of a hexagonal or honeycomb monolayer of lead [3–8], and silicon carbide (SiC) was proposed as a substrate [6]. Remarkably large band gaps were found, ranging from 0.5 eV - 1 eV for a simple monolayer [3] to 1 eV - 1.34 eV for hydrogen-decorated layers [4], depending on the model used. These large band gaps originate from the large intrinsic spin-orbit coupling (SOC) of Pb atoms. However, experimental confirmation of these theoretical predictions on Pb/SiC is still needed. Simultaneously, monolayer Bi on SiC(0001) was demonstrated to host edge states compatible with the QSHE theoretically expected in this system, with a large gap of 0.8 eV at room temperature [9]. Another wide-gap system that seems promising is hexagonal Sn on SiC(0001), in which a 2 eV gap was measured, with hopes for TI states [10].

A question therefore arises: can a hexagonal or honeycomb Pb monolayer be synthesized on SiC, and if so, with what crystalline structure and with which electronic properties? Even if such a Pb monolayer did not exhibit the QSHE, it could still display rich physics. Indeed the similar Pb/Si(111) system showed evidence for a strongly correlated 2D metal phase at low Pb density [11] or 2D superconductivity in dense Pb layers [12]. With these perspectives in mind, we present below our preliminary work on the growth and characterisation of Pb on SiC(0001), starting with an introduction to SiC and its complex surfaces.

5.2 An introduction to SiC

5.2.1 What is SiC?

Silicon carbide is a large-gap semiconductor full of qualities. It has a hardness comparable to diamond, a good thermal conductivity, high radiation resistance, and a high breakdown voltage. It is also well suited for demanding applications in harsh environments, such as high temperature, high power, and high-frequency ones due to its high carrier saturation velocity [13]. It is also to be noted that it oxidizes in the same way as silicon. It is also a substrate commercially available, facilitating widespread studies using it.

The structure of silicon carbide (SiC) can be viewed as a stack of planar layers of silicon and carbon atoms. These layers go by pair (one Si, one C), the distance between the Si plane and the C plane in a bilayer being much smaller than between a bilayer and the next. Their atoms are placed on three possible groups of sites we will call A, B and C, represented in Figure 5.1. In total, more than 250 polymorphisms have been identified [14], and while some belong to amorphic phases, many of them are crystalline and are called polytypes. The polytypes differ only in the stacking sequence of the hexagonally close-packed bilayers of Si and C atoms along the cubic [111] (or equivalent hexagonal [0001]) direction. For example, stacking ABCABC... correspond to a cubic structure, called 3C-SiC in Ramsdell notation, while a stacking order of ABAB... correspond to a hexagonal structure called 2H-SiC. The Ramsdell notation is a compact notation indicating the periodicity by a number and the geometry by a letter (C for cubic, H for hexagonal, R for rhombohedral). Due to its bilayered structure, the two sides of a SiC crystal are not equivalent: one side will end with a carbon plane, while the other will end with a Si plane. To differentiate between the sides, an overline is used: the Si-terminated side of a hexagonal SiC will be designated as (0001), while its C-terminated side

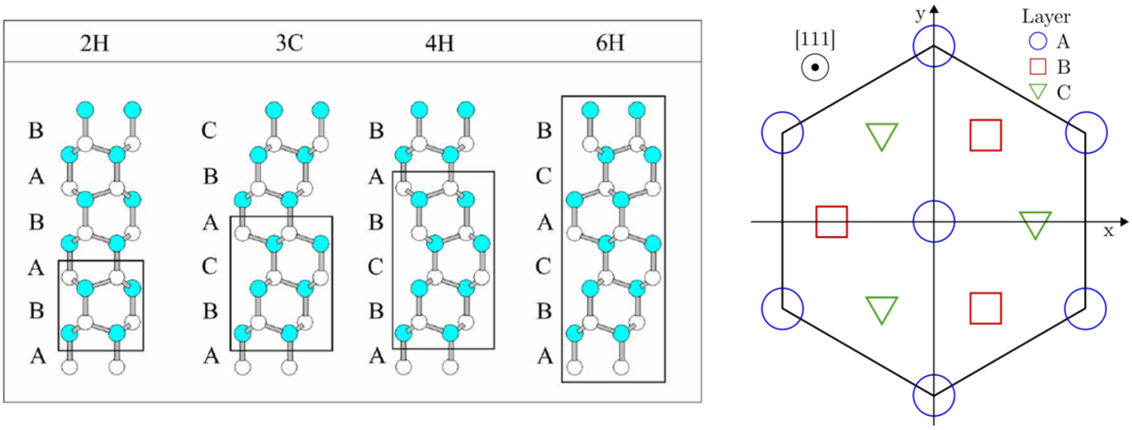

Fig. 5.1 – *On the left is represented the stacking order of the main SiC polytypes. The rectangle shows the smallest unit reproduced to obtain the polytype. Figure from [15]. On the right is the top view of the A, B, C positions.*

will be designated as $(000\bar{1})$, or sometimes as (000-1). All these polytypes result in a semiconductive material with a large gap, ranging from 2.39 eV (3C) to 3.26 eV (4H) [13].

5.2.2 SiC surface preparation

SiC has native silicon oxide on its surface, as well as possible contaminants, that need to be removed to obtain a clean substrate. Over time various cleaning methods have been proposed and used for SiC, often deriving from the ones used for silicon. While wet etching was popular at a time [16–18], leaving the SiC as a (1×1) unreconstructed surface, it often leaves traces of contaminants and/or oxide, and is not able to remove the surface scratches and subsurface defects left behind by polishing. Dry etching has been shown to overcome those issues [9, 19, 20]. It consists of heating the substrate in a UHV chamber to up to 1230°C under a H_2 and He atmosphere (close to 1 atm of gas pressure is used), leaving an H-passivated (1×1) surface. The main limitation of dry etching is the very specific equipment and UHV chamber it requires.

We adopted a third approach: deoxidation and cleaning by direct-current heating. Commonly used, sometimes after wet etching, this technique requires passing a current through a SiC sample inside a UHV chamber, high enough for the topmost

Si layers to evaporate, removing the native oxide and any surface contaminants in the process [13, 18, 21]. This method results in an array of possible surface reconstructions dictated by the heating temperature. Figure 5.2 shows the LEED pattern of the three main surface reconstructions obtainable from 6H- or 4H-SiC(0001): (3×3), $(\sqrt{3}\times\sqrt{3})$R30° and $(6\sqrt{3}\times6\sqrt{3})$R30°, from the most silicon-rich to the most carbon-rich surface. Indeed, as the silicon evaporates at a lower temperature than the carbon, continuous heating will deplete the surface in silicon. It is then possible to enrich the surface again by evaporating Si on it.

Usually, the SiC substrate is kept for a night at 600°C, to outgas most of the contaminants while keeping intact the oxide layer. It is then flashed around 1100°C to remove the oxide, in a vacuum pressure always kept below 10^{-9} mbar. To obtain the (3×3) surface reconstruction, it is then necessary to heat at 650-800°C under a constant flux of Si. This surface is pyramids of Si atoms (one adatom on top of three trimers) resting on top of an additional Si layer, as shown in Figure 5.3 (a). Further annealing at 1000°C will deplete most of the surface Si and result in the $(\sqrt{3}\times\sqrt{3})$R30° reconstruction, formed by a Si adlayer as shown in Figure 5.3 (b). These adatoms adsorb on the T4 sites, directly above some of the C atoms of the last SiC bulk layer. This model is the most recently accepted one [22]. Above 1100 °C, the $(6\sqrt{3}\times6\sqrt{3})$R30° surface reconstruction will appear. Its exact composition is still debated, but it is now agreed upon that its topmost layer is a honeycomb carbon layer partially covalently bonded to the Si-terminated SiC substrate [23], sometimes called the zero-layer graphene (ZLG), as shown in Figure 5.4. Higher annealing temperatures results in the graphitization of SiC [24, 25]: the silicon atoms in the SiC bilayers will evaporate, resulting in a graphitized surface. By finely controlling the annealing it is possible to obtain a single graphene layer on top of SiC [23, 26–28], a possibility that renewed interest in SiC as a substrate.In addition to these well-known surface reconstructions, a large amount of meta-stable phases exist, especially in-between the (3×3) and the $(\sqrt{3}\times\sqrt{3})$R30° reconstructions.

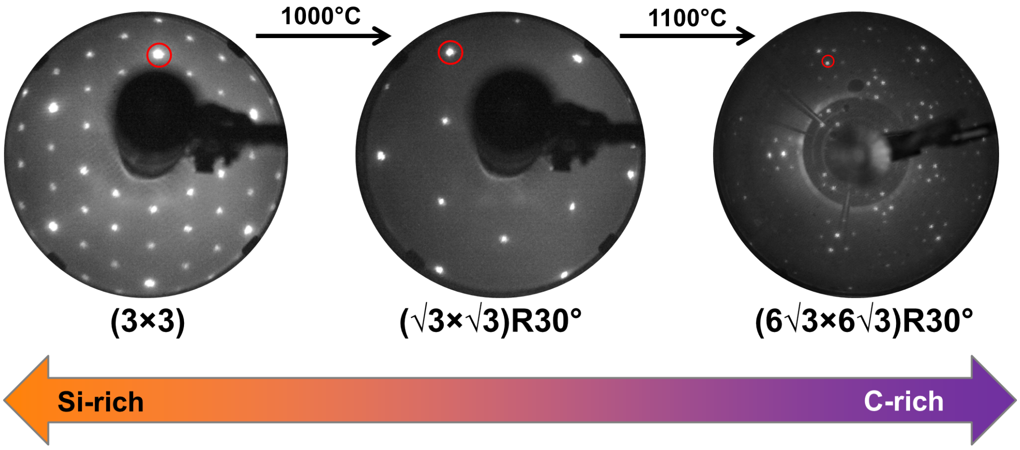

Fig. 5.2 – *Phase diagram of SiC(0001) with LEED images, measured at 75 eV, 100 eV and 100 eV respectively. Under annealing, the surface gets depleted in Si, and different surface reconstructions with increasing C/Si surface ratios are being observed. The (1x1) bulk periodicity is identified by a red circle.*

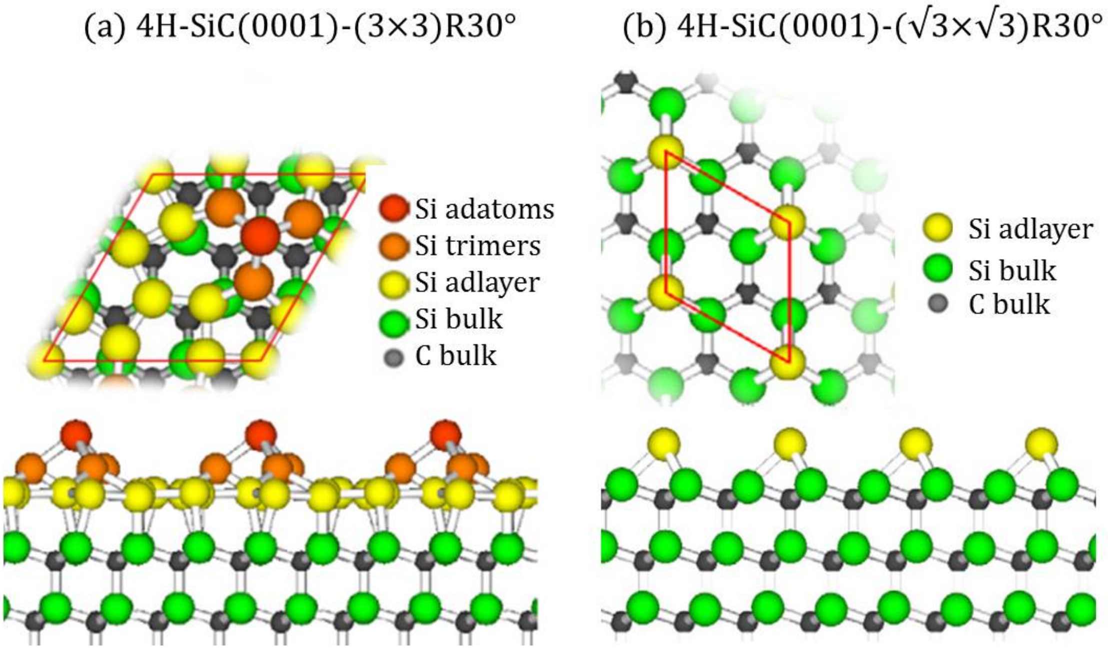

Fig. 5.3 – *Atomic models of SiC(0001) reconstructions. (a) shows the (3×3) surface, where Si adatoms and trimers rest on top of an additional Si layer. (b) shows the* $(\sqrt{3} \times \sqrt{3})R30°$*, formed by an Si adlayer.*

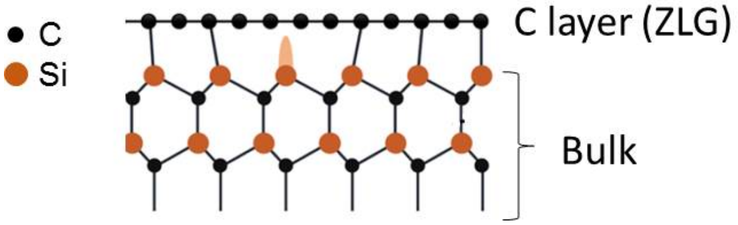

Fig. 5.4 – *Side view of the* $(6\sqrt{3}\times6\sqrt{3})R30°$ *structure. It is terminated by a honeycomb carbon layer, the zero-layer graphene, that is partially bonded to the SiC bulk.*

5.3 Pb/SiC Experimental results

5.3.1 Growth and sample preparation

The growth of Pb on SiC(0001) has been investigated for the three main surface reconstructions of SiC(0001): (3×3), $(\sqrt{3} \times \sqrt{3})$R30° and $(6\sqrt{3} \times 6\sqrt{3})$R30°, with more interest given towards the first two.

The first step of this study was the preparation of a 4H-SiC(0001) substrate as described above.From there, Pb was deposited from an evaporation cell on the SiC kept at room temperature, and anneals were performed in front of the LEED by steps of 50°C. One new crystalline phase, with periodicity (2×2), was observed by LEED after Pb deposition on a SiC-$(\sqrt{3}\times\sqrt{3})$R30° surface, as shown in Figure 5.5. Deposition of 1 ML of Pb led to the dissipation of the $(\sqrt{3} \times \sqrt{3})$R30° LEED pattern, leaving only the bulk (1×1) visible. A subsequent anneal with T°= 200-250°C results in a (2×2) pattern, stable up to 500°C, above which the LEED pattern reverts to the $(\sqrt{3}\times\sqrt{3})$R30° surface reconstruction, indicating Pb desorption. We note that the Pb coverage given is only indicative, due to the large imprecision in the calibration realized from a quartz microbalance.

Figure 5.6 shows a top-view schematic representation of the SiC $(\sqrt{3}\times\sqrt{3})$R30° surface reconstruction. On it is represented the (1×1) unit cell, the $(\sqrt{3}\times\sqrt{3})$R30° unit cell, as well as a (2×2) unit cell. Different simple models of adsorption sites for Pb atoms result in a (2×2) periodicity. Most likely, they could rest on H3 sites (at the centre of the hexagons, i.e. at the corners of the unit cell drawn), or occupy some of the T4 sites left empty as well as replace some T4 Si atoms.

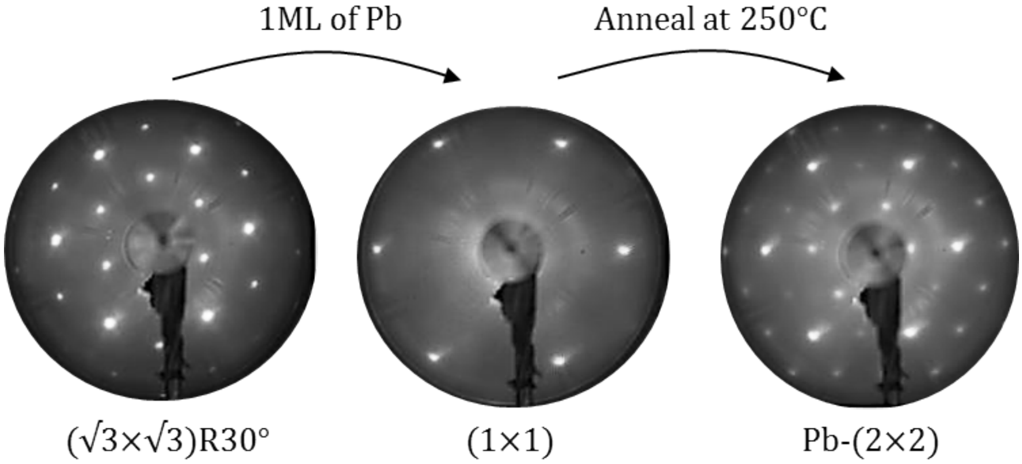

Fig. 5.5 – *Phase diagram of Pb evaporation on SiC* $(\sqrt{3}\times\sqrt{3})R30°$*. Evaporation of 1 ML at room temperature covers the surface reconstruction. After an anneal at 250°C, a (2×2) periodicity appears. Pictures taken at 100 eV, 80 eV and 110 eV respectively.*

In Figure 5.7, we show STM images of the Pb induced (2×2) surface reconstruction. On the large scale image, the formation of 3D faceted Pb islands is observed.Zooming in between the islands, we observe an atomic arrangement with periodicity (2×2) with respect to SiC(0001) surface. By varying the Pb deposition amount and annealing temperature it has been deduced that Pb forms a wetting layer that can crystallize with a (2×2) periodicity under the right conditions, and that extra Pb will form 3D islands, increasing in size with the annealing temperature.

While this (2×2) surface reconstruction has been reproduced on different samples and with different Pb sources in our laboratory, an attempt to reproduce it at Soleil synchrotron failed, possibly due to a difficulty in monitoring precisely the annealing temperatures. However, a complete set of XPS measurements was taken, both on the clean SiC surfaces and after Pb deposition, for the Si 2p, C 1s and Pb 4f core levels. From the LEED patterns, no supplementary crystalline phase was observed. The STM images shown above, as well as most of the fits presented in the next section, are mainly the work of Axel Malecot who will pursue this research project in his ongoing PhD work in our team.

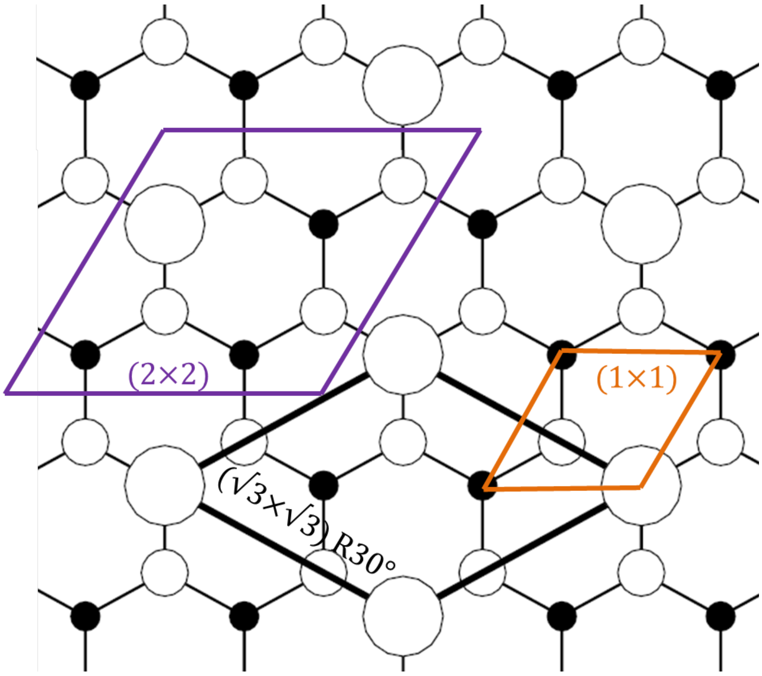

Fig. 5.6 – *Schematic representation of the unit cells of the SiC* $(\sqrt{3}\times\sqrt{3})R30°$ *in black and SiC (1×1) in orange, and a (2×2) unit cell in purple. White circles represent Si atoms, with the larger ones being one atomic plan above, on the T4 adsorption sites. Black circles represent C atoms, located below the Si ones.*

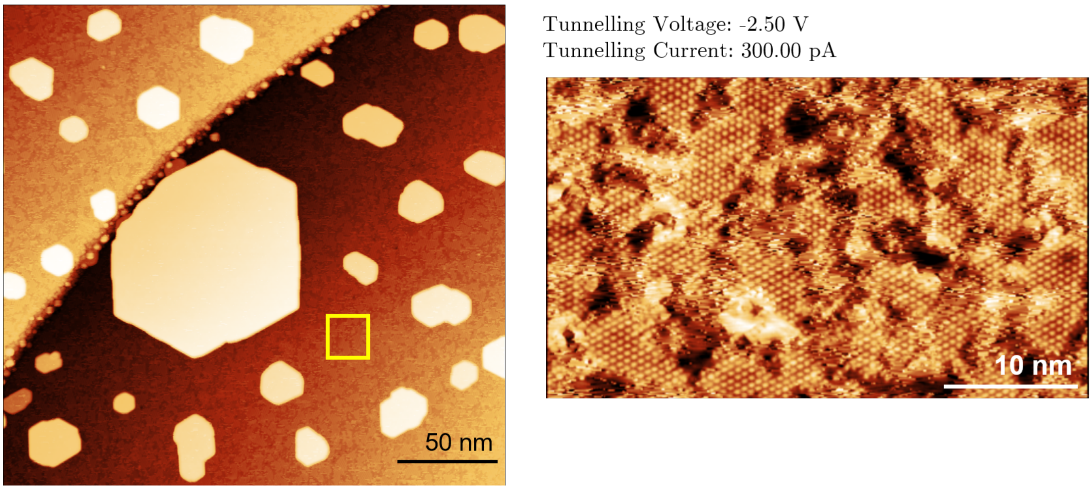

Fig. 5.7 – *STM images of Pb/SiC (2×2) reconstruction. On the large scale image, the formation of Pb 3D islands is observed. On the small scale image, measured in the yellow square area, we observe the atomic resolution of the Pb induced (2×2) phase. Images provided by A. Malecot.*

5.3.2 XPS measurements on Pb/SiC-(3×3)

In Figure 5.8 is shown the Si 2p core level measured on a clean SiC-(3×3) surface, for three photon energies (170 eV, 250 eV, 350 eV). The fits and attribution were made following existing work [29, 30]. In all cases, Voigt functions were used, with a Lorentzian FWHM of 0.15 eV. Four doublets are necessary to fit the spectra: two originates from the bulk (B and B*) and two are surface states (SS1 and SS2), whose origins are represented on the atomic model. The SS1 component comes from the Si adatoms, while the SS2 originates from the Si trimers and Si adlayer atoms. The attribution to the bulk or the surface is justified by the evolution of the peaks' relative area with the photon energy. Bulk peaks increase with increasing photon energy, while surface ones decrease in intensity. It is worth noting that two bulk components are observed, a specificity of the 4H polytype of SiC [30]. The B and B* components originate from the presence of two domains corresponding to different stacking sequences of the last Si-C bilayers. They are however usually not observed on other surface reconstructions than the (3×3).

After deposition of 0.75 ML of Pb on top of a SiC-(3×3) at room temperature, the LEED still shows a clear (3×3) pattern, with no additional spots. In Figure 5.9 (a), (b), and (c), Si 2p fits are presented for photon energies of 170 eV, 250 eV, and 350 eV. The same four doublets as used before Pb deposition yield a good fit. A comparison of the peaks' relative positions, as well as their Gaussian widths are shown in Table 5.1. Here again, Voigt functions were used, with a Lorentzian FWHM of 0.15 eV. Two peak shifts are observed with respect to the bulk peak B: a 0.10 eV shift of the SS2 peak towards lower BE, and a 0.05 eV shift of the B* towards higher BE. We also remark that the SS1 peak, attributed to Si adatoms, has lowered in intensity.

By looking at Figure 5.10 (a) and (b), showing the Pb 4f core level for hv = 287 eV and 387 eV respectively, we see that only one component is sufficient to account for the spectra recorded. The fits were done by a Doniach-Sunjic line-shape to account for the asymmetry of the core level, as is usual for Pb fits, with an FWHM of 0.3 eV and a Gaussian broadening of 0.34 eV. This implies that all Pb atoms have a similar chemical environment. Additionally, the C 1s core level, which remains unchanged before and after Pb deposition as shown in Figure 5.10 (c), indicates

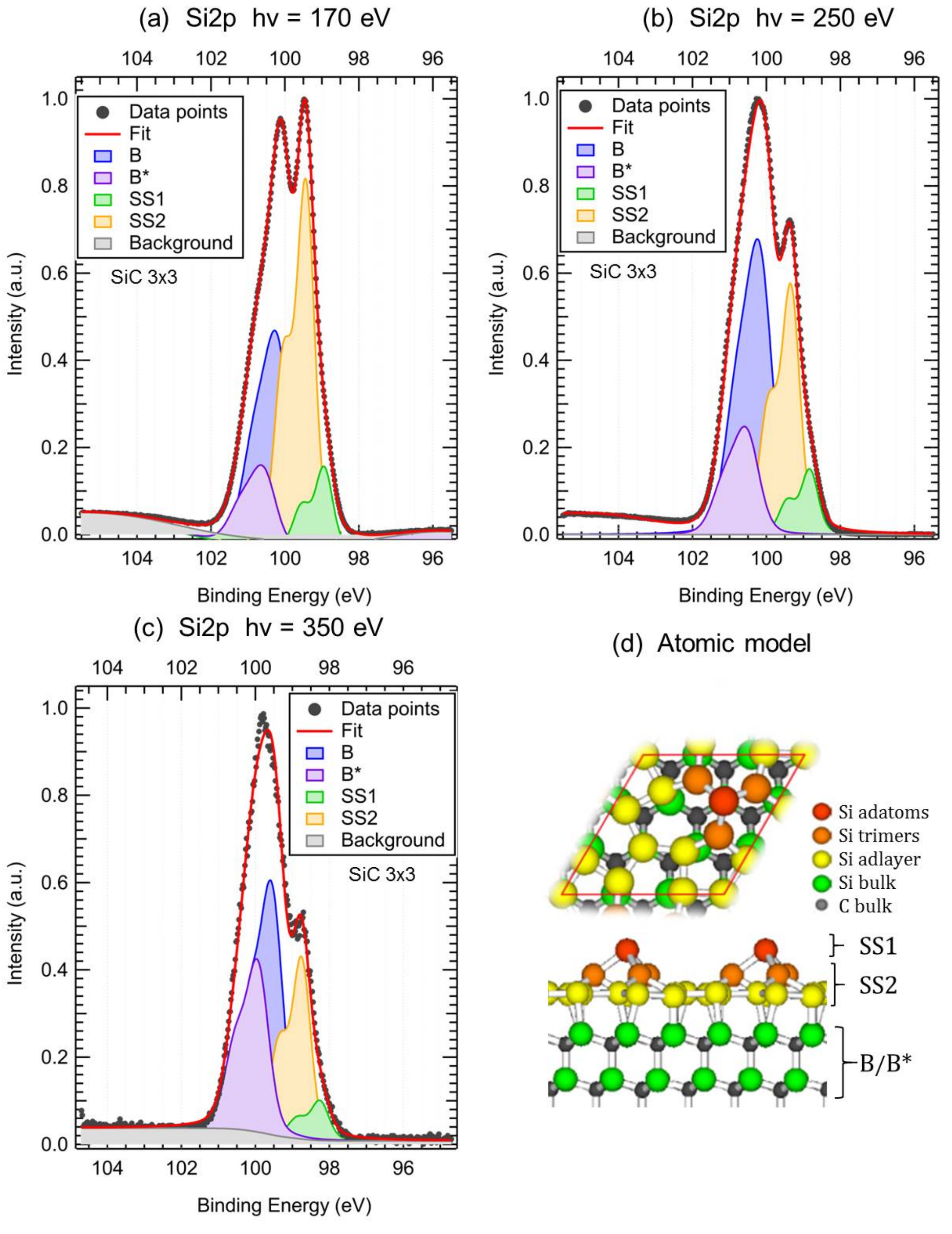

Fig. 5.8 – *Si 2p core level of SiC-(3×3) for three photon energies. For all spectra, an identical set of four doublets are used for the fit. Two doublets originate from the bulk (B and B*) and two from the surface (SS1 and SS2). The origin of the contributions is represented on the atomic model in (d), image from [31]. Fits parameters are given in Table 5.1.*

Relative positions (eV)	B-B*	B-SS1	B-SS2
SiC (3×3)	0.36	1.30	0.80
Pb + SiC (3×3)	0.41	1.31	0.90

Gaussian widths (eV)	B	B*	SS1	SS2
SiC (3×3)	0.80	0.80	0.48	0.48
Pb + SiC (3×3)	0.80	0.80	0.48	0.48

Table 5.1 – Fit parameters and peak positions relative to the bulk peak (BE scale) for the Si 2p core level before and after deposition of 0.75 ML of Pb on SiC-(3×3). All peaks are fitted using Voigt line-shape with a Lorentzian FWHM of 0.15 eV. The precision is given at ±0.02 eV for the binding energies and at ±0.05 eV for the Gaussian broadening.

that Pb atoms stay on the surface and do not interact with the bulk C atoms, only present in the bulk. One possible explanation is that the Pb atoms replace some of the Si adatoms, which would explain nicely the shift observed in SS2, and the diminution in intensity if SS1, which would then be comprised of fewer Si atoms than before Pb deposition. We note however that to be fully coherent with this picture, the presence of the S1 component after Pb depositions indicates that not all Si adatoms are replaced by Pb. We should then have another SS2 peak at the same binding energy as before. It is not clear why it is not observed here, possibly it is not resolved. Another possibility would be that the Pb atoms lie in-between the tetrahedrons formed by the Si adatoms and trimers. Yet another possibility would be that the Pb atoms form an amorphous phase, adsorbing in-between the Si trimers, and that there are unresolved components in the Pb 4f core level. However, the first hypothesis appears favoured by the recent STM measurements performed in our group by A. Malecot at the time of the writing. The existence of a crystalline Pb-(3×3) phase forming on SiC-(3×3) is thus a possibility to explore.

As a side note, measurement of Pb core level showed that annealing above 370°C resulted in the complete desorption of Pb on the SiC-(3×3) surface, indicating a lower adherence on this surface than on the SiC-($\sqrt{3} \times \sqrt{3}$) where we observed Pb up to 550°C, and on epitaxial graphene on a SiC-($6\sqrt{3} \times 6\sqrt{3}$) surface, where

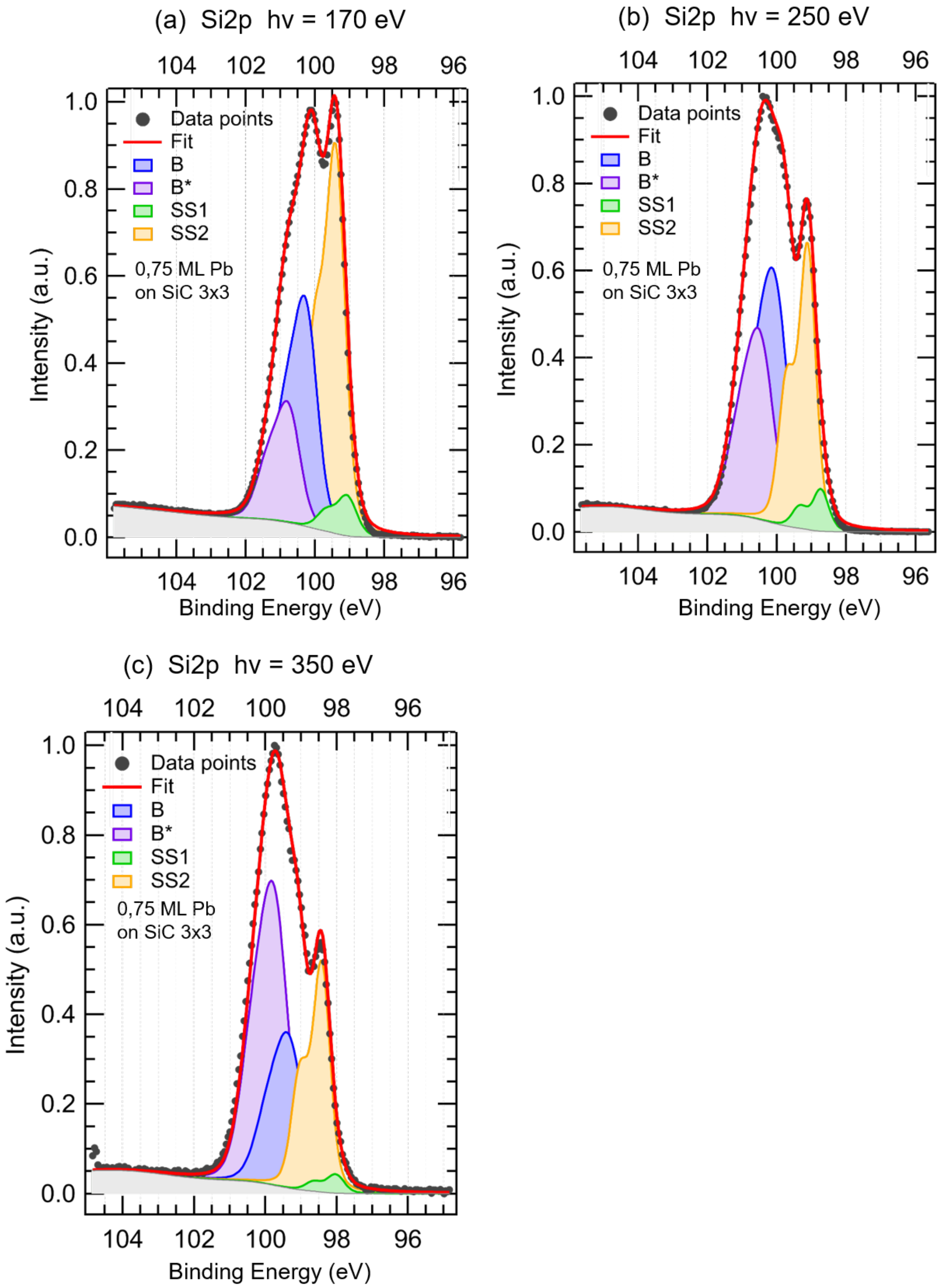

Fig. 5.9 – *Si 2p core level measured after deposition of 0.75 ML of Pb on SiC-(3×3) for three photon energies. (a) shows a superposition of the before/after Pb deposition Si 2p spectra For all spectra, an identical set of four doublets are used for the fit, labelled in the same manner as in Figure 5.8. Fits parameters are given in Table 5.1.*

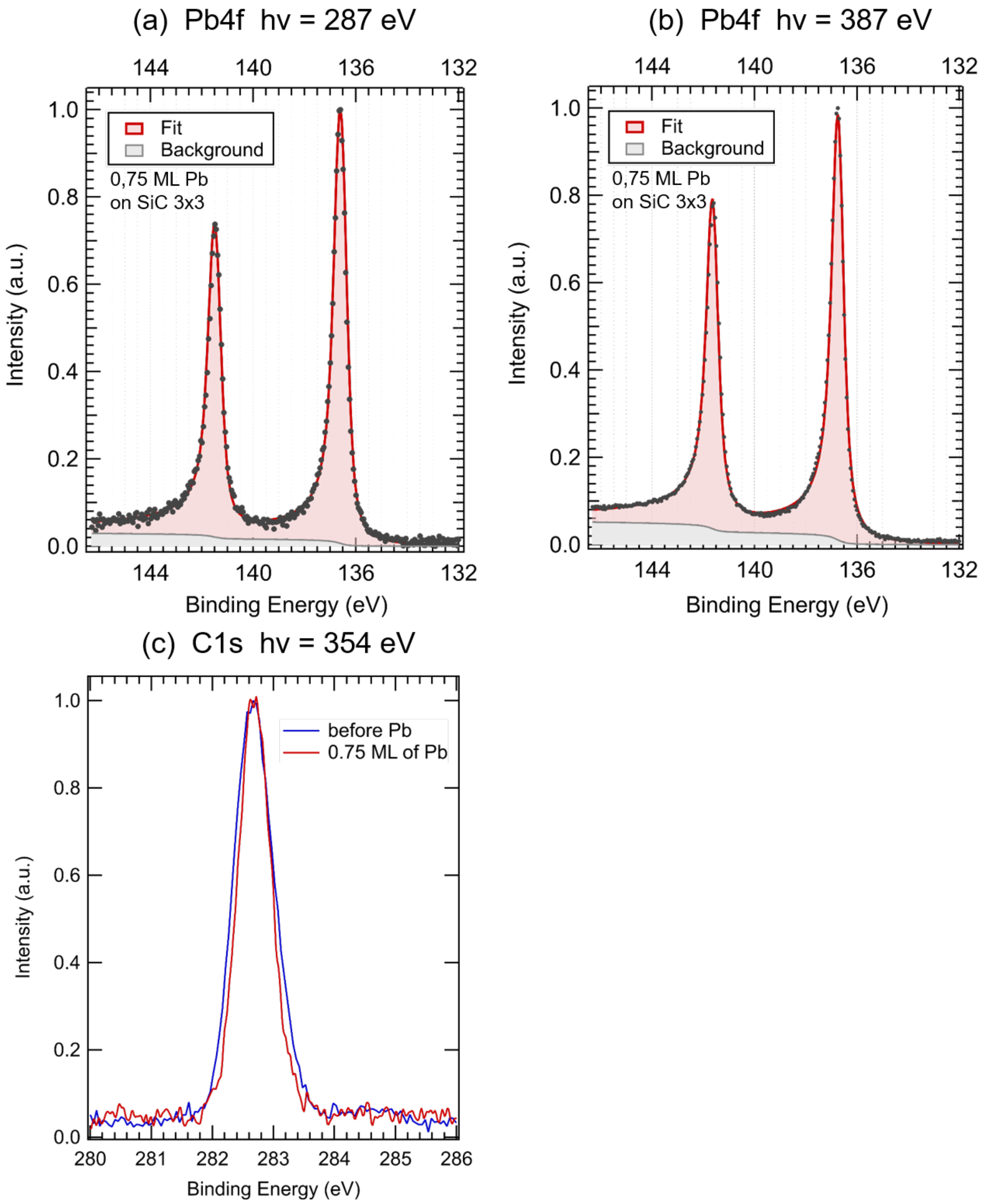

(a) Pb4f hv = 287 eV

(b) Pb4f hv = 387 eV

(c) C1s hv = 354 eV

Fig. 5.10 – *(a) and (b) show the Pb 4f core level measured after deposition of 0.75 ML of Pb on SiC-(3×3) for hv = 287 eV and 387 eV respectively. Only one asymmetric doublet is observed. (c) shows a superposition before/after Pb deposition of the C 1s core level. No difference is observed.*

annealings up to 1250°C have been reported [32] before Pb desorption.

5.3.3 XPS measurements on Pb/SiC-($\sqrt{3}\times\sqrt{3}$)R30°

We now turn to the SiC-($\sqrt{3}\times\sqrt{3}$)R30° surface. Its Si 2p core level was measured and is shown in Figure 5.11. In addition to the bulk peak, three surface components are identified, their area diminishing with increasing photon energy (i.e. with surface sensitivity). Their attributions are represented on the atomic model of the SiC-($\sqrt{3}\times\sqrt{3}$)R30° shown in Figure 5.13: the SS1 peak originates from the last Si atomic layer, while the SS2 peak originates from the Si adlayer, by analogy with the peak attributions made on the SiC-(3×3) surface. The SS3 peak, indistinguishable at less surface sensitive energy, is attributed to the formation of small Si islands on the surface, resulting from the Si deposition that is part of the surface preparation process. Such a component is often found in the literature, such as in [23].

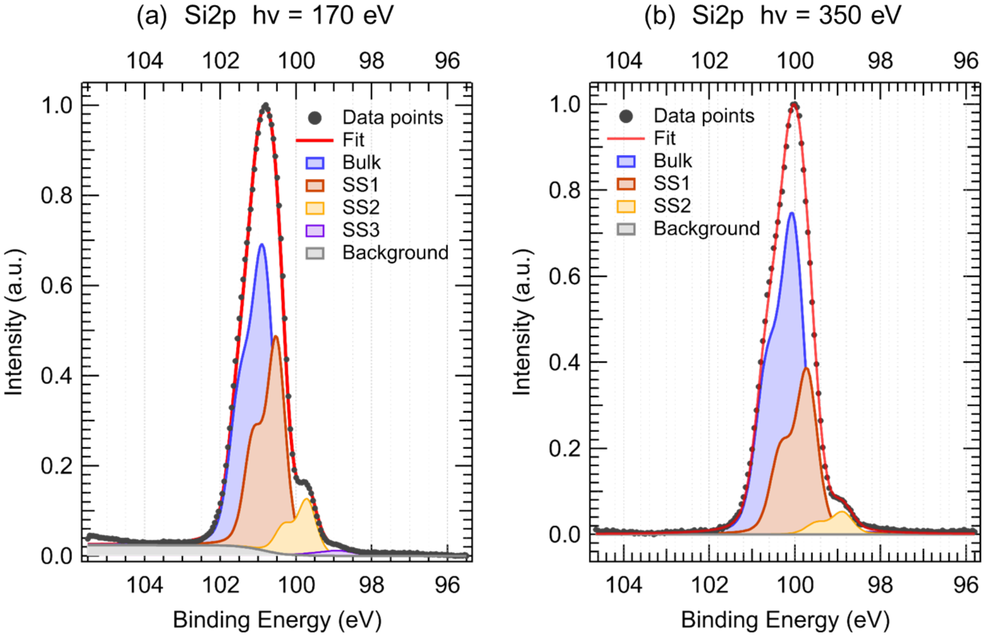

Fig. 5.11 – *Si2p core level of SiC-($\sqrt{3}\times\sqrt{3}$)R30° measured at (a) hv = 170 eV, and (b) hv = 350 eV. Three and four doublets are observed, respectively.*

1 ML of Pb was then deposited on the surface, followed by an anneal at 150-300°C, the exact temperature being difficult to measure with the pyrometer available. The LEED observed is a ($\sqrt{3}\times\sqrt{3}$)R30°, with increased background noise before the annealing. The Si 2p core level is once again measured, shown in Figure 5.12. While the bulk and SS1 peak remained unchanged, a shift of -0.20 eV is

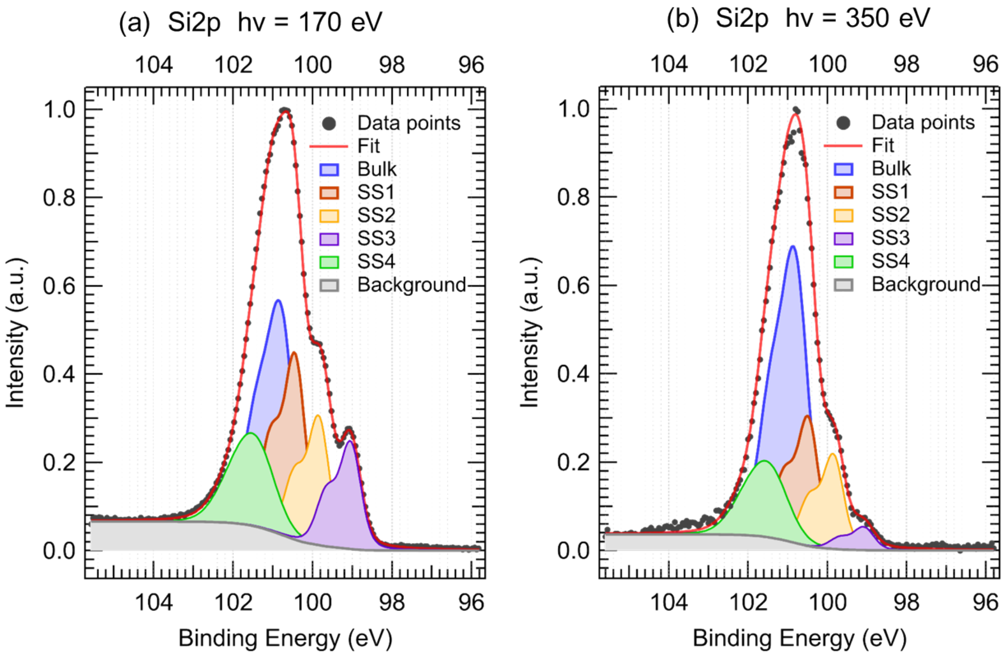

Fig. 5.12 – *Si2p core level of ML of Pb on SiC-($\sqrt{3}\times\sqrt{3}$)R30° measured at (a) hv = 170 eV, and (b) hv = 350 eV. New components are observed.*

observed for SS2, and two new surface components appear, labelled SS3 and SS4. Their attribution to the surface is made once again by looking at the variation of relative areas. Tables comparing the peaks positions, Gaussian broadening, and percentage of the total fit area before and after Pb deposition are shown in Table 5.2. To understand the origin of the new components observed, we will look at the C 1s and Pb 4f core levels, shown in Figure 5.14 and Figure 5.15 respectively.

The C 1s level appears unchanged by the Pb deposition and is in both cases nicely accounted for by a unique Voigt peak with Lorentzian FWHM of 0.30 eV and a Gaussian broadening of 0.48 eV. This indicates that the Pb atoms do not migrate toward the bulk. From the Pb 4f core level, measured at hv = 287 eV and 387 eV, two components are observed. They are fitted with Doniach-Sunjic peaks of width 0.3 eV, as for the (3×3) surface, and a Gaussian broadening of 0.48 eV. The separation between the peaks is 0.75 eV. When surface sensitivity decreases (higher photon energy), a slight increase of SS1 is observed from 89% to 92% of the total fitted area, while SS2 decreases from 11% to 8% of the total fitted area. While this variation is weak, we can posit that the SS1 peak originates from Pb islands, while the SS2 comes from a purely surface component. This interpretation is mo-

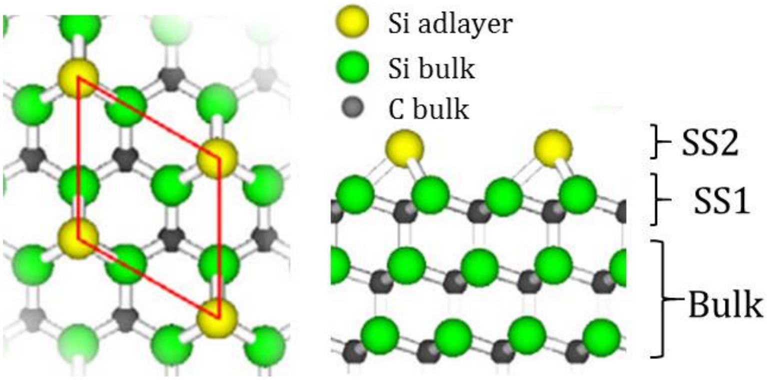

Fig. 5.13 – *Atomic model of SiC-($\sqrt{3}\times\sqrt{3}$)R30° surface reconstruction, formed by a Si adlayer on top of the Si terminated SiC surface. The unit cell is shown in red. The components observed in the Si 2p spectra shown in Figure 5.11 are attributed to atomic positions. Image from [31]*

tivated by STM results: we have observed that Pb on SiC-($\sqrt{3}\times\sqrt{3}$)R30° forms a wetting layer followed by the creation of islands, increasing in size after annealing. The (2×2) periodicity observed in our laboratory is formed by the wetting Pb layer.

Without more information on the atomic structure, it appears difficult to assign a precise origin to the new surface peaks observed in the Si 2p core level. Furthermore, it appears that Pb does not form a crystalline layer on the surface measured: no new LEED spots were seen here, nor bands by ARPES. Further investigation should focus on the Pb induced (2×2) crystalline phase observed on this substrate.

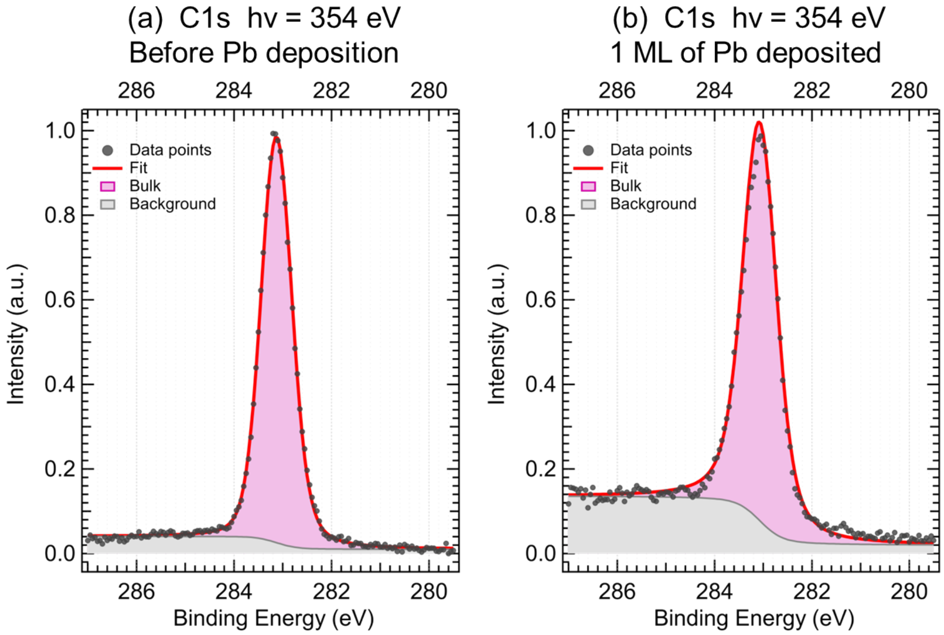

Fig. 5.14 – *C 1s core level before (a) and after (b) 1 ML Pb deposition on SiC-($\sqrt{3}\times\sqrt{3}$)R30°, at hv = 354 eV. The C 1s intensity remains unchanged, originating only from the bulk of SiC, non-interacting with Pb atoms.*

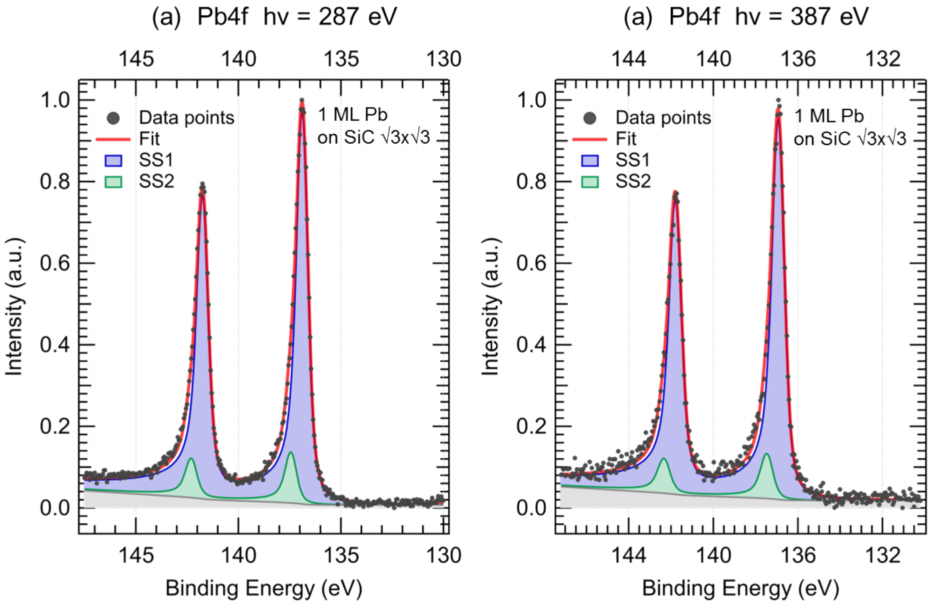

Fig. 5.15 – *Pb 4f core level after deposition of 1 ML of Pb on SiC-($\sqrt{3}\times\sqrt{3}$)R30°, at (a) hv = 287 eV and (b) hv = 387 eV.*

Relative peaks positions (eV)	B-SS1	B-SS2	B-SS3	B-SS4
SiC-($\sqrt{3}\times\sqrt{3}$)R30°	-0.34	-1.17	-2.05	—
1 ML Pb on SiC-($\sqrt{3}\times\sqrt{3}$)R30°	-0.33	-0.97	-1.75	+0.60

Gaussian broadening	B	SS1	SS2	SS3	SS4
SiC-($\sqrt{3}\times\sqrt{3}$)R30°	0.58	0.49	0.49	0.49	—
1 ML Pb on SiC-($\sqrt{3}\times\sqrt{3}$)R30°	0.65	0.52	0.52	0.52	1.00

% of total area		B	SS1	SS2	SS3	SS4
SiC-($\sqrt{3}\times\sqrt{3}$)R30°	170 eV	55.0	34.9	8.9	1.1	—
	350 eV	64.6	31.1	4.3	—	—
1 ML Pb on SiC-($\sqrt{3}\times\sqrt{3}$)R30°	170 eV	38.5	27.1	18.8	15.7	19.0
	350 eV	57.6	22.2	16.2	4.0	18.5

Table 5.2 – Fit parameters for the Si 2p core level before and after deposition of 1 ML of Pb on SiC-($\sqrt{3}\times\sqrt{3}$)R30°. The peak positions are relative to the bulk peak, in BE scale. All peaks are fitted using Voigt line-shape with a Lorentzian FWHM of 0.15 eV. The precision is given at ±0.02 eV for the binding energies and at ±0.05 eV for the Gaussian broadening.

5.3.4 XPS measurements on Pb/SiC-($6\sqrt{3}\times6\sqrt{3}$)R30°

The SiC-($6\sqrt{3}\times6\sqrt{3}$)R30° surface reconstruction has a honeycomb surface organization, terminated by a carbon plan covalently bonded to the Si terminated SiC substrate, as shown above in Figure 5.4. Higher annealing temperatures lead to the creation of graphene/graphite layers on top of the surface [24, 25], which we took care to avoid during our sample preparation. Once the ($6\sqrt{3}\times6\sqrt{3}$)R30° surface was obtained, 1 ML of Pb was evaporated on it, followed by a short anneal at 150-200°C. Following the Pb deposition, the LEED pattern observed was still a ($6\sqrt{3}\times6\sqrt{3}$)R30°. All the fits on the clean SiC surfaces were made in agreement with the work of Silly *et al.* [23]. The C 1s core levels were measured before and after Pb depositions, and are shown in Figure 5.16, and the fit parameters are presented in Table 5.3. On the clean surface, before Pb deposition, three components are observed. By looking at their evolution with photon energy, the bulk peak is easily identified. The two others components, labelled S1 and S2, belong to surface C atoms. The S1 component, located +0.94 eV from the bulk peak, is identified as originating from the C-Si bonds between the surface C layer and the Si layer beneath, and from the Si-C van der Waals interactions between Si left on the surface with the C surface layer. The S2 component, at +1.78 eV, is identified as originating from the C-C bonds in the surface C layer.

After Pb deposition, a new component, labelled S3, is observed at -1.16 eV from the bulk peak and is attributed to C-Pb interactions. From its evolution with photon energy, we see that the C atoms at the origin of this peak are buried. This could be explained by the presence of 3D Pb islands forming on top of the C layer. The C atoms directly below the Pb atoms would then be at the origin of the S3 peak.

The Si 2p core level, presented in Figure 5.17 with its fitting parameter in Table 5.4 appear to support this hypothesis. In addition to the bulk component, three surface components are observed. S1 is attributed to the covalent Si-C bonds between the C layer and the Si bulk last layer. S2 is attributed to the van der Waals Si-C interactions originating from Si that did not sublime during the surface preparation, staying above the C surface layer. Finally, the S3 component is attributed to Si-Si bonds in the non-sublimated surface Si.
After Pb deposition, no new component is observed. There is however 0.2 eV shift in the S2 component, now closer to the bulk peak, and an overall diminution on the intensity of the bulk peak proportionally to the others. The S2 component corresponds to Si atoms resulting from the incomplete sublimation of the last Si layer during the sample preparation, these atoms can be covered by Pb islands, thus explaining the energy shift. Due to the preparation method, a temperature gradient exists on the sample during annealing. A shift in the measurement position before/after Pb deposition could lead to different proportions of non-sublimed Si atoms on the surface.

Finally, we point out that an STM study on graphitized SiC found that Pb forms islands on the last C atomic plan (rather than on graphene domains) and that on the SiC-($6\sqrt{3}\times6\sqrt{3}$)R30°, no wetting layer exists [33], which forms a coherent picture

C 1s SiC-($6\sqrt{3}\times6\sqrt{3}$)R30°

SiC-6V3	B	S1	S2	S3
Relative position to bulk peak (eV)	0	+0.94	+1.78	—
Gaussian width (eV) (hv = 354 eV / hv = 534 eV)	0.74 / 0.65	0.74 / 0.65	0.74 / 0.70	—
Normalized area (hv = 354 eV / hv = 534 eV	0.37 / 1.03	0.40 / 0.37	1.06 / 0.95	—

C 1s Pb/SiC-($6\sqrt{3}\times6\sqrt{3}$)R30°

Relative position to bulk peak (eV)	0	+0.84	+1.76	-1.16
Gaussian width (eV)	0.54	0.77	0.77	0.57
Normalized area (hv = 354 eV / hv = 534 eV	0.27 / 0.91	0.40 / 0.43	1.12 / 1.01	0.04 / 0.10

Table 5.3 – Fit parameters used for the C 1s core level, before and after 1 ML Pb deposition on the SiC-($6\sqrt{3}\times6\sqrt{3}$)R30° surface. Peak positions are given relatively to the bulk peak, in the BE scale. Two photon energies are used and are specified when the parameters used vary from one energy to the other. Voigt functions were used, with a Lorentzian width of 0.39 eV for all peaks. Precision is given at 0.02 eV for the binding energy, 0.05 eV for the Gaussian width, and approximately 5% of a given area.

with our XPS measurements. The last two carbon plans of graphitized SiC can also be decoupled from the substrate by Pb intercalation [28, 32]. It has also been shown that the ZLG could be decoupled from the SiC substrate by intercalation of Si atoms, forming a single layer graphene [23].

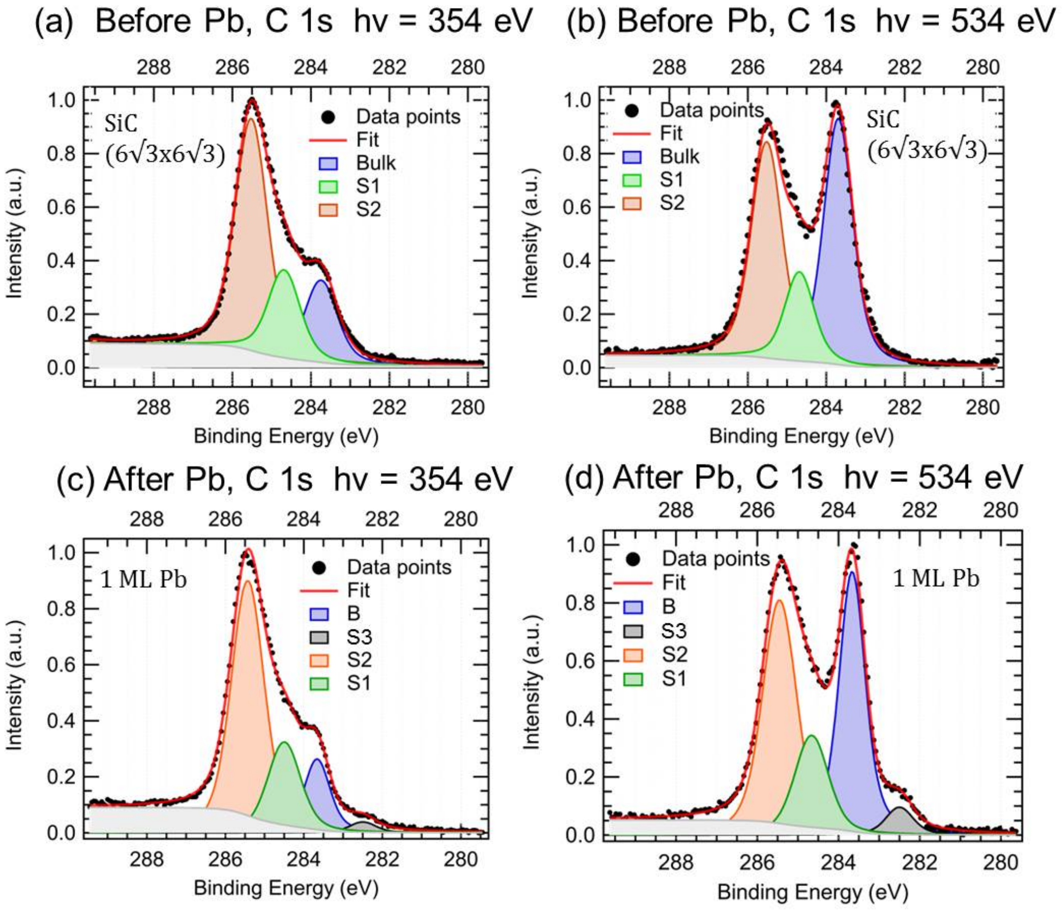

(e) C 1s peaks attribution

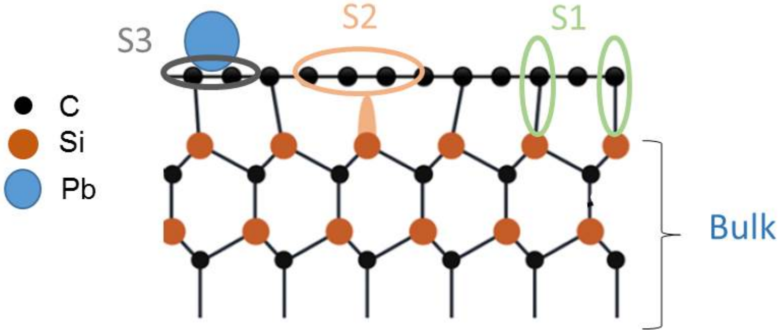

Fig. 5.16 – *C 1s core level before (a, b) and after (c, d) 1 ML Pb deposition on SiC-($6\sqrt{3}\times6\sqrt{3}$)R30°. The doublets are attributed to specific C atoms following the atomic model (e)*

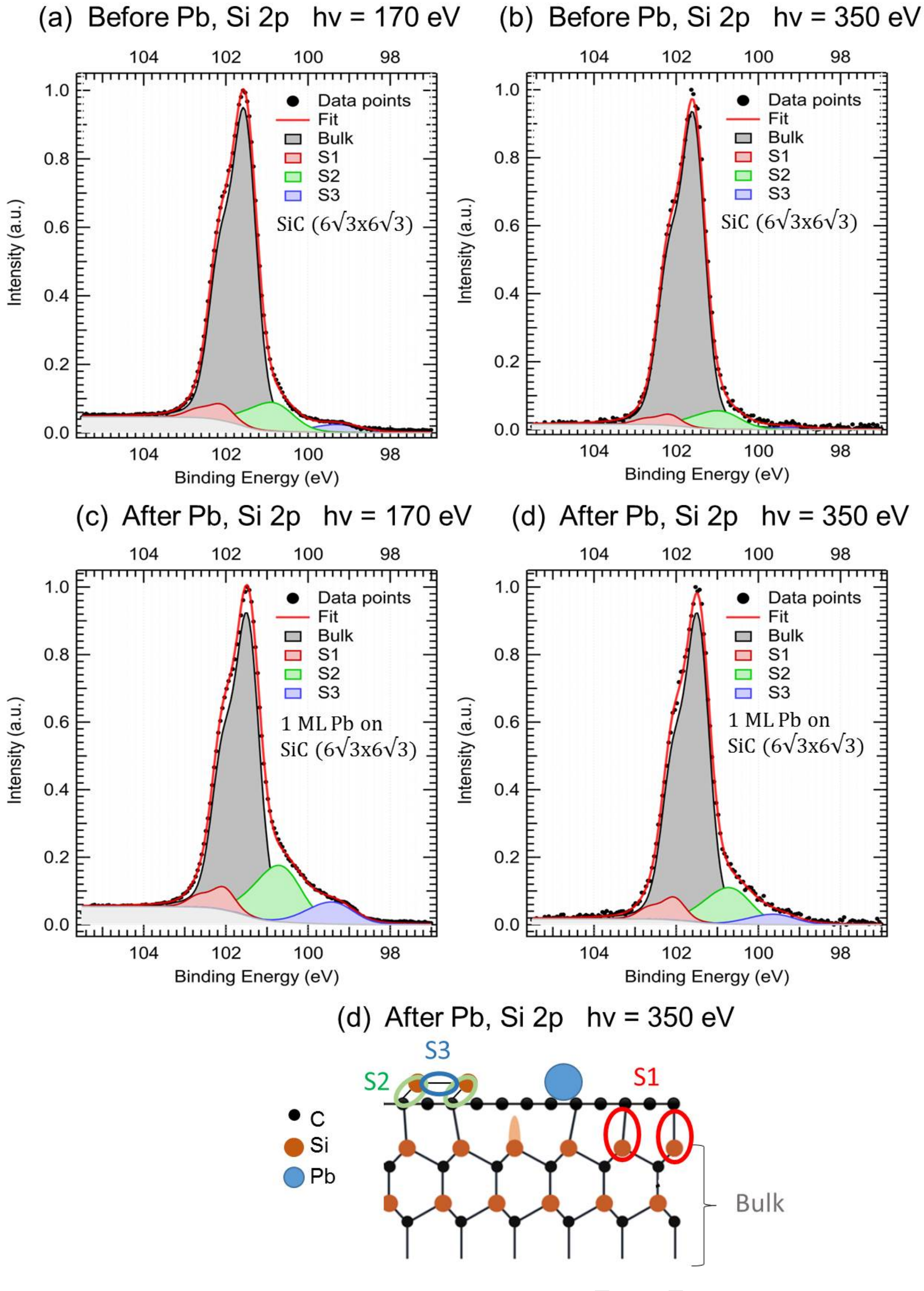

Fig. 5.17 – *Si 2p core level measured on SiC-($6\sqrt{3}\times6\sqrt{3}$)R30° before (a, b) and after deposition of 1 ML of Pb (c, d), for two photon energies. In all spectra, four components are observed, and their attribution is shown in (e) on the atomic model.*

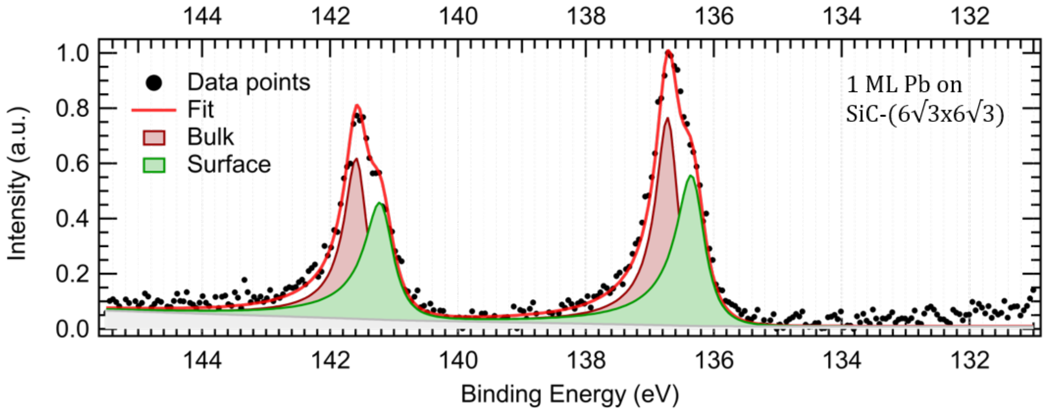

(a) Pb 4f hv = 287 eV

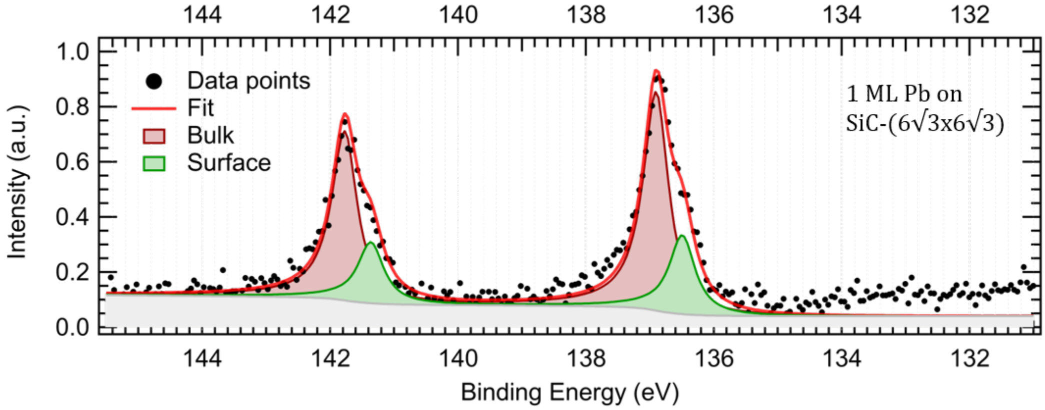

(b) Pb 4f hv = 387 eV

Fig. 5.18 – *Pb 4f core level of 1 ML Pb/SiC-*$(6\sqrt{3}\times6\sqrt{3})R30°$*, for two photon energies. Two components are observed, separated by 0.40 eV. One increases in intensity with photon energy and is attributed to bulk Pb, and one diminishes in intensity with increasing photon energy and is attributed to surface Pb atoms.*

Si 2p SiC-(6$\sqrt{3}$×6$\sqrt{3}$)R30°

SiC-6V3	B	S3	S2	S1
Relative position to bulk peak (eV)	0	-2.15 ± 0.1	-0.73	+0.55
Gaussian width (eV)	0.58	0.99	1.00	0.55
Normalized area (hv = 170 eV / hv = 350 eV	1.01 / 1.02	0.03 / 0.01	0.14 / 0.05	0.07 / 0.04
Si 2p Pb/SiC-(6$\sqrt{3}$×6$\sqrt{3}$)R30°				
Relative position to bulk peak (eV)	0	-2.15 ± 0.1	-0.92	+0.58
Gaussian width (eV)	0.58	0.99	1.00	0.55
Normalized area (hv = 170 eV / hv = 350 eV	0.97 / 1.01	0.09 / 0.04	0.24 / 0.16	0.06 / 0.07

Table 5.4 – Fit parameters used for the Si 2p core level, before and after 1 ML Pb deposition on the SiC-(6$\sqrt{3}$×6$\sqrt{3}$)R30° surface. Peak positions are given relatively to the bulk peak, in the BE scale. Two photon energies are used and are specified when the parameters used vary from one energy to the other. Voigt functions were used, with a Lorentzian width of 0.15 eV for all peaks. Precision is given at 0.02 eV for the binding energy, 0.05 eV for the Gaussian width, and approximately 5% of a given area.

5.3.5 Conclusion and perspectives

From this exploratory work of Pb deposition on SiC(0001), some interesting new results were obtained. A Pb induced (2×2) phase was observed after Pb deposition and annealing on a SiC-($\sqrt{3} \times \sqrt{3}$)R30° surface. Our results also raise the possibility of an ordered Pb phase on SiC-(3 × 3) preserving the lattice periodicity. This hypothesis of a (3×3) Pb adatom layer replacing the ones of the SiC-(3×3) is being tested by STM as part of the ongoing experimental work carried out in our team. Those crystalline Pb-induced phases are not reported in the literature so far. No other crystalline periodicity has been observed by LEED after Pb deposition on SiC-(3 × 3) or SiC-($\sqrt{3} \times \sqrt{3}$)R30°. No crystalline layer was observed after Pb deposition on the SiC-(6$\sqrt{3} \times 6\sqrt{3}$)R30° surface. Instead, it appears that Pb forms 3D islands when annealed at low temperature (≈ 250°C).

The results presented here will serve as the groundwork for the ongoing PhD thesis of Axel Malecot, in which STM and spectroscopy for Pb on all surfaces reconstruction of SiC, including the ones from the C-terminated face, will be investigated. Additionally, the possibility to prepare a clean, unreconstructed SiC(0001) surface by chemical preparation will be taken into consideration. The electronic properties of the crystalline layers of Pb on SiC should be investigated, with the prospect of finding a topological insulator phase with a large gap, while keeping open other possibilities.

Bibliography of Chapter 5

[1] C. L. Kane and E. J. Mele, "Z_2 topological order and the quantum spin Hall effect", *Phys. Rev. Lett.*, vol. 95, p. 146 802, 14 Sep. 2005. DOI: 10.1103/PhysRevLett.95.146802 (cited on p. 193).

[2] C. L. Kane and E. J. Mele, "Quantum spin Hall effect in graphene", *Phys. Rev. Lett.*, vol. 95, p. 226 801, 22 Nov. 2005. DOI: 10.1103/PhysRevLett.95.226801 (cited on p. 193).

[3] Y. H. Lu, D. Zhou, T. Wang, S. A. Yang, and J. Z. Jiang, "Topological properties of atomic lead film with honeycomb structure", *Scientific Reports*, vol. 6, no. 1, Apr. 2016. DOI: 10.1038/srep21723 (cited on p. 193).

[4] H. Zhao, C.-W. Zhang, W.-X. Ji, R.-W. Zhang, S.-S. Li, S.-S. Yan, B.-M. Zhang, P. Li, and P.-J. Wang, "Unexpected giant-gap quantum spin hall insulator in chemically decorated plumbene monolayer", *Scientific Reports*, vol. 6, no. 1, Apr. 2016. DOI: 10.1038/srep20152 (cited on p. 193).

[5] X.-L. Yu, L. Huang, and J. Wu, "From a normal insulator to a topological insulator in plumbene", *Physical Review B*, vol. 95, no. 12, Mar. 9, 2017. DOI: 10.1103/PhysRevB.95.125113 (cited on p. 193).

[6] A. Visikovskiy, S. Hayashi, T. Kajiwara, F. Komori, K. Yaji, and S. Tanaka, "Computational study of heavy group IV elements (Ge, Sn, Pb) triangular lattice atomic layers on SiC(0001) surface", *arXiv:1809.00829 [cond-mat]*, Sep. 4, 2018. arXiv: 1809.00829 (cited on p. 193).

[7] J. Yuhara and G. Le Lay, "Beyond silicene: synthesis of germanene, stanene and plumbene", *Japanese Journal of Applied Physics*, vol. 59, SN0801, SN Aug. 1, 2020. DOI: 10.35848/1347-4065/ab8410 (cited on p. 193).

[8] J. Yuhara, B. He, N. Matsunami, M. Nakatake, and G. Le Lay, "Graphene's latest cousin: plumbene epitaxial growth on a "nano WaterCube"", *Advanced Materials*, vol. 31, no. 27, p. 1 901 017, Jul. 2019. DOI: 10.1002/adma.201901017 (cited on p. 193).

[9] F. Reis, G. Li, L. Dudy, M. Bauernfeind, S. Glass, W. Hanke, R. Thomale, J. Schäfer, and R. Claessen, “Bismuthene on a SiC substrate: a candidate for a high-temperature quantum spin hall material”, *Science*, vol. 357, no. 6348, pp. 287–290, Jul. 21, 2017. DOI: `10.1126/science.aai8142` (cited on pp. 193, 195).

[10] S. Glass, G. Li, F. Adler, J. Aulbach, A. Fleszar, R. Thomale, W. Hanke, R. Claessen, and J. Schäfer, “Triangular spin-orbit-coupled lattice with strong Coulomb correlations: Sn atoms on a SiC(0001) substrate”, *Phys. Rev. Lett.*, vol. 114, p. 247 602, 24 Jun. 2015. DOI: `10.1103/PhysRevLett.114.247602` (cited on p. 193).

[11] C. Tresca, C. Brun, T. Bilgeri, G. Menard, V. Cherkez, R. Federicci, D. Longo, F. Debontridder, M. D’angelo, D. Roditchev, G. Profeta, M. Calandra, and T. Cren, “Chiral spin texture in the charge-density-wave phase of the correlated metallic Pb/Si(111) monolayer”, *Phys. Rev. Lett.*, vol. 120, p. 196 402, 19 May 2018. DOI: `10.1103/PhysRevLett.120.196402` (cited on p. 194).

[12] C. Brun, T. Cren, and D. Roditchev, “Review of 2D superconductivity: the ultimate case of epitaxial monolayers”, *Superconductor Science and Technology*, vol. 30, no. 1, p. 013 003, Nov. 2016. DOI: `10.1088/0953-2048/30/1/013003` (cited on p. 194).

[13] W. J. Choyke, H. Matsunami, and G. Pensl, Eds., *Silicon carbide: recent major advances*, Advanced Texts in Physics, Berlin: Springer Berlin, 2013, ISBN: 3642623336 (cited on pp. 194–196).

[14] R. Cheung, *Silicon Carbide Microelectromechanical Systems for Harsh Environments.* Imperial College Press, 2006, ISBN: 9781860946240 (cited on p. 194).

[15] S. Mitridis, in *Determination of lattice site location of impurities in compound semiconductors, by transmission electron microscopy*, ser. Physics of Advanced Materials Winter School 2008, Mar. 2011 (cited on p. 195).

[16] T. Teraji and S. Hara, “Control of interface states at metal/6H-SiC(0001) interfaces”, *Physical Review B*, vol. 70, no. 3, Jul. 22, 2004. DOI: `10.1103/PhysRevB.70.035312` (cited on p. 195).

[17] M. Losurdo, M. M. Giangregorio, P. Capezzuto, G. Bruno, A. S. Brown, T.-H. Kim, and C. Yi, “Modification of 4H-SiC and 6H-SiC(0001)Si surfaces through the interaction with atomic hydrogen and nitrogen”, *Journal of Electronic Materials*, vol. 34, no. 4, pp. 457–465, Apr. 2005. DOI: `10.1007/s11664-005-0127-0` (cited on p. 195).

[18] U. Starke, “Surface reconstruction on SiC(0001) and SiC(000-1): atomic structure and potential application for oxidation, stacking and growth”, *Materials Science Forum*, vol. 353-356, pp. 205–210, Jan. 2001. DOI: `10.4028/www.scientific.net/MSF.353-356.205` (cited on pp. 195, 196).

[19] T. Seyller, “Passivation of hexagonal SiC surfaces by hydrogen termination”, *Journal of Physics: Condensed Matter*, vol. 16, no. 17, S1755–S1782, Apr. 2004. DOI: `10.1088/0953-8984/16/17/016` (cited on p. 195).

[20] S. Glass, F. Reis, M. Bauernfeind, J. Aulbach, M. R. Scholz, F. Adler, L. Dudy, G. Li, R. Claessen, and J. Schäfer, “Atomic-scale mapping of layer-by-layer hydrogen etching and passivation of SiC(0001) substrates”, *The Journal of Physical Chemistry C*, vol. 120, no. 19, pp. 10 361–10 367, May 19, 2016. DOI: `10.1021/acs.jpcc.6b01493` (cited on p. 195).

[21] K. Heinz, J. Bernhardt, J. Schardt, and U. Starke, “Functional surface reconstructions of hexagonal SiC”, *Journal of Physics: Condensed Matter*, vol. 16, no. 17, S1705–S1720, May 5, 2004. DOI: `10.1088/0953-8984/16/17/013` (cited on p. 196).

[22] A. Coati, M. Sauvage-Simkin, Y. Garreau, R. Pinchaux, T. Argunova, and K. Aïd, “$(\sqrt{3}\times\sqrt{3})$R30° reconstruction of the 6H-SiC (0001) surface: a simple T4 Si adatom structure solved by grazing-incidence x-ray diffraction”, *Phys. Rev. B*, vol. 59, pp. 12 224–12 227, 19 Jun. 1999. DOI: `10.1103/PhysRevB.59.12224` (cited on p. 196).

[23] M. Silly, M. D’Angelo, A. Besson, Y. Dappe, S. Kubsky, G. Li, F. Nicolas, D. Pierucci, and M. Thomasset, “Electronic and structural properties of graphene-based metal-semiconducting heterostructures engineered by silicon intercalation”, *Carbon*, vol. 76, pp. 27–39, Sep. 2014. DOI: `10.1016/j.carbon.2014.04.033` (cited on pp. 196, 207, 211, 213).

[24] X. Xie, H. Wang, A. Wee, and K. P. Loh, “The evolution of 3×3, 6×6, $(\sqrt{3} \times \sqrt{3})$R30° and $(6\sqrt{3} \times 6\sqrt{3})$R30° superstructures on 6H–SiC (0001) surfaces studied by reflection high energy electron diffraction”, *Surface Science*, vol. 478, no. 1, pp. 57–71, 2001, ISSN: 0039-6028. DOI: `10.1016/S0039-6028(00)01064-5` (cited on pp. 196, 211).

[25] W. Chen, H. Xu, L. Liu, X. Gao, D.-c. Qi, G.-w. Peng, S. C. Tan, Y. P. Feng, K. P. Loh, and A. T. S. Wee, “Atomic structure of the 6H-SiC(0001) nanomesh”, *Science & Engineering Faculty*, 2005. DOI: `10.1016/j.susc.2005.09.013` (cited on pp. 196, 211).

[26] F. Hiebel, P. Mallet, L. Magaud, and J.-Y. Veuillen, “Atomic and electronic structure of monolayer graphene on 6H-SiC(000-1)(3×3): a scanning tunneling microscopy study”, *Physical Review B*, vol. 80, p. 235 429, 23 Dec. 2009. DOI: `10.1103/PhysRevB.80.235429` (cited on p. 196).

[27] C. Riedl, C. Coletti, and U. Starke, “Structural and electronic properties of epitaxial graphene on SiC(0001): a review of growth, characterization, transfer doping and hydrogen intercalation”, *Journal of Physics D: Applied Physics*, vol. 43, no. 37, p. 374 009, Sep. 22, 2010. DOI: `10.1088/0022-3727/43/37/374009` (cited on p. 196).

[28] D. Yang, Q. Xia, H. Gao, S. Dong, G. Zhao, Y. Zeng, F. Ma, and T. Hu, “Fabrication and mechanism of Pb-intercalated graphene on SiC”, *Applied Surface Science*, vol. 569, p. 151 012, Dec. 2021. DOI: `10.1016/j.apsusc.2021.151012` (cited on pp. 196, 213).

[29] F. Amy, “Identification of the 6H-SiC(0001) 3×3 surface reconstruction core-level shifted components”, *Surface Science*, p. 6, 2000. DOI: `10.1016/S0039-6028(00)00637-3` (cited on p. 201).

[30] F. Amy, “Oxydation a l’echelle atomique de la surface (0001)-(3×3) du SiC hexagonal (α) et formation/controle de l’interface SiO_2/ α-SiC”, Fr, PhD thesis, Université de Paris Sud, 2000. [Online]. Available: `http://www.theses.fr/2000PA112251` (cited on p. 201).

[31] G. Baffou, “Luminescence induite par microscopie à effet tunnel et étude des propriétés électroniques, chimiques et optiques de la surface de carbure de silicium 6H-SiC(0001)3×3”, Fr, PhD thesis, Université Paris Sud - Paris XI,

Sep. 2007. [Online]. Available: `https://tel.archives-ouvertes.fr/tel-00190955` (cited on pp. 202, 209).

[32] A. Yurtsever, J. Onoda, T. Iimori, K. Niki, T. Miyamachi, M. Abe, S. Mizuno, S. Tanaka, F. Komori, and Y. Sugimoto, “Effects of pb intercalation on the structural and electronic properties of epitaxial graphene on SiC”, *Small*, vol. 12, no. 29, pp. 3956–3966, Aug. 2016. DOI: `10.1002/smll.201600666` (cited on pp. 206, 213).

[33] X. T. Liu, T. W. Hu, Y. P. Miao, D. Y. Ma, P. K. Chu, F. Ma, and K. W. Xu, “Selective growth of Pb islands on graphene/SiC buffer layers”, *Journal of Applied Physics*, vol. 117, no. 6, p. 065 304, Feb. 14, 2015. DOI: `10.1063/1.4908013` (cited on p. 212).

Conclusions and perspectives

Conclusions and perspectives

The research presented here aimed at providing a better understanding of two-dimensional Dirac nodal line systems, with a focus on the experimental realization, as there are hardly any reported in the literature so far. These systems can serve as good platforms to study topological phase transitions in two-dimensional materials, and could be used for high-speed electronics devices.

The main techniques used for characterization were x-ray photoelectron and angle-resolved photoelectron spectroscopy (XPS and ARPES), mostly performed using synchrotron sources, as well as some low energy electron diffraction (LEED) and scanning tunnelling microscopy (STM). Two systems are at the centre of our work: Cu_2Si and Cu_2Ge. They are 2D systems with a hexagonal lattice, which have been predicted to host Dirac nodal lines as free-standing monolayers. In 2017, Cu_2Si was the first 2D Dirac nodal line (DNL) system to have been experimentally realized, and one of the starting points of our project, while prediction of the electronic properties of Cu_2Ge made in 2020 extended our research scope.

In chapter 3 we presented our work on Cu_2Si. As a first step, we successfully synthesized and characterized Cu_2Si on a Cu(111) substrate, confirming the results existing in the literature: the presence of two concentric Dirac nodal lines centred around Γ, located in the first eV below the Fermi level. This indicates negligible interactions between the surface monolayer and the Cu bulk.

In a second step, we investigated the effect of heavy element deposition, namely Pb, on the system Cu_2Si/Cu(111). Heavy-element adsorption of 2D systems has been shown to increase its intrinsic spin-orbit coupling, leading to possible gap openings and/or lift of degeneracy in electronic bands. Furthermore, any adsorption would break the mirror symmetry of a 2D layer, which should also result in a gap opening in one of the nodal lines of Cu_2Si. Instead, we find that the Dirac nodal lines are preserved in the presence of Pb: no gap opening has been observed within our experimental resolution. Additionally, a splitting of one of the electronic bands has been observed, attributed to a SOC increase induced by Pb, but spin-

ARPES measurements were inconclusive in determining if the split bands were spin-polarized. A surface state originating in the Pb overlayer has also been measured. This is an encouraging result in the optics of future devices: the nodal lines are more robust than expected, increasing the possibilities for capping of the monolayer and for the realization of heterostructures with 2D systems, each preserving their properties.

Finally, we studied the properties of Cu_2Si/Si(111), as finding a non-conductive substrate is necessary for electronic applications. While this system was already described in the literature, the question of the presence of DNLs and comparison with freestanding Cu_2Si was not raised at the time of these studies. XPS measurements were realized, showing good agreement with the established structural model. We furthermore provided a complete characterization of the band structure of the system, improving on previously reported results with the help of synchrotron radiation. By comparing the experimental results with density functional theory (DFT) band calculations, we observed that the electronic states originating from x-y (in-plane) orbitals remained unchanged but those originating from z- (out-of-plane) orbitals, especially p_z orbitals, are modified when the Cu_2Si layer is prepared on a Si substrate. One of the bands predicted for the free-standing system strongly hybridizes with the substrate, preventing the existence of nodal lines in this system. The two other electronic bands remain almost unperturbed, and display a linear dispersion. The challenge of finding a non-metallic substrate for Cu_2Si is thus still open.

In chapter 4 we take interest in Cu_2Ge, which has been predicted to host DNLs as a monolayer but lacks any experimental realization. We showed, supported by an array of measurements, that the surface synthesized exhibits properties compatible with the successful realization of Cu_2Ge on Cu(111). Regarding the atomic structure, a $(\sqrt{3} \times \sqrt{3})R30°$ LEED pattern was observed after Ge evaporation on Cu(111) and Ge atoms showed a single adsorption site using XPS, in agreement with the expectations for a monolayer Cu_2Ge. More importantly, we observed by ARPES the presence of three bands crossing each other without any detectable gap, in excellent agreement with the DFT predictions, save for a vertical shift of 0.15 eV attributed to charge transfer from the Cu substrate. We thus posit to have successfully synthesized Cu_2Ge, with interactions weak enough with its Cu(111) substrate to not disturb or gap the DNLs. This would be one of the few experimental reports of a two-dimensional DNL material.

Concomitantly, we studied the growth of Ge on Cu(111), resulting in a ("8.88×8.88")R30° surface reconstruction, in an attempt to obtain Cu_2Ge on a semiconductor substrate and performed mirror experiments to the ones realized above. The electronic structure of the surface obtained differs vastly from the Cu_2Ge monolayer, with a notable absence of band crossing, the presence of intense bands near the Γ point originating from Ge(111), and strong umklapp features observed on the Fermi surface. Two elements are proposed to explain those differences. The most obvious originates from the study of the atomic structure: indeed, from the existing literature and our results, it appears clear that Cu/Ge(111) does not form a planar surface and could have a different surface stoichiometry than Cu_2Ge, resulting in a system entirely different from the theoretical Cu_2Ge or the experimental Cu_2Ge/Cu(111). However, we note that a buckled Cu_2Ge surface could have led to gaped DNL states, interesting on their own. This gets us to the second element explaining the different electronic band structure: the choice of substrate. Indeed, the Ge(111) substrate presents dangling bonds and forms strong bonds with the Cu evaporated on top, making it impossible in this case to obtain a surface decoupled from the substrate as in the case of Cu_2Ge/Cu(111), which also leads to the discommensuration and thus the umklapp states. By analogy with Cu_2Si/Si(111), we also hypothesize that the absence of an electron-like band might originate from the hybridization of out-of-plane orbitals of the substrate with the surface. Despite the absence of DNLs in this system, this work is, to our knowledge, the first complete electronic structure characterization of the ("8.88×8.88")R30° surface reconstruction of Cu/Ge(111).

In the last chapter, chapter 5, we present an initial work on the system Pb/SiC, motivated by the prediction of large gap quantum spin hall effect in honeycomb monolayer Pb and SiC being a suitable substrate for electronic applications. Pb was evaporated on the three main SiC(0001) surface reconstructions, and XPS spectra are presented. A (2×2) Pb-induced surface reconstruction was observed for the first time after deposition of the SiC $(\sqrt{3} \times \sqrt{3})$ surface, showing a crystalline organisation, and our measurement point towards the existence of a crystalline (3×3) Pb-induced phase on the SiC-(3×3) substrate. This work will be pursued in a fullyfledged PhD thesis.

The work presented here is a step towards the understanding and use of two-dimensional Dirac nodal line materials. We illustrated the difficulties arising from semiconductor substrates, while successfully preparing monolayers on Cu(111) substrate. We confirmed the properties of Cu_2Si and showed their stability even after Pb adsorption, while realizing for the first time the 2D DNL material Cu_2Ge. These systems are possible candidates for high-frequency electronic applications due to the high-velocity charges carriers arising from the linear dispersion, and to the high density of states at the DNL. Potential applications also include nanoscale and gas sensors.

Several avenues of work would be worth investigating. One is finding a suitable non-conductive substrate on which to grow Cu_2Si or Cu_2Ge, possibly by using passivated surfaces that minimize surface interactions. Another would be to develop a method to transfer a monolayer grown on Cu(111) on another substrate. Doping of the monolayer could also shift the nodal lines closer to the Fermi level, which is important for applications. A study of the air stability of these systems would also be necessary. From a more fundamental approach, one could take interest in the study of gap openings at the nodal lines, and in the characterization of the topological order of the resulting insulator. Additionally, the superconductivity predicted in Cu_2Si could be worth investigating but would require a substrate inducing less strain than Cu(111) in the monolayer. Finally, it was predicted that edge states of Cu_2Si could be magnetic, which has not been the object of experimental measurements yet.

Subject : An experimental approach to the realization and characterization of the two-dimensional Dirac nodal line materials Cu_2Si and Cu_2Ge: Influence of the substrate and of Pb-deposition on the electronic band structure.

Abstract: The realization of new two-dimensional materials is a booming field of condensed matter, at once for the fundamental aspects, with the exotic properties emerging from the reduced dimensionality, and for the potential technological applications, with promises such as dissipationless currents and 2D heterostructures outperforming the current silicon-based technology at a fraction of the size.

In this work, we took an experimental approach to the realization and characterization of materials predicted to host Dirac nodal lines (DNLs), which despite many theoretical predictions have seen few experimental realizations reported so far. These materials belong to the recently evidenced class of topological semimetals, whose specificity is a symmetry-protected band crossing of the valence and conduction bands along a line in momentum space, with linear dispersion. As a first step, we focused on Cu_2Si, the first 2D material in which DNLs have been evidenced when prepared on a Cu(111) substrate. After successfully reproducing existing results, we showed using ARPES and XPS that contrary to expectations, the DNLs were preserved after deposition of Pb on the surface without any gap, and that a band splitting occured. We followed by the investigation of Cu_2Si/Si(111), and found that despite a strongly related atomic structure, the Si(111) substrate interacts strongly enough with the out-of-plane orbitals of the Cu_2Si layer to prevent the existence of the nodal lines.

We then looked at the 2D Cu_2Ge system, predicted to host DNL, and attempted to synthesize it by depositing Ge on Cu(111). By combining our LEED, XPS and ARPES results we found that all measurements matched closely what was expected from a free-standing Cu_2Ge monolayer, showing the almost complete absence of interactions between the Cu(111) substrate and the surface Cu_2Ge layer grown on it. This is the first reported experimental realization of the two-dimensional Dirac nodal line semimetal Cu_2Ge. In a mirroring study, we deposited Cu on Ge(111) and observed a dissimilar band structure. Helped by STM, we explained those differences by a different atomic structure, and by a strongly interacting substrate.

We highlight through this work the influence of the substrate, whether metallic or semiconductor, on the electronic properties of 2D DNL systems.

Keywords : 2D materials, Dirac nodal lines, Topological semimetals, XPS, ARPES